STUDIES OF OPTICAL PARAMETRIC OSCILLATORS FOR THE ULTRAVIOLET AND VISIBLE SPECTRAL REGIONS

Angus Henderson

A Thesis Submitted for the Degree of PhD
at the
University of St Andrews

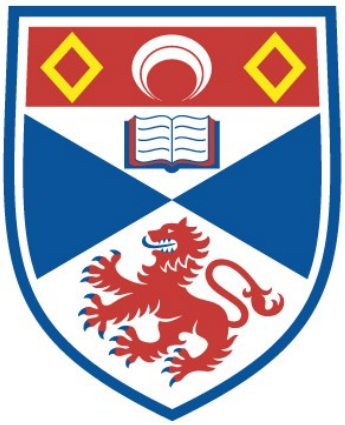

1993

Studies of optical parametric oscillators for the ultraviolet and visible spectral regions

A thesis submitted for the degree
of Doctor of Philosophy
to the University of St. Andrews
by
Angus Henderson, B. Sc.
September 1992

ProQuest LLC.
789 East Eisenhower Parkway
P.O. Box 1346
Ann Arbor, MI 48106 – 1346

Declarations

I hereby certify that this thesis has been composed by myself, that it is a record of my own work, and that it has not been accepted in partial or complete fulfilment of any other degree or professional qualification. I was admitted to the Faculty of Science of the University of St. Andrews under Ordinance General No. 12 on 1 October 1988.

In submitting this thesis to the University of St. Andrews, I understand that I am giving permission for it to be made available for use in accordance with the regulations of the University Library for the time being in force, subject to any copyright vested in the work not being affected thereby. I also understand that the title and abstract will be published, and that a copy of the work may be made and supplied to any bona fide library or research worker.

A. Henderson
September 1992

I hereby certify that the candidate has fulfilled the conditions of the Resolution and Regulations appropriate to the Degree of Ph. D.

M.H. Dunn
Research Supervisor
September 1992

Abstract

The work described herein concerns the characterisation and development of optical parametric oscillators (OPOs) tunable in the ultraviolet, visible and near infrared regions. These devices were pumped by the 308nm output from line-narrowed Xenon Chloride excimer lasers of pulse energy up to 150mJ.

The behaviour of Type 2 phase-matched Urea, and Type 1 phase-matched Barium Borate OPOs in terms of oscillation threshold and conversion efficiency, has been explored. The detrimental effects of pump beam walkoff on the threshold of the critically phase-matched Barium Borate OPO have been quantified. It was found that minimum 17ns pulse energies of 5mJ were required to reach threshold in a device based on a crystal of 20mm length. By contrast, noncritically phase-matched Urea OPOs using crystal lengths of 25mm were operated with as little as 0.6mJ pump energy. A deterioration in performance was observed in both cases with decreasing pump beam waist. Maximum pump depletions of 72% and 64% were observed in Urea and BBO respectively. The useful output from the urea device reached 65%, while higher absorption/scattering losses meant that the useful fraction in BBO was very much lower.

Two different types of noncollinear phase-matching were studied in the BBO-OPO. The first recorded observation of operation of a Type 1 OPO at crystal angles beyond the degenerate wavelength point was made. The output took the form of two concentric rings and was attributed to simultaneous singly and doubly resonant operation.

Finally, single longitudinal mode operation of the BBO-OPO was demonstrated using a dispersive cavity arrangement. The widely varying inherent linewidth of the device required that different strategies be adopted over different wavelength ranges. Encouraging performance in terms of threshold was observed using the dispersive cavity, and the feasibility of using this device as a low-power first stage for an oscillator/amplifier set-up was studied.

Acknowledgements

I would like to mention a number of people for their assistance and their patience during my time in St. Andrews. Thanks must go to my supervisor, Prof. Malcolm Dunn for imparting some of his wide-ranging knowledge of lasers, and for his general enthusiasm throughout the course of the project. I would like to acknowledge the work of Majid Ebrahimzadeh in developing the 30mJ excimer laser, for the initial success of work on parametric oscillators at St. Andrews. The cooperation of Gordon Robertson in collaborative work on Lithium Borate and on OPO linewidth control was much appreciated, as was the tolerance shown by Gordon and Sara during my occupation of their office. The mechanical workshop, and in particular Jim Clark must be thanked for fabrication of essential components for the OPO.

Finally, I would like to thank those in the department who shared extra-curricular entertainments either in the Whey Pat Tavern, the Athletic Union or on the St. Andrews Links. A particular debt is owed to Callum and Cameron, who helped maintain high morale through the general ineptitude of their golf!

Publications

A.J. Henderson, M. Ebrahimzadeh and M.H. Dunn, "Optical parametric oscillators pumped by excimer lasers", paper 180, in Technical Digest of The Ninth Quantum Electronics Conference, Oxford, UK, 1989.

A.J. Henderson, M. Ebrahimzadeh and M.H. Dunn, "Characterisation of urea optical parametric oscillators pumped by excimer lasers", J. Opt. Soc. Am. B **7**, p1402, 1990.

M. Ebrahimzadeh, A.J. Henderson and M.H. Dunn, "An excimer-pumped β-BaB_2O_4 optical parametric oscillator tunable from 354nm to 2.37μm", IEEE J. Quant. Elect. **QE-26**, p1241, 1990.

M. Ebrahimzadeh, G. Robertson, M.H. Dunn and A.J. Henderson, "Excimer-pumped LiB_3O_5 optical parametric oscillators", paper CPD26 in Conference on Lasers and Electro-optics, 1990 Technical Digest series Vol. 7 (O.S.A., Washington D.C. 1990).

G. Robertson, A.J. Henderson and M.H. Dunn, "Attainment of high efficiencies in optical parametric oscillators", Optics Letters **16**, p1584, 1991.

G. Robertson, A.J. Henderson and M.H. Dunn, "Broadly tunable LiB_3O_5 optical parametric oscillator", Applied Physics Letters **60**, p271, 1992.

A.J. Henderson, G. Robertson and M.H. Dunn, "Efficient line-narrowing of an excimer-pumped β-BaB_2O_4 optical parametric oscillator", paper CTuR2 in Conference on Lasers and Electro-optics, 1992 Technical Digest series Vol. 12 (O.S.A., Washington D.C. 1992).

A.J. Henderson and M.H. Dunn, "Simultaneous singly and doubly resonant noncollinear phase-matching in a β-BaB_2O_4 optical parametric oscillator", paper CTuK1 in Conference on Lasers and

Electro-optics, 1992 Technical Digest series Vol. 12 (O.S.A., Washington D.C. 1992).

A.J. Henderson and M.H. Dunn, "Noncollinear phase-matching in a β-BaB_2O_4 optical parametric oscillator", submitted to Applied Optics, July 1992.

G. Robertson, A.J. Henderson and M.H. Dunn, "Efficient, single-axial-mode oscillation of a beta-Barium-Borate optical parametric oscillator pumped by an excimer laser", submitted to Applied Physics Letters, July 1992.

Contents

Chapter 1 : Introduction

Chapter 2 : Theory of parametric interaction

Chapter 3 : Nonlinear materials for the UV-visible range

Chapter 1
Introduction

1.0 Introduction

The advent of the laser in 1960 brought about revolutionary progress in the field of optics and spectroscopy. The high power and spectral resolution of the device gave rise to the study of nonlinear phenomena which had been inaccessible using conventional optical sources. However, early lasers operated at fixed frequency, with tunability over only a few wavenumbers, and thus it was possible to probe transitions only in the laser medium itself. Hence considerable research has since gone into the development of "broadly tunable" sources which can be tuned through resonances of interest, at any point in the spectrum.

There now exists a wide variety of tunable sources which when allied with various frequency conversion techniques, provide coherent radiation across most of the spectrum from 100nm to 100μm (see fig. 1.1). Until recently the only practical source widely tunable in the ultraviolet (UV) and visible regions, capable of fulfilling the requirements for high average power and narrow linewidth, in applications such as photochemistry, lidar and isotope separation, has been the dye laser. The optical parametric oscillator (OPO), although having become an established method of producing exceptionally wide tunability in the infra-red, since its first demonstration in 1965, has had limited application to the UV and visible regions through the lack of nonlinear materials possessing suitable properties in terms of damage susceptibility, nonlinear coefficient and transparency. Recently development of such materials and of improved UV pump sources has stimulated a great deal of interest in exploiting a device which is inherently simple to operate, efficient, and can tune continuously through the equivalent of many dye bandwidths. In particular, the potential of OPOs pumped by excimer lasers, in terms of exceptionally wide tunability, has been clearly demonstrated. This thesis presents a detailed assessment

of the performance of these devices and their development as high power, narrow linewidth sources for the ultraviolet and visible spectral ranges. This chapter aims to put this work in context with alternative methods of generating tunable output in this part of the spectrum, and with contemporary research on parametric oscillators and the problem of producing line-narrowed output.

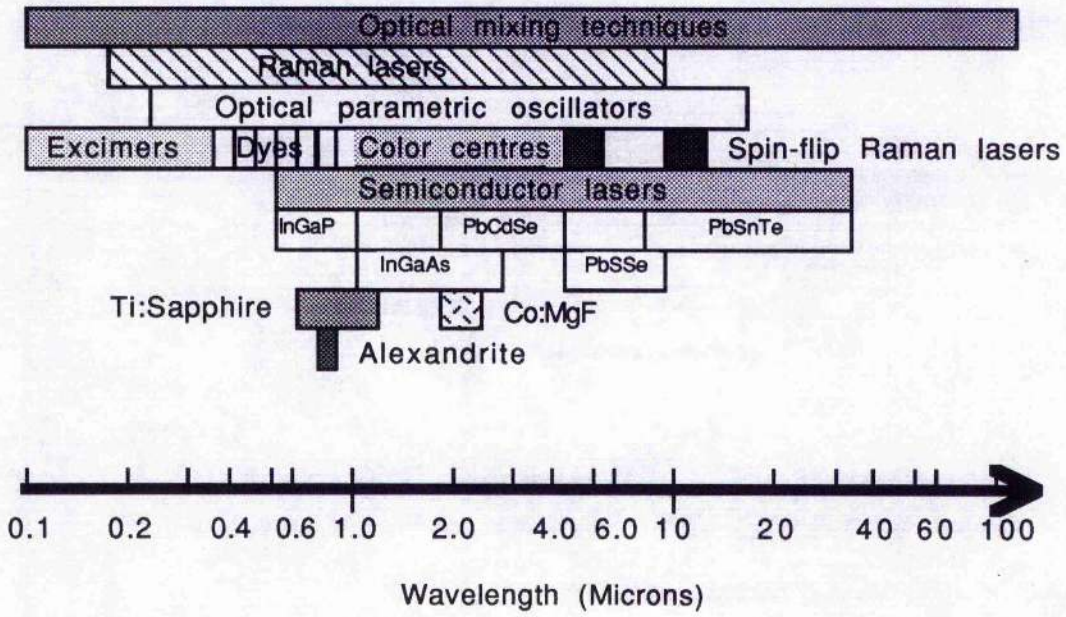

Fig. 1.1 Tuning ranges of currently available sources of tunable coherent radiation.

1.1 Tunable sources for the UV-visible range

The following sections describe the main characteristics of currently available methods for generation of widely tunable coherent radiation in the range 300 to 700nm.

1.1.1 The Titanium Sapphire laser

Lasing was first observed in Ti: Sapphire in 1982[1] and the laser has since become an established commercial product. Its tuning range extends from around 670nm to 1060nm (the equivalent of the tuning ranges of four dyes) and has been

demonstrated[2] to produce as much as 17W CW and 40W average power pulsed, at around 800nm. Continuous wave (CW) single longitudinal mode operation is easily attainable. Pump sources used are Argon ion, dye, frequency doubled Nd:YAG and Nd:YLF lasers, and flashlamps. The future development of suitable diode lasers offers a further attractive possibility as a pump source. As a source of tunable UV-visible output , frequency doubling of Ti: Sapphire offers a potential tuning range from 340nm to 530nm. Polzik and Kimble[3] have demonstrated generation of 0.65W CW single frequency blue light at around 430nm by conversion of 1.35W from a Ti: Sapphire laser. Similar conversion efficiencies have been demonstrated in the pulsed regime[4]. It must be noted, however that these two ranges leave a 'hole in the middle' of inaccessible wavelengths from 530 to 670nm.

1.1.2 Semiconductor lasers

Semiconductor diode lasers are commercially available at almost any wavelength between 650nm and 1.5μm. Diffraction limited output is attainable in a single spatial mode with power levels up to around 100mW and with typical electrical-to-optical efficiency of 35%[2]. Emission is typically on three to six longitudinal modes although single mode operation is attainable through the inclusion of a grating structure in the waveguide. Tuning is accomplished by changing the bandgap through alteration of temperature or magnetic field, and tuning ranges of several tens of nanometres are possible. Furthermore the centre wavelength of emission can be initially chosen by altering the dopant composition. Production of visible laser diodes has been limited by the difficulty of producing high quality wide-bandgap material selectively n-type and p-type. Although some demonstrations of operation of blue diodes have been made, it is likely to be a considerable time before they are commercially available. Extension into the visible region looks more likely to come from direct frequency doubling of laser diodes. Recently[5] electrical to optical conversion efficiencies of 10% have been demonstrated, producing 39mW of 423nm light from 101mW of single axial mode input at 858nm. The compact, solid state nature

of laser diodes, coupled with the ability to scale power levels using arrays of such devices, make diode lasers extremely practical tunable sources.

1.1.3 Dye lasers

The dye laser[6] currently holds a position of pre-eminence as a commercially available spectroscopic source for the UV and visible regions. Using several different dye types (coumarins, rhodamines, oxazines etc.) and various solvents the spectral region from 350 to 1000nm can be covered. A single dye/solvent combination typically can be tuned several hundred wavenumbers away from the spectral peak of the gain curve. Dye lasers fall into three broad technology categories as follows. Continuous wave jet-streamed dye lasers can provide narrow CW bandwidths (subMHz) and can be synchronously pumped or passively mode-locked to generate short (below 250fs) pulses. Flashlamp-pumped dye lasers have a larger bandwidth and less wavelength stability than CW laser-pumped dye lasers, but have the advantage that large volumes of active dye medium can be pumped yielding large output pulse energies (up to 50J) and average powers (50W). Dye lasers pumped by the ultraviolet output from pulsed nitrogen or excimer lasers or by the frequency-doubled or tripled output from pulsed Nd:YAG lasers provide high brightness, narrow linewidths (0.002nm) and high peak powers.

1.1.4 Other tunable sources

Molecular excimer lasers[7] should be mentioned since their output is in the difficult ultraviolet range, and because they can produce high pulse energies (1J) at high efficiency (4%) and with narrow linewidth ($0.2cm^{-1}$). Wavelengths of 193, 249, 308 and 351nm and tuning ranges of around 2nm are accessible.

Other tunable sources which should be mentioned in the context either of their potential for frequency doubling or direct generation in the UV-visible range, are Alexandrite[8], colour centre[8] and Raman lasers.

The Alexandrite laser is one of the family of 'vibronic' lasers, to which the Ti: Sapphire and Co:MgF_2 lasers also belong, and has likewise been commercially developed. Its tuning range is a subset of that of the Ti: Sapphire laser, from around 700nm to 800nm, and it possesses one notable advantage over that device in its ability to be effectively flashlamp pumped, producing considerably higher average powers (up to 100W). CW operation is however difficult to obtain.

The main drawback to the colour centre laser is the need for cryogenic cooling of the alkali halide crystal. Although tuning ranges in different crystals span 0.8μm to 4μm, many of these materials are chemically unstable and commercial devices are available only for tuning ranges around 1.5μm and between 2.3 and 3.5μm.

Raman lasers[11] operate through the process of stimulated Raman scattering, such that photon energy at an available laser wavelength is partitioned between scattered 'Stokes photons' and excitation energy of molecules. The possibility of scattering by molecules in excited vibrational levels, gives rise to Anti-Stokes generation by which the pump photons may in fact be shifted upwards in frequency, rather than downwards as is the case for Stokes generation. Raman shifting has most commonly been demonstrated in Hydrogen gas, with efficiencies of conversion to the first Stokes line in tens of percent. However, although Raman shifting allows access to wavelengths from the infrared to the vacuum ultraviolet, continuous tunability is dependent on the use of a tunable pump source. Furthermore the necessity for a high pressure gas cell makes the Raman laser unattractive in some applications.

1.1.5 Optical parametric oscillators

Figure 1.2 illustrates schematically the configuration of the optical parametric oscillator and reveals a basic resemblance to the conventional laser. Both convert energy from a primary source, to coherent radiation through light amplification in a resonant cavity. However in an OPO, tunable radiation is generated through an entirely different process. By contrast to the

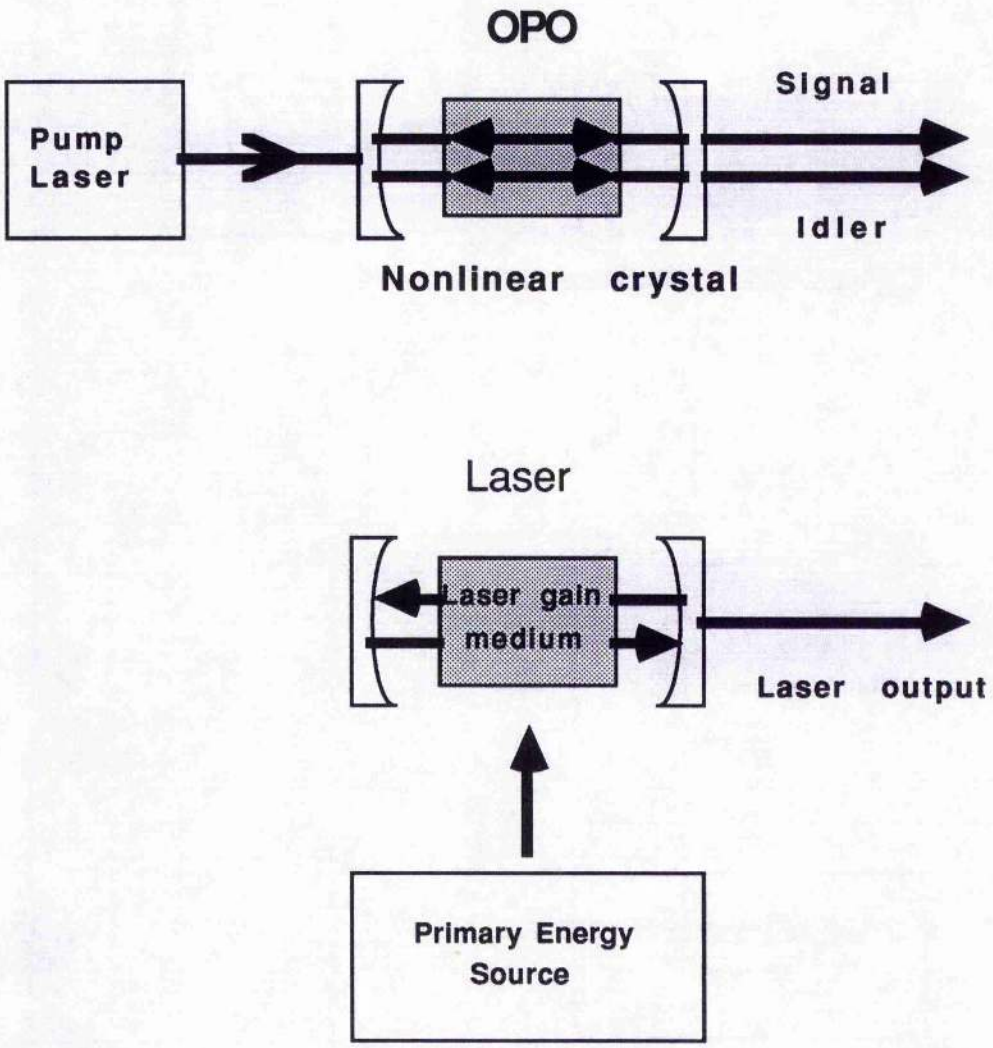

Fig. 1.2 Schematic diagram of the configurations of the optical parametric oscillator and the laser oscillator.

laser, parametric generation is an instantaneous process, without any means of energy storage. Output is produced simultaneously at two distinct wavelengths, rather than one, and while the initial energy source for a laser can take various forms, the pump source for an OPO is constrained to be a high intensity source of coherent radiation in its own right.

The OPO is inherently an extremely compact, all-solid-state device-the cavity need initially be no longer than the nonlinear crystal contained therein (typically several cm). A single nonlinear material and pump wavelength can provide close to a decade of continuous tuning, and different materials extend tuning

throughout the range 250nm to 16μm. Devices can be operated in pulsed mode or continuously, such that the temporal nature of the output reflects that of the pump source. Conversion efficiency can in theory reach unity and so power levels are again limited only by those of the pump source and by the damage capabilities of the OPO components-average powers in Watts are quite possible. Several different coarse and fine tuning methods can be used, and single longitudinal mode operation can be achieved (see chapter 7). Drawbacks to the OPO include: the difficulty of obtaining frequency-stable CW output, the fact that one 'unwanted' output is always generated, and its critical dependence on the coherence properties of a tightly constrained pump source.

1.1.6 Conclusion

The long availability and resulting advanced state of development of the dye laser makes it clearly the most accessible spectroscopic source for the visible region and for some way into the ultraviolet. However the use of dyes of short useful lifetime and unknown toxicity make these rather 'user unfriendly' devices. The compactness and solid state nature of diode and Ti: Sapphire lasers allied to the potential extension of tuning ranges through frequency conversion techniques, make them feasible alternatives over restricted tuning ranges. The optical parametric oscillator has long been recognised as potentially offering a combination of most of the attractive features of these sources, and providing much wider continuous tuning. Recent advances in ultraviolet pump sources and particularly in UV-transmitting nonlinear materials have meant that the UV-visible OPO is already a practical source in this spectral region. It thus seems likely that in the near future, the OPO will become a commercial instrument of great importance in the field of tunable lasers.

1.2 Recent development of the parametric oscillator

Research on optical parametric oscillators has been in progress since 1961 when Franken et al.[12] demonstrated second

harmonic generation, stimulating work throughout the field of nonlinear optics. The first experimental demonstration of an OPO was in 1965 when a pulsed device was operated by Giordmaine and Miller[9]. CW operation was shown shortly afterwards[10] and in the following decade a very considerable amount of research was devoted to the operation of the OPO. Comprehensive surveys of the work done in this period can be found in the review papers by Smith[14], Byer[15] and Harris[16].

The body of work on parametric generation can be separated into three main categories:

(1) Continuous wave OPOs pumped by CW laser sources.

(2) Pulsed OPOs pumped by Q-switched solid state lasers or nanosecond pulse gas lasers.

(3) Ultrashort pulsed optical parametric generation using mode-locked lasers as pump sources.

In each case the possible schemes for generation of tunable coherent radiation are determined by the properties of the available pump sources and nonlinear media. The nature of the parametric process dictates that an OPO pump source should:

(a) be of wavelength lower than those of the desired tuning range;

(b) possess narrow linewidth and low beam divergence with respect to the requirements of the particular nonlinear material.

In addition, the nonlinear material is required to possess:

(a) a sufficiently high effective nonlinear coefficient to allow achievement of threshold for OPO operation , in crystal lengths and for pump powers available;

(b) a wide transparency range with corresponding low absorption at pump and output wavelengths;

(c) dispersion and birefringence allowing phase-matching conditions to be satisfied;

(d) an optical damage threshold allowing operation well above OPO threshold pumping levels.

Clearly, relatively few materials fully satisfy these requirements, and it has largely been through the inadequacy of nonlinear materials that the OPO has never become an established commercial device. However, as stated in the review paper by Fischer and Kulevskii[13], between 1965 and 1977 continuous

tuning from 0.4μm to 16μm had been shown to be accessible using parametric oscillators based on the materials Ammonium Dihydrogen Phosphate (ADP), Lithium Niobate ($LiNbO_3$), Proustite($AgAsS_3$), and Cadmium Selenide (CdSe).

In general, by far the most satisfactory material up to 1977 had been $LiNbO_3$, due to its high nonlinear coefficient and availability in large high quality samples. CW OPOs had been demonstrated in $LiNbO_3$[17] and Barium Sodium Niobate[18] ($Ba_2NaN_5bO_{15}$) pumped either by Argon-ion or frequency-doubled Nd:YAG lasers, over restricted tuning ranges from 600nm upwards. However, the requirement to operate as a doubly resonant oscillator (DRO) produced undesirable frequency tuning and stability problems. Pulsed oscillators meanwhile, being generally operated as singly resonant oscillators (SRO), avoided these problems, and were mainly restricted by crystal damage at high peak pump powers. This was particularly true in the UV-visible end of the spectrum, where ADP, and KDP (Ammonium and Potassium diHydrogen Phosphate) were the most prevalent materials.

The most significant developments since 1977 have come almost entirely through the arrival of new nonlinear materials. From 1983 onwards an enormous amount of interest in OPOs for the UV-visible region has been stimulated by the reported properties of firstly urea, followed by β-Barium Borate (BBO) and Lithium Borate(LBO). Meanwhile, improvement in the growth techniques of Potassium Niobate[19] ($KNbO_3$) and the development of Potassium Titanyl Phosphate[20] have made these crystals viable alternatives to $LiNbO_3$ for generation of wavelengths from 0.7μm to 3μm. In the range 2μm to 8μm, pulsed parametric oscillation has been demonstrated in Silver Gallium Selenide[21] ($AgGaSe_3$) , with operation comfortably below damage limits. Magnesium Oxide-doped Lithium Niobate ($MgO:LiNbO_3$) has the advantages of slightly improved damage properties , accessibility of 90° phase-matching and hence efficient temperature tuning , over the undoped material. This material has been put to several different applications, including demonstration of a low threshold, CW monolithic OPO[22]. The monolithic design, with cavity reflectors coated directly onto the crystal surfaces, ensures a low loss at the

resonant waves, essential for CW operation. Use of a stable, single mode, diode-pumped laser as pump source also ensured that this completely solid-state device had much improved frequency stability and tuning properties.

There has, meantime, been a proliferation of work on ultrashort pulse OPOs. Tunable radiation of around 100fsec pulse duration has been generated using dispersion compensation, in a CW-mode-locked intracavity KTP OPO[23] , and separately in a BBO OPO[24] synchronously pumped by pulse trains from a mode-locked laser. Externally pumped CW femtosecond OPOs in KTP have recently been reported by two separate groups[55,56], with pulse lengths as short as 75fs.

In the picosecond pulse regime, synchronous pumping by Q-switched mode-locked lasers has variously been demonstrated in BBO[25], KTP[26], $Ba_2NaNb_5O_{15}$[27], $LiNbO_3$[28] and KDP[29], while CW mode-locked lasers have been used as the pump sources for devices in $Ba_2NaNb_5O_{15}$[57] and LBO[58]. The technique of parametric amplification in one nonlinear crystal of a narrow band of parametric superluminescence generated in a second crystal, has been employed in BBO[30], LBO[31], $AgGaS_2$[32],Proustite[35], ADP[33], and $LiNbO_3$[36], when pumped by picosecond pulses.

1.3 OPOs for the UV and visible ranges

1.3.1 Visible-UV nonlinear materials

Visible and ultraviolet parametric oscillation prior to the 1980s was limited to a few demonstrations involving ADP[36] and KDP[37] pumped by the third and fourth harmonics of Nd lasers. These materials proved to be quite seriously flawed by the proximity of their UV damage threshold to the OPO threshold pump power level. The first material to offer the promise of reliable operation throughout the visible range was the organic compound Urea. The first OPO based on Urea was developed by Donaldson and Tang[38] in 1984. It was pumped by a frequency-tripled Nd:YAG laser at 355nm and had tuning ranges of 498-640nm and 1.23-0.79μm at a maximum of 24% efficiency. The

first demonstration of excimer pumping of OPOs[39], in our own laboratories, involved Urea. This work was to lead to remarkable external efficiencies of 66%[40] at noncritical phase matching, and a tuning range from 537-720nm. Despite its undoubted merits, questions over the long-term damage resistance of Urea, and the development in China of the new UV-damage-proof materials, BBO and LBO, meant that interest in Urea has been perhaps prematurely superseded.

Type I[41] and Type II[42] phase-matched OPOs have been operated in BBO, with high efficiency, high average power[41], narrow linewidth[43] and extremely wide tuning range[41]. Multishot damage resistance appears to be much greater than in Urea, and UV wavelengths can be accessed more easily.

The biaxial nature of the LBO crystal provides several tuning options in the different principal planes. Critical phase-matching is possible over a range similar to that of Type I phase-matching in BBO , and room temperature non-critical phase-matching (NCPM) at UV output wavelengths can be achieved when pumped by 308nm excimer radiation[44,45]. LBO shows improved damage resistance, higher crystal quality than BBO but its lower nonlinear coefficient means that both materials probably have a role to play as UV-visible nonlinear materials.

A comprehensive assessment of the available nonlinear materials for the generation of UV-visible wavelengths can be found in chapter 3.

1.3.2 Pump sources for UV-visible OPOs

Until 1988, the requirement of an OPO for high power, narrow linewidth and low beam divergence in its pump source, meant that only frequency-converted Neodymium lasers were suited to the task. However the development and commercial introduction of line-narrowed excimer lasers was of considerable interest in extending OPO tuning ranges further into the UV region. Excimer lasers currently hold the following advantages over the conventional frequency converted Nd: YAG laser:

(1) Considerably higher electrical to optical efficiency

(2) Higher pulse and average power

(3) Wide range of pump wavelengths

Our work on excimer-pumping of OPOs has demonstrated beyond doubt that equivalent if not superior performance can be obtained in comparison to Nd:YAG pumping, and that the excimer is likely to remain for some time to come, the better option as a pump source for a high average power UV OPO.

However the rapid advances being made in terms of output power and cost, in diode-pumping of solid-state lasers, allied to the use of BBO and LBO in efficient frequency conversion to the UV, give the promise of all solid state UV-visible OPOs genuine appeal. The first holosteric visible OPO has, in fact, recently been demonstrated[46], using a diode-pumped Nd:YAG laser, frequency tripled in LBO and BBO, to pump an NCPM LBO device. Such success gives rise to the expectation that the high crystal quality of LBO may allow the development of a holosteric CW UV-Visible source in the near future.

1.4 Line-narrowing of OPOs

Bandwidth narrowing techniques for lasers are by now well established. Single longitudinal mode operation allows linewidths of around 1MHz to be accessed. The relatively wide tunability of dye lasers allied to frequency stable output of such linewidths has produced new opportunities in high resolution spectroscopy. Thus the frequency control of OPOs, with their potential for extremely wide tunability and high average power, is an important issue.

A library of laser line-narrowing techniques, summarised in references 47-49 , is available for transfer to frequency control of OPOs. Relatively little work has been done on OPO cavity line-narrowing , with the majority of experiments involving $LiNbO_3$ infrared devices[50-54]. However single longitudinal mode operation using grating and etalon methods has been observed on several occasions in $LiNbO_3$[60-63], and more recently in KTP[59]. Work on visible OPOs has been restricted to one demonstration of grating cavity narrowing which was limited by resulting threshold increase[43].

A more considerable body of work exists involving line-narrowing of OPOs by injection-seeding. This is a very familiar technique for producing narrowband laser radiation, and although many injection-seeded parametric devices have accurately reproduced the bandwidth of the seed source, there exists little thorough quantitative work on required signal energies and dependence on other parameters.

Our work on line-narrowing of a BBO-OPO is aimed at filling a clear need to produce a reliable, efficient, narrow-line OPO for the visible and ultraviolet regions. We have harnessed both cavity-line-narrowing and injection-seeding techniques to achieve single longitudinal mode operation.

1.5 Thesis outline

This thesis is organised as follows. A brief summary of the essential theory of parametric interaction is presented in chapter 2. The relative merits of the different nonlinear materials for the generation of tunable radiation in the UV-visible region are described in chapter 3, with reference to the properties discussed in the previous chapter. Chapter 4 describes the experimental arrangement of the pump laser and OPO. Chapters 5 and 6 provide a characterisation of urea and BBO OPOs in terms of oscillation threshold and conversion efficiency respectively. Chapter 7 considers the progress made in producing a line-narrowed UV-visible OPO. Noncollinear phase-matching in a BBO OPO is described in chapter 8 and the final chapter discusses future work and provides some conclusions on the project as a whole.

1 Solid state research report, Lincoln Laboratory MIT 1982-3, p15.
2 Laser Focus World, **27**, p144 (1991).
3 E.S. Polzik and H.J. Kimble, Opt lett.**16**, p1400 (1991).
4 P.F. Curley and A. I. Ferguson, Opt. comm. **80**, p365 (1991).
5 Laser Focus World **25**(9), p36 (1989).
6 Laser Focus World **26**(2), p57 (1990).
7 Laser Focus World **26**(9), p71 (1990).
8 W. Koechner, Solid-state Laser Engineering, Springer-Verlag Berlin, p66 (1988).
9 J.A. Giordmaine and R.C. Miller, Phys. Rev. Lett. **14**, p973 (1965).
10 R.G. Smith et al., Appl. Phys. Lett. **12**, p308 (1968).
11 J.C. White, in Tunable Lasers, Springer-Verlag Berlin, p115 (1987).
12. P. A. Franken et al. Phys. Rev. Lett. **7**, p118 (1961).
13. R. Fischer and L. A. Kulevskii, Sov. J. Quant. Elect. **7** , p135 (1977).
14. R. G. Smith, in "Lasers", Vol. 4. Edited by A.K. Levine and A. J. De Maria. Marcel Dekker, New York (1976).
15. R.L. Byer, Chapter 9, "Optical Parametric Oscillators", in "Quantum Electronics: a treatise". Edited by H. Rabin and C. L. Tang (Academic, New York) Vol. 1, Pt B, pp 587-702.
16. S. E. Harris, Proceedings of the IEEE **57** , p2096 (1969).
17. R. L. Byer, A. Kovrigin, and J. F. Young, Appl. Phys. Lett. **15**, p136 (1969).
18. R.G. Smith, IEEE J. Quant. Elect. **QE-9**, p530 (1973).
19. K. Kato, IEEE J. Quant. Elect. **QE-18**, p451 (1982).
20. K. Kato, IEEE J. Quant. Elect. **QE-27**, p1137 (1991).
21. R. C. Eckardt et al., Appl. Phys. Lett. **49** , p608 (1986).
22. C.D. Nabors et al. Opt. Lett. **14** , p1134 (1989).
23. E. S. Wachman, D. C. Edelstein and C.L. Tang, Opt. Lett. **15** , p136 (1990).
24. R. Laenen, H. Graener and A. Laubereau, Opt. Lett. **15**, p971 (1990).
25. S. Burdulis et al., Opt. Comm. **74**, p398 (1990).
26. L. J. Bromley, A. Guy and D.C. Hanna, Opt. Comm. **70**, p350 (1989).
27. A. Piskarskas, V. Smilgevicius and A. Umbrasas, Opt. Comm. **73** , p322 (1989).

28. R. Laenen, A. Graener and A. Laubereau, Opt. Comm. **77**, p226 (1990).
29. B. Bareika et al. Sov. J. Quant. Elect., **13**, p1507 (1983).
30. J.Y. Huang et al. Appl. Phys Lett. **57**, p1961 (1990).
31. J.Y. Huang et al. Appl. Phys Lett. **58**, p1579 (1991).
32. T. Elsaesser et al., Appl. Phys Lett. **44**, p383 (1984).
33. R. Danyelus et al., Sov. J. Quant. Elect. **8**, p398 (1978).
34. W. Kranitzky et al., Opt. Comm. **34** , p483 (1980).
35. T. Elsaesser, A. Seilmeier and W. Kaiser, Opt. Comm. **44**, p293 (1983).
36. J. M. Yarborough and G. A. Massey, Appl. Phys. Lett. **18**, p438 (1971).
37. S. A. Akhamanov et al. Modern Optics **17**, Polytechnic Press, New York p343.
38. W.R. Donaldson and C. L. Tang, Appl. Phys Lett. **44**, p25 (1984).
39. M. Ebrahimzadeh and M. H. Dunn in Postdeadline Papers, Conference on Lasers and Electro-optics (Opt. Soc. Am., Washington D. C. 1988) Paper PD30.
40. A. J. Henderson et al., J. Opt. Soc. Am. B **7**, p1402 (1990).
41. G. Robertson, A. Henderson and M.H. Dunn, Opt. Lett. **16**, p1584 (1991).
42. W.R. Bosenberg and C.L. Tang, Appl. Phys Lett. **56**, p1819 (1990).
43. W.R. Bosenberg, W. S. Pelouch and C.L. Tang, Appl. Phys Lett. **55**, p1952 (1989).
44. G. Robertson, A. Henderson and M.H. Dunn, Appl. Phys. Lett. **60**, p271 (1992).
45. M. Ebrahimzadeh, G. Robertson, M.H. Dunn and A. J. Henderson in Tech. Dig., Conference on Lasers and Electro-optics (Opt. Soc. Am., Washington D. C. 1990) Paper CPDP21.
46. Y. Cui et al., Opt Lett. **17**, p646 (1992).
47. D. A. Kleinmann, P. P. Kisliuk, Bell System Technical Journal, p453 (1962).
48. P.W. Smith, Proc. of the IEEE **60**, p422 (1972).
49. M. G. Littman and H. J. Metcalf, Appl. Opt. **17**, p2224 (1978).
50. D. Andreou, Opt. Comm. **27**, p171 (1978).
51. L.B. Kreuzer, Appl. Phys Lett. **15**, p263 (1969).

52. J.F. Pinard and J.F. Young, Opt. Comm. **4**, p425 (1972).
53. S.J. Brosnan and R. L. Byer, IEEE J. Quant. Elect. **QE-15**, p415 (1979).
54. T. K. Minton et al. Opt. Comm. **69**, p289 (1989).
55. W.S. Pelouch, P.E. Powers and C.L. Tang in Tech. Dig., Conference on Lasers and Electro-optics (Opt. Soc. Am., Washington D. C. 1992) Paper CPD14.
56. G. Fu, G. Mak and H.M. van Driel in Tech. Dig., Conference on Lasers and Electro-optics (Opt. Soc. Am., Washington D. C. 1992) Paper CWD1.
57. A. Piskarskas, V. Smil'gyavichyus and A. Umbrasas, Sov. J. Quant. Elect. **18**, p155 (1988).
58. A. Robertson, G.P.A. Malcolm, M. Ebrahimzadeh and A.I. Ferguson in Tech. Dig., Conference on Lasers and Electro-optics (Opt. Soc. Am., Washington D. C. 1992) Paper CPD15.
59. W.R. Bosenberg, D.R. Guyer, S.E. Moody in Tech. Dig., Conference on Lasers and Electro-optics (Opt. Soc. Am., Washington D. C. 1992) Paper CWQ1.
60. L.B. Kreuzer, Appl. Phys. Lett. **15**, p263 (1969).
61. J. Pinard and J.F. Young, Opt. Comm. **4**, p425 (1972).
62. A. Hordvik and P.B. Sackett, Appl. Opt. **13**, p1060 (1974).
63 S.J. Brosnan and R.L. Byer, IEEE J. Quant. Elect., **QE-15**, p.415 (1979).

Chapter 2
Theory

2.0 Introduction

This chapter shows how second order nonlinear optical interactions lead to the possibility of parametric amplification, and sets out the essential equations describing this process. Since comprehensive reviews[1,2,6] on this topic are available, this section is kept fairly brief. The remainder of the material presented here is restricted in scope to those aspects of the theory which allow an understanding of the selection process for nonlinear materials and pump sources for optical parametric oscillators, and of those characteristics of OPO operation examined in chapters 5 to 8. The analysis is performed using the MKS system of units, as in ref. 1.

2.1 Parametric amplification

2.1.1 Three-wave parametric interaction

Propagation of electromagnetic radiation in a dielectric medium induces a polarisation wave which is normally described by the relation

$$\underline{P} = \varepsilon_0 \chi^{(1)} \underline{E}\,, \qquad (2.1)$$

where ε_0 is the free space permettivity, $\chi^{(1)}$ is the linear susceptibility and $\underline{E}$ the applied field. However, for intense fields this linear approximation may no longer be appropriate, and the polarisation may also involve higher powers of the field strength E. These higher order terms in the polarisation can couple together harmonic fields of different frequencies; for example the polarisation component proportional to E^2 can couple together two waves to generate a third (three wave mixing). Parametric amplification is one example of this three-wave nonlinear interaction involving the transfer of energy between fields of

distinct frequencies , via the second order nonlinear polarisation which may be induced in certain noncentrosymmetric crystals. This nonlinear polarisation may be expressed as

$$\underline{P}_i = \varepsilon_o \sum_{jk} \chi^{(2)}_{ijk} : \underline{E}_j \underline{E}_k \ , \qquad (2.2)$$

where the subscripts refer to the cartesian components of the various fields. $\chi^{(2)}_{ijk}$ are the components of the nonlinear polarisability tensor $\chi^{(2)}$, which characterises the second order nonlinearity of the material. The components $\chi^{(2)}_{ijk}$ of $\chi^{(2)}$ can alternatively be listed using the d notation, such that $\chi^{(2)}_{ijk} = 2d_{ijk}$. The d coefficients are generally given in a simplified form involving only two subscripts, such that

$$d_{i(jk)} \equiv d_{im} \ ,$$

where the subscripts are related as follows:

(jk) =	(11)	(22)	(33)	(23)	(13)	(12)
m =	1	2	3	4	5	6

In general for a specific interaction geometry, the generation of a nonlinear wave depends on a single effective nonlinear coefficient d_{eff} which involves the projection of all the three field eigenvectors onto the d tensor. Expressions for the effective nonlinear coefficients d_{eff} in terms of the d coefficients and the wave propagation directions have been tabulated for the different crystal classes in ref. 3.

In a three field interaction we assume fields at frequencies ω_j (j = 1,2,3) propagating along the z-direction, given by

$$\underline{E}_j = \frac{1}{2} \{ \underline{\mathcal{E}}_j(z) \exp[\, i\,(k_j z - \omega_j t + \varphi_j)\,] + c.c. \}, \qquad (2.3)$$

where $\underline{\mathcal{E}}_j(z)$ are the complex amplitudes of the fields, φ_j are the initial phases, k_j are the propagation constants given by

$$k_j = \frac{\omega_j n_j}{c} \quad , \tag{2.4}$$

and

$$\omega_3 = \omega_1 + \omega_2 . \tag{2.5}$$

The refractive indices are n_j and c is the speed of light. Substitution into Maxwell's equations, subject to the assumption that the field amplitudes change slowly over the interaction length (i.e. $k\partial\mathcal{E}/\partial z >> \partial^2\mathcal{E}/\partial z^2$), gives us a set of coupled differential equations, which we may write in a form specific to the case of parametric amplification, namely

$$\begin{aligned}
\frac{d\mathcal{E}_s(z)}{dz} + \alpha_s \mathcal{E}_s(z) &= i\kappa_s \mathcal{E}_p(z)\, \mathcal{E}^*_i(z)\, \exp[i(\Delta kz + \varphi)] \\
\frac{d\mathcal{E}_i(z)}{dz} + \alpha_i \mathcal{E}_i(z) &= i\kappa_i \mathcal{E}_p(z)\, \mathcal{E}^*_s(z)\, \exp[i(\Delta kz + \varphi)] \\
\frac{d\mathcal{E}_p(z)}{dz} + \alpha_p \mathcal{E}_p(z) &= i\kappa_p \mathcal{E}_i(z)\, \mathcal{E}_s(z)\, \exp[-i(\Delta kz + \varphi)]
\end{aligned} \tag{2.6}$$

where the subscripts (j = 1,2,3) have been replaced by those referring to pump, signal, and idler fields (j = p,s,i). α_j are the field absorption coefficients, $\Delta k = k_p - k_s - k_i$ is the phase mismatch, κ_j are the interaction coefficients defined by

$$\kappa_j = \frac{\omega_j d_{eff}}{n_j c} \quad , \tag{2.7}$$

and $\varphi = \varphi_p - \varphi_s - \varphi_i$ is the initial phase difference between the three fields. In general, of course, these coupled equations describe all types of three wave, second order nonlinear interaction, i.e. sum and difference frequency mixing, and second harmonic generation. The direction of energy transfer between the three fields is in each case determined by their initial relative phases.

2.1.2 Solutions of the coupled equations for parametric amplification

Solutions of the coupled equations for the case of parametric amplification, through which energy is transferred from an intense high frequency pump field to lower frequency signal and idler fields, are usually developed assuming negligible depletion of the pump field by those of the signal and idler. The solutions in terms of the plane wave power densities at signal and idler S_s and S_i.are

$$S_s(z) = \frac{S_o}{\Gamma^2}\{[\Gamma\cosh(\Gamma z)+ \Gamma_o r\sin\varphi\sinh(\Gamma z)]^2 + (\frac{\Delta k}{2} - \Gamma_o r\cos\varphi)^2 \sinh^2(\Gamma z)\} \quad (2.8)$$

and

$$S_i(z) = \frac{\omega_s}{\omega_i}\frac{S_o}{\Gamma^2}\{([\Gamma r\cosh(\Gamma z) + \Gamma_o \sin\varphi\sinh(\Gamma z)]^2 + (\Gamma_o r\cos\varphi - \frac{\Delta k}{2} r)^2 \sinh^2(\Gamma z)\}\ , \quad (2.9)$$

where

$$\Gamma_o^2 = \pi K S_p\ , \quad (2.10)$$

$$K = \frac{2\omega_s\omega_i d_{eff}^2}{\pi c^2 n_p n_s n_i} Z_o\ , \quad (2.11)$$

$$\Gamma^2 = \Gamma_o^2 - \left(\frac{\Delta k}{2}\right)^2\ , \quad (2.12)$$

$$S_o = S_s(z=0) = \frac{n_s|\mathcal{E}_s(0)|^2}{2Z_o}\ , \quad (2.13)$$

$$r = \frac{\omega_s}{\omega_i}\frac{S_i(z=0)}{S_o}\ , \quad (2.14)$$

and

$$Z_o = \sqrt{\frac{\mu_o}{\varepsilon_o}}\ . \quad (2.15)$$

Γ_o is the maximum gain constant, Γ is the reduced gain constant, S_o is the incident signal power density at $z = 0$, and r is the ratio of incident signal to idler photon density. These solutions can be used to develop an expression for the single pass signal power gain for an interaction length ℓ, i.e.

$$G_s = \frac{S_s(\ell)}{S_s(0)} \quad . \tag{2.16}$$

The signal gain is usually calculated on the assumption that only the signal frequency is incident on the crystal i.e. $\underline{\mathcal{E}}_i(0) = 0$. The gain in the case where input fields at both frequencies are incident, is dependent on their relative phases. For the former case,

$$G_s(r = 0) = 1 + \frac{\Gamma_o^2}{\Gamma^2}\sinh^2(\Gamma\ell) \tag{2.17}$$

Thus the gain is dependent on the pump power level and on the phase mismatch Δk. In the low gain limit where $\Gamma_o^2 < (\Delta k/2)^2$, (2.17) becomes

$$G_s(r = 0) = 1 + \Gamma_o^2\,\ell^2\,\mathrm{sinc}^2(|\Gamma^2|^{1/2}\,\ell) \tag{2.18}$$

and for $\Gamma_o^2\,\ell^2 << 1$ this can be written

$$G_s(r = 0) = 1 + \Gamma_o^2\,\ell^2\,\mathrm{sinc}^2(\Delta k\ell/2) \quad . \tag{2.19}$$

2.1.3 Phase-matching in parametric amplification

Parametric amplification is constrained by the requirements of energy conservation, expressed by the relation

$$\omega_p = \omega_s + \omega_i \tag{2.20}$$

and by conservation of momentum, such that

$$\underline{k}_p = \underline{k}_s + \underline{k}_i \ . \qquad (2.21)$$

Expression (2.12) shows the strong dependence of parametric gain on the phase mismatch Δk, or equivalently on deviation from the phase-matching condition (2.21). Maximum gain is obtained for zero phase mismatch

$$\underline{\Delta k} = 0 \ . \qquad (2.22)$$

In this state, the electromagnetic fields and their nonlinear polarisation source terms are perfectly in phase throughout their propagation through the crystal. In a dispersive medium, the phase matching condition will not in general be satisfied and Δk may be large. In a parametric amplifier, compensation for dispersion is most commonly achieved through the birefringence of the nonlinear material. In birefringent crystals the index of refraction of a wave is dependent on frequency, sense of polarisation, and direction of propagation with respect to the crystal axes. Figure 2.1(a) shows the typical pattern of variation of the refractive index experienced by waves linearly polarised along each of the three principal optical axes x, y and z (known as the principal refractive indices) of a crystal. In uniaxial crystals, two of the principal refractive indices are equal, or degenerate, and the degenerate and nondegenerate refractive indices are known as the principal ordinary and extraordinary indices n_o and n_e, respectively. If we assume, for the moment, collinear interaction the phase matching condition can be rewritten in the scalar form

$$n_p\omega_p = n_s\omega_s + n_i\omega_i \ . \qquad (2.23)$$

From this it can be seen, for example, that phase-matching is not possible when both $n_p > n_i$ and $n_p > n_s$. For three given frequencies and for a given direction of propagation phase-matching is possible only for certain combinations of polarisations. In uniaxial nonlinear crystals, with which this text is principally concerned, the two eigen-polarisations associated with any general propagation direction are denoted ordinary and

extraordinary polarisations. The ordinary wave is that polarised such that the refractive index is independent of the direction of propagation, while the extraordinary wave, by contrast, experiences a refractive index dependent on the wave normal direction. The extraordinary refractive index is a function of the direction of propagation and of the two principal refractive indices associated with the plane of rotation of the pump beam. The refractive index $n_e(\theta)$ for an extraordinary wave propagating at an angle θ to the optic axis (the direction of propagation for which both polarisations experience equal refractive indices) is given by

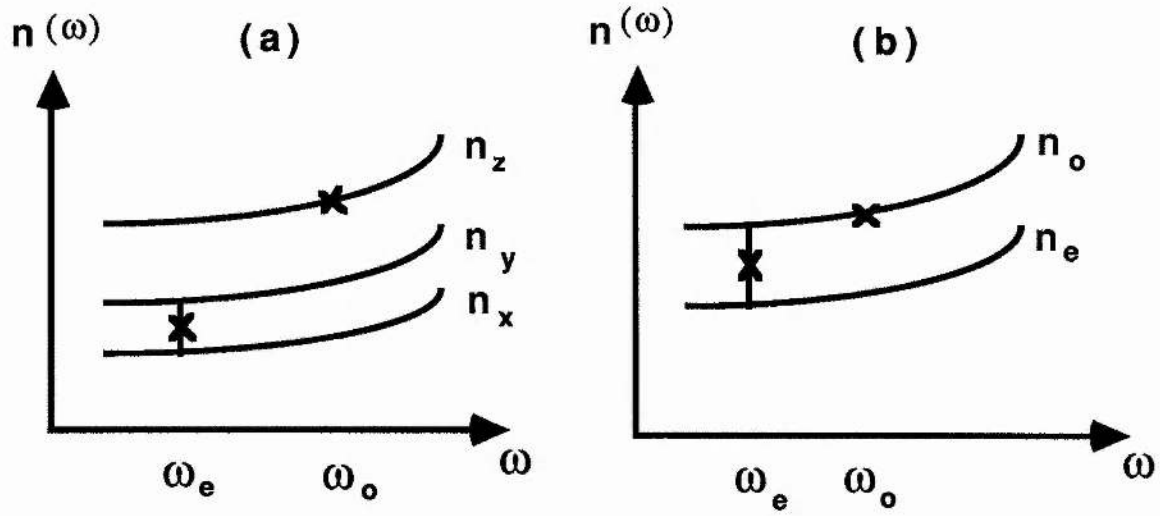

Fig. 2.1 (a) Variation of principal refractive indices with frequency in a biaxial crystal with $n_X < n_Y < n_Z$. As depicted the refractive index for an extraordinary wave, frequency ω_e, polarised in the xy plane lies on a line between the values $n_X(\omega_e)$ and $n_Y(\omega_e)$, while for an ordinary wave, frequency ω_o polarised along the z axis, the refractive index is fixed at $n_Z(\omega_o)$. (b) Variation of principal refractive indices with frequency in a uniaxial crystal with $n_o > n_e$. Again the extraordinary refractive index lies between the values $n_e(\omega_e)$ and $n_o(\omega_e)$, while the ordinary refractive index is fixed at $n_o(\omega_o)$.

the expression

$$\frac{1}{n_e^2(\theta)} = \frac{\cos^2\theta}{n_o^2} + \frac{\sin^2\theta}{n_e^2} \qquad (2.24)$$

This produces a value for $n_e(\theta)$ lying between those of n_o and n_e as depicted in fig. 2.1(b). Uniaxial crystals are classified in the categories positive and negative, dependent on whether $n_o < n_e$ or $n_e < n_o$ respectively.

The possible combinations of polarisations are shown in Table 2.1. Type 1 phase-matching refers to the condition of parallel-polarised signal and idler waves, while Type 2 phase-matching involves orthogonally polarised signal and idler. The index diagrams for both of these cases are shown for positive and negative uniaxial crystals in figures 2.2(a)-(d). Three-wave collinear interaction such that the direction of propagation is along a principal axis of the nonlinear crystal is referred to as noncritical or 90° phase-matched. This condition, under which the rate of change of extraordinary refractive index with propagation angle is zero, will be shown in the following sections to engender various properties important in facilitating efficient interaction. Collinear interaction in other directions is known as critically phase-matched.

Table 2.1 : Phase-matching in uniaxial crystals

	-ve uniaxial	+ve uniaxial
Type 1	e → o + o	o → e + e
Type 2	e → o + e	o → o + e

2.1.4 Parametric oscillation

Parametric amplification is a process of magnification of a finite existing signal and/or idler field, and as such, it is not obvious that it should be viable in the case where only a pump

field is incident on the nonlinear crystal. However a finite input field is in fact created through the process of spontaneous parametric fluorescence[4], by which a very small amount of pump power is converted to energy in the signal and idler fields such that these satisfy the conditions (2.20) and (2.21). As shown in

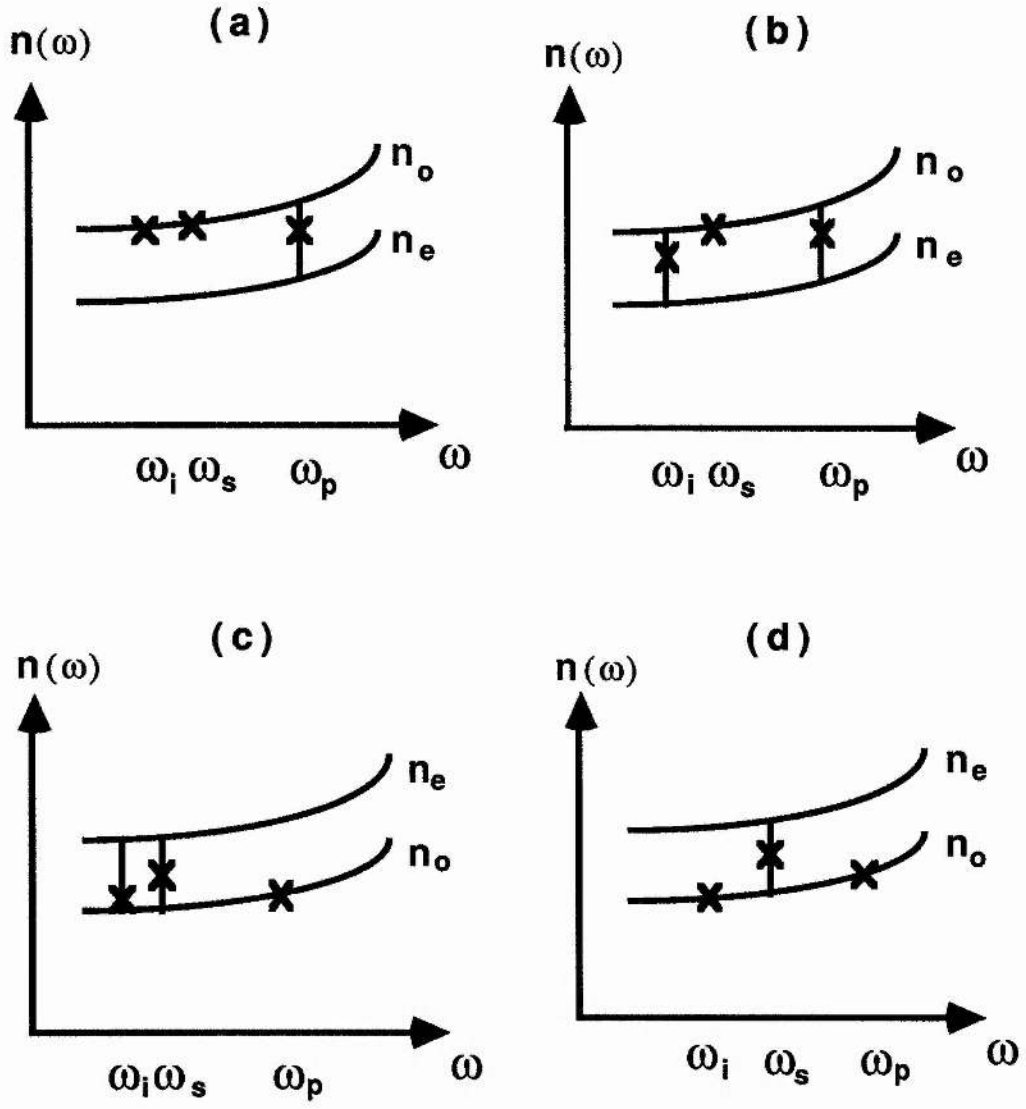

Fig. 2.2 Index diagrams as in figure 2.1, for (a) Type 1 phase-matching, negative uniaxial crystal, (b) Type 2 phase-matching, negative uniaxial crystal, (c) Type 1 phase-matching, positive uniaxial crystal, (d) Type 2 phase-matching, positive uniaxial crystal.

section 5.2.1 the total power so converted can be as little as 10^{-10}W, and typical values of signal gain for available crystal lengths are insufficient to allow single pass amplification of the spontaneously emitted power to levels comparable with the pump field. Hence a resonator cavity allowing multiple passes for one or both of the signal and idler in the nonlinear crystal may be utilised. The optical parametric oscillator provides amplification of phase-matched spontaneous fluorescence within a small directional bandwidth of the resonator axis. The need for multipass spatial interaction between the fields means that in general the further restriction of collinearity is imposed on the phase-matching condition in an oscillator configuration, and hence (2.21) can be treated as the scalar condition (2.23) in this case.

2.2 Theoretical aspects of optical parametric oscillation

2.2.1 Wavelength tuning

The generated signal and idler wavelengths in a collinearly phase-matched OPO are determined by conditions (2.20) and (2.23) i.e.

$$\omega_p = \omega_s + \omega_i \quad \text{and} \quad n_p\omega_p = n_s\omega_s + n_i\omega_i \quad .$$

For a fixed frequency pump wave, any process which changes the refractive indices at the signal, idler or pump wavelengths will tune the oscillator. Rapid tuning is generally accomplished through variation of temperature or direction of pump beam propagation with respect to the crystal optic axis. Fine tuning may be obtained via the electro-optic effect. Alternatively, the use of a tunable pump source may allow rapid tuning of the output wavelength without any adjustment of the OPO. Tuning can also be achieved in a noncollinearly phase-matched device, through adjustment of the pump beam direction with respect to the cavity axis. Operation in such a configuration is subject, as shown in chapter 8, to the use of a pump beam of sufficient dimension to allow multipass spatial coupling of the three fields.

2.2.2 Poynting vector walk-off

Although the interaction of the three fields in an OPO is generally assumed to be collinearly phase-matched, the collinearity refers only to the wave normal directions in the crystal. In an anisotropic medium the wave normal direction is not in general the same as the ray direction, which is the direction of energy propagation. The ray direction for an extraordinary wave can be found as in the index diagram, figure 2.3 The curve is the locus of points $(n_e(\theta), \theta)$ given by the relation (2.24) where θ is as defined above. The angle ρ between the wave normal direction and the ray direction, known as the walk-off angle is given implicitly by

$$\tan (\theta + \rho) = \frac{n_o^2}{n_e^2} \tan\theta \ . \qquad (2.25)$$

Hence over a finite interaction length in the nonlinear crystal the different ray directions of ordinary and extraordinary waves result in a spatial separation of the beams and loss of parametric interaction. It is thus advantageous for OPO operation to occur under conditions of minimal walk-off. This can be achieved using a noncritically phase-matched configuration, such that $\theta = 0$ or $\theta = \pi/2$, in which case the wave normal and ray directions are fully coincident.

2.2.3 Effective nonlinear coefficient and Figure of merit

As was stated in section 2.1.1, the effective nonlinear coefficient for a particular three wave interaction is a function of the the nonzero d coefficients and the interacting wave normal directions. The wave normal direction in a uniaxial nonlinear crystal is generally defined by the angles θ and ϕ. θ has been previously defined as the angle between the wave vector and the optic axis (or NLO reporting frame 3-axis as defined in Appendix A), while ϕ is the azimuthal angle between the projection of the wave-vector on the plane orthogonal to the optic axis, and the NLO

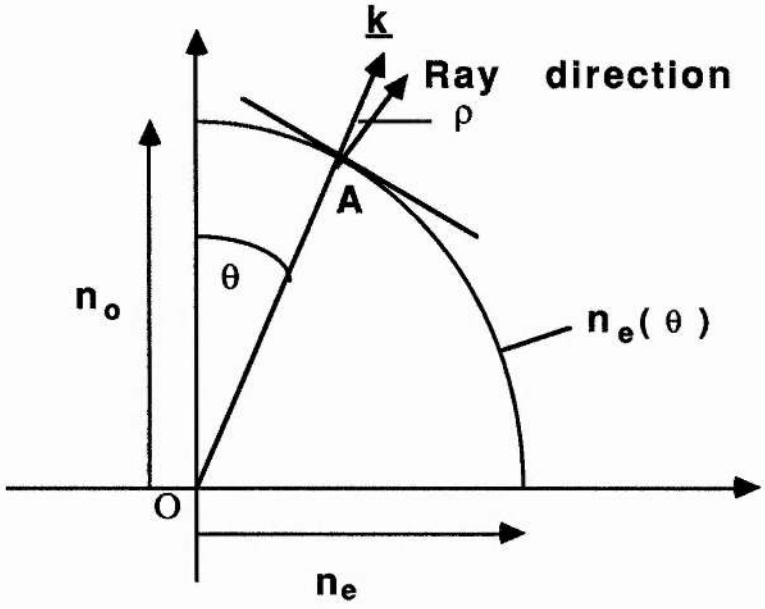

Fig. 2.3 The locus of points $n_e(\theta)$ defined by the extraordinary refractive index as a function of the phase-matching angle. The ray direction is parallel to the normal to the ellipse at its intersection A with the momentum vector.

reporting frame 1-axis. The expressions for d_{eff} in various crystal classes for each phase-matching type can be found in ref 3.

It can be seen from expressions (2.10) and (2.11) that the parametric gain constant Γ_o is proportional to d_{eff}^2 and inversely proportional to the product of the three refractive indices n_p, n_s, and n_i. Hence a useful quantity in assessing nonlinear materials for the purpose of OPO gain media, is the figure of merit

$$\text{F.o.M.} = \frac{d_{eff}^2}{n_p n_s n_i} \qquad (2.26)$$

The figure of merit is a quantity which has no standard definition, and other authors[5] have defined it so as to take into account effects such as walkoff, pump beam focussing, and wavelength of operation. In chapter 3 where the characteristics of various nonlinear materials are compared in detail, we have preferred to treat each property separately, and so this simple definition has been used.

2.2.4 Phase-matching constraints on the OPO pump source

It can be seen from expression (2.12) that a finite phase mismatch

$$\Delta k = k_p - k_s - k_i \neq 0$$

results in a reduction in parametric gain at the resonant signal wavelength. In the small gain approximation ($\Gamma_0^2 \ell^2 << 1$), a value of Δk for which

$$|\Delta k| \ell = \pi \qquad (2.27)$$

results in a gain of approximately half the value for which $\Delta k = 0$. The phase mismatch resulting from deviation of the signal wavelength from that at which perfect phase-matching ($\Delta k = 0$) is achieved allows us to define a gain bandwidth according to (2.27) at each point of the tuning curve.

However, phase mismatch may also be caused by the non-ideal nature of the pump beam. In the case of perfect phase-matching as in figure 2.4(a) the pump wave has a fixed wavelength and its wavevector direction is aligned parallel with the cavity axis in order to achieve collinear phase-matching. However in reality the pump laser output is characterised by a finite linewidth and angular divergence. Both of these properties lead to some deviation from phase-matching for a fixed signal frequency, and the resultant reduction in parametric gain produces an increase in oscillation threshold. In the following sections, we develop expressions for working limits on pump beam linewidth and divergence.

(a) Pump laser linewidth

Under the constraint of collinear phase-matching, any departure of the pump wavelength from its mean value causes an amount of phase mismatch as in figure 2.4(b). In this case we assume a constant signal momentum vector k_s and the phase mismatch due to a pump bandwidth $\Delta\omega_p$ is given by

$$\Delta k = k_p - k_s - k_i \qquad (2.28)$$

$$= \Delta(k_p - k_i) \qquad \text{for constant } k_s \qquad (2.29)$$

$$= \left[\frac{\partial k_p}{\partial \omega_p} - \frac{\partial k_i}{\partial \omega_i}\right] \Delta\omega_p \quad . \qquad (2.30)$$

Thus the half gain pump bandwidth (halfwidth) given by (2.27) and (2.30) is

$$\Delta\omega_p = \frac{\pi}{l}\left[\frac{\partial k_p}{\partial \omega_p} - \frac{\partial k_i}{\partial \omega_i}\right]^{-1} \quad . \qquad (2.31)$$

The full width half power gain pump bandwidth in wavenumbers is given by

$$l\ \Delta\nu_p(cm^{-1}) = \left[\ n_p - n_i + \lambda_i \frac{\partial n_i}{\partial \lambda_i} - \lambda_p \frac{\partial n_p}{\partial \lambda_p}\ \right]^{-1}, \qquad (2.32)$$

where the dimensions are in centimetres. This can be used to determine the maximum allowable bandwidth for a pump source for a singly resonant OPO.

(b) Pump laser divergence

In the case where the pump is fixed in wavelength but has a finite spread of directions, there are two distinct ways in which momentum mismatch of the type depicted in figure 2.4(c) may result. Firstly the extraordinary momentum vectors may experience a change in magnitude due to the angular variation of the refractive index. We have

$$\Delta k = k_p - k_s - k_i$$

$$\therefore \quad \frac{\partial(\Delta k)}{\partial \phi_3} = 2\pi \left\{\frac{1}{\lambda_p}\frac{\partial n_p}{\partial \phi_3} - \frac{1}{\lambda_i}\frac{\partial n_i}{\partial \phi_3}\right\}, \qquad (2.33)$$

where angles ϕ_2 and ϕ_3 are as shown in figure 2.4(c), and we can use the transformation

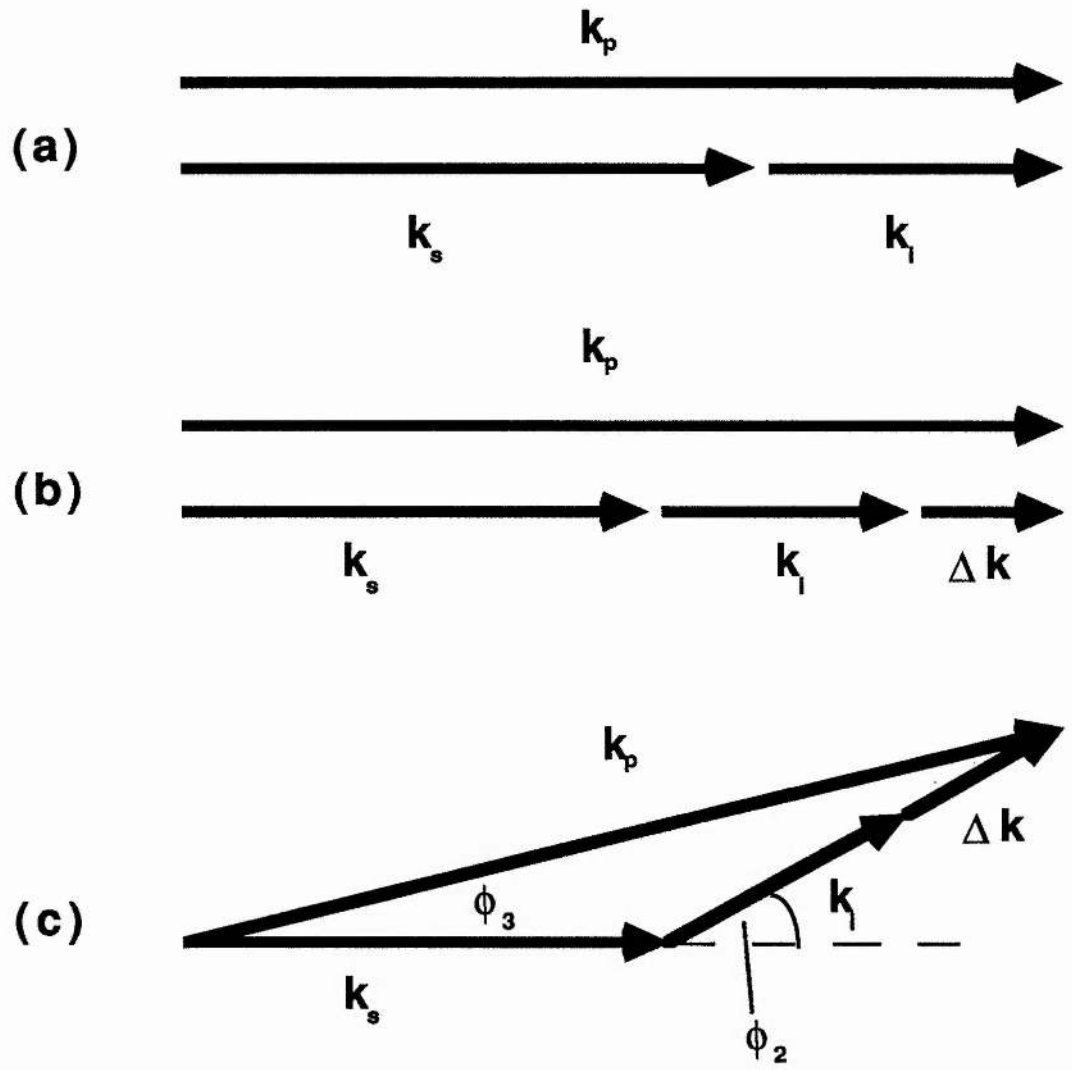

Fig. 2.4 Phase-matching vector diagrams under conditions of (a) $\Delta k = 0$, collinear phase-matching, (b) finite Δk, collinear phase-matching, (c) finite Δk, resulting from a pump wave-vector noncollinear with the cavity axis.

$$\frac{\partial \phi_2}{\partial \phi_3} = \frac{\lambda_i n_p}{\lambda_p n_i} \tag{2.34}$$

to rearrange this as

$$\Delta k = 2\pi \left\{ \frac{1}{\lambda_p} \frac{\partial n_p}{\partial \theta} - \frac{n_p}{\lambda_p n_i} \frac{\partial n_i}{\partial \theta} \right\} \phi_3 \quad , \tag{2.35}$$

since k_s is constant and for small departures from collinear phase-matching, k_p and k_i are at approximately the same angle θ to the optic axis. Hence using (2.27) the full angle half maximum gain pump divergence angle $\Delta\theta_{fa}$ is given by

$$\Delta\theta_{fa} = \left\{\frac{1}{\lambda_p}\frac{\partial n_p}{\partial\theta} - \frac{n_p}{\lambda_p n_i}\frac{\partial n_i}{\partial\theta}\right\}^{-1} \qquad (2.36)$$

This is the dominant mechanism for phase mismatch in critically phase-matched parametric processes such that the resonant wave is an ordinary wave. However, if the resonant wave is of the extraordinary polarisation and the pump and nonresonant wave are ordinary waves having no angular refractive index variation, then the phase-mismatch does not result from this mechanism. In this case, and also under conditions of near-noncritical phase-matching, where the angular refractive index variation is very slow, phase mismatch occurs through the inability of the constant magnitude momentum vectors to complete the vector triangle as in figure 2.4(c), such that

$$\Delta k = \frac{k_p k_s}{k_i}\frac{(\delta\theta)^2}{2} \quad . \qquad (2.37)$$

Near degeneracy, as for noncritical phase-matching in urea we can approximate this by

$$\Delta k = k_p\frac{(\delta\theta)^2}{2} \quad . \qquad (2.38)$$

The general half gain condition (2.27) gives us the full angle half maximum gain pump divergence requirement $\Delta\theta_{fa}$ for 'near-noncritical' phase-matching as follows:

$$(\Delta\theta_{fa})^2 = \frac{8\pi k_i}{k_p k_s} \qquad (2.39)$$

1. R. G. Smith, "Lasers", Vol. 4. Edited by A.K. Levine and A. J. De Maria. Marcel Dekker, New York (1976).
2. R.L. Byer, Chapter 9, "Optical Parametric Oscillators", in "Quantum Electronics: a treatise". Edited by H. Rabin and C. L. Tang (Academic, New York) Vol. 1, Pt B, pp 587-702 (1973).
3. F.A. Hopf, G.I. Stegeman, Applied classical electrodynamics, vol. 2: Nonlinear Optics., Wiley-Interscience (1986)
4. R.L.Byer and S. E. Harris, Phys. Rev. **168**, p1064 (1968).
5. A. Guy, Ph. D. thesis, University of Southampton, (1991).
6. R. Fischer and L. A. Kulevskii, Sov. J. Quant. Elect. **7** , p135 (1977).

Chapter 3
Nonlinear materials for the UV-visible range

3.0 Introduction

It is intended in this chapter to outline a general procedure for the assessment of nonlinear materials to support parametric oscillation over a desired wavelength tuning range. Using this selection procedure we shall consider the problem of the development of an OPO for the UV-visible range, comparing the available nonlinear materials appropriate to this purpose with respect to the criteria developed in chapter 2. We shall highlight in particular the merits of OPOs based on urea and BBO.

3.1 Assessment of nonlinear materials

For a given pump laser source, it is possible to define a sequence of criteria which must be satisfied in order to demonstrate the utility of a nonlinear material as an OPO gain medium. For a fixed set of pump laser parameters, in terms of wavelength, pulse energy, linewidth and divergence, the flowchart of figure 3.1 indicates the conditions by which a material may be assessed for the generation of a particular wavelength range. The initial assessments are made on the basis of the crystal's transparency. Firstly, and foremostly, it must show high transmission at the wavelength of the chosen pump source. Secondly, the requirement for transmission of both signal and idler wavelengths, and the material's high wavelength transmission cut-off, place both an upper and lower bound on the possible OPO output wavelengths, via the energy conservation condition. However, it is the birefringence of the material which actually defines the range of wavelengths within this 'window' which may be generated. Phase-matching calculations may readily be made on the basis of known Sellmeier relations on refractive index variation, and hence potental tuning ranges may be computed. Throughout these tuning ranges, the compatibility of

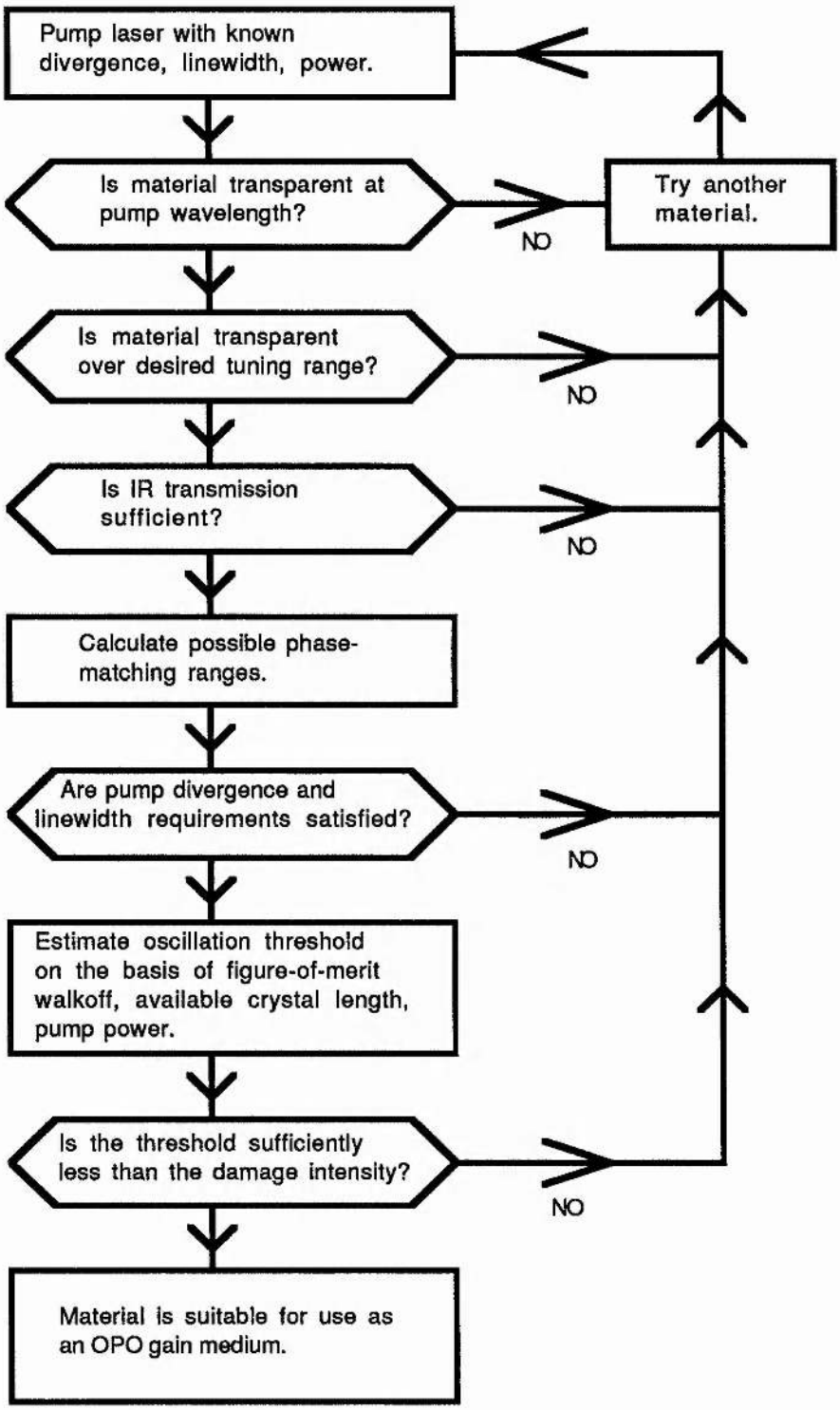

Fig. 3.1 Flowchart illustrating the criteria involved in assessing a nonlinear material for an OPO.

the material and the pump source may be assessed in terms of the linewidth and angular acceptances developed in section 2.2.4. If the linewidth and divergence of the pump laser are found to be within these limits, then the final condition to be satisfied is that the OPO oscillation threshold intensity must be a sufficient factor less than the crystal (or OPO optics) damage threshold value. Hence some kind of estimate of the oscillation threshold must be made on the basis of the available crystal lengths and pump powers. The theory of OPO threshold behaviour has been developed for the cases of CW[5] oscillators, and pulsed SROs (see chapter 5), taking into account the variation of the figure of merit and the extraordinary wave walkoff angle across the tuning range. However the threshold is not necessarily determined by these factors alone. The limitations on focussing imposed by e-wave walkoff in critically phase-matched configurations may mean that the threshold is made prohibitively high by the focussing necessary for the available pump power level.

Assuming the threshold and damage criteria are fulfilled, the suitable nonlinear materials may be chosen according to the needs of the application-e.g. requirements for a particular tuning method, inherent linewidth, frequency stability etc. However, if no material is found to be suitable for the desired tuning range, it may be necessary to seek a pump laser of different wavelength, or possessing more strictly controlled divergence and linewidth.

3.2 Nonlinear materials for the ultraviolet and visible

We shall now use this general procedure to compare nonlinear materials appropriate to the generation of wavelengths in the ultraviolet and visible spectral ranges. We will make quantitative assessments of available nonlinear crystals on the assumption of a 308nm pump wavelength as provided by a XeCl excimer laser. Although this is by no means the only viable UV pump wavelength, it will serve to illustrate the relative qualities of the different materials.

For our current purpose, the majority of commonly utilised nonlinear materials may be disregarded on account of their

inadequate UV transmission. We can immediately discard $LiNbO_3$ as a possibility, since transmission does not extend below 400nm[24]. Materials such as KTP[18], $KNbO_3$[19,20] and $LiIO_3$[21,22] possess large nonlinear coefficients (between 3 and 5pm/V) and are reported as transparent at wavelengths as low as 350nm. As a result, these materials are very close to being useful for OPOs pumped by tripled Nd:YAG lasers. As yet, no reports have been made of UV-pumped OPOs in KTP and $KNbO_3$. However, an OPO for the visible region has been demonstrated in $LiIO_3$ pumped at 347nm by a doubled ruby laser[25]. This device had a low threshold and no damage problems. The main drawback to this material was considered to be its high birefringence and associated resistance to tight focussing.

Materials with deeper UV transmission include KB5[23] (Potassium PentaBorate) and LFM[23] (Lithium Formate), whose UV transmission cut-off wavelengths are as low as 165 and 230nm respectively. However, these materials are hindered by low nonlinear coefficients and damage thresholds. The recent development of the organic crystal d-LAP (deuterated L-Arginine Phosphate) which has transparency from 0.2 to 1.9μm, and moderate nonlinear coefficient, has introduced another new possibility, but it has yet to be fully assessed as an OPO gain medium. Hence, for the purposes of pumping at excimer wavelength such as 249 and 308nm, the main options are KDP and its various isomorphs, and more recently, Urea, BBO and LBO.

KDP, ADP and isomorphic crystals[10] such as CDA, RDA and RDP (C and R denote Caesium and Rubidium, while A denotes Arsenate) were until the mid-eighties the only practical options as UV-transmitting nonlinear crystals. KDP is a negative uniaxial crystal belonging to the class $\bar{4}2m$, and having a transparency range from 0.2-1.5μm. Somewhat higher nonlinear coefficients are seen in ADP, while the deuterated versions of these materials have transmission ranges shifted upwards slightly in wavelength. The infra-red cut-off limits the lower wavelength output of an OPO pumped at 308nm, to 390nm. KDP will henceforth be used as a representative example of this type of material.

Urea[3] is an organic compound of crystal class $\bar{4}2m$. It is positive uniaxial and is transmissive from 0.2 to 1.4μm. Hence as for KDP the OPO is restricted to signal wavelengths greater than 390nm. In practice it is a difficult material to polish and is hygroscopic and so requires careful handling.

Low temperature flux-grown β-phase Barium Borate[13] is a negative uniaxial material of the class R3c. It has a UV transmission cut-off at around 200nm, while the infra-red cut-off is at between 2.6 and 3μm. Thus the OPO signal wavelength potentially extends to 345nm. Although BBO is a robust material, it is slightly hygroscopic and therefore benefits from protective surface coatings.

Lithium Borate[9] is a biaxial belonging to the mm2 class, with transmission from 160nm to 2.6μm. Clearly this deeper UV transmission makes LBO an important material for generation of wavelengths in this range. It is also more robust than BBO and is non-hygroscopic. The OPO signal cut-off corresponding to this transmission is around 350nm.

3.3 Tuning ranges

In each of KDP, urea and BBO, both the Type 1 and 2 phase-matched angle-tuned wavelength ranges have been calculated for the case of 308nm pumping and are shown in figures 3.2 to 3.4. In LBO three tuning options are shown (fig. 3.5) corresponding to propagation in each of the principal planes. It is a characteristic feature of the Type 1 tuning ranges that they terminate at the degenerate wavelength, such that $d\theta/d\lambda = 0$, whereas the Type 2 tuning curves show phase-matching on either side of the angle at which the degenerate wavelength is generated. This feature has important implications in terms of OPO linewidth, as will be discussed in chapter 7. The Sellmeier relations used in the calculation of these phase-matching wavelengths are given in Appendix B.

Type 1 phase-matching in KDP produces continuous tuning with nonzero nonlinear coefficient from 390nm to degeneracy. Although Type 2 phase-matching is possible, it can be seen in

Table 3.1(a) Characteristics of nonlinear media over the range 330-480nm

Material and phase-matching type	Range of internal Pump beam-0ptic axis angles (degrees)	Range of signal wavelengths (nm)	Range of Effective non-linear coefficient (pm/V)	Range of extra-ordinary wave walkoff angles (degrees)	Pump laser line-width require-ment (FWHM gain) in a 1cm xtal (cm-1)	Pump laser divergence reqt. (FWHM gain) in a 1cm crystal (mRad)
KDP Type 1 e-o+o	θ = 49-57	390-480	0.33-0.37	1.7-1.6	50-25	0.67-0.73
KDP Type 2 e-o+e	θ = 52-90	390-490	0.42-0	2.2	58-39	1.5-infinity ($\Delta\theta$ NCPM =3.4mR)
Urea Type 1 o-e+e	θ = 35-43	390-480	1.27-1.35	2.2	13.4-9.4	0.32-0.30
Urea Type 2 o-o+e	θ = 35-55	390-480	0.87-1.11	2.3-2.1	15.8-12.9	4.7-6.5
BBO Type 1 e-o+o	θ = 25-38	345-480	2.0-1.7	3.7-4.6	42.7-12.0	0.28-0.23

Table 3.1(a) contd. Characteristics of nonlinear media over the range 330-480nm

Material and phase-matching type	Range of internal Pump beam-Optic axis angles (Degrees)	Range of signal wavelengths (nm)	Range of effective nonlinear coefficient (pm/V)	Range of extraordinary wave walkoff angles (Degrees)	Pump laser linewidth requirement (FWHM gain) in a 1cm xtal (cm-1)	Pump laser divergence requirement (FWHM gain) in a 1cm xtal (mRad)
BBO Type 2 e-o+e	θ = 25-47	345-480	1.8-1.0	3.7-4.5	56.5-19.0	0.72-2.04
LBO xy plane e-o+o	ϕ = 24-53	350-480	1.2-0.8	0.8-1.0	46-19	1.3-1.0
LBO xz plane o-e+e	θ = 0-29	385-348	1.2-0.6	0-0.8	52-154	infinity-2.0 ($\Delta\theta_{NCPM}$ = 4.3mR)
LBO yz plane o-o+e	θ = 0-90	385-452	1.2-0	0-0.3	52-33	4.3-5.9

Table 3.1(b) Characteristics of nonlinear media over the range 480-616nm

Material and phase-matching type	Range of Internal Pump beam-Optic axis angles (Degrees)	Range of signal wavelengths (nm)	Range of effective nonlinear coefficient (pm/V)	Range of extraordinary wave walkoff angles (Degrees)	Pump laser linewidth requirement (FWHM gain) in a 1cm xtal (cm-1)	Pump laser divergence requirement (FWHM gain) in a 1cm xtal (mRad)
KDP Type 1 e-o+o	$\theta = 57\text{-}63$	480-616	0.37-0.39	1.6-1.4	25-18	0.73-0.75
KDP Type 2 e-o+e						
Urea Type 1 o-e+e	$\theta = 43\text{-}47$	480-616	1.35	2.2	9.4-6.9	0.30-0.28
Urea Type 2 o-o+e	$\theta = 55\text{-}90$	480-616	1.11-1.35	2.1-0	12.9-12.2	6.5-9.2
BBO Type 1 e-o+o	$\theta = 38\text{-}39$	480-616	1.7	4.6	12.0-9.3	0.23

Table 3.1(b) contd. Characteristics of nonlinear media over the range 480-616nm

Material and phase-matching type	Range of Internal Pump beam-Optic axis angles (Degrees)	Range of signal wavelengths (nm)	Range of effective nonlinear coefficient (pm/V)	Range of extra-ordinary wave walkoff angles (degrees)	Pump laser linewidth requirement (FWHM gain) in a 1cm xtal (cm-1)	Pump laser divergence reqt. (FWHM gain) in a 1cm crystal (mRad)
BBO Type 2 e-o+e	θ = 47-60	480-616	1.0-0.55	4.5-3.5	19.0-19.5	2.04-3.15
LBO xy plane e-o+o	ϕ = 53-60	480-616	0.8-0.7	1.0	19-14	1.3-1.0
LBO xz plane o-e+o						
LBO yz plane o-o+e						

Table 3.1 that the nonlinear coefficient decreases towards zero at the noncritical point. Both phase-matching options in Urea offer broad tuning ranges with a maximum value of d_{eff} at NCPM for Type 2 phase-matching. Again in BBO both phase-matching types offer broad tuning ranges limited only by the crystal infra-red transmission cut-off. Degeneracy for Type 2 phase-matching in BBO occurs at a value of $\theta = 60^o$ and although phase-matching continues to be possible at greater angles, as in KDP the nonlinear coefficient decreases towards zero at NCPM.

In LBO, Type 1 phase-matching is utilised for propagation in the xy plane, with nonzero d_{eff} from 350nm up to degeneracy. More restricted tuning is possible at UV-blue wavelengths using Type 2 phase-matching in the xz and yz planes. Propagation along the z-axis where the latter tuning ranges become degenerate, results in NCPM at 385nm with a nonzero d_{eff}.

Further coarse tuning possibilities exist through the variation of crystal temperature. Temperature tuning is most advantageous when it is desired to maintain noncritical phase-matching, or when spatial stability of the beam is important. Unfortunately, information on temperature tuning is generally rather sketchy and general temperature-related Sellmeier equations are rarely available. Table 3.2 shows details of temperature tuning in varying configurations which at least give an impression of the relative usefulness of this tuning method in each case. In general it can be said that the magnitudes of the dn/dT coefficients are such that temperature tuning is only of real significance in KDP and LBO. KDP is, however, limited by crystal decomposition at 100°C. LBO, however has been used in second harmonic generation experiments at as much as 200°C [2] and NCPM optical parametric oscillators in our own laboratories[2] have shown a tuning rate of 0.1nm/°C at the signal wavelength over a range of 150°C.

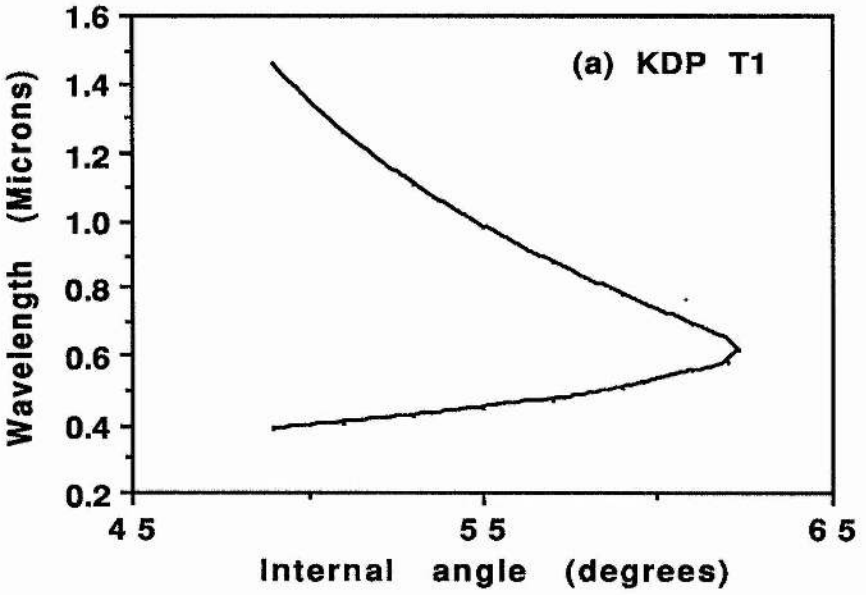

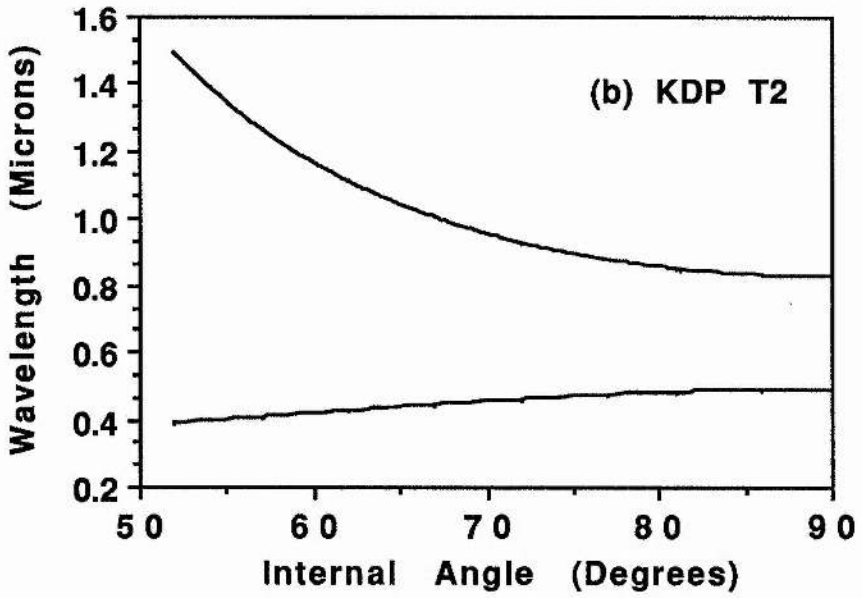

Fig. 3.2 (a) Type 1 and (b) Type 2 phase-matched tuning ranges for 308nm pumped parametric oscillation, as a function of the phase-matching angle in KDP.

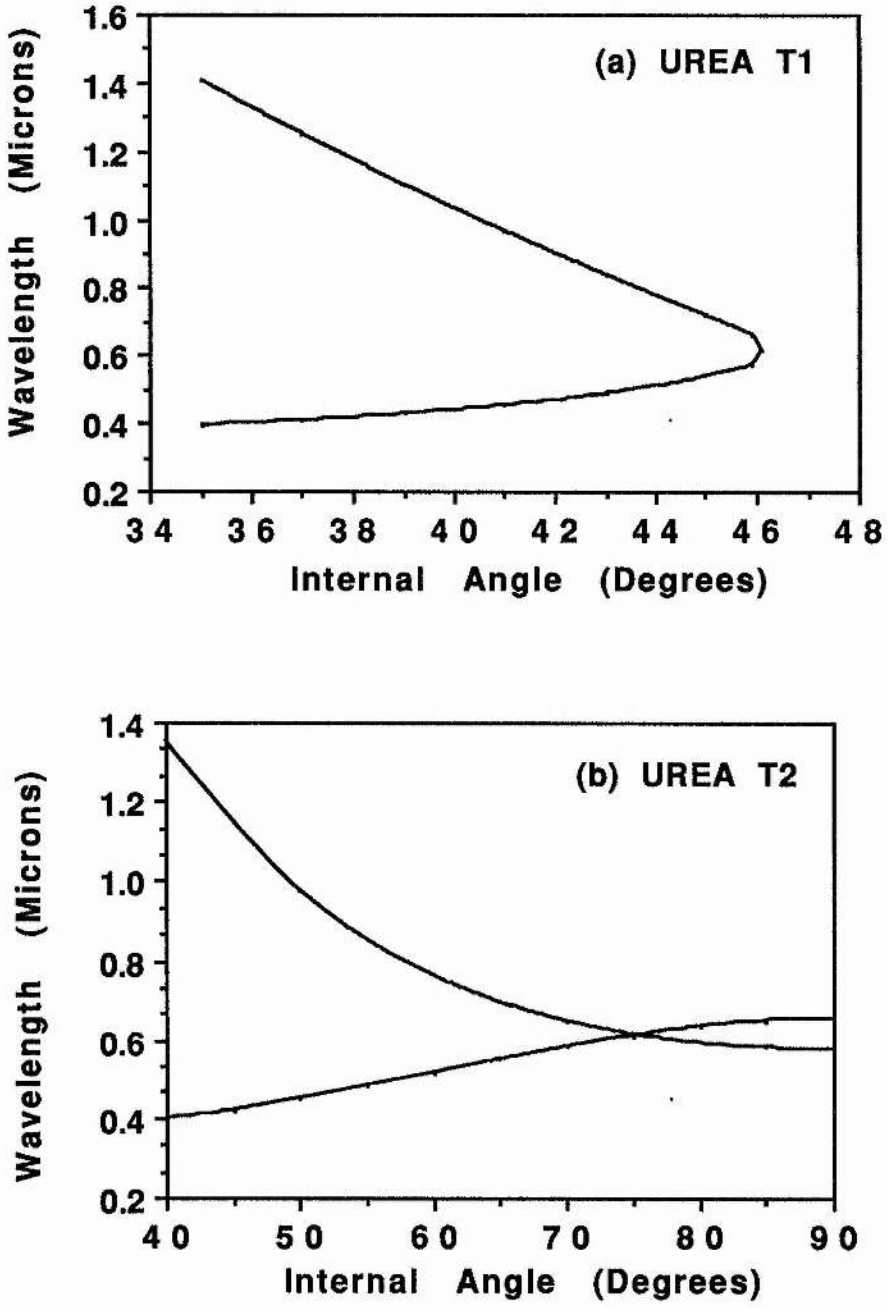

Fig. 3.3 (a) Type 1 and (b) Type 2 phase-matched tuning ranges for 308nm pumped parametric oscillation, as a function of the phase-matching angle in Urea.

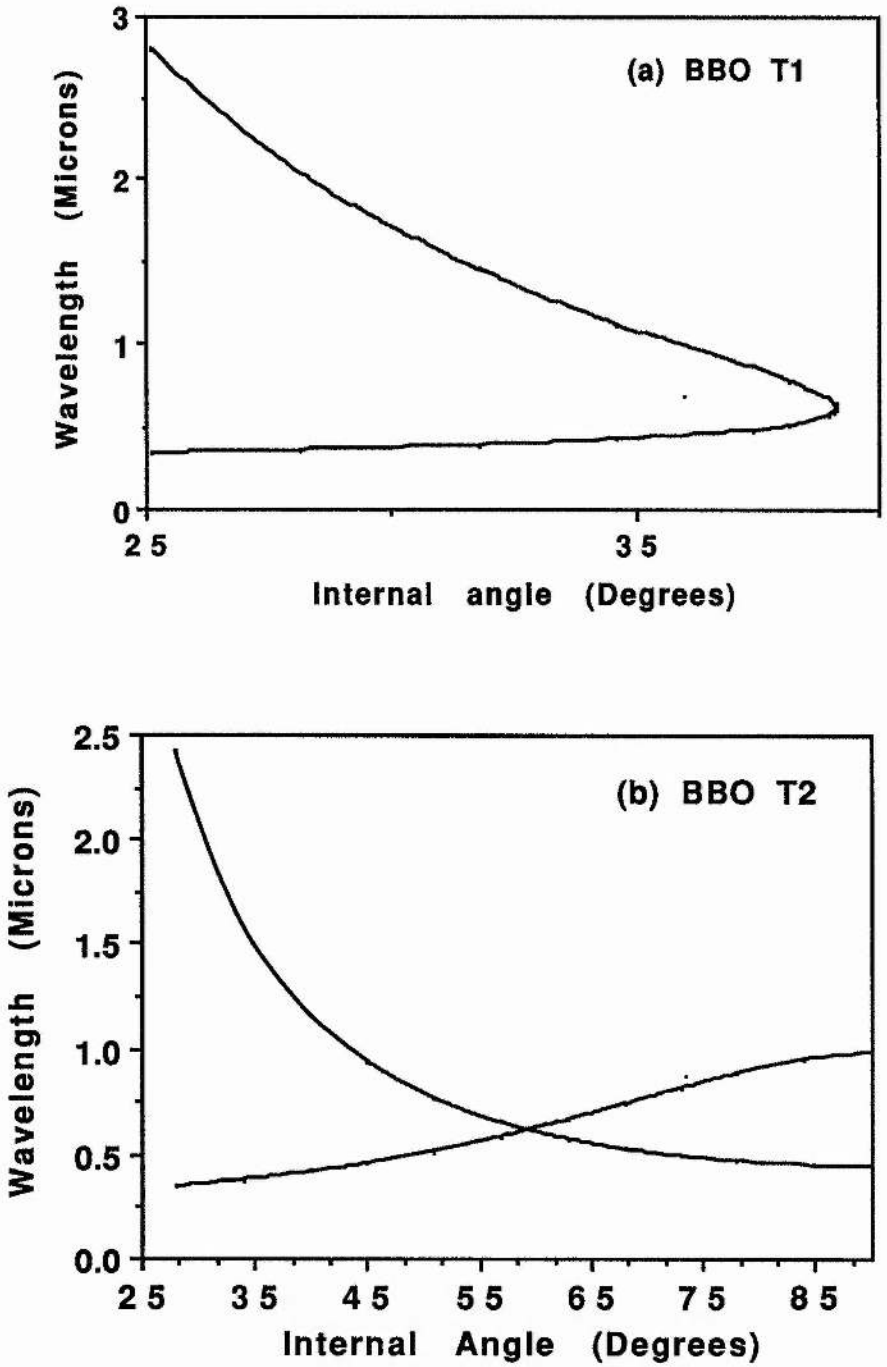

Fig. 3.4 (a) Type 1 and (b) Type 2 phase-matched tuning ranges for 308nm pumped parametric oscillation, as a function of the phase-matching angle in BBO.

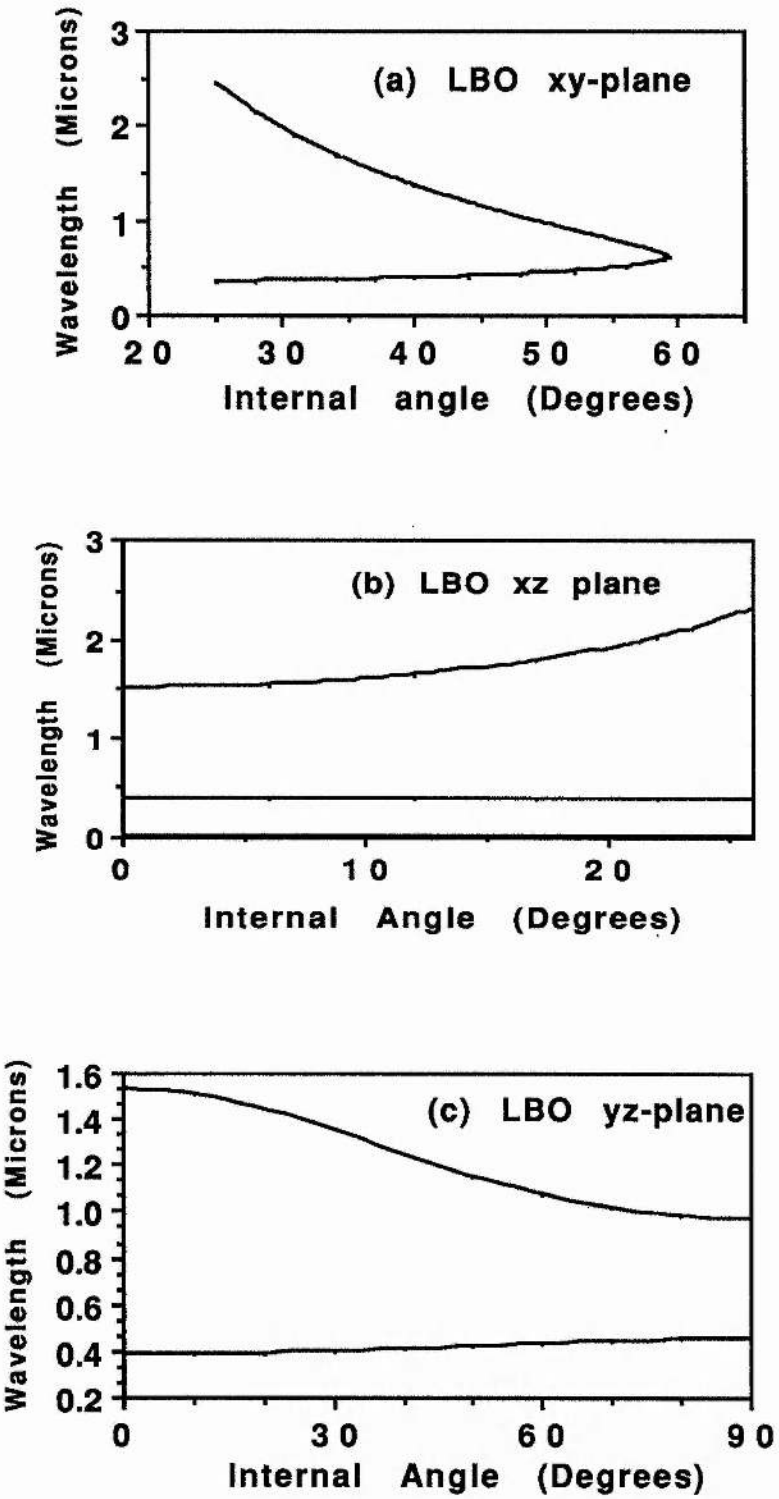

Fig. 3.5 Tuning ranges for 308nm pumped parametric oscillation in LBO, as a function of the phase-matching angle, for propagation in (a) the xy plane, (b) the xz plane, (c) the yz plane.

Table 3.2 Temperature tuning of UV-visible materials		
Material	**Reference**	**Comments**
KDP	3	Type 1 NCPM SHG of dye laser @ 597nm. Tuning rate 0.05nm/C at room temp.
	4	$(d\Delta n/dT)/\Delta n = 2.6e\text{-}4$ @ 1064nm ($\Delta n = n_e - n_o$)
Urea	3	Type 1 NCPM SHG of dye laser @ 597nm. Tuning rate 0.013nm/C at room temp.
BBO	5	$(d\Delta n/dT)/\Delta n = 5.9e\text{-}5$ @ 1064nm
LBO	1	NCPM SHG of 1.1μm (λ_f) $d\lambda_f/dT = -0.125nm/C$
	2	Type 2 NCPM OPO pumped @355nm, signal 470nm $d\lambda_s/dT = -0.11nm/C$ $d\lambda_i/dT = -0.87nm/C$

3.4 Pump laser requirements

Having established which materials offer tuning over the wavelength range of interest, it must be determined whether the chosen pump source possesses linewidth and divergence which are within the limits imposed by gain reduction through phase-mismatch.

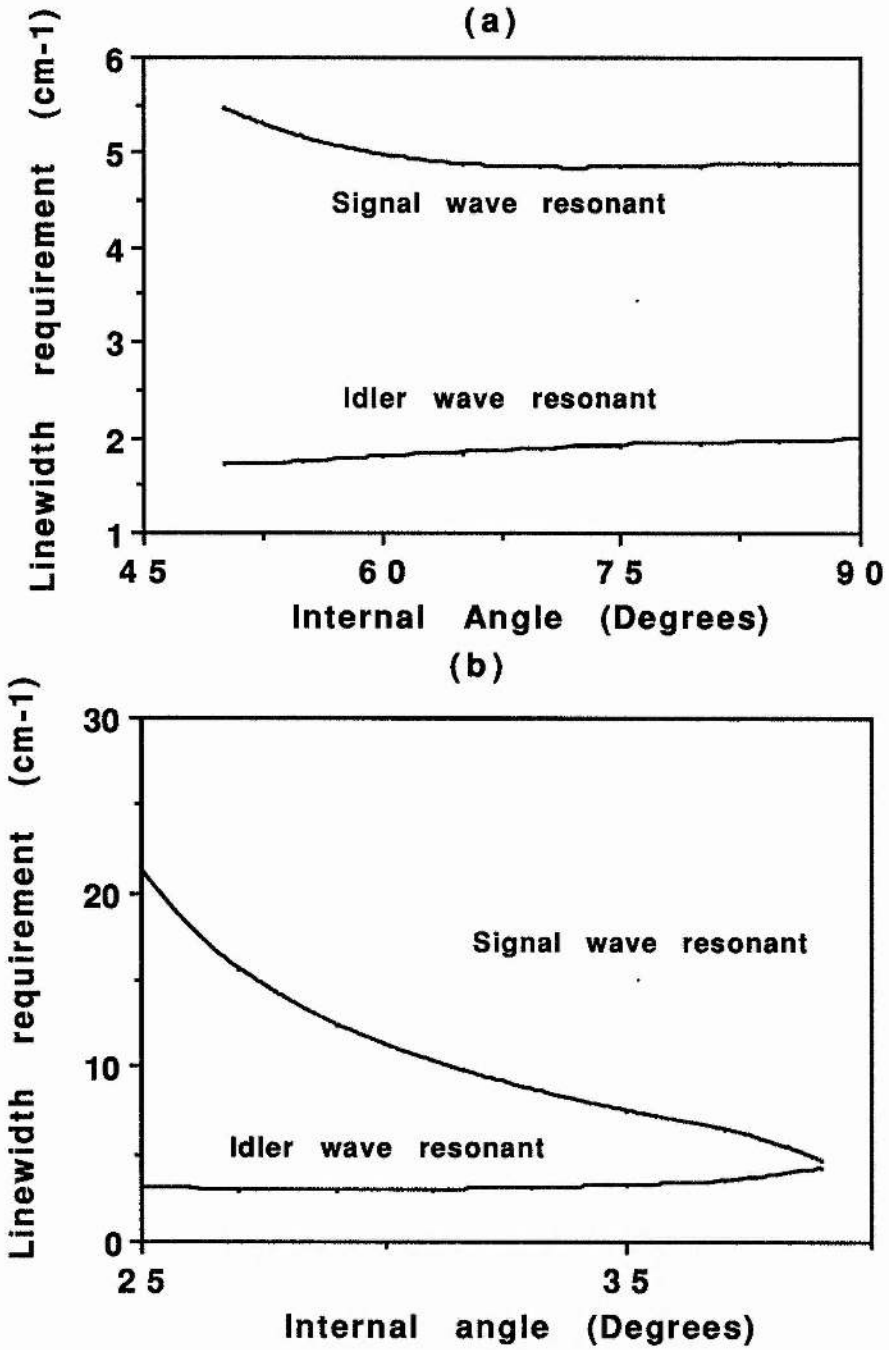

Fig. 3.6 Pump linewidth requirements calculated from expression (2.32) across the tuning range in OPOs based on (a) a 25mm Type 2 phase-matched Urea crystal, and (b) a 20mm Type 1 phase-matched BBO crystal.

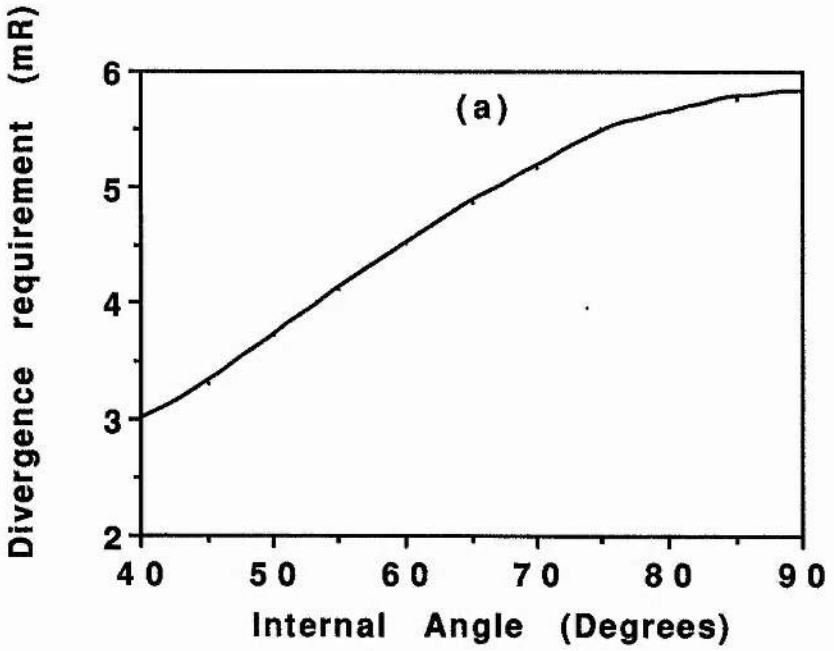

Fig. 3.7 (a) Pump divergence requirements calculated from expression (2.39) across the tuning range in an OPO based on a 25mm Type 2 phase-matched urea crystal.

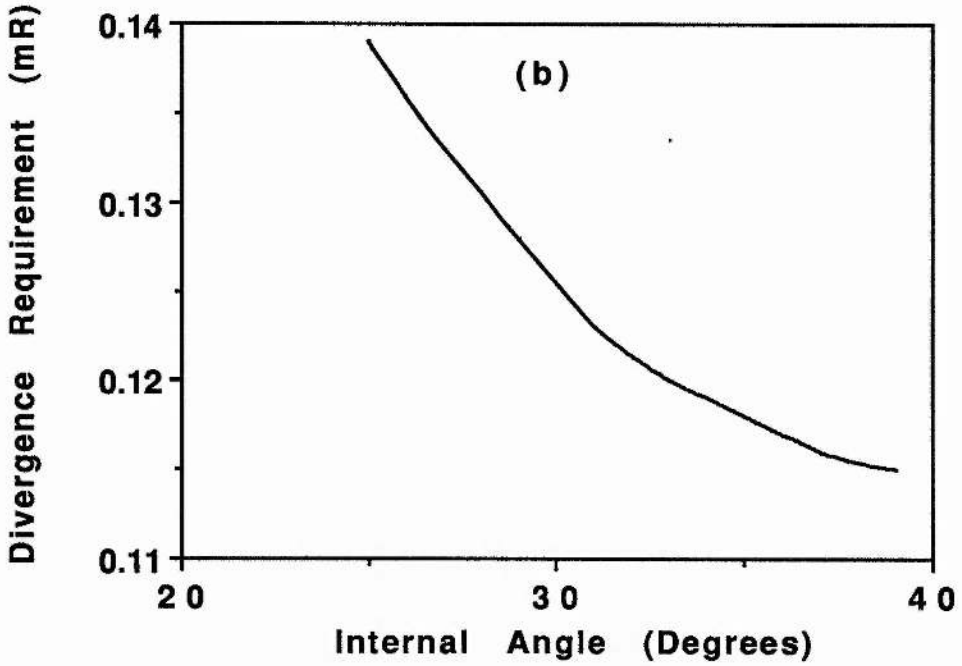

Fig. 3.7 (b) Pump divergence requirements calculated from expression (2.36) across the tuning range in an OPO based on a 20mm Type 1 phase-matched BBO crystal.

3.4.1 Linewidth

In general it can be seen from table 3.1 that in all the materials considered the requirement defined by (2.27) and calculated using (2.32), for OPOs pumped by the XeCl excimer wavelength is that the pump linewidth should be less than a few wavenumbers, for a 1cm crystal. The strictest limit as calculated using expression (2.32) is imposed by Type 1 phase-matching in urea, where the full-width half-gain limit is $6.9cm^{-1}.cm$. In the context that a free-running excimer laser has a linewidth in hundreds of wavenumbers, it is clear that some linewidth control is necessary. Figures 3.6(a) and (b) show the linewidth limits for signal and idler resonance in OPOs using 25mm 90° phase-matched urea and 20mm Type 1 phase-matched BBO crystals respectively. The urea device is able to accommodate a $5cm^{-1}$ linewidth for short wavelength resonance and $2cm^{-1}$ for long wavelength resonance. The bandwidth acceptance in BBO converges to around $5cm^{-1}$ at degeneracy. These values indicate that the $0.25cm^{-1}$ linewidth of our injection-seeded excimer lasers is entirely consistent with their use as pump sources for UV-visible OPOs.

3.4.2 Divergence

The divergence limits shown in table 3.1 have been calculated assuming resonance of the short wavelength in an OPO based on a 1cm long nonlinear crystal. Acceptance angles are calculated using expression (2.36) for critically phase-matched o-wave resonance, and using (2.39) for the cases of noncritical phase-matching and critically phase-matched e-wave resonance. In general it can be said that in the context of excimer-pumping, the acceptance angle is more of an issue than is the pump linewidth. Our pump lasers had full-angle divergences up to 0.2mR and although none of the acceptance angles calulated are below this value, it must be remembered firstly that compression of the pump beam has the effect of magnifying the beam divergence, and secondly that the use of longer crystal path

lengths tightens the requirements further. Hence, in critically phase-matched configurations such as Type 1 KDP, BBO and Urea, it may be anticipated that some reduction in parametric gain may result from beam compressions which are necessary to achieve threshold. Full discussion of results relating to this question is given in chapters 5 and 6. Meanwhile it may be seen that the low birefringence of LBO produces comparatively relaxed angular requirements of several milliRadians in each of the three planes, and so it should be more suitable for situations involving low pulse energies and beam focussing.

Figures 3.7(a) and (b) illustrate the specific figures calculated appropriate to the Type 1 BBO, and Type 2 Urea OPOs operated in this work. In an OPO based on a 25mm Type 2 Urea crystal, such that the resonant signal wavelength is an e-wave and the pump and nonresonant waves are o-waves, expression (2.39) affords relatively generous limits ranging from 3.0mR at $\theta = 40^{o}$ to 5.8mR at NCPM. The constraints are considerably more relaxed than in the case of idler wavelength resonance as shown in ref. 17. In a Type 1 OPO based on a 20mm BBO crystal, the divergence limits range from 0.14mR to 0.10mR at degeneracy. Allowing for beam compressions of between 2.5 and 20 and resulting divergences up to 4mR as in our experiments, this could be expected to be a severe restriction on OPO operation. In practice this was not the case, and again detailed consideration of this specific case is given in chapters 5 and 6.

3.5 Estimation of optimum threshold intensity

Once it has been shown that the chosen pump source is a suitable one in terms of linewidth and divergence, it must be determined whether the power output will be adequate to reach oscillation threshold in nonlinear crystal samples of the length and quality available. Furthermore, the usefulness of the material will be judged on the probability of optical damage at realistic supra-threshold pumping levels. Although it may seem that the nonlinear coefficient or figure of merit provides an effective comparative measure of the necessary pump intensity, the threshold is in fact dependent on a number of interconnected

factors and direct comparison of these values may not be useful given a particular crystal orientation and pump source. The available pump power and the crystal acceptance angle place an initial upper limit on the amount of focussing which may be tolerated, and hence also on the usable pump intensity. Further limits on focussing and intensity derive from the loss of spatial coupling produced by the extraordinary wave walk-off. Thus an optimal value of threshold must be a compromise taking all of these factors into account.

3.5.1 Walkoff

By inspection of figure 2.3 it can be seen that for values of θ other than 0^o and 90^o , i.e. for critical phase-matching, there is a finite angle between ray and momentum vector directions. In highly birefringent materials such as BBO, the walkoff angle can limit the maximum useful length of the nonlinear crystal through loss of coupling between the waves due to spatial separation. Table 3.1 shows values of around 4^o for 308nm pumping. (Note: where two extraordinary waves are present, the range is defined by the extremes of both values) In KDP and Urea the two polarisations separate by around 2^o, while the walkoff in the different phase-matching configurations in LBO is of a degree or less. As a result this material would be expected to be most favourable to critically phase-matched interactions involving low power. This is also true under conditions of noncritical phase-matching which may be achieved with maximal d_{eff} and zero walkoff in Type 2 urea and xz-plane LBO.

3.5.2 d_{eff} and figure of merit

The most current values of the relevant d coefficients for KDP, Urea, BBO and LBO are given in table 3.3, alongside expressions for the maximum values of d_{eff} as a function of the phase-matching angle. Table 3.1 shows the variation of d_{eff} for each material over each of their UV-visible OPO tuning ranges when pumped at 308nm. Similarly, the appropriate figure of

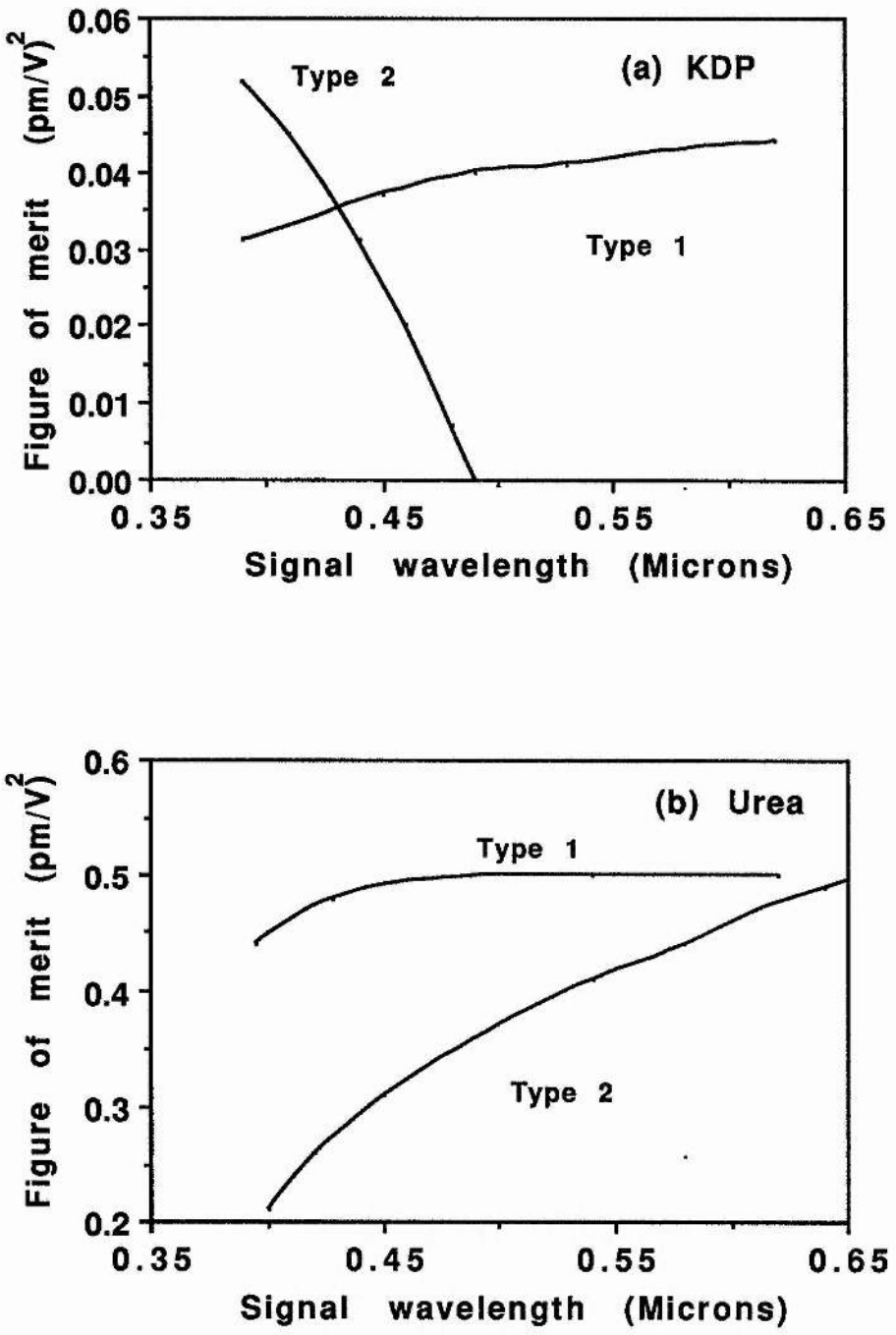

Fig. 3.8 Figure of merit as calculated using expression (2.26) as a function of signal wavelength for 308nm pumped OPOs based on (a) KDP and (b) Urea.

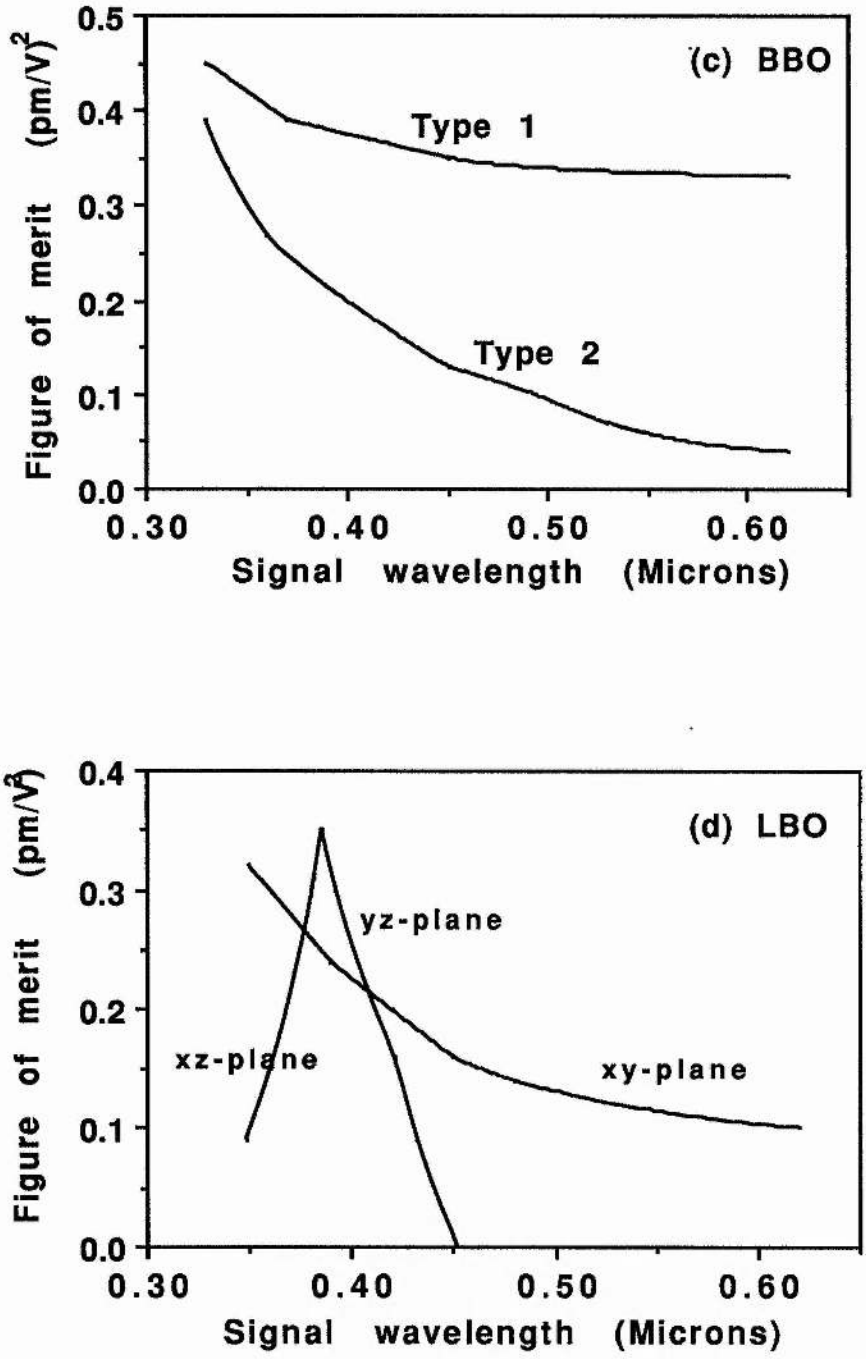

Fig. 3.8 Figure of merit as calculated using expression (2.26) as a function of signal wavelength for 308nm pumped OPOs based on (c) BBO and (d) LBO.

Table 3.3 Effective nonlinear coefficient of UV-visible materials		
KDP	d_{36} = 0.435pm/V [8]	Type 1: $d_{eff} = d_{36}\sin\theta$ Type 2: $d_{eff} = d_{36}\sin 2\theta$
Urea	d_{14} = 1.4pm/V [7]	Type 1: $d_{eff} = d_{14}\sin 2\theta$ Type 2: $d_{eff} = d_{14}\sin\theta$
BBO	d_{22} = 2.2pm/V $d_{31} < 0.05\ d_{22}$ [6]	Type 1: $d_{eff} = d_{31}\sin\theta + d_{22}\cos\theta$ Type 2: $d_{eff} = d_{22}\cos^2\theta$
LBO	d_{33} = 0.07pm/V d_{32} = 1.29pm/V d_{31} = -1.19pm/V [9]	xy-plane: $d_{eff} = d_{32}\cos\phi$ xz-plane: $d_{eff} = d_{31}\cos^2\theta + d_{32}\sin^2\theta$ yz-plane: $d_{eff} = d_{31}\cos\theta$

merit is shown as a function of signal wavelength in figures 3.8(a) to (d).

The figures of merit across the Type 1 and Type 2 tuning ranges of KDP are an order of magnitude below the maximum values in urea, BBO and LBO. The phase-matching ranges in BBO and urea are complementary in that their maximum f.o.m. occur at opposite extremes of the signal wavelength. The Type 1 phase-matched BBO devices used in this work have a maximum f.o.m. of $0.5 \times 10^{-24}\ m^2/V^2$ at 350nm in the UV, while Type 2 phase-matching in urea displays a similar figure at a noncritically phase-matched wavelength pair 570 and 670nm. Figure 3.8(d) shows that the figure of merit in LBO, although not quite as high as in urea and BBO, retains sizeable values well into the UV in all three tuning ranges with a peak value of around $0.3 \times 10^{-24}\ m^2/V^2$ for noncritical phase-matching at 385nm.

Table 3.4: Optical damage threshold in nonlinear materials		
Material	**Damage threshold estimates**	
KDP	$0.4GWcm^{-2}$ @ 694.3nm [10]	$10.9Jcm^{-2}$ @1.064 μm (1.3ns) [14]
Urea	$1.4GWcm^{-2}$ (single shot) @ 355nm (10ns) [11] $40MWcm^{-2}$ (multi-shot) @ 355nm (8ns) [12]	
BBO	$25GWcm^{-2}$ (single shot) @ 355nm (8ns) [13] $18GWcm^{-2}$ (multi-shot) @ 355nm (8ns) [13]	$12.9Jcm^{-2}$ @1.064 μm (1.3ns) [14]
LBO		$24.6Jcm^{-2}$ @1.064 μm (1.3ns) [14]

3.5.3 Ultraviolet damage threshold

A selection of reported values of damage threshold at various wavelengths are shown in table 3.4. It should be realised that damage problems are more severe at lower wavelengths and that constraints for 308nm or below may be stricter than those quoted. The information available indicates that the damage threshold of KDP is comparable with, but slightly less than those of urea, BBO and LBO. Our own experience with these materials in use with the 308nm excimer is that a level of $2Jcm^{-2}$ should not be exceeded. Urea, as discussed in ref. 17 shows no single shot damage even up to this level, but over a period of irradiation of several thousand shots at $0.4Jcm^{-2}$ (10ns pulse) cloudy damage tracks appear. We have also observed occasional evidence of single shot surface and internal damage in BBO at $1.5Jcm^{-2}$ (17ns

pulse). LBO, however has proven damage resistant at this level, and the constraint on pump intensity in devices using this material has been damage to the cavity mirrors.

3.6 Conclusion

The aim of this chapter has been to show that for the objective of obtaining tunable radiation over a range such as that chosen here, it is not possible to specify one particular material as the most suitable. The choice is dependent on the specific details of the pump source, the particular wavelength desired, the tuning method to be used and on the properties required of the output.

The two materials and phase-matching types used in this work offer highly efficient tuning for particular applications. Type 2 phase-matching in urea shows a high nonlinear coefficient for visible wavelengths, relatively high angular acceptance and low walkoff angle and has a noncritical phase-matching point with two visible output wavelengths. The main drawbacks of urea are its hygroscopic nature and its low multishot damage threshold. BBO is considerably more damage resistant and its Type 1 phase-matching range offers very broad spectral coverage with uniformly high d_{eff}. The low angular acceptance and high walkoff angle in BBO largely restrict use of this material to use with high power pump sources. By comparison the properties of LBO allow its use in conjunction with pump sources of lower power and less strictly controlled divergence. By comparison with these materials, the low figures of merit of KDP and similar materials make them relatively unattractive options.

---

1 T. Ukachi et al., App. Phys. Lett. **57** , p980 (1990).
2 Y. Cui et al., Opt Lett. **17**, p646 (1992).
3 J. Halbout, S.Blit, W. Donaldson and C.L. Tang, IEEE J. Quant. Elect. **QE-15**, p1176, (1979).
4 R. A. Phillips, J. Opt. Soc. Am. **56**, p629, (1966).
5 G.D. Boyd and D.A. Kleinman, J. Appl. Phys. **39**, p3597 (1968).
6 R.C. Eckardt, H. Masuda, Y.X. Fan, R.L. Byer, IEEE J. Quant. Elect. **QE-26**, p922, (1990).
7 M.J. Rosker, K. Cheng, C.L. Tang, IEEE J. Quant. Elect. **QE-21**, p1600, (1985).
8 R.F. Belt, G. Gashurov and Y. S. Liu, Laser Focus No.**110**, (1985).
9 C.Chen, Y.Wu, A. Jiang, B. Wu, G. You, R. Li, S. Lin, J. Opt. Soc. Am. B, Vol. **6**, p616, (1989).
10 D. Nikogosyan, Sov. J. Quant. Elect. **7**, p1, (1977).
11 M. J. Rosker, C. L. Tang, J. Opt. Soc. Am. B, Vol. **2**, p691, (1985).
12 G.C. Catella, J.H. Bohn, J.R. Luken, IEEE J. Quant. Elect. **QE-24**, p 1201 (1988).
13 D. Eimerl, L. Davis, S.Velsko, J. App. Phys. **62**, p1968, (1987).
14 S. Lin, Z. Sun, B. Wu, C. Chen, J. App. Phys. **67**, p634 (1990).
15 G.A. Skripko, S.G. Bartoshevich, I.V. Mikhnyuk, I.G. Tarazevich, Opt. Lett. **16**, p1726 (1991).
17 A. J. Henderson et al., J. Opt. Soc. Am. B **7**, p1402 (1990).
18 F.C. Zumsteg, J.D. Bierlein and T.E. Gier, J. Appl. Phys. **47**, p4980 (1976).
19 Y. Uematsu, Jap. J. Appl. Phys. **13**, p1362 (1974).
20 P. Gunter, Proc. SPIE 236, 8 (1981).
21 B.F. Levine and C.G. Bethea, App. Phys. Lett. **20**, p272 (1972).
22 G. Nath, H. Mehmanesch and M. Gsanger, Appl. Phys. Lett. **17**, p286 (1975).
23 D.N. Nikogosyan and G.G. Gurzadyan, Sov. J. Quant. Elect. **17**, p970 (1987).
24 G.D. Boyd, R. C. Miller, K. Nassau, W.L. Bond, and A. Savage, Appl. Phys. Lett. **5**, p234 (1964).
25 G. Nath and G. Pauli, Appl. Phys. Lett. **22**, p75 (1972).

Chapter 4
The excimer-pumped OPO system

4.0 Experimental arrangement

The excimer-pumped OPO system was configured as depicted in figure 4.1. The XeCl excimer beam power and polarisation were controlled using a gas cell attenuator and a dielectric coated polarising plate. The beam was compressed using a reverse-telescope lens combination of variable compression. The OPO in its simplest form consisted of a nonlinear crystal surrounded by two plane mirrors of appropriate reflectivity at the signal wavelength, and highly transmitting at the pump wavelength, while the unconverted fraction of the pump beam was separated from the signal and idler using several dichroic plates. It was found to be necessary to allow the pump beam to propagate a distance of around 3m between the polariser and the beam compressor, in order that any on-axis pump reflections should be returned to the excimer outwith the duration of the pump pulse, thus avoiding amplification within the power oscillator, and resulting damage to the laser optics.

4.1 The pump laser

Two lasers were in fact used in the course of this work. Both were injection-seeded excimer lasers operating on the Xenon Chloride wavelength (308nm). The laser initially used was built by Majid Ebrahimzadeh, who began the St. Andrews experimental programme on OPO research, and it is extensively described in Ref. 1 The master oscillator/ power oscillator combination is extremely similar in design to that of the more powerful commercial device (Lambda Physik EMG150ET) which was used latterly. The homebuilt system used a pair of coated etalons to produce a narrow bandwidth master oscillator output, and its polarisation was determined by Brewster-angled windows. This low power line-narrowed beam was then injected into the power

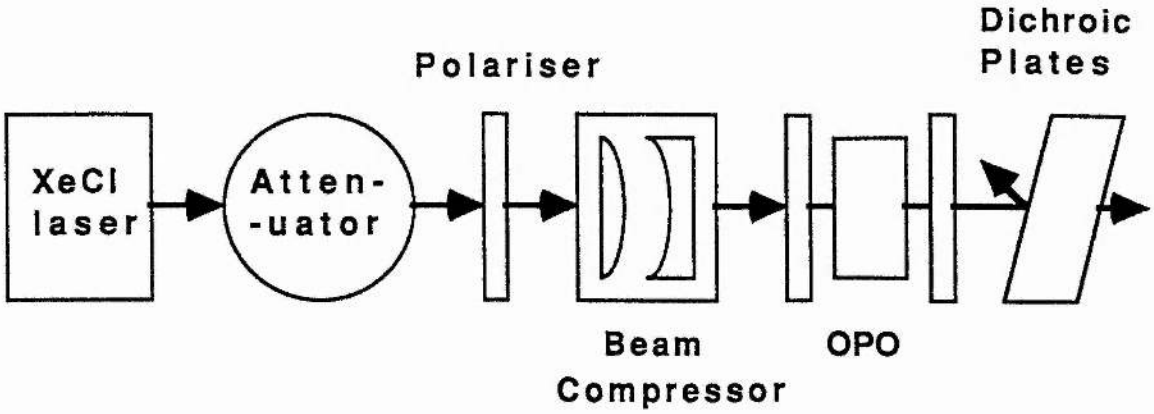

Figure 4.1 Schematic diagram of the configuration of the excimer-pumped OPO .

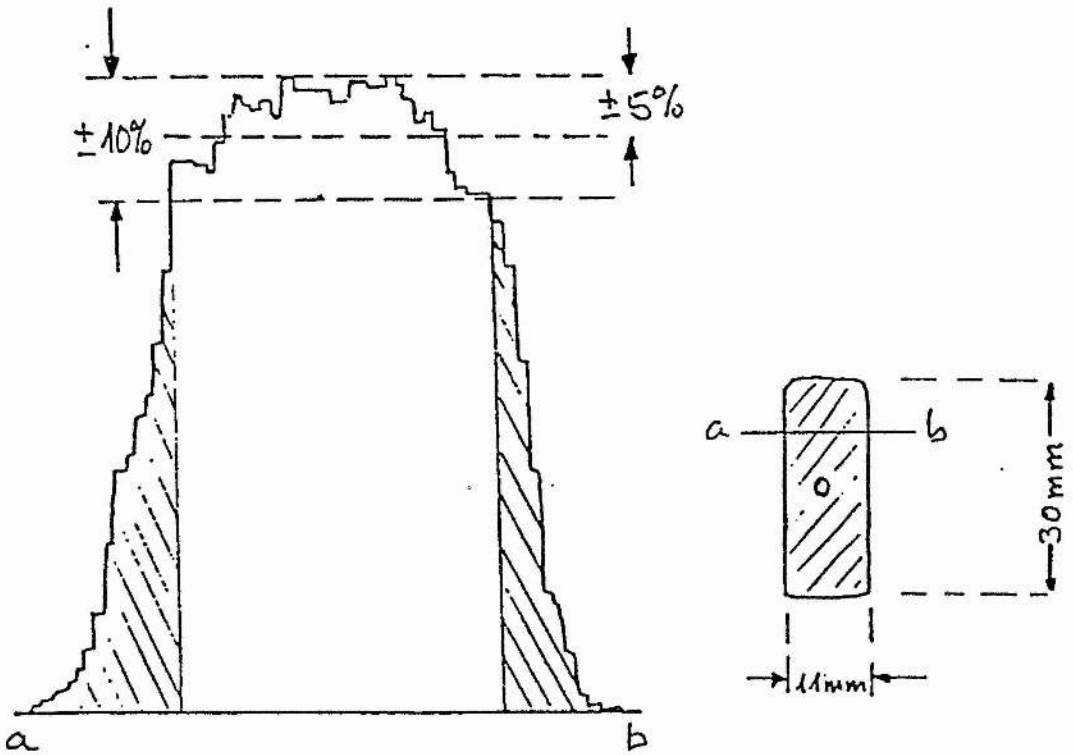

Figure 4.2 Spatial intensity profile of the Lambda Physik EMG150ET output.

oscillator through a hole at the centre of the rear mirror. The linewidth of the power oscillator output thus matched that of the master oscillator seed signal, while the beam divergence was minimised by the design of the power oscillator as an unstable resonator. Pulses of up to 25mJ were produced by this device at a 1Hz repetition rate.

Line-narrowing in the Lambda Physik EMG 150 excimer laser was achieved through the use of beam expansion prisms and a diffraction grating to provide dispersive feedback in the master oscillator. Otherwise this laser operated along similar lines to the homebuilt system. However, it was also equipped with optics to allow operation on XeF (351nm) and KrF (249nm) wavelengths. The 10Hz operation of the EMG150 provided the system with a potential maximum average power in excess of one watt, while ease of alignment of the OPO was considerably improved by this higher repetition rate. The pulse energy of this device was, on a day-to-day basis, no more than 100mJ, despite the 150mJ specification (seemingly based on "absolute maximum" performance). The excimer beam spatial profile was as depicted in fig. 4.2. Excluding the 'hole' in the output resulting from the high-reflecting spot on the slave oscillator output coupler, the intensity profile in each dimension is more accurately approximated by a uniform top-hat intensity, than by a Gaussian. It can be seen that the spatial profile, even in the minor dimension of the excimer beam^2, is such that 70% of the energy is located within a region in which the spatial distribution is constant within +/-10%. The main properties of both lasers are summarised in Table 4.1. The magnitude of the linewidth and divergence of these devices with respect to the phase-mismatch constraints of various nonlinear materials, have been considered in sections 3.4.1 and 3.4.2.

4.2 Energy attenuation and beam focussing

The excimer attenuator provided a relatively compact, easily adjustable means of controlling the laser power to an accuracy of better than +/-0.1mJ. Attenuation was provided by a cell

Table 4.1: Pump laser characteristics		
Property	Homebuilt laser	Lambda Physik EMG 150
Output wavelength	308nm	308nm (also 249,351nm)
Divergence (FWHM)	0.06mR	0.2mR
Linewidth (FWHM)	0.2cm-1	0.2cm-1
Pulse Energy	25mJ	150mJ
Rep. rate	1Hz	10Hz
Pulse duration	10ns	17ns
Polarisation	>90%	>95%
Cross section	10x25mm	10x25mm

containing a variable pressure sample of UV-absorbing gas as depicted in fig. 4.3. The cell was made up of two 3" aperture fused silica windows, sealed into an aluminium cell using corrosion-resistant 'Eriks' Viton O-rings. The internal distance between the windows was 2cm and thus the total internal volume was around $75cm^3$. The cell was connected by several metres of PTFE tubing to the gas system which was housed in a fume cupboard. The gas system consisted of a lecture bottle of Nitrogen Dioxide and a small vacuum pump (Leybold Heraeus S1.5). connected to a central manifold where the pressure was monitored by a gauge. The attenuation observed for the XeCl wavelength (308nm) can be seen in figure 4.4(a). alongside figures for the absorbtivity of NO_2 over a range of ultraviolet wavelengths (fig. 4.4(b)). The laser pulse energy was in general measured prior to the beam

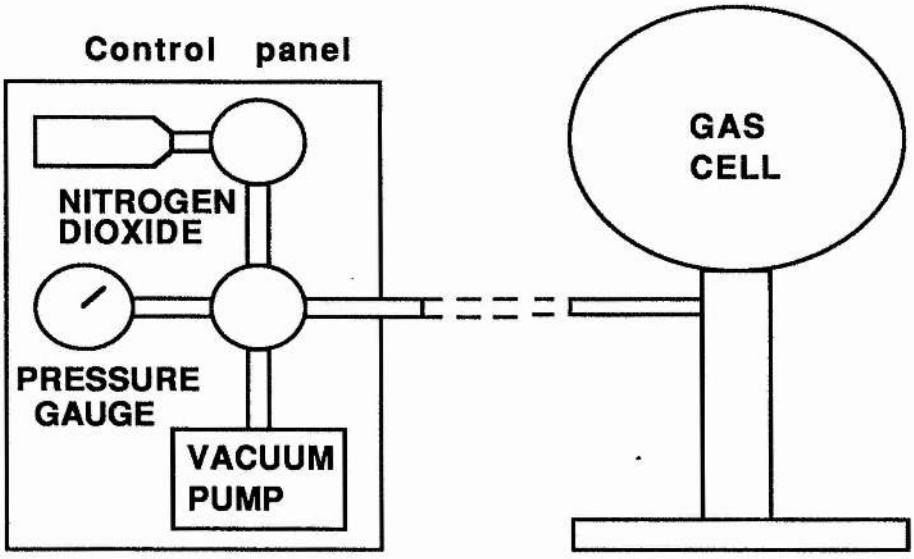

Figure 4.3 Schematic diagram of the Nitrogen Dioxide excimer laser attenuator.

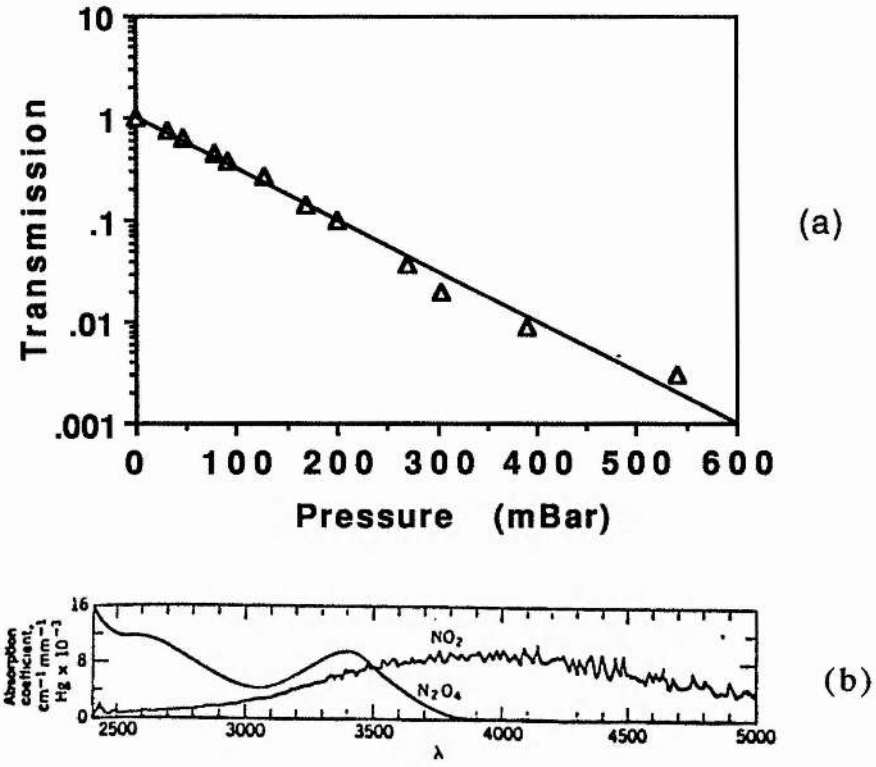

Figure 4.4 (a) Transmission of 308nm radiation observed as a function of the NO_2 pressure in the gas cell attenuator and (b) absorption coefficient of NO_2 as a function of wavelength in Angstroms.

compressor using a pyroelectric detector (Scientech Model 362).

Suitable beam compression was provided using a combination of a long focal length (1.5 to 2m) convex fused silica lens and a short focal length (-10cm to -60cm) plano-concave lens placed at a distance equal to the concave lens focal length away from the focal point of the convex lens. Computer analysis of the telescope lens configuration indicated that aberrations could be usefully reduced by using doublets rather than singlets. However, in practice the improvement in beam quality was only marginal, while the doublet arrangement incurred a much increased Fresnel loss (the lenses were not anti-reflection coated). In the end, best-form singlet lenses were found to be more practicable. Compression ratios of between 2.5 and 20 could be achieved, allowing pump energy fluences of several Joules/cm^2 in collimated beams of up to 6x2mm in cross-section.

4.3 The optical parametric oscillator

The normal configuration of the parametric oscillator was as shown in figure 4.5(a). The nonlinear crystal was located with its optic axis in the vertical plane, in a perspex mount attached to a rotation stage, capable of rotation accuracy better than 0.01° around a horizontal axis. The design of the crystal mount for Urea has been described in ref. 1. While this was a sealed cell accommodating the crystal immersed in index-matching fluid (Hexane) between two quartz windows, the mount for BBO held the crystal open to the atmosphere. The crystal mount assembly itself was supported on a stage which allowed rotation around a vertical axis, and other translation stages allowed the crystal aperture to be translated both horizontally and vertically with respect to the pump beam. The cavity mirrors were mounted separately in differentially adjustable gimbal mounts which could be positioned at the desired spacing from the nonlinear crystal, and the OPO as a unit was initially aligned such that the cavity mirrors and crystal faces were perpendicular to the pump beam.

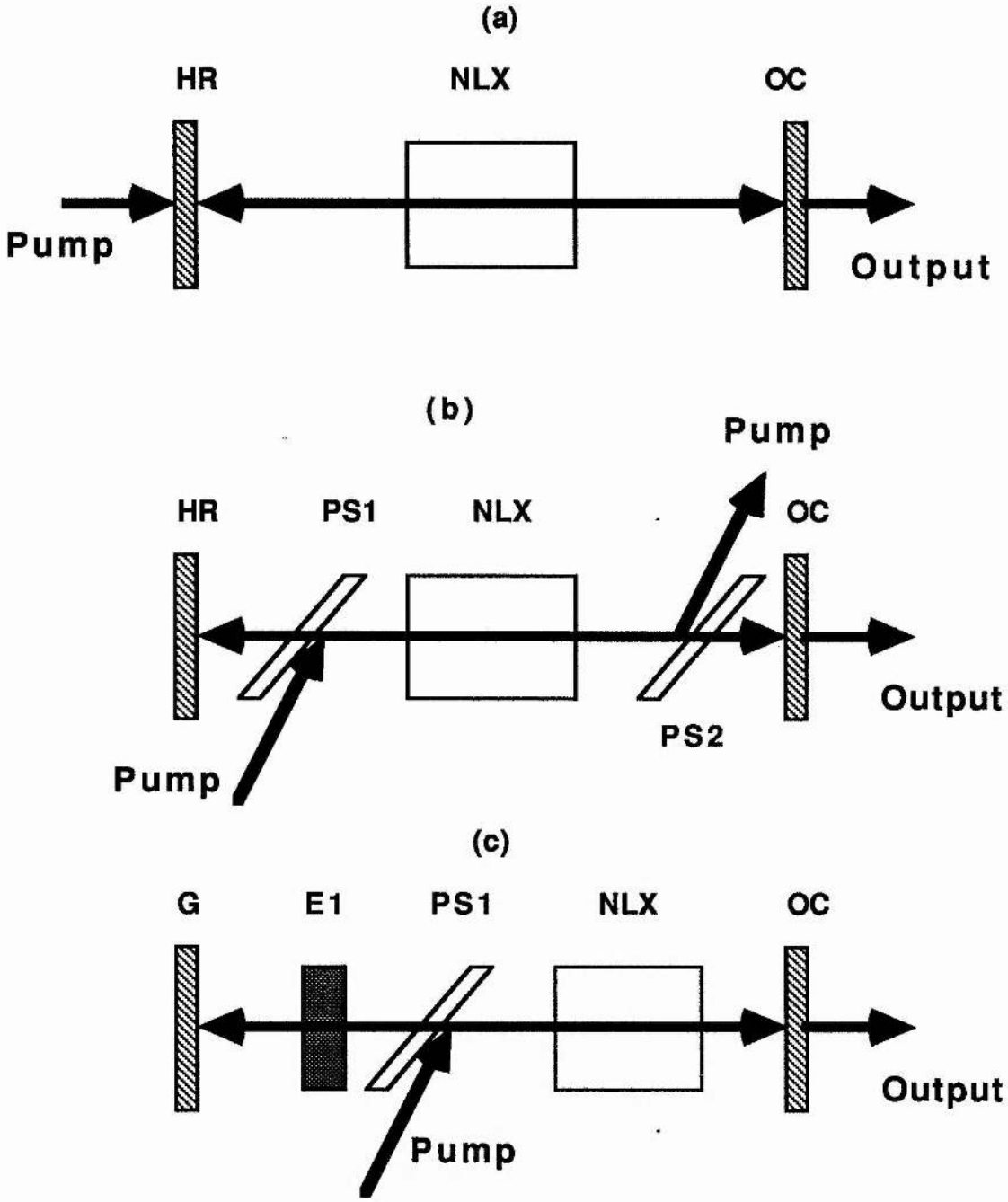

Figure 4.5 Possible OPO cavity configurations, allowing coupling of the pump beam either through the cavity mirrors or via dichroic steering plates. HR is a highly reflecting plane mirror, OC is an output coupler, NLX is the nonlinear crystal, PS1, PS2 are dichroic pump steering plates and E1 is a signal line-narrowing element. G is a further dispersive element, such as a diffraction grating.

The pump beam direction could be defined for alignment purposes using a He-Ne laser and two pinholes. The device is shown in the photograph of Figure 4.6.

In this configuration, quite severe constraints were placed on the cavity mirror coatings, in that high transmission at the 308nm pump wavelength was required as well as the desired reflectivity over as wide a wavelength range as possible. In practice, this meant that a compromise had to be reached between the reflectivity bandwidth and the ultraviolet damage resistance, since typically a signal bandwidth of only 100nm was possible for any one mirror set. However, assuming an e-o+o interaction as in Type 1 phase-matching in BBO, this could be overcome using the cavity design of figure 4.5(b). In order to sidestep the requirement for ultraviolet damage-proof cavity mirrors, the pump light could be coupled in and out of the cavity using a pair of damage resistant Brewster-angled dichroic steering plates which reflect the vertically polarised pump wave and transmit the horizontally polarised signal and idler waves. These were produced by Laseroptik GmbH and had a transmission greater than 98% for the p-polarisation between 450nm and 1900nm, and over 99% reflectivity at 308nm for the s-polarisation. No damage was observed using these plates for pump fluences up to $2Jcm^{-2}$. In conjunction with these plates, cavity mirrors of wider reflectivity range (e.g. 95%R @ 400-700nm) could be used for the same pump intensity, at the cost of some increase in cavity length. The plates used had dimensions 10 x 10 x 1.5mm and were mounted on perspex posts which allowed independent rotation of the plates around a vertical axis. Alternatively, a single steering plate could be used as in figure 4.5(c), to allow the use of further elements, such as Fabry-Perot etalons and diffraction gratings, lacking the capability to transmit the pump wavelength, at a minimum cost in terms of cavity length increase. Throughout the experiments plane mirror substrates were used, such that there was a 30' wedge between the front and rear surfaces. The rear surfaces were anti-reflection coated at the pump wavelength.

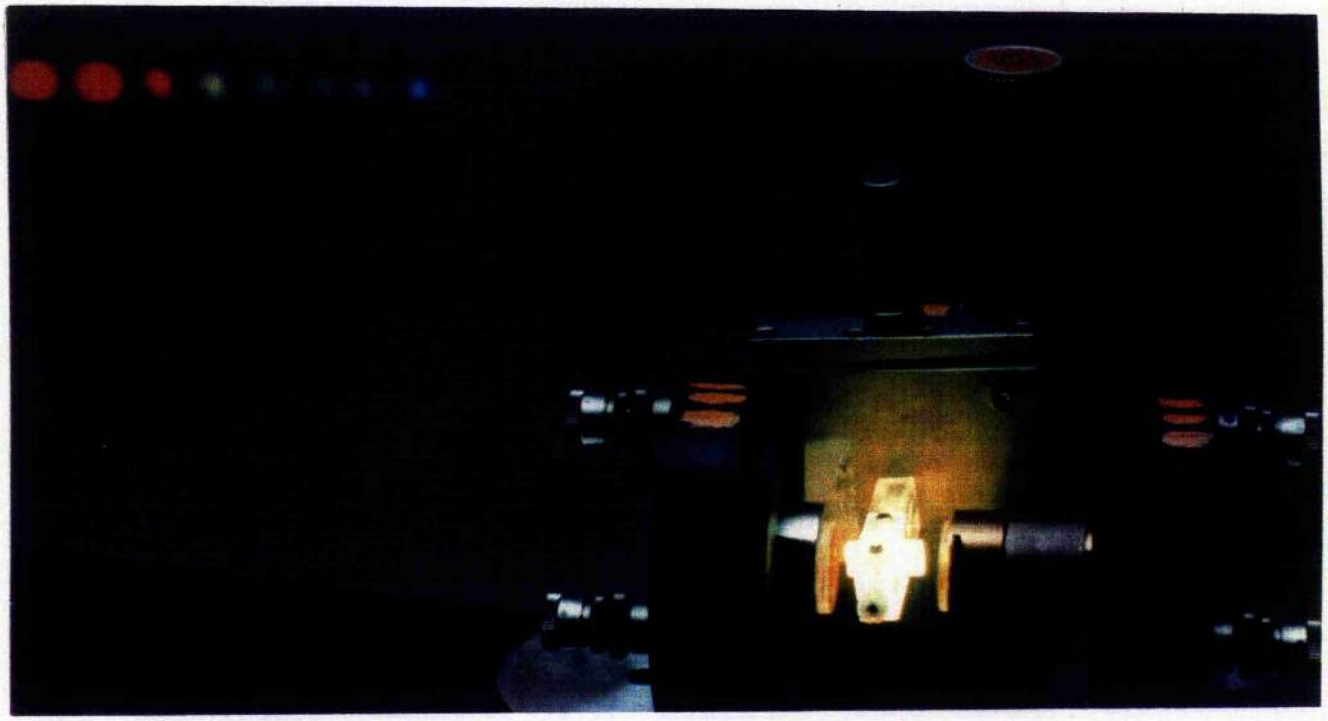

Figure 4.6 Multiple exposure photograph of the OPO assembly. The cavity shown is formed by a 20mm Type 1 phase-matched BBO crystal surrounded by two plane mirrors of reflectivity 95% over the range 500-600nm. The output using this mirror set is shown dispersed by a diffraction grating (off photograph).

4.4 Nonlinear crystals; crystals and OPO tuning ranges

Two materials and phase-matching configurations were employed in the work on visible OPOs described here: Type 2 phase-matching in urea and Type 1 phase-matching in BBO. Our first experiments on urea were performed using crystals grown in our own laboratories, while samples of 20mm or more in length were later purchased from the Fujian Institute on the Structure of Matter, in China. This was also the source of both the BBO crystals used. All nonlinear crystals used in this work were cut as regular cuboids, with polished entrance and exit faces, and dimensions A, B and C (These are laboratory dimensions only. The relative orientation of the piezoelectric, crystallographic, and principal optic axis systems has been listed in Appendix A). Here C corresponds to the normal incidence propagation direction, while A and B are the two dimensions of the entrance and exit faces.

The crystal dimensions with respect to the principal optical axes, are shown in figures 4.7(a)-(c).

Urea crystals were cut to maximise the nonlinear coefficient experienced for propagation of the pump beam normal to the crystal entrance and exit faces. The effective nonlinear coefficient for Type 2 phase-matching in Urea is given by

$$d_{eff} = d_{14} \sin\theta \ \sin 2\phi \qquad (4.1)$$

It can thus be seen that this direction of propagation implies that the crystal axes should be oriented such that $\theta = 90^o$ and $\phi = 45^o$ for propagation at normal incidence. The phase-matched signal and idler wavelengths under these conditions are 570nm and 670nm respectively. The crystal surface normals were perpendicular to the optic axis (z-axis) and the B-dimension was oriented at 45^o to the x-axis. The dimensions (A x B x C) of the samples used were as follows:

20 x 10 x 8mm
16 x 7 x 14mm
12 x 10 x 15mm
4 x 8 x 25mm

Here the A direction is that parallel to the z-axis, and C is defined by the normals to the entrance and exit faces.

In BBO the crystals were cut so that propagation of the pump beam normal to the entrance and exit faces produced phase-matching at a signal wavelength fairly central in the 308nm pumped OPO tuning range. Phase-matching in BBO is achieved for a range of angles θ between the pump beam direction and the optic axis (x-axis) of between 25^o and 39^o. The effective nonlinear coefficient for Type 1 phase-matching in BBO is given approximately by

$$d_{eff} = d_{22} \cos\theta \ \cos 3\phi \qquad (4.2)$$

Therefore in order to maximise d_{eff} the crystals were cut so that $\phi = 0^o$ for propagation parallel to the surface normals. The dimensions (A x B x C) of the samples used were:

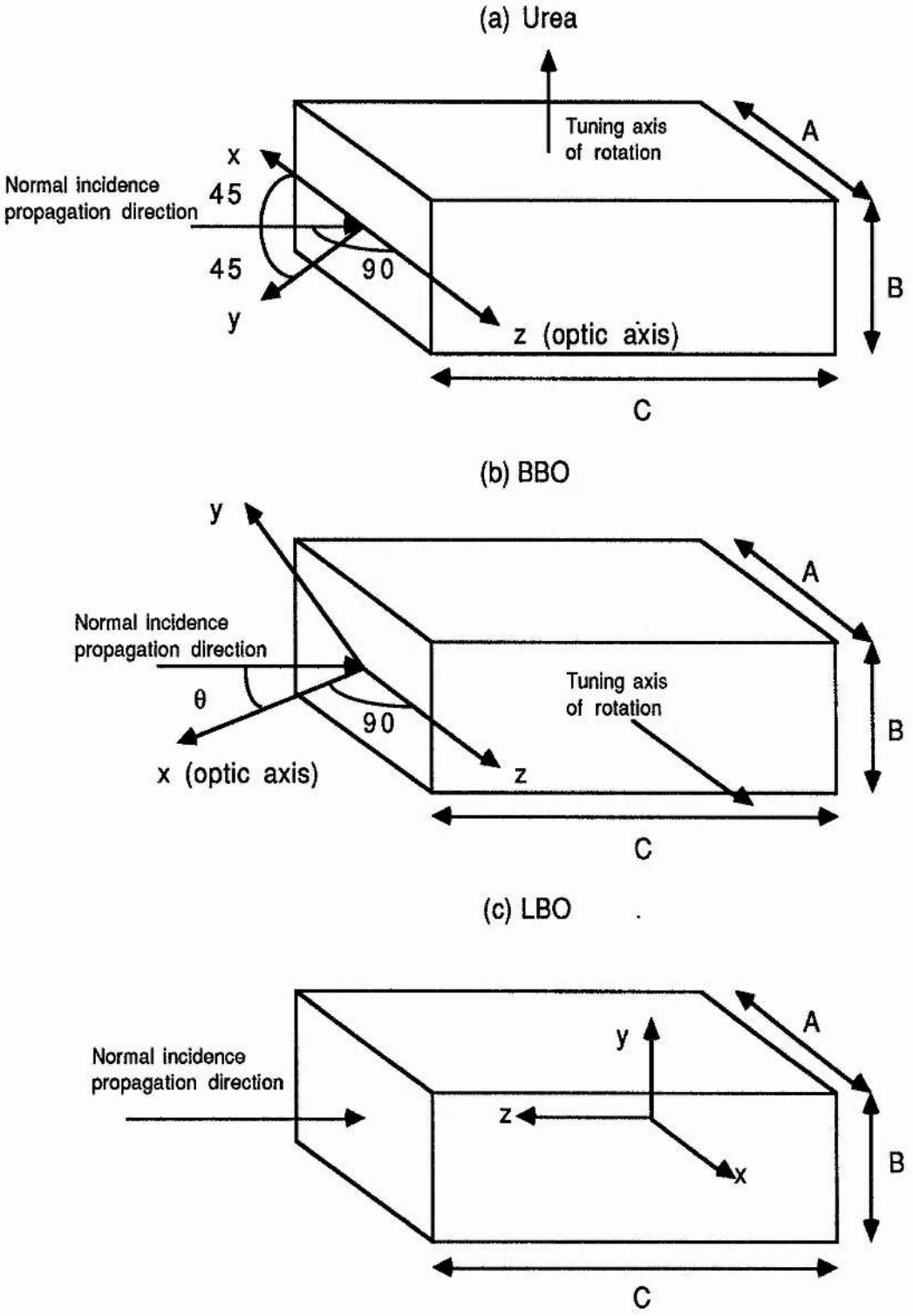

Fig. 4.7 Crystal dimensions and orientation with respect to principal axes (x,y,z) for (a) Urea, (b) BBO and (c) LBO.

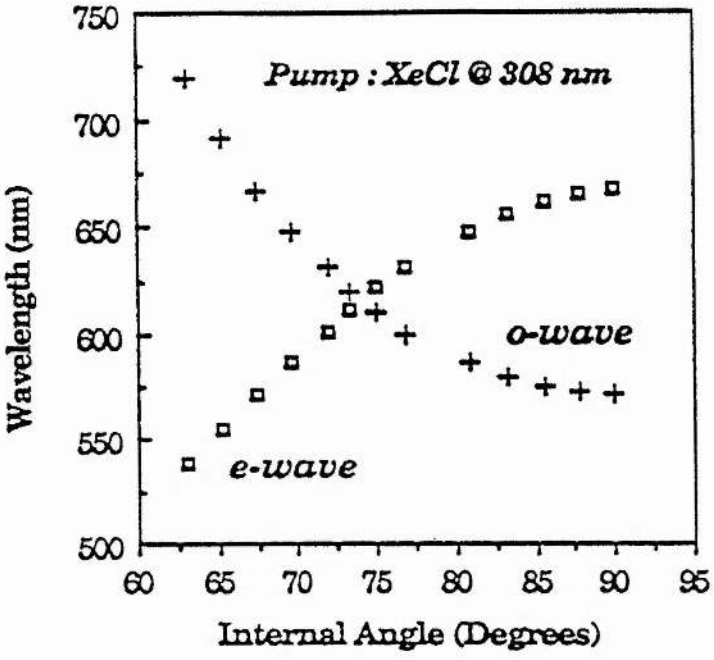

Fig. 4.8(a) : The observed OPO tuning range in the 15mm long Urea crystal pumped at 308nm.

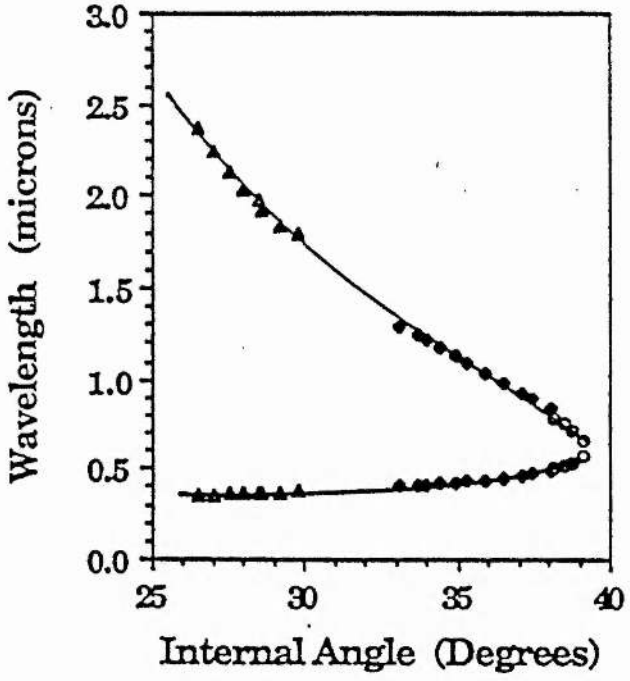

Fig. 4.8(b): Observed tuning range in the 12mm BBO crystal shown against the tuning curve calculated from Sellmeier equations given in Appendix B. The different sets of points correspond to the use of different mirror sets.

6 x 8 x 12mm

4 x 8 x 20mm

and the optic axis in these crystals was oriented at $\theta = 32^{o}$ and $\theta = 35^{o}$ to the A-B plane surface normals, respectively.

The experimentally determined tuning ranges (shown in figs. 4.8(a) and (b)) for 308nm pumping have been previously shown[1] to match closely the theoretical values of figures 3.3(b) and 3.4(a). In urea, tuning was achieved in the 15mm interaction length sample over the range 537 to 720nm at internal angles between 63^{o} and 90^{o}, while output has been observed in BBO over a continuous range from 354nm to 2370nm. In both these cases the tuning was limited by reduction in the crystal aperture as the crystal was tilted to tune the signal wave towards the ultraviolet.

A number of experiments were also carried out in OPOs based on Lithium Triborate (LBO), generating ultraviolet wavelengths, and comparison was drawn with Barium Borate for the same spectral range. The LBO crystal was cut to allow Type 2 noncritical phase-matching for propagation normal to the entrance and exit faces. This configuration corresponds to propagation parallel to the z-axis with a pump beam polarised along the x-axis, and results in maximal effective nonlinear coefficient. Resultant signal and idler wavelengths at room temperature are 385nm and 1.5μm respectively. The dimensions (A x B x C) of the LBO crystal used were

3.5 x 3.5 x 16mm

Here (A x B x C) correpond to the optical (x x y x z) axes. These dimensions restricted the possible angle tuning to only a small range, while temperature tuning allowed noncritically phase-matched tuning to be maintained over several tens of nanometres.

References

1 M. Ebrahimzadeh, Ph. D. Thesis, University of St. Andrews (1989).

2 Operation Manual, Lambda Physik EMG150ET. Lambda Physik GmbH, Hans Boeckler Straβe 12, Gottingen, D-3400, Germany.

Chapter 5
OPO threshold

5.0 Introduction

The following two chapters are intended to provide a comprehensive characterisation of the parameters involved in obtaining optimal power conversion in parametric oscillators of the type here utilising Urea and BBO. As in a laser, a specific threshold level of pump energy must be exceeded in order to obtain a useful level of output from an OPO. Thus the parametric generator can be a useful device only if the oscillation threshold is sufficiently far below the damage threshold of the components involved (i.e. the nonlinear crystal and cavity optics). In this chapter we will consider the oscillation threshold of pulsed singly resonant OPOs, and draw conclusions from comparison of results in urea and BBO with predictions of theory.

5.1 Steady state threshold for interaction of plane waves

In order to achieve useful levels of output from an OPO , the small amounts of power at the signal and idler wavelengths present in the cavity in the form of spontaneous parametric emission must be amplified to the order of magnitude of the pump field. Parametric amplification can occur only when the total gain at the resonant wavelengths over the period of a round trip in the cavity exceeds the sum of the losses over the same period. For the steady state case, this threshold condition can be expressed for both an SRO and a DRO, as follows[1]:

$$\left\{\Gamma_0 \ell\right\}^2 \frac{\sin^2(\Delta k \ell/2)}{(\Delta k \ell/2)^2} \approx \frac{\Delta_s \Delta_i}{4} \qquad \text{(DRO)} \qquad (5.1)$$

$$\left\{\Gamma_0 \ell\right\}^2 \frac{\sin^2(\Delta k \ell/2)}{(\Delta k \ell/2)^2} \approx \Delta_s \qquad \text{(SRO)} \qquad (5.2)$$

assuming small round trip power losses Δ at the resonant wavelength(s). In terms of the threshold pump power densities S_p^{th} required, we can combine equations (2.10), (5.1) and (5.2) to obtain the following expressions:

$$S_p^{th} = \frac{\Delta_s \Delta_i}{4\pi K \ell^2} \left\{ \frac{\sin^2(\Delta k \ell/2)}{(\Delta k \ell/2)^2} \right\}^{-1} \qquad \text{(DRO)} \qquad (5.3)$$

$$S_p^{th} = \frac{\Delta_s}{\pi K \ell^2} \left\{ \frac{\sin^2(\Delta k \ell/2)}{(\Delta k \ell/2)^2} \right\}^{-1} \qquad \text{(SRO)} \qquad (5.4)$$

These are the steady state oscillation thresholds for interaction of uniform plane waves. Equivalent expressions for the threshold power for the case of focussed Gaussian intensity profile beams in a DRO, were developed by Boyd and Kleinman[2]. Their work assumed equal confocal parameters (a measure of the beam focussing) for pump, signal and idler waves, and gave an expression for the optimum focussing in the presence of double refraction. Further studies have extended this work to consider the threshold for elliptical focussing in the presence of double refraction in doubly[3] and singly[4] resonant OPOs. Again both of these authors assumed equal confocal parameters. This assumption is not however made in the treatment of Guha et al.[5], who developed threshold equations for SRO and DRO allowing for double refraction, and for generalised values of Gaussian beam waist for signal, idler and pump.

It can be seen from the plane wave expressions (5.3) and (5.4), that the threshold pump power density for an SRO is greater than that for a DRO with equivalent losses at the resonant waves, by a factor $4/\Delta_i$. If the damage thresholds of the elements of the OPO are sufficiently high to allow pumping at this higher level, it is desirable to operate as an SRO in order to avoid the undesirable frequency-tuning properties of the DRO. In general SRO threshold pump intensities are attainable only through the use of pulsed pump sources, and in our own case we have used a XeCl excimer as the pump laser. Thus the following section relates the oscillation threshold of a pump source of this nature to the expressions already given for the steady state situation.

5.2 Pulsed OPO threshold: Oscillator rise-time

In a pulsed OPO, once the pump intensity has reached a level to provide net gain greater than unity, the resonant wave requires to propagate a finite number of cavity round trips in order to be amplified to a 'threshold' level. This propagation time or 'risetime' can be a considerable fraction of the total pump pulse length, and amounts to a part of the pump pulse during which significant frequency conversion does not take place (Specific expressions for SRO and DRO risetime have been developed by Pearson et al. in ref. 6). The idea of the OPO risetime as an effective cavity loss additional to absorption, scattering and output coupling losses, is central to a theoretical treatment of pulsed OPO threshold. A detailed theoretical model of pulsed OPO threshold has been developed by Brosnan and Byer[7] based on Type 1 phase-matching in the negatively uniaxial material $LiNbO_3$, but relatively simply adaptable to other situations.

5.2.1 The Brosnan and Byer threshold model

The treatment is founded on the following initial assumptions:

[1] Type 1 phase matching in a negative uniaxial nonlinear material (e - o + o)

[2] Gaussian spatial intensity profiles.

[3] Time dependent gain coefficient Γ

[4] A value of initial signal noise power as given by expression (5.7)

[5] Threshold defined by a signal power of 100μJ

An iterative solution could be produced on the basis of these assumptions but the model sets out to produce a simplified expression for threshold through the following steps:

[1] A time independent gain profile of width $\bar{\tau}$ and constant magnitude $\bar{\Gamma}$ is developed such that $\bar{\tau}$ is the period of the pulse (τ is the pulse half width, $1/e^2$ intensity) with net instantaneous gain greater than unity, and the average gain $\bar{\Gamma}$ is determined by

requiring that $\bar{\Gamma}\,\bar{\tau}$ be equivalent to the total integrated gain over the duration of the temporally Gaussian pulse.

[2] An effective parametric gain length $\mathcal{L}$ is used to take into account birefringent walk-off of the pump wave from the signal and idler waves.

[3] It is assumed that the threshold signal power level is reached at the end of the period τ, equivalent to p cavity round trips.

[4] An iterative expression is derived for the signal power P_m after m round trips, in terms of that after m-1 round trips.

[5] τ is assumed to be approximately equal to 2τ for most practical OPO configurations.

The resulting threshold condition

$$\Gamma \mathcal{L} = \frac{L}{\tau c} \ln \frac{P_n}{P_0} + 2\alpha\mathcal{L} + \ln\frac{1}{\sqrt{R}} + \ln 2 \qquad (5.5)$$

(where L is the cavity optical length, α is the field absorption coefficient, assumed equal at signal and idler, and R is the product of the mirror signal reflectivities), is similar in character to the steady state threshold condition in that it expresses an equivalence of gain and effective losses. It can be rearranged to produce a threshold pump energy fluence:

$$J_o = \frac{2.25}{\kappa g_s \mathcal{L}^2}\tau\left[\frac{L}{2\tau c}\ln\frac{P_n}{P_0} + 2\alpha\mathcal{L} + \ln\frac{1}{\sqrt{R}} + \ln 2\right]^2 \qquad (5.6)$$

where κ is defined by

$$\kappa = \frac{2\omega_s\omega_i d_{eff}^2}{\varepsilon_o c^3 n_p n_s n_i}$$

and g_s is a spatial mode coupling coefficient defined in ref. 7.
The risetime loss term is evaluated using a value of 33 for $\ln(P_n/P_0)$ which assumes a minimum detectable threshold signal level of 100μJ as stated, and a value of the spontaneous parametric signal noise power radiated into a cone of semiangle Θ about the pump wave normal direction, calculated from the following expression[8]:

$$P_s = \left(\frac{\beta \; P_p \ell}{b}\right)\pi\Theta^2 \qquad (5.7)$$

where ℓ is the nonlinear crystal length, P_p is the pump power, and the factors b and β are defined as follows:

$$\beta = \frac{2\nu_s^4 \nu_i d_{eff}^2 h n_s}{(2\pi)^3 \varepsilon_o^3 c^5 n_i n_p} \qquad (5.8)$$

$$b = \frac{\delta k_s}{\delta \nu_s} - \frac{\delta k_i}{\delta \nu_i} \quad , \qquad (5.9)$$

and where ν_s and ν_i are the signal and idler frequencies, and h is Planck's constant.

Expression (5.7) is obtained on the assumption that a plane collimated pump wave mixes with an effective idler flux of one photon in each black-body mode of a quantizing volume, to produce signal at all frequencies and in all directions, in amounts of power dependent on the phase-matching. In order to illustrate the level of amplification required we have evaluated this figure for the case of a 20mm BBO crystal, by equating Θ to half the acceptance angle as defined by (2.36), and under the following typical conditions:

Angular acceptance $\Delta\theta$ = 0.2mR, pump energy E_p = 20mJ, pulse width 17ns (FWHM), λ_s = 580nm, λ_p = 308nm, ℓ = 20mm, d_{22} = 2.2pm/V

These values produce an initial signal noise power P_s, corresponding to an energy

$$E_s = 2.8 \times 10^{-18} J$$

For this value $\ln(P_n/P_o)$ has a value of 31, corresponding quite closely to the figure used in ref. 7. The relative importance of risetime loss in determining OPO threshold is further illustrated in Table 5.1. Values for the three loss components involved in expression (5.6) are given for a range of typical operating conditions. The calculations of threshold shown are made assuming that $[\ln (P_n/P_o)] = 33$, and for the appropriate pulse duration. The value used for $2\alpha\ell$ was inclusive of absorption,

scattering and Fresnel losses, and was based on measured transmission values for the crystals used.

It is clear that an ultimate lower limit in threshold is set by the sum of the risetime, field absorption/scattering and output coupling losses. Risetime loss becomes more significant for large cavity lengths as the number of round trips within the duration of the pump pulse decreases. The crystal surface and bulk losses for the two samples are high in both cases and this highlights the lack of anti-reflection coatings and the relatively poor bulk quality of BBO.

Table 5.1: Cavity losses under typical conditions in BBO

Cavity	Risetime loss	Absorption Scattering and surface loss	Output coupling loss
20mm xtal 23mm cavity 2x95% mirrors	0.14	0.24	0.05
20mm xtal 50mm cavity 2x95% mirrors	0.24	0.24	0.05
20mm xtal 23mm cavity 95% x 40%	0.14	0.24	0.48
12mm xtal 23mm cavity 2x95% mirrors	0.11	0.14	0.05

5.2.2 Application to excimer pumping of Urea and BBO

It should be noted that the Brosnan and Byer expression is derived on the basis of interaction between three Gaussian beams of differing waist dimensions. However, figure 4.2 shows that the spatial profile of the excimer beam[10] is such that 70% of the

energy is located within a region in which the spatial distribution is constant within +/- 10% . Hence it is more appropriate to assume a simple "top-hat" spatial profile such that at all points distant r from the beam centre

$$E_j = E_{j0} \qquad (-W_j < r < W_j,\ j = p, s, i) \tag{5.10}$$

where W is the beam half-waist.

Further, we also assume that the interaction between constant intensity fields results in polarisation wave dimensions $\bar{W}_j$ equal to the electric field dimensions (i.e. $\bar{W}_j = W_j$, j = p, s, i). This matching of field extents gives us an effective signal spatial mode coupling coefficient g_s, as defined in ref. 13 as

$$g_s = \frac{2\bar{W}_s^2}{\bar{W}_s^2 + W_s^2}\ , \tag{5.11}$$

of unity. In the case of a noncritically phase-matched geometry such as that utilised in Urea, where there is no birefringent walkoff between the pump, signal and idler beams, the effective interaction length is equivalent to the crystal length. We can thus use the following expression for threshold:

$$J_o = \frac{2.25}{\kappa l^2}\tau\left[\frac{L}{2\tau c}\ln\frac{P_n}{P_0} + 2\alpha l + \ln\frac{1}{\sqrt{R}} + \ln 2\right]^2 \tag{5.12}$$

However, in the case of a critically phase-matched negatively uniaxial material, in which the extraordinary pump wave walks off from the ordinary signal and idler, we must define an effective interaction length l as in Ref. 7. For a "top-hat" spatial profile we can define signal and idler coupling coefficients $c_{s,i}$ as the fractional beam interaction as a function of the propagation distance z through the nonlinear crystal as in figure 5.1, i.e.

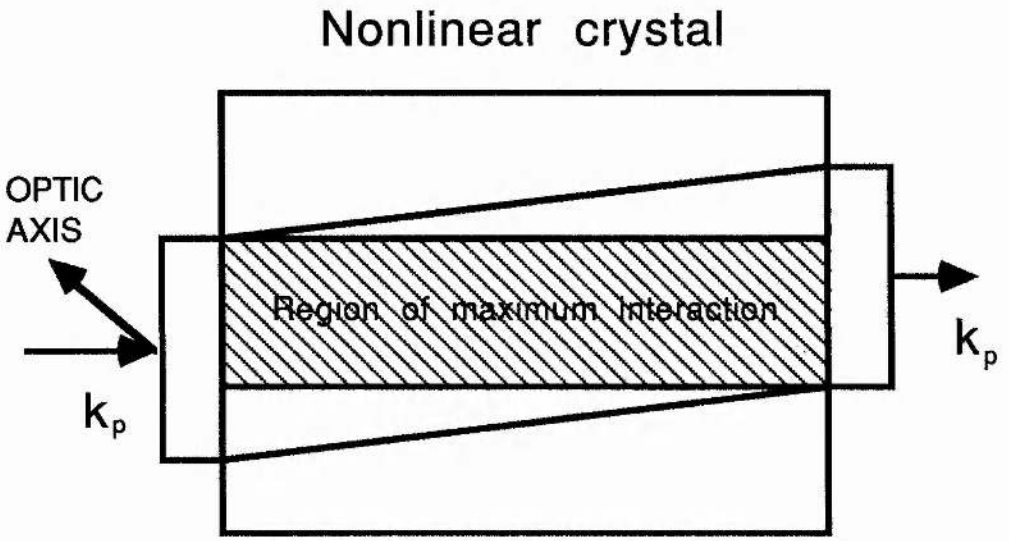

Fig. 5.1 Schematic diagram of beam interaction in a negatively uniaxial nonlinear crystal. Shaded area shows region of maximum interaction between the ordinary signal and idler waves, and the extraordinary pump wave which undergoes birefringent walk-off from the other two waves.

$$c_{s,i} = \frac{1}{\left(1 + \frac{\rho z}{2W_y}\right)} \qquad (5.13)$$

where ρ is the internal walk-off angle and W_y is the beam half-waist in the walk-off dimension. Substitution of the coupling coefficient into (2.6) as in ref. 7 results in modified coupled equations:

$$\frac{d\mathcal{E}_s(z)}{dz} + \alpha_s \mathcal{E}_s(z) = i\kappa_s c_{s,i} \mathcal{E}_p(z) \mathcal{E}^*_i(z) \exp[i(\Delta kz + \varphi)]$$

$$\frac{d\mathcal{E}_i(z)}{dz} + \alpha_i \mathcal{E}_i(z) = i\kappa_i c_{s,i} \mathcal{E}_p(z) \mathcal{E}^*_s(z) \exp[i(\Delta kz + \varphi)] \qquad (5.14)$$

These can be solved to give a threshold expression appropriate to negatively uniaxial materials such as BBO as in (5.6), where the effective parametric gain length is $\mathcal{L}$,

$$\mathcal{L} = \frac{2W_y}{\rho} \ln\left(1 + \frac{\rho L}{2W_y}\right) \qquad (5.15)$$

5.3 Experimental results

Threshold measurements were made by adjustment of the attenuator gas pressure to a point where OPO output was observed on 50% of shots on average.

5.3.1 Urea

Initial experiments on urea were performed using the homebuilt excimer laser and results have been reported in references 9. An 8mm 90° phase-matching sample was used in an OPO which was the first such device to be pumped by an excimer laser. Urea was found to be a very useful material for use in conjunction with relatively low energy pump pulses, due to its low oscillation threshold. The variation of threshold with various parameters is described in the following sections.

(a) Threshold vs crystal length

The oscillation threshold in 90° phase-matching samples of length 8,14,15 and 25mm was measured for pumping at 308nm using the 10ns pulse laser. The pump beam was compressed using a 2m x -25cm lens combination and the threshold was measured using neutral density filters to attenuate the pump beam. The OPO cavity was formed by two plane mirrors of reflectivity 95% and 40% at the 570nm resonant wave, separated by 54mm. Figure 5.2 shows that the threshold energy fluence drops from a value of $0.3 Jcm^{-2}$ in the 8mm sample to $0.023 Jcm^{-2}$ in the 25mm sample. The threshold value in the 25mm sample represents an energy of 0.9mJ and thus we were able to pump the OPO at a level many times above threshold. Theoretical calculations of threshold using expression (5.12) and assuming a value of 1.4pm/V for d_{14} were found to be up to four times in excess of the experimentally measured thresholds. Such a large discrepancy cannot be explained in terms of reasonable adjustment of the various loss parameters involved and we would assert that it can be attributed to inaccuracy in the value of the nonlinear coefficient. Throughout our experimental work on urea, calculations of threshold show

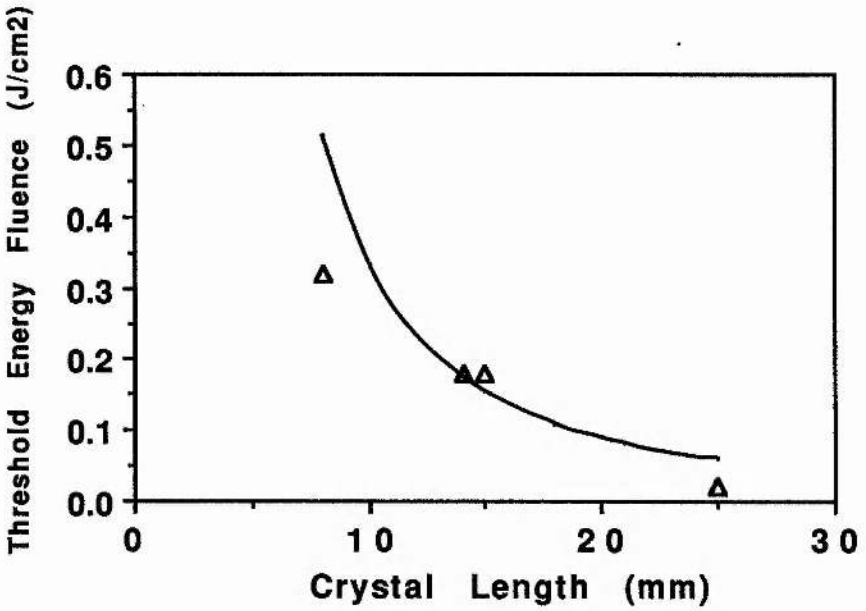

Fig. 5.2 Threshold Energy Fluence in an NCPM urea OPO vs crystal length under the following conditions: Mirror separation l_c = 54mm, Mirror reflectivities R_1 = 0.95, R_2 = 0.40. Solid curve shows calculations of threshold made using (5.12) and d_{14} = 2.3pm/V.

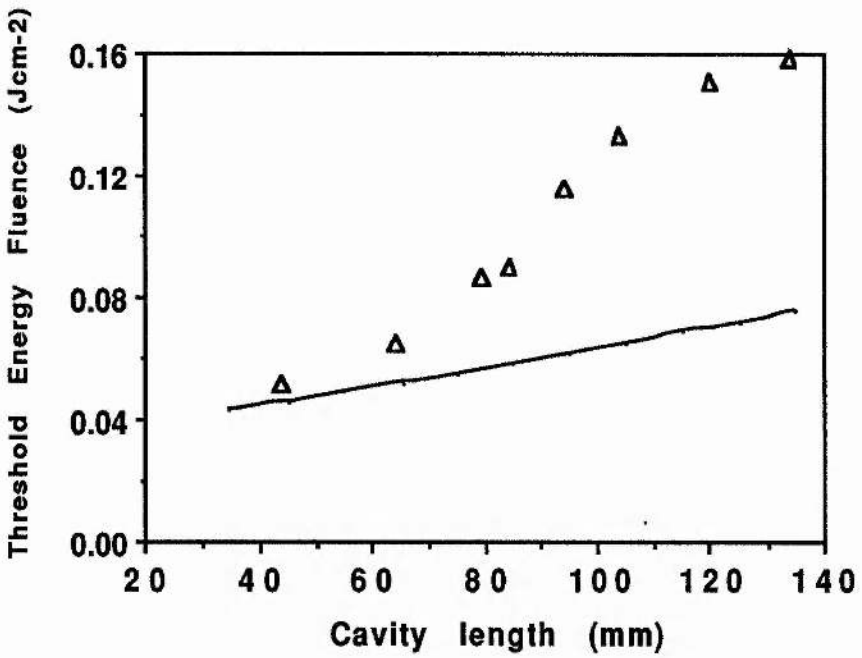

Fig. 5.3 Threshold Energy Fluence in an NCPM Urea OPO vs cavity length under the following conditions: l = 25mm, R_1 = 0.95, R_2 = 0.95 . Solid curve shows calculations of threshold made using (5.12) and a value for d_{14} of 2.3pm/V.

closer agreement using a value of 2.3pm/V for d_{14}. These calculations were made for Urea OPOs assuming a single pass power loss of 10%, i.e. that corresponding to Fresnel losses from two crystal faces.

(b) Threshold vs cavity length

Expression (5.6) indicates that the OPO rise-time loss varies in proportion with the cavity optical length as a result of the reduction in the number of double passes through the crystal which may be made by the resonant wave within the duration of the pump pulse. The fractional change in the overall OPO threshold is dependent on the relative magnitudes of the risetime loss and the other loss components expressed in (5.6). Figure 5.3 shows the thresholds experimentally observed in an OPO using 90° phase-matching in a crystal of Urea of length 25mm, with 95% reflecting cavity mirrors, and pumped by the 17ns pulse laser. It can be seen that the threshold scales in

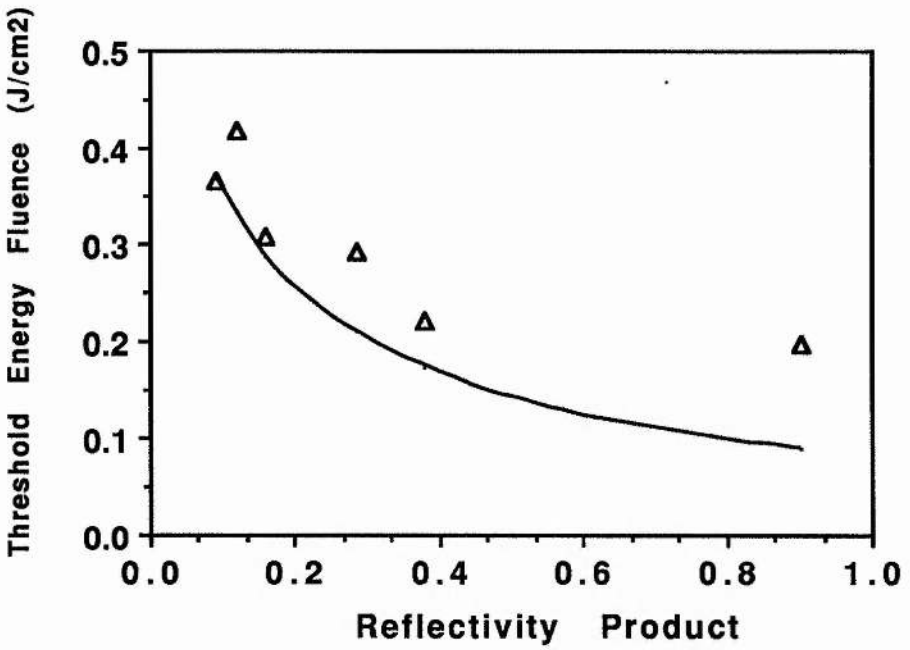

Fig. 5.4 (a) Threshold Energy Fluence in an NCPM Urea OPO vs cavity reflectivity under conditions: ℓ = 14mm, l_c = 54mm.

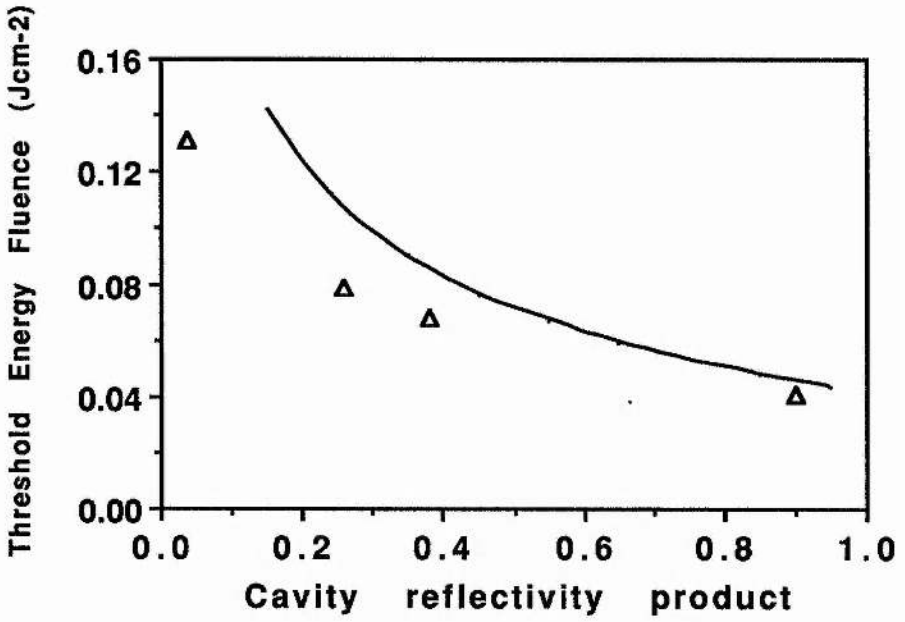

Fig. 5.4(b) Threshold Energy Fluence in an NCPM urea OPO vs cavity reflectivity under conditions: ℓ = 25mm, l_c = 44mm. Solid curve in each case show calculations of threshold made using (5.12) and a value for d_{14} of 2.3pm/V.

proportion to the cavity length. However, the theoretical curve calculated on the basis that d_{14} = 2.3pm/V, shows a considerably slower increase in threshold. This could be attributed to the use of an excessively large estimated value of the parasitic loss term in expression (5.6), coupled with the fact that the output coupling losses are in this case relatively low. Under such circumstances, the threshold predicted by (5.6) is a much more sensitive function of the cavity length, and associated risetime losses. The value used here for parasitic loss allowed for Fresnel reflection from two crystal surfaces. However, with the crystal surfaces aligned, as here, parallel to the cavity mirrors, the Fresnel reflections are recirculated in the cavity, this reducing the effective parasitic losses. The rate of increase in threshold with cavity length (i.e. slope of fig. 5.3) could thus be expected to be closer to that shown by the device.

(c) Threshold vs cavity reflectivity

In expression (5.6) the reflectivity R considered is the product of the reflectivities at the signal wavelength of the two cavity mirrors. The output coupling forms one of the three loss terms in the threshold expression. We have studied the threshold variation in two noncritically phase-matched OPOs; one based on a 14mm sample in a 54mm cavity pumped by 10ns pulses, the other a 25mm crystal in a 44mm cavity pumped by 17ns pulses. The results are displayed in figures 5.4(a) and (b). The fractional increase in threshold was somewhat greater in the 14mm device. In both cases the calculated theoretical curves are in reasonable agreement with the data. It is worthwhile to note that the parametric gain in NCPM urea is sufficient that even with a very small amount of feedback at the resonant wave, the OPO is able to reach threshold at quite low pump energy fluences. In fact the 25mm urea OPO was able to operate in a cavity formed by a 95% reflective rear mirror and the rear surface of the crystal (i.e. no output coupler) with a threshold of only $0.13 Jcm^{-2}$.

(d) Threshold vs pump beam dimension

As discussed in section 5.2.2 the threshold is ideally expected to be constant in a noncritically phase-matched OPO for any dimension of collimated pump beam, since there is no birefringent walk-off between the three interacting waves. We have investigated the variation of threshold with beam dimension in an OPO cavity consisting of a 25mm noncritically phase-matched urea crystal surrounded by two 95% reflectors at the resonant wave, separated by 44mm. The OPO was pumped by the 17ns laser and the beam dimension was altered by varying the beam compression from 2.5 to 20. Figure 5.5 shows that the threshold as expected remains constant for beam compressions up to ten. However when the beam vertical dimension is less than 1.4mm there is a sharp increase in threshold up to a factor of four at 1.0mm. As shown in the following chapter this is accompanied by a decrease in the saturated conversion efficiency for smaller spot sizes.

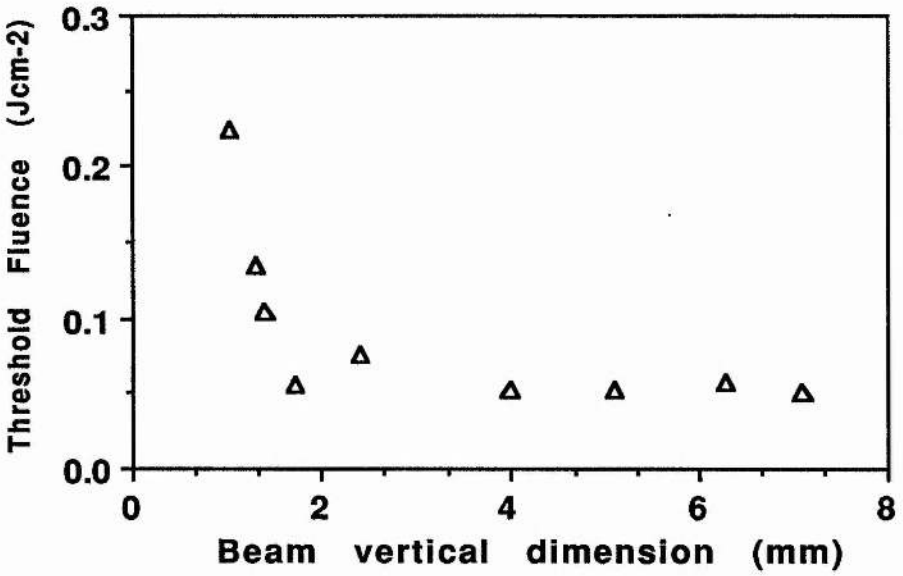

Fig. 5.5 Threshold Energy Fluence in an NCPM Urea OPO vs pump beam major dimension under conditions: (a) ℓ = 25mm, l_c = 44mm, $R_1 = R_2 = 0.95$.

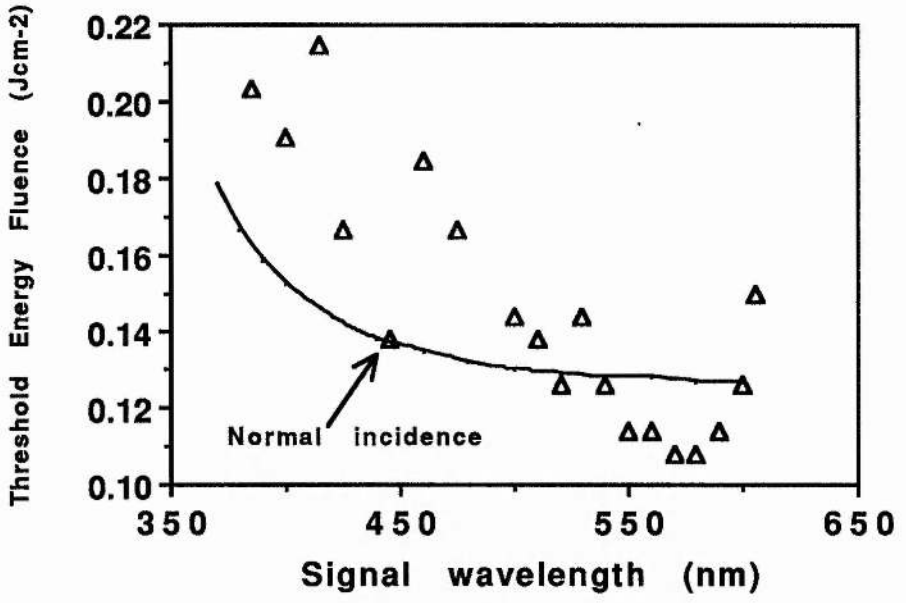

Fig. 5.6 Threshold Energy Fluence in a critically phase-matched Type 1 BBO OPO across the tuning range under conditions ℓ = 20mm, l_c = 45mm, $R_1 = R_2 = 0.95$. Solid curve represents theoretical calculations using (5.6) and a value of 3.6pm/V for d_{22}.

In the absence of extraordinary wave walkoff, the threshold increase must be attributed to the increase in pump beam divergence. The angular acceptance limit for a 25mm 90° phase-matched urea OPO, defined by (2.39) is relatively high at around 5.8mR. The pump beam divergence for a diffraction limited, single spatial mode beam could be expected to be given by the uncompressed divergence value times the beam compression. On this basis, the maximum divergence of the compressed excimer beam would be 4mR for a 20x compression. However, it has been observed that when the excimer beam is compressed to this level, it shows a tendency to 'break up' on propagation over distances greater than a metre. This indicates that the the divergence of the compressed multimode beam is likely to be considerably in excess of the predicted value. Thus we believe that the threshold increase occurring for beam compressions of 12 and above are a result of beam divergences in excess of the angular acceptance.

5.3.2 BBO

In the case of BBO all work was carried out using the 17ns pulse laser. As will be shown in the following section the higher pulse energies provided by this laser were more important than in the case of urea in order to reach OPO threshold.

(a) Threshold vs tuning range

As can be seen in figure 3.8(c) the figure of merit of Type 1 phase-matched BBO is high and relatively constant across the whole tuning range from degeneracy down to the ultraviolet region. This compares favourably with Type 2 phase-matching in urea, where the figure of merit declines steadily from the 90° phase-matching point to zero at a signal wavelength of 400nm. Although the figure of merit in BBO increases towards the ultraviolet, it is predicted that the oscillation threshold should increase through the increase in the degeneracy factor $1-\delta^2$ (whereδ is defined by the relation $\omega_s\omega_i = \omega_o^2(1-\delta^2)$, $\omega_o = \omega_p/2$). This trend is observed in the 20mm BBO OPO and the results are shown

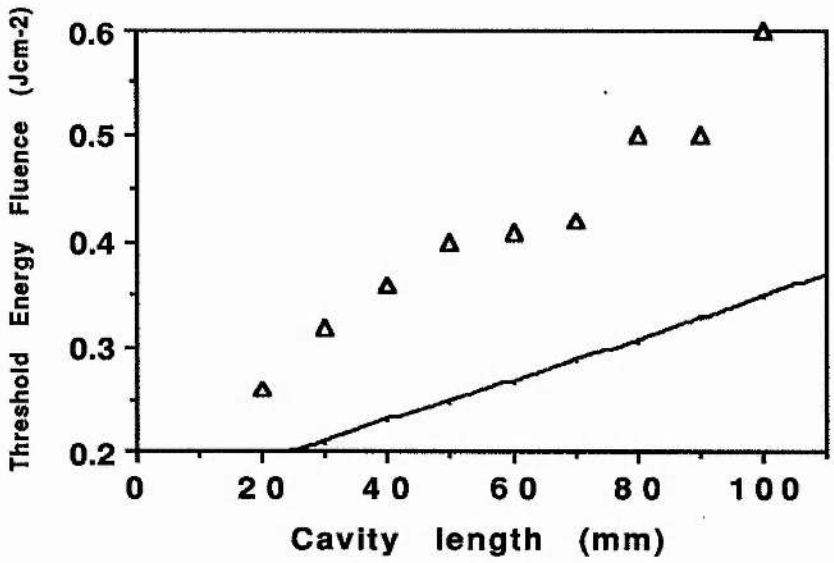

Fig. 5.7 (a) Threshold Energy Fluence in a critically phase-matched Type 1 BBO OPO vs cavity length under conditions ℓ = 12mm, $R_1 = R_2$ = 0.95, λ_S = 460nm.

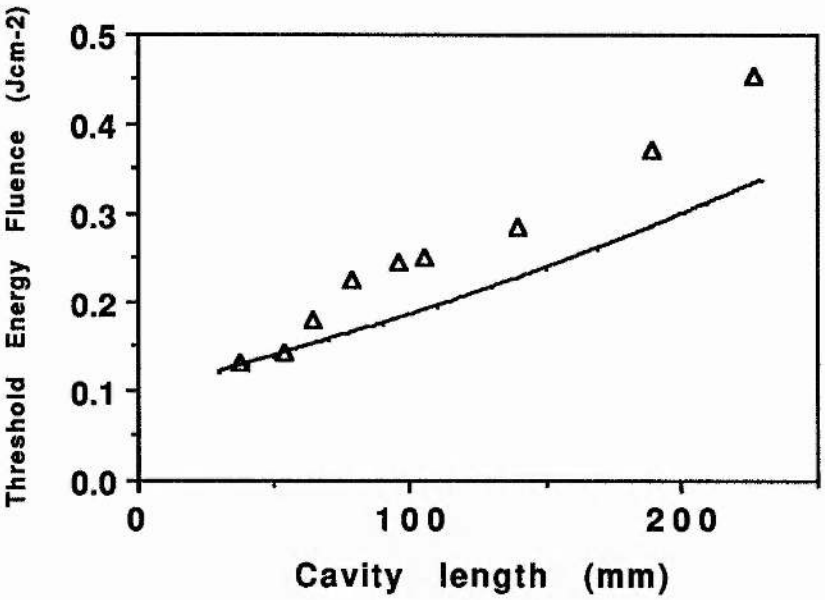

Fig. 5.7 (b) Threshold Energy Fluence in a critically phase-matched Type 1 BBO OPO vs cavity length under conditions ℓ = 20mm, $R_1 = R_2$ = 0.95, λ_S = 550nm. Solid curves in each case represent theoretical calculations using (5.6) and a value of 3.6pm/V for d_{22}.

in figure 5.6 alongside modelled calculations based on a value of 3.6pm/V for d_{22} in BBO, and measured values of parasitic loss, as shown in Table 5.1. These values have been used in all theoretical calculations of threshold in BBO producing a reasonable level of agreement with experiment. Thresholds of two to three times the predicted value in BBO-OPOs were also observed by Fan et al., in ref. 12. The relatively high scatter shown in figure 5.6 is a result of the use of three different mirror sets, over the ranges 370-420nm, 420-480nm and 500-600nm. Each of the mirror coatings were nominally of 95% reflectivity, but in general a decrease in reflectivity and associated increase in threshold was observed towards the edges of the mirror bandwidths. Features of fig. 5.6 to be noted include the low value of threshold at a signal wavelength of 445nm. This occurred when the crystal faces were normal to the pump beam direction, allowing the signal wave surface reflections to recirculate in the cavity and hence increasing the effective cavity reflectivity. This is an indication of the level of threshold decrease which could be obtained through antireflection coating of the crystal. The threshold increase towards 600nm signal is a function of the reflectivity profile of the particular mirrors used and is a feature which is instrumental in producing the noncollinear phase-matching effects observed in chapter 8. It should be pointed out that over the entire tuning range the threshold is less than a fifth of the estimated crystal damage limit which was around $1Jcm^{-2}$. Thus the OPO could be operated efficiently across the full wavelength range. Threshold at signal wavelengths below 370nm was further increased through beam clipping by the limited crystal aperture.

(b) Threshold vs cavity length

The OPO threshold as a function of cavity length was measured in both crystals in cavities formed by two 95% reflectors for the signal wavelength (see figures 5.7(a) and (b)). As in Urea, the increase in threshold with cavity length was steeper than that predicted from theory. In the context of our aim to produce a line-narrowed OPO based on BBO it is important to note

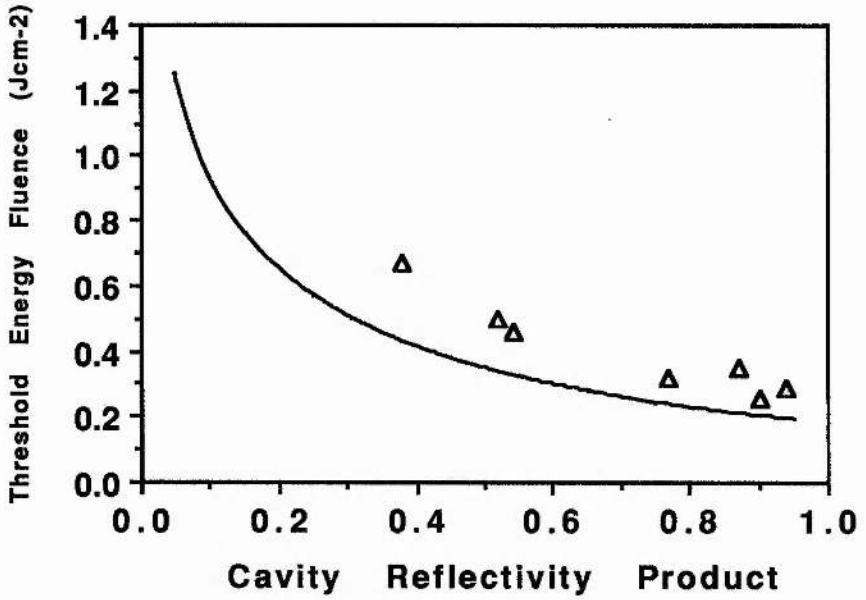

Fig. 5.8 (a) Threshold Energy Fluence in a critically phase-matched Type 1 BBO OPO vs cavity reflectivity under conditions ℓ = 12mm, l_c = 23mm, λ_s = 460nm.

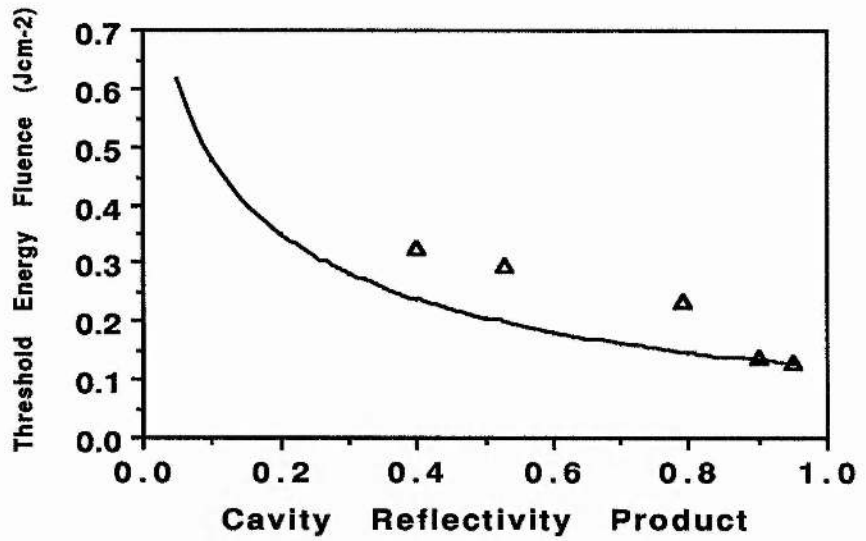

Fig. 5.8 (b) Threshold Energy Fluence in a critically phase-matched Type 1 BBO OPO vs cavity reflectivity under conditions ℓ = 20mm, l_c = 43mm, λ_s = 550nm. Solid curves represent theoretical calculations using (5.6) and a value of 3.6pm/V for d_{22}.

that despite the resultant threshold increase it was possible to operate the OPO at a point such that the threshold was less than 20% of the crystal damage limit with the cavity at a sufficient length (up to 100mm) to accommodate appropriate line-narrowing elements.

(c) Threshold vs cavity reflectivity

Again the variation of threshold with cavity reflectivity in OPOs based on both BBO samples was measured and the data is displayed in figures 5.8(a) and (b). Clearly the threshold was seen to increase with decreasing reflectivity product, and the data is in reasonable agreement with calculated values.

(d) Threshold vs pump beam dimension

As in Urea, a pattern of threshold increase towards small pump beam waist and high pump beam divergence, has been observed in OPOs based on BBO. In the case of urea the OPO was noncritically phase-matched, and was thus expected to be highly tolerant of angular deviation of the pump beam. Under NCPM conditions there is no birefringent walk-off of the pump wave from the signal and idler, and hence maximal three field interaction results. However in critically phase-matched BBO, walkoff of around 4^{o} across the tuning range results in lateral beam deviation of around 1.5mm, over an interaction length of 20mm. The threshold values shown in figure 5.9 indicate that dramatic increase in threshold is observed for beam dimensions in the walk-off plane of less than 2mm. The threshold for a 1.3mm dimension beam is more than six times that for a 6.4mm beam. The modelled calculations shown, based on a value of 3.6pm/V for d_{22} in BBO, predict a rather smaller critical dimension. It should be noted that during the course of these experiments, beam compressions of between 2.5 and 20 resulted in pump beam divergences of between 6 and 40 times the calculated angular acceptance limit of 0.1mR. However, as Brosnan and Byer point out in ref. 7, the requirement for pump beam collimation in an SRO is somewhat relaxed, since the idler is free to propagate noncollinearly with phase-matching being preserved. We believe

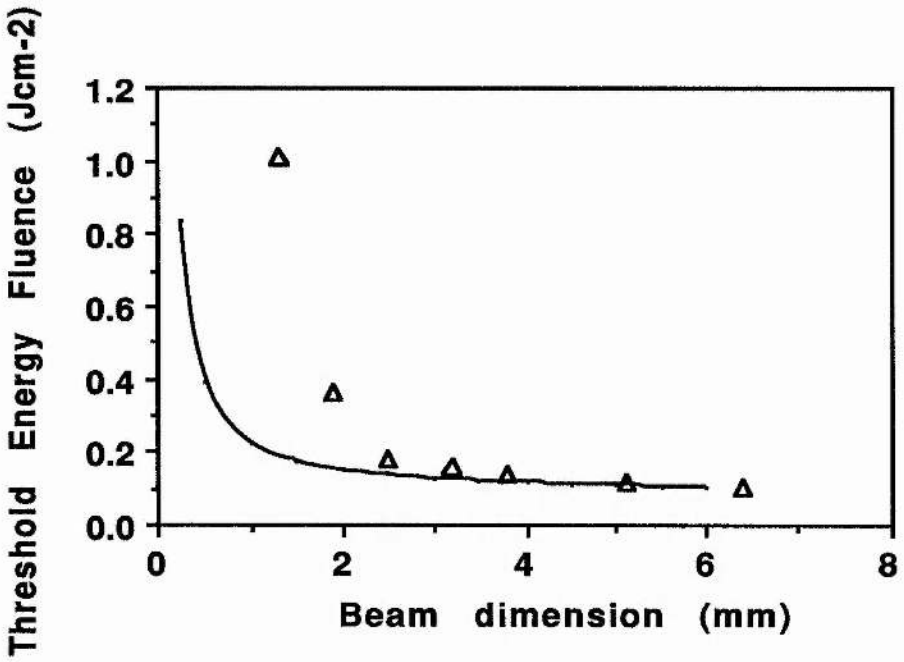

Fig. 5.9 Threshold Energy Fluence in a critically phase-matched Type 1 BBO OPO vs beam waist in walkoff dimension under conditions: ℓ = 20mm, l_c = 23mm, $R_1 = R_2 = 0.95$. Solid curve represents theoretical calculations using (5.6) and a value of 3.6pm/V for d_{22}.

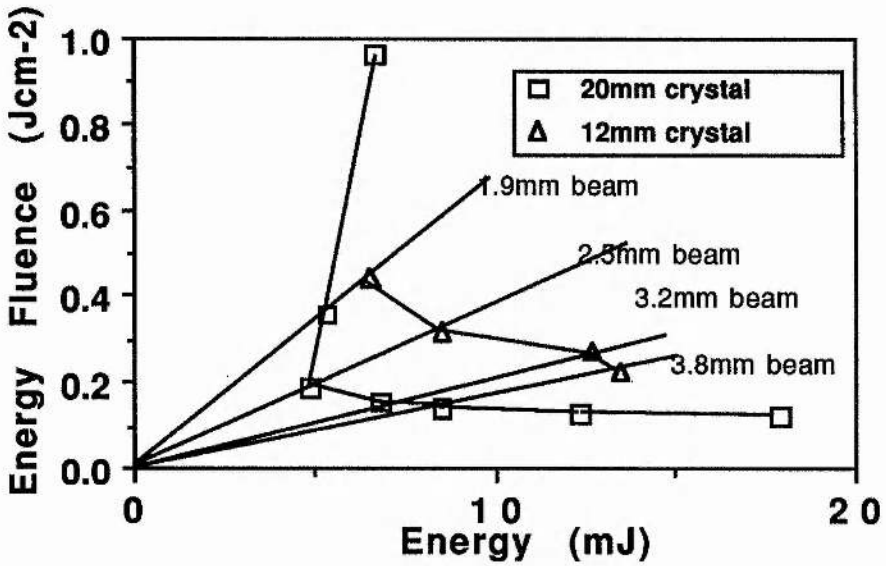

Figure 5.10 Threshold Energy Fluence versus corresponding Threshold Energy in a critically phase-matched BBO-OPO for different collimated beam waists. Details as for Figure 5.9.

that for the large beam waists involved in this work, noncollinearly phase-matched interaction allows the OPO to operate despite pump beam divergence far in excess of the angular acceptance. The rise in threshold seen for small beam waists in BBO, can be straightforwardly attributed to the loss of coupling between the three fields which results from double refraction. However, it may be that the decrease in beam quality upon tight focussing of the pump beam also makes a contribution to this effect in BBO. Comparison between the threshold increase observed in NCPM Urea OPOs and critically phase-matched BBO-OPOs (fig. 5.11) shows that threshold increase occurs for smaller beam dimensions in Urea, and is less pronounced. This observation is consistent with less efficient interaction resulting from both decreased pump wavefront uniformity due to focussing, and reduced beam overlap through pump beam walkoff.

The threshold fluences shown in Fig. 5.9 have also been plotted as a function of the corresponding pulse energies in Fig. 5.10. This indicates firstly that the minimum attainable threshold for an OPO based on a 20mm BBO crystal is around 0.1Jcm^{-2}, and secondly that the minimum required pulse energy to reach threshold is around 5mJ. Also shown are threshold values for an OPO based on a 12mm BBO crystal. As expected the minimum threshold values in terms of both energy and fluence for this device, are shifted upwards compared to the 20mm device. These figures are important in that they define minimum pulse energies required to obtain efficient conversion from a critically phase-matched BBO-OPO. One would typically wish to operate at a pump energy at least three times threshold and thus at least 15mJ would be required for this pump laser. This figure can be contrasted with recent work[11] in LBO in which the walkoff angle of only 1^{o} allowed thresholds of around 0.3mJ to be achieved. Critically phase-matched BBO is thus an OPO gain medium requiring relatively energetic pump pulses in order to achieve efficient operation.

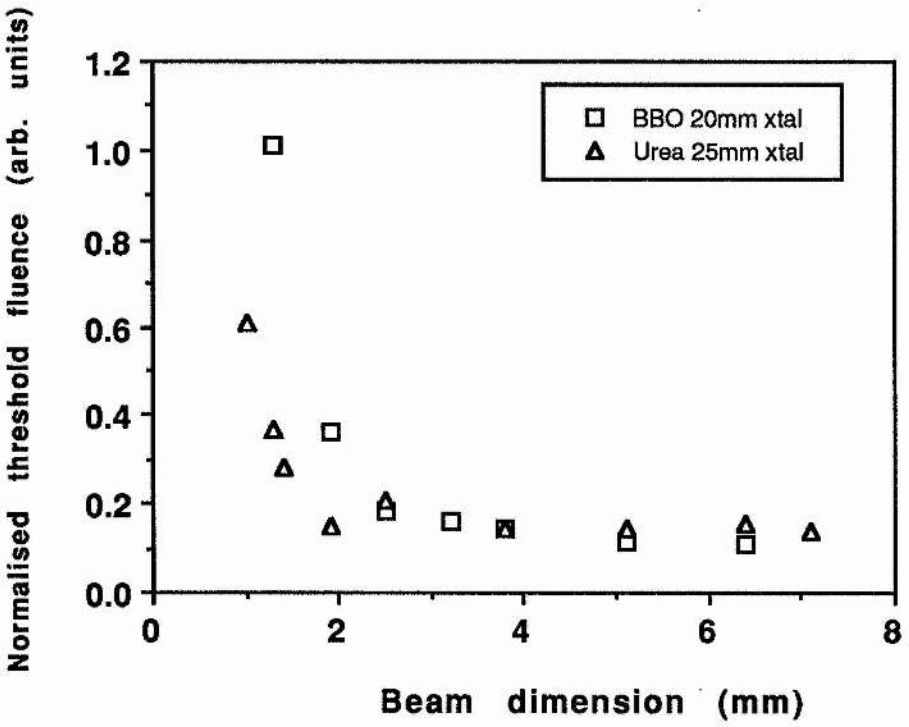

Fig. 5.11 Threshold fluence in OPOs based on Urea and BBO, normalised to the BBO value for a 3.8mm beam dimension. The cavity details for Urea and BBO are as in figs. 5.5 and 5.9 respectively.

1 R. G. Smith, "Lasers", Vol. 4. Edited by A.K. Levine and A. J. De Maria. Marcel Dekker, New York (1976).

2 G.D. Boyd and D.A. Kleinman, J. Appl. Phys. **39**, p3597 (1968).

3 D.J. Kuizenga, Appl. Phys. Lett. **21**, p570 (1972).

4 R. Fischer, C. Tran-Ba, L.W. Wieczorek, Sov. J. Quant. Elect. **7**, p1455 (1977).

5 S. Guha, F.-J. Wu, and J. Falk, IEEE J. Quant. Elect. **QE-18**, p907 (1982).

6 J. E. Pearson, U. Ganiel and A. Yariv, IEEE J. Quant. Elect. **QE-8**, p433 (1972).

7 S.J. Brosnan and R. L. Byer, IEEE J. Quant. Elect. **QE-15**, p415 (1979).

8 R.L.Byer and S. E. Harris, Phys. Rev. **168**, p1064 (1968).

9 M. Ebrahimzadeh and M. H. Dunn in Postdeadline Papers, Conference on Lasers and Electro-optics (Opt. Soc. Am., Washington D. C. 1988) Paper PD30.

A. J. Henderson et al., J. Opt. Soc. Am. B **7**, p1402 (1990).

10 Operation Manual, Lambda Physik EMG150ET.

11 Y. Cui et al ,'Widely tunable, all-solid-state, optical parametric oscillator for the visible and near infrared' submitted to Optics Letters, June 1992.

12 Y.X. Fan, et al. Appl. Phys. Lett. **53**, p2014 (1988).

13 S.E. Harris, Proc. I.E.E.E. **57**, p2096 (1969).

Chapter 6
Conversion Efficiency

6.0 Introduction

In this chapter we will characterise the efficiency of conversion of energy from pump to signal and idler fields in parametric oscillators of the type described in this work. We will consider the variation of the conversion efficiency at pump intensities in excess of the oscillation threshold level defined in chapter 5. The energy conversion in pulsed singly resonant oscillators will be contrasted with the predicted steady state behaviour.

6.1 Parametric oscillator operation at pump intensities above steady state threshold level

The standard analysis of optical parametric oscillator power conversion is performed assuming, as in section 5.1, interaction of plane waves and further assuming that the resonant fields vary slowly in propagating through the nonlinear medium. These assumptions allow expressions for conversion efficiency in terms of pump intensity to be developed without the need to produce an exact solution of the coupled nonlinear equations (2.6). Hence for a singly resonant oscillator in which the signal wave is resonant and in which it is assumed that in the steady state and for small losses such that the signal amplitude is constant throughout the nonlinear medium i.e.

$$\mathcal{E}_s(z) = \mathcal{E}_{so} \tag{6.1}$$

we have

$$\frac{d\mathcal{E}_p(z)}{dz} = i\kappa_p \mathcal{E}_{so} \mathcal{E}_i(z) \exp[-i(\Delta k z + \varphi)] \tag{6.2}$$

$$\frac{d\mathcal{E}_i(z)}{dz} = i\kappa_i \mathcal{E}_{so}^* \mathcal{E}_p(z) \exp[i(\Delta k z + \varphi)]$$

where $\mathcal{E}_{so}$, $\mathcal{E}_{po}$ are field amplitudes at $z = 0$. The boundary conditions $\mathcal{E}_i(0) = 0$ and $\mathcal{E}_p(0) = \mathcal{E}_{po}$ allow us to solve the coupled equations and produce expressions for the pump and idler fields as a function of the propagation distance through the nonlinear medium, as follows

$$|\mathcal{E}_i(z)|^2 = \mathcal{E}_{po}{}^2 \frac{\omega_i n_p}{\omega_p n_i} \left(\frac{\sin^2 \beta z}{1 + (\Delta k/2\alpha)^2} \right) \tag{6.3}$$

and

$$|\mathcal{E}_p(z)|^2 = \mathcal{E}_{po}{}^2 \left[\cos^2 \beta z + \left(\frac{\Delta k}{2\beta} \right)^2 \sin^2 \beta z \right] \tag{6.4}$$

where β is defined by the relation

$$\frac{\sin^2 \beta \ell}{(\beta \ell)^2} = \frac{P_p{}^{th}}{P_p{}^{inc}} \left(\frac{\sin^2 (\Delta k \ell/2)}{(\Delta k \ell/2)^2} \right) \tag{6.5}$$

where $P_p{}^{th}$ is the steady state threshold pump power and $P_p{}^{inc}$ is the pump power incident on the nonlinear crystal. Hence the internal efficiency, or pump depletion of the OPO is defined by

$$\eta_{int} = \left[1 - \left(\frac{\Delta k}{2\beta} \right)^2 \right] \sin^2 \beta \ell \tag{6.6}$$

For $\Delta k \ell = 0$ or perfect phase-matching it can be seen in figure 6.1 that the internal efficiency has a maximum value of 100% at a pumping ratio $P_p{}^{inc}/P_p{}^{th} = (\pi/2)^2$. As the pumping level increases beyond this value, the pump wave once again begins to grow at the expense of the signal. For nonzero values of $\Delta k \ell$ the maximum conversion efficiency occurs for the same value of $P_p{}^{inc}/P_p{}^{th}$, but is decreased. The variation of the maximum attainable pump depletion $\eta_{int}{}^{max}$ is shown in figure 6.2

The external conversion efficiency at the resonant wave, $\eta_{ext}{}^{res}$, in this plane wave analysis is given by

$$\eta_{ext}{}^{res} = \frac{\omega_{res}}{\omega_p} \left(\frac{t}{l + t} \right) \eta_{int} \tag{6.7}$$

where t is the round trip signal power output coupling loss and l is the round trip power loss at the signal and idler waves (these are assumed to be equal) attributable to absorption, scattering and surface reflections.

6.2 Conversion Efficiency for Gaussian spatial intensity profile pump beam

It is instructive to consider the case where the pump beam is a multimode plane wave with a Gaussian spatial intensity profile

$$I(r) = I_o \exp \frac{-2r^2}{w_o^2} \qquad (6.8)$$

where w_o is the radius of the beam incident on the parametric oscillator and r is the distance of the point considered from the beam centre. It can be assumed that parts of the incident pump beam of intensity I greater than the steady state threshold I_{th} sustain parametric conversion and suffer depletion while the remainder of the beam is unaffected.

The transmitted pump power can be calculated by integration of the transmitted pump intensity I' across the pump spatial profile using the expression (6.6) with $\Delta k = 0$, for the transmitted pump power in regions above threshold and assuming 100% transmission for the remainder, i.e.

$$I' = I\cos^2\beta l \qquad \text{for } I > I_{th} \qquad (6.9)$$

$$I' = I \qquad \text{for } I < I_{th} \qquad (6.10)$$

This analysis has been performed by Bjorkholm[1] for an SRO. Figure 6.3 shows that the internal efficiency reaches a maximum of 71% at 6.5 times threshold. The spatial intensity profile of the excimer laser used in this work (figure 4.2) more closely

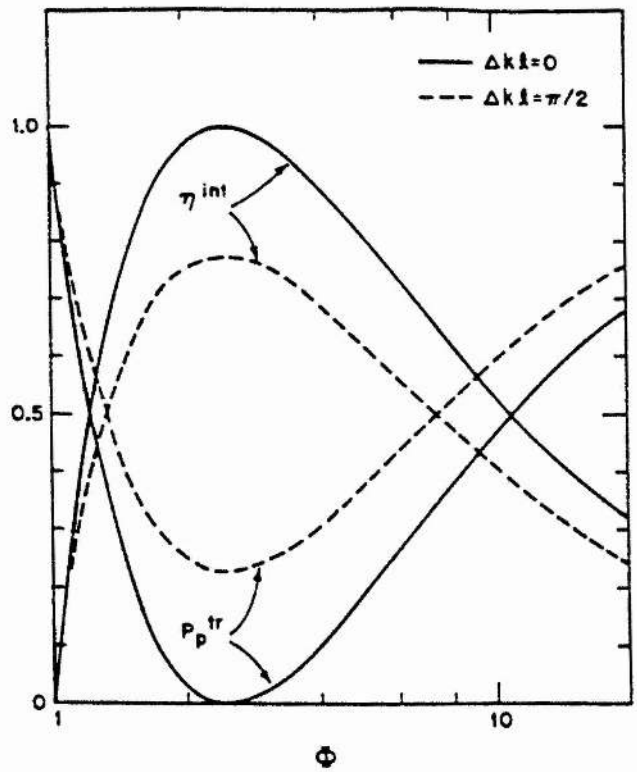

Fig. 6.1 Transmitted pump power and internal efficiency for a singly resonant oscillator assuming plane wave fields, as functions of the pumping ratio for phase mismatch levels $\Delta k\ell = 0$ and $\Delta k\ell = \pi/2$ (after ref. 6).

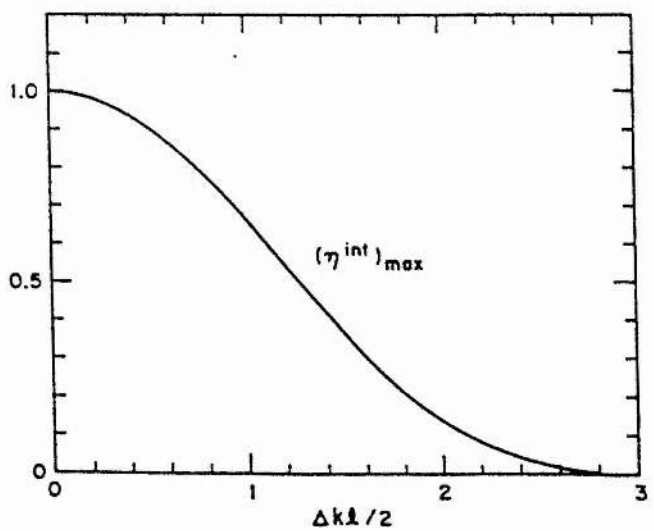

Fig. 6.2 Maximum internal efficiency of a singly resonant oscillator as a function of the phase mismatch $\Delta k\ell/2$ (after ref. 6.)

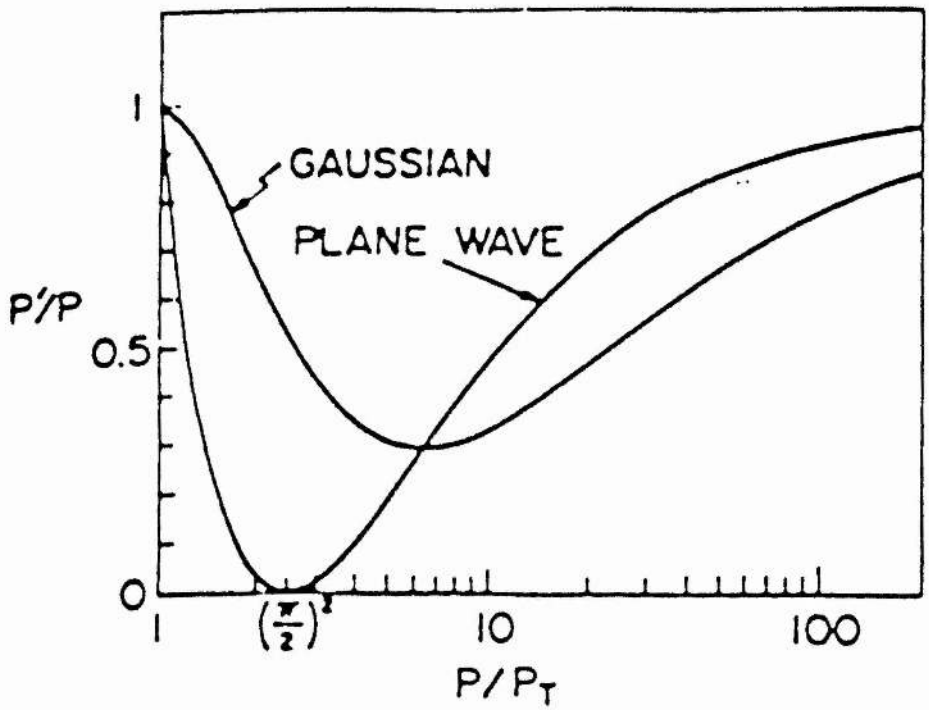

Fig. 6.3 Transmitted pump power P'/P as a function of the pumping ratio for a singly resonant oscillator for the cases of plane-wave pumping and pumping with a Gaussian intensity wave (after ref. 1).

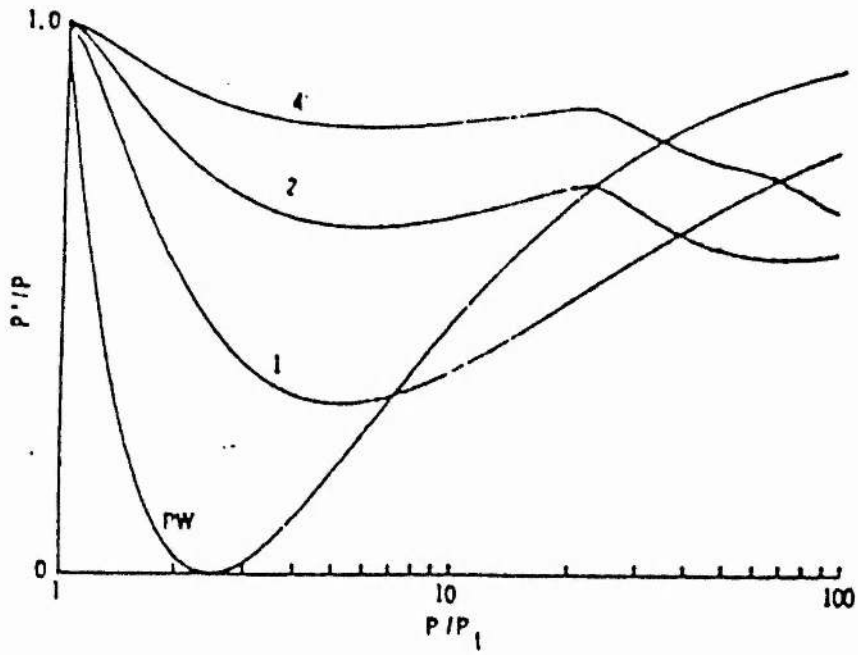

Fig. 6.4 Transmitted pump power P'/P, as a function of the pumping ratio in a singly resonant oscillator for spherical pump waves with 0.5, 1, and 2mRad maximum k-vector misorientation (corresponding to 1, 2, and 4mRad full angle divergence). Plane-wave data is shown for comparison (after ref. 2).

resembles a 'top-hat' distribution than a Gaussian. Thus, in the steady state, the conversion efficiency could be expected to show a pattern of behaviour somewhere between those displayed in figures 6.1 and 6.3.

6.3 Effect of pump beam divergence on conversion efficiency

Further deviation from the behaviour predicted by the uniform intensity plane wave theory may be caused by the finite spread of wavevector directions of the pump beam. If we restrict $|\mathbf{k_p}|$ to a fixed value, it has been shown in section 2.2.4 that pump beam divergence introduces phase mismatch Δk and reduces parametric gain according to expression (2.12). The threshold intensity for a given level of phase mismatch, $I_{th}(\Delta k)$, in terms of the plane wave threshold intensity for zero phase mismatch I_{tho}, is given by

$$I_{th}(\Delta k) = \frac{I_{tho}}{\mathrm{sinc}^2(\Delta k \ell/2)} \qquad (6.11)$$

In a singly resonant oscillator the transmitted pump intensity I' is given by (6.9) and (6.10).
subject to

$$\frac{\sin^2\beta\ell}{(\beta\ell)^2} = \frac{I_{tho}}{I} \qquad (6.12)$$

A model for the overall pump depletion of a parametric oscillator pumped by a laser having a finite full-angle beam divergence $\Delta\theta$ can be developed as follows[3]. The pump wave is assumed to be a circularly truncated portion of a uniform intensity spherical wave, radius R such that R is related to the beam radius w_o by

$$R = \frac{2w_o}{\Delta\theta} \qquad (6.13)$$

The phasefront normal is assumed to be properly oriented for perfect phase-matching at some angle θ to the crystal optic axis.

Hence each point on the beam cross-section corresponds to a distinct value of Δk, and by integration of the transmitted intensity with respect to area across the beam cross section, it is possible to evaluate the pump energy depletion for a particular pumping ratio and beam divergence. The SRO pump depletion as a function of pumping ratio P/P_{th} as calculated in ref. 2 for a Type 1 OPO based on $LiNbO_3$ is shown for various values of beam divergence in figure 6.4. A pattern similar to figure 6.3 is displayed in that the maximum values are reduced, and shifted to progressively higher values of P/P_{th}.

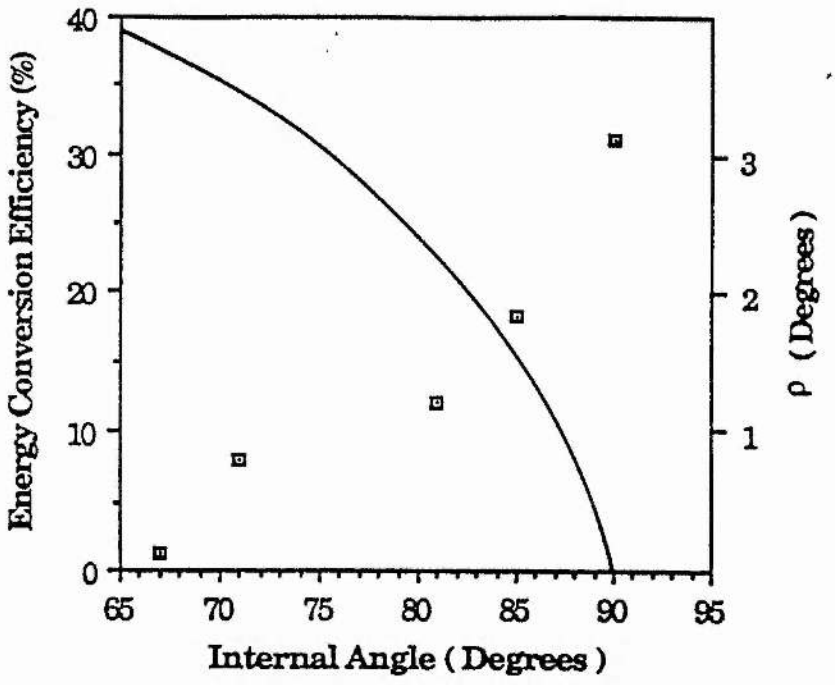

Fig. 6.5 Measured Urea NCPM OPO external energy conversion efficiency as a function of the internal phase-match angle θ, for a fixed pump pulse energy of 19mJ. The solid curve represents the variation in the crystal double refraction angle ρ across the tuning range of the oscillator. l_c = 55mm, R_1 = 95%, R_2 = 40%, l = 15mm.

6.4 Pulsed OPO conversion efficiency

The expressions for conversion efficiency which have been developed up to this point apply to operation in the low-gain, essentially steady state condition. In practice the steady state condition is achieved only after a finite build-up time. Thus the energy conversion efficiency is less than the conversion efficiency by approximately the fraction of the pumping time that the oscillator is above threshold. For a pulsed oscillator, Pearson[3] describes a method of estimating the risetime for a Gaussian temporal intensity profile. Alternatively the iterative expression used in section 5.2.1 for the generated signal power as a function of the number of cavity round trips propagated can be used to calculate the time for the oscillator to generate a defined level (100μJ) of signal output. This expression assumes a top-hat temporal intensity profile pulse of total gain equivalent to that of a Gaussian profile pulse of defined intensity.

Hence the risetime resulting from the pulsed nature of the excimer pump source is a further cause of deviation from the steady state plane wave behaviour. The behaviour observed can be interpreted as resulting from a combination of the effects discussed in sections 6.2 to 6.4.

6.5 Experimental results

This section presents results and analysis of conversion efficiency in urea and BBO with reference to the effects just discussed. In addition, comparison is made between Barium Borate and Lithium Borate (LBO) for the purpose of efficient conversion to ultraviolet wavelengths.

6.5.1 Measurement and calculation of conversion efficiency

The total useful external output was calculated using measurements of the total forward-propagating output

transmitted through the dichroic filters external to the OPO cavity, and the proportion of this quantity contributed by each of the two output wavelengths. The transmission of each of the optical components at both wavelengths was taken into account in calculating the forward propagating pulse energy. The backward propagating fraction of the useful output was calculated assuming all of the energy in the nonresonant wave to be coupled out in the forward direction and the backward propagating resonant wave energy deduced from the forward travelling value and the ratio of the output coupling losses of front and rear mirrors. In producing an external efficiency value the pump energy incident on the rear mirror M1 (as in figure 4.5(a)) was used. Measurements of the pump energy were thus adjusted to take account of losses at the beam compressor lens surfaces.

The pump depletion (or internal conversion efficiency) was calculated from measurements of the pump power reflected from one of the dichroic filters. The pump power reflected was measured when the cavity was misaligned and oscillation did not take place (P_{misal}) and when the cavity was perfectly aligned and maximum useful output was obtained (P_{al}). The depletion was then calculated as follows:

$$\eta_{int} = \frac{P_{misal} - P_{al}}{P_{misal}} \qquad (6.14)$$

The proportion of energy in each wavelength was measured using an RG610 cut-off filter which was highly transmitting at wavelengths above 610nm (approximate wavelength degeneracy).

6.5.2 Urea

(a) Conversion efficiency vs tuning range

OPO external energy conversion efficiciency was measured in a 15mm long sample of urea noncritically phase-matched for propagation of the pump wave at normal incidence to crystal surfaces. The pump energy was held constant while the crystal orientation was altered with respect to the pump beam. Here the 10ns pulse laser provided a fixed pulse energy of 19mJ while the

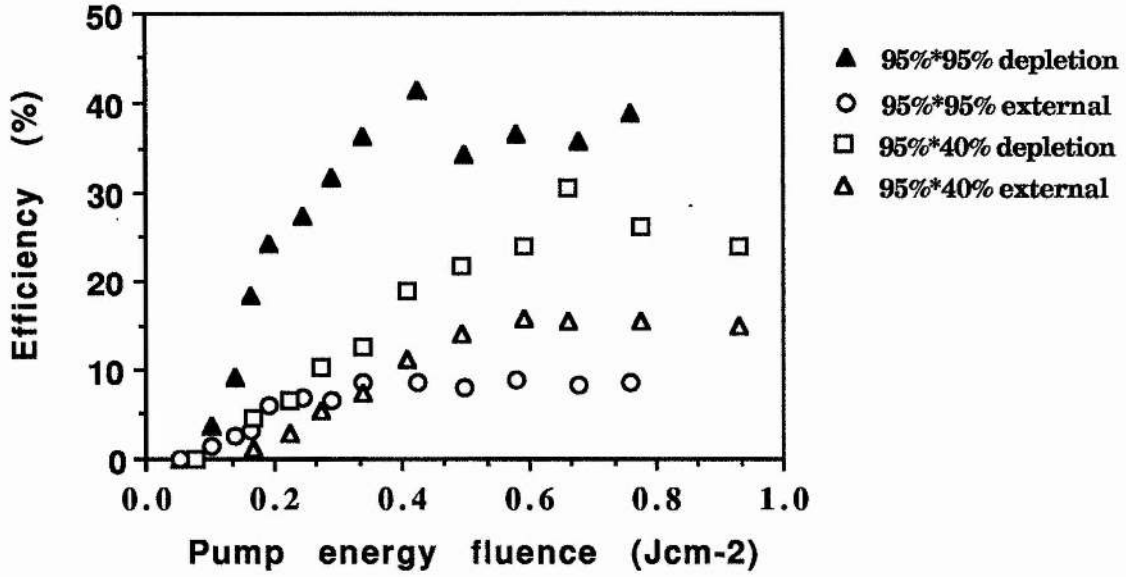

Fig. 6.6 (a) Measured pump depletion and external energy conversion efficiency of a Urea NCPM OPO as a function of incident pump energy fluence, for cavity reflectivities $R_1 = R_2 = 95\%$ and $R_1 = 95\%$, $R_2 = 40\%$. $l_c = 44$mm, $\ell = 25$mm.

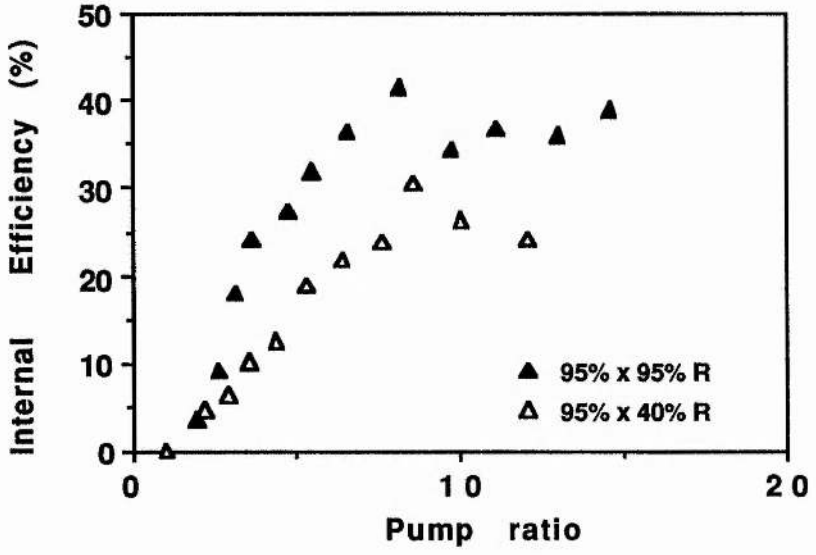

Fig. 6.6 (b) Measured pump depletion of a Urea NCPM OPO as a function of pumping ratio, for cavity reflectivities $R_1 = R_2 = 95\%$ and $R_1 = 95\%$, $R_2 = 40\%$. $l_c = 44$mm, $\ell = 25$mm.

OPO cavity was formed by a 95% and a 40% reflector for the resonant wavelength, separated by 55mm. The results shown in figure 6.5 show that the efficiency falls quite rapidly from 32% at 90° phase-matching to 1% at $\theta = 67°$. Also shown is the calculated variation over the same range of the angle of walkoff ρ between the nonresonant wave and the pump beam, given by

$$\tan(\rho+\theta) = \frac{n_o^2}{n_e^2} \tan\theta \qquad (6.15)$$

This figure increases from zero at NCPM to around 4° at $\theta = 67°$. Hence the decline in efficiency over the tuning range is consistent with the decrease in beam overlap and interaction resulting from increased walk-off. The advantages inherent in noncritical phase-matching are clearly demonstrated. Considerably greater efficiency of conversion has been achieved, as reported in ref. 4, using the 25mm 90° phase-matched urea crystal. For a cavity formed by a 95% rear reflector for 570nm and a 40% front reflector, separated by 54mm, the oscillation threshold was $0.023 Jcm^{-2}$ (an order of magnitude less than that for the 15mm NCPM sample, under similar conditions). A pump pulse of 19mJ produced 5mJ of forward output in the green wavelength, and adjustment for losses gave a figure of 65% overall external conversion efficiency. The corresponding pump depletion was 72%. The pump power density required in order to reach threshold was $2.3 MWcm^{-2}$ while that required to achieve 65% external conversion was $44 MWcm^{-2}$ i.e. around 20 times threshold.

(b) Efficiency vs output coupling

The variation of both internal and external efficiency as a function of pump intensity for different output coupling levels was investigated in an OPO based on a 25mm 90° phase-matched urea crystal. The OPO was pumped by the 17ns pulse laser and the cavity was formed by a 95% rear reflector at the resonant wave and either a 95% or 40% reflector as the front mirror. The mirrors were separated by a distance of 44mm. The pump beam was compressed by a factor of 5 to a spot size of 4 x 1.5mm

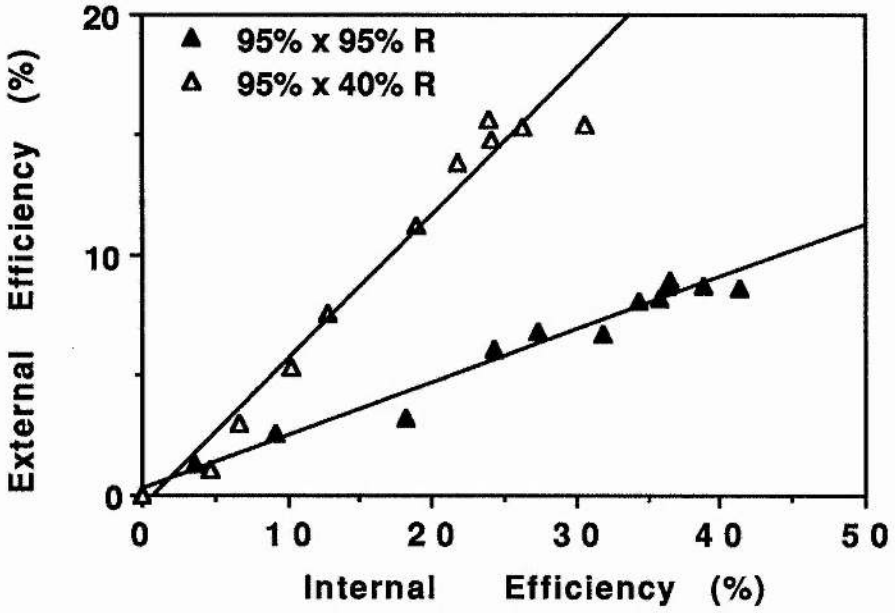

Fig. 6.7 External energy conversion efficiency as a function of internal efficiency for a Urea OPO. Conditions as in figure 6.6.

(where the major dimension was in the walk-off plane). The pump energy fluence was varied up to $1Jcm^{-2}$ which is the expected damage limit of the cavity mirrors. Figure 6.6(a) shows the external and internal efficiencies for both output coupling levels as a function of the pump energy fluence. The threshold energy fluences are $0.05Jcm^{-2}$ and $0.08Jcm^{-2}$ for the 95% and 40% reflectors respectively. It can be seen that for any given energy fluence the resultant pump depletion is higher for the higher finesse cavity. This is also true when the pump depletion is displayed as a function of the pumping ratio (pump energy/ pump threshold energy) as in figure 6.6(b). A distinct feature of figure 6.6(a) is the crossover shown by the external efficiencies for the two cavity arrangements at a pump fluence $0.3Jcm^{-2}$. Below this pump intensity the conversion efficiency is greater in the high finesse cavity. However beyond this level the low finesse cavity gives considerably greater external efficiency, up to around 16% or about twice the maximum value of the high finesse cavity. In figure 6.7 it can be seen that the external efficiency is a constant fraction of the pump depletion. The gradients (η_{ext}/η_{int}) are 0.33

for the 95% reflector and 0.66 for the 40% reflector. The increased proportion of useful output to total output results from the higher fraction of the total loss contributed by the useful output coupling loss in the latter case. Table 6.1 shows the values of η_{ext}/η_{int}, $\eta_{ext}^{res}/\eta_{ext}$, and $\eta_{ext}^{nonres}/\eta_{ext}$ for each case (η_{ext}^{res} and η_{ext}^{nonres} are defined as the useful external energy divided by the total input pump energy, at the resonant and nonresonant wavelengths respectively). These figures are consistent with a single pass loss of around 15%, calculated using expression (6.7). This is in reasonable agreement with the value of transmission measured for the urea cell at 633nm, which was 87+/-2%.

Table 6.1: External efficiency in urea

Cavity reflectivity	96.5% * 96.5%	96.5% * 40%
η_{ext} / η_{int}	0.33	0.66
$\eta_{ext}^{res} / \eta_{ext}$	0.30	0.56
$\eta_{ext}^{nonres} / \eta_{ext}$	0.70	0.44
l (calculated)	0.30	0.30

Both the internal and external efficiencies display saturation effects as predicted by the steady state theory. The pump depletion saturates at levels of around 30% and 40% for the low and high finesse cavities respectively. Saturation occurs at a pumping ratio of approx. 8.5, compared with the maximum depletion of 100% at a pumping ratio of $(\pi/2)^2$ predicted by steady state theory. As discussed in sections 6.2 to 6.4 the reduced maximum conversion efficiency and its occurrence at much higher pumping ratios can be attributed to a combination of the pulsed nature of the device, the phase mismatch contributed by laser linewidth and divergence and the non-uniform intensity of the pump beam. The efficiencies displayed through the use of

the 25mm urea crystal with the 17ns laser are lower than those previously obtained with the 10ns laser. We attribute this to crystal surface degradation, after repolishing to a poorer level of flatness and parallelism than previously attained.

(c) Efficiency vs beam dimension

Further measurements of internal and external conversion were made on the same 90° phase-matched urea OPO for a cavity formed by two 95% reflectors for 570nm spaced by 44mm (figs. 6.8(a) and (b)). Beam compressions of 5 and 12, produced pump beam dimensions in the walk-off plane of 4mm and 1.4mm respectively. Maximum pump depletions of around 23% and 37% are observed for the 1.4mm and 4mm beam waists respectively. Saturation can also be seen (fig. 6.8(b)) to have set in at a lesser value of pumping ratio for the 1.4mm beam. It is believed that the reduced pump depletion and the increased oscillation threshold are, as discussed in section 5.4.1(d), results of the reduced ability of the OPO to convert the highly divergent fraction of the pump beam for a narrower beam waist. It may be noted here that the saturated external efficiencies measured using the 1.4mm beam are higher than would be predicted from the corresponding internal efficiencies, and from the ratio of output coupling to parasitic losses. This feature has not been explained and may simply result from systematic error in the measurement of the low output energies involved.

6.5.3 BBO : (a) Efficiency vs tuning range

The figure of merit for Type 1 phase-matched parametric oscillation in BBO has been shown in section 3.5.2 to be high and relatively uniform throughout the tuning range. The decrease in nonlinear coefficient with increasing angle θ between the pump and the optic axis, is balanced in some measure by the increase in the degeneracy factor $(1-\delta^2)$. The range of efficient tuning is limited both by the infra-red transmission cut-off at around 3μm, and in our particular crystals, by the reduced crystal aperture at

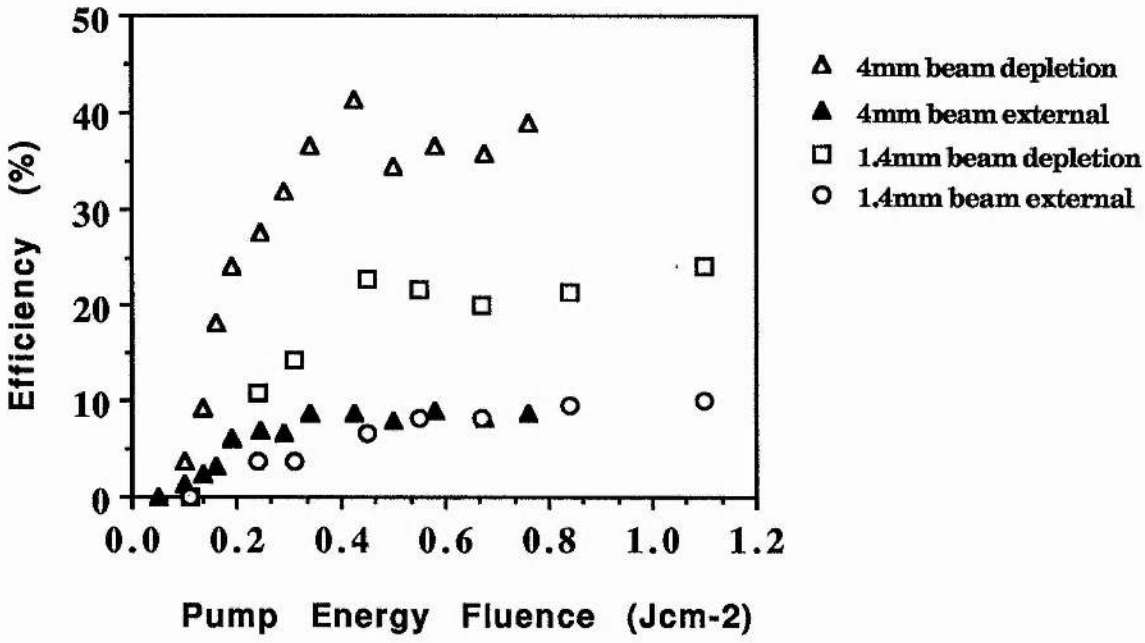

Fig. 6.8 (a) Measured pump depletion and external energy conversion efficiency of a Urea NCPM OPO as a functions of incident pump energy fluence for pump beam compressions of 5 and 12. l_c = 44mm, l = 25mm, $R_1 = R_2$ = 95%.

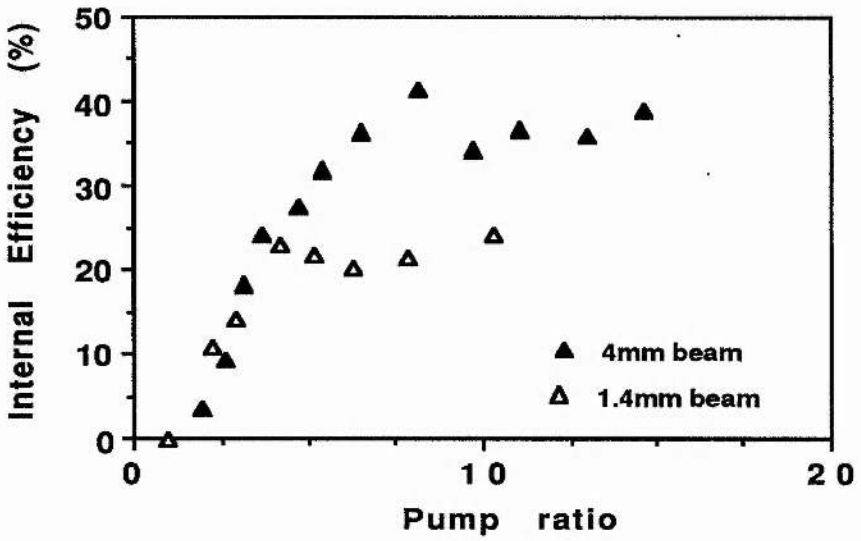

Fig. 6.8 (b) Measured pump depletion in a Urea NCPM OPO as a function of pumping ratio, for pump beam compressions of 5 and 12. l_c = 44mm, l = 25mm, $R_1 = R_2$ = 95%.

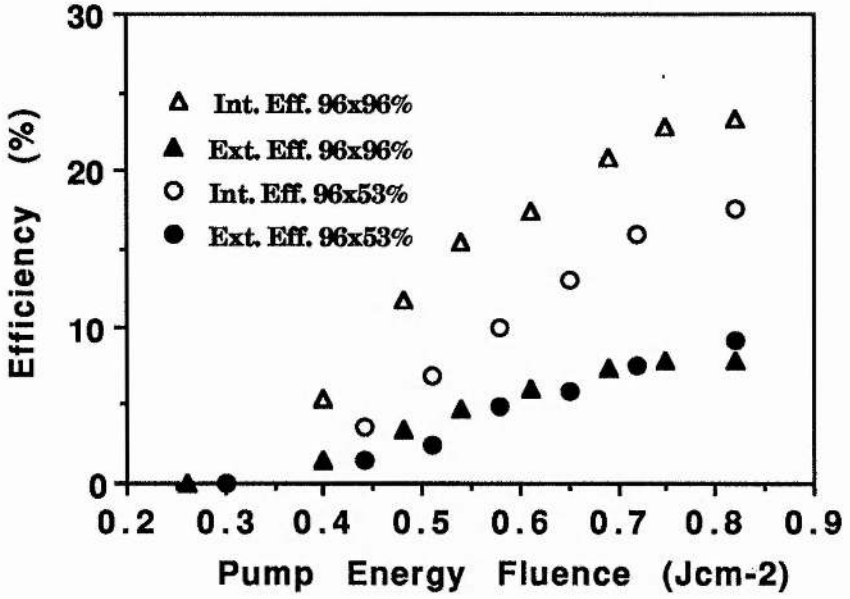

Fig. 6.9 Measured pump depletion and external energy conversion efficiency of a Type 1 BBO OPO as a function of incident pump energy fluence, for cavity reflectivities $R_1 = R_2 = 96\%$ and $R_1 = 96\%$, $R_2 = 53\%$. $l_c = 23$mm, $\ell = 20$mm, $\lambda_s = 540$nm.

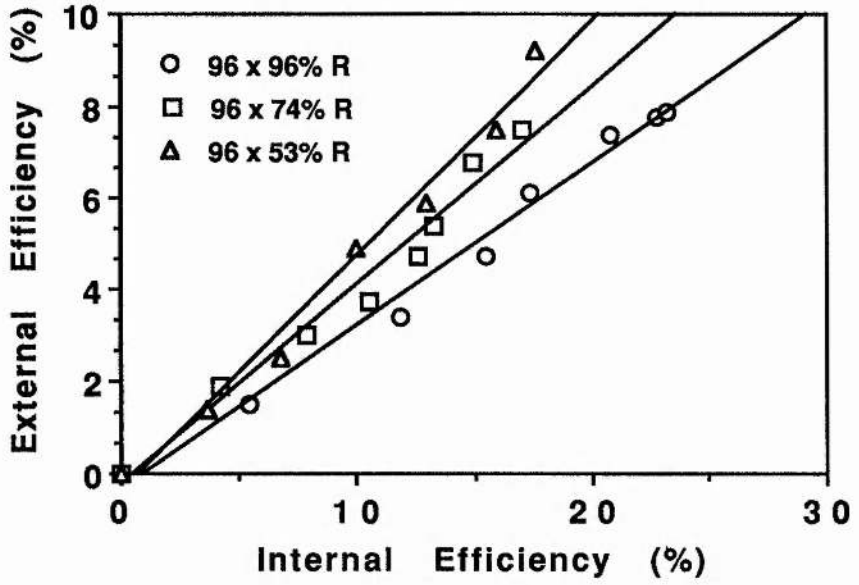

Fig. 6.10 External energy conversion efficiency as a function of internal efficiency for a Type 1 BBO OPO where cavity reflectivities are $R_1 = R_2 = 96\%$, $R_1 = 96\%$, $R_2 = 74\%$ and $R_1 = 96\%$, $R_2 = 53\%$. Other conditions as in figure 6.9.

low values of θ. It was found, as shown in the following two sections, that pump depletions in excess of 50% could be achieved throughout the range 385nm to degeneracy at 616nm, for pumping ratios of around six.

(b) Efficiency vs output coupling

The effect of varying the output coupling was investigated in OPOs based on the 20mm BBO crystal, and operated at a signal wavelength of 540nm and complementary idler wavelength 700nm. The pump beam was compressed by a factor of 7.5 to a spot size of 2.5mm (in the walkoff dimension) x 1.1mm and the cavity was formed by a 96% reflector at the resonant wavelength, separated by 23mm from an output coupler of reflectivity 96%, 74% or 53%. Figure 6.9 shows the internal and external efficiencies as a function of pump energy fluence for the 96% and 53% reflectivity output couplers. The oscillation thresholds are $0.26 Jcm^{-2}$ and $0.30 Jcm^{-2}$ respectively. The pattern observed is similar to that seen in urea. The pump depletion is higher for any given pump energy fluence in the high finesse cavity, while the external efficiencies display signs of the crossover seen in fig. 6.6(a).The external efficiency as a function of pump depletion for all three cavity arrangements is shown in fig. 6.10. The gradients η_{ext}/η_{int}, are shown in Table 6.2 alongside the proportion of the external efficiencies at each wavelength, $\eta_{ext}{}^{res}/\eta_{ext}$, and $\eta_{ext}{}^{nonres}/\eta_{ext}$. Also shown are the round trip values calculated from these figures, according to expression (6.7). These correspond fairly closely to the measured single pass parasitic loss value of 24%.

(c) Efficiency vs beam dimension

The pump depletion as a function of pump energy fluence was investigated in BBO for different pump beam dimensions. Beam compressions of 3.75 and 7.5 were employed, resulting in pump beam cross-sections of 5.1 x 2.1mm and 2.5 x 1.1mm respectively where the major dimension is in the birefringent walk-off plane. Measurements were performed at wavelength

pairs 540 and 700nm, and 385nm and 1.5μm. In each case the cavity lengths were 23mm and the cavities were formed by two 95% reflectors at the resonant wavelengths, which were 540nm and 1.5μm. Figures 6.11(a) and (b) show the pump depletion

Table 6.2: External efficiency in BBO

Cavity reflectivity	96% * 96%	96% * 74%	96% * 53%
η_{ext} / η_{int}	0.32	0.41	0.47
$\eta_{ext}^{res} / \eta_{ext}$	0.25	0.48	0.55
$\eta_{ext}^{nonres} / \eta_{ext}$	0.75	0.52	0.45
l (calculated)	0.49	0.57	0.61

versus pump energy fluence, while figs 6.12(a) and (b) show the same results as a function of pumping ratio. The first feature to note is the increase in conversion efficiency for a given pump intensity afforded by the use of a lower beam compression and correspondingly higher collimated beam dimension. Secondly the large beam waist shows no sign of saturation in conversion efficiency, while the higher compression produces distinct saturation beyond a pumping ratio of around 6. The maximum pump depletions observed were 64% and 50% for 540nm and 385nm respectively and in each case this was limited by the available pump energy rather than by damage constraints. The figure of 64% depletion corresponds to a pulse energy of 105mJ incident on the first beam compression lens and 82mJ incident on the OPO. Thus 53mJ of visible light is parametrically generated, although only around 25% of that amount is given out as useful output due to extraneous cavity losses.

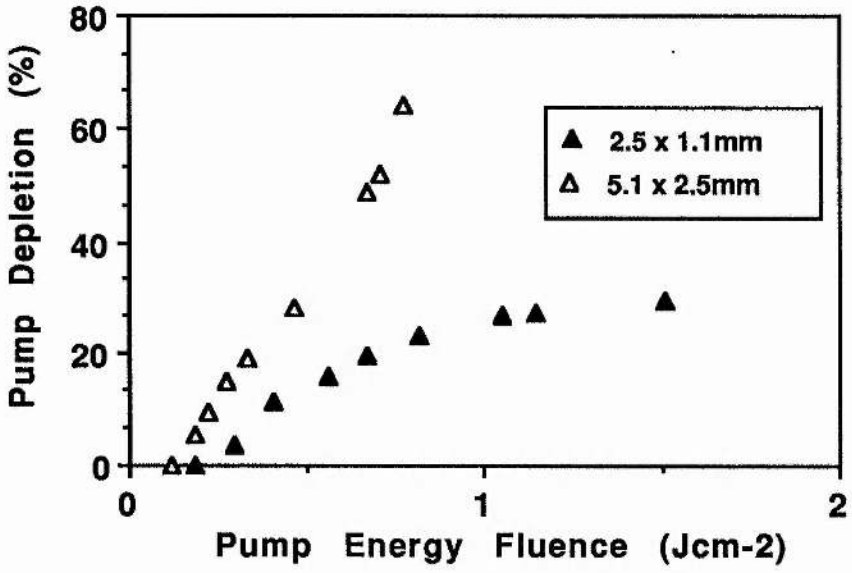

Fig. 6.11 (a) Pump depletion in a Type 1 BBO OPO as a function of incident pump energy fluence for pump beam compressions 3.75 and 7.5 for λ_s = 540nm, λ_i = 700nm, l_c = 23mm, ℓ = 20mm, $R_1 = R_2$ = 95% at resonant wavelength 540nm.

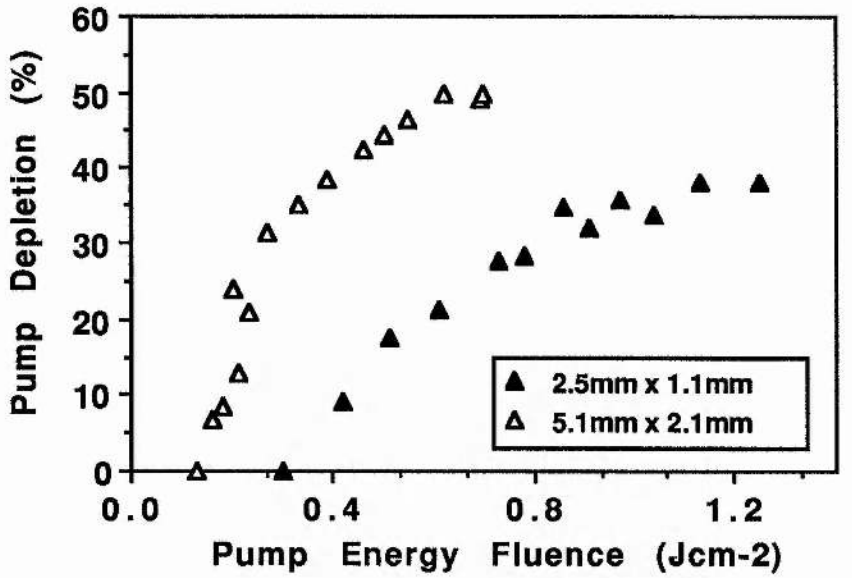

Fig. 6.11 (b) Pump depletion in a Type 1 BBO OPO as a function of incident pump energy fluence for pump beam compressions 3.75 and 7.5 for λ_s = 385nm, λ_i = 1.5μm. l_c = 23mm, ℓ = 20mm, $R_1 = R_2$ = 95% at resonant wavelength 1.5μm.

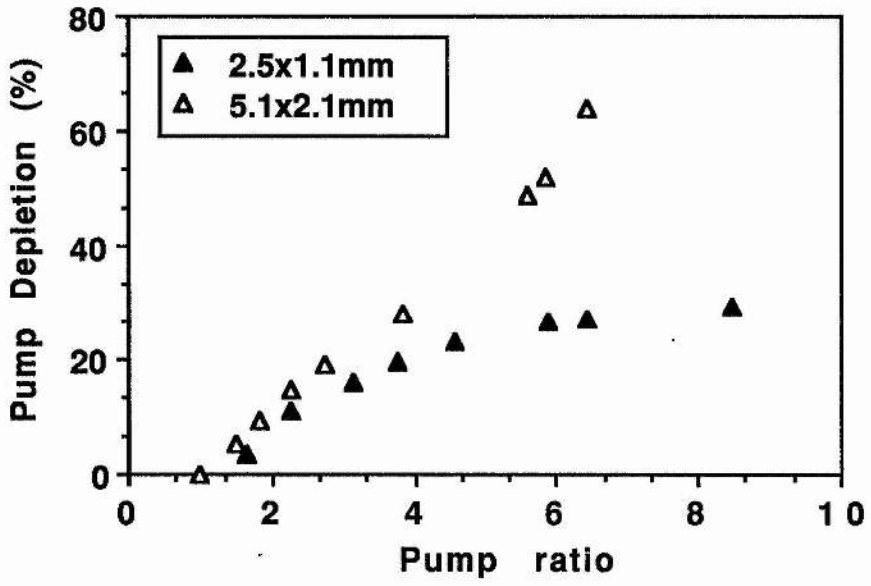

Fig. 6.12 (a) Pump depletion in a Type 1 BBO OPO as a function of pumping ratio for λ_S = 540nm, λ_i = 700nm. Conditions as in figure 6.11.

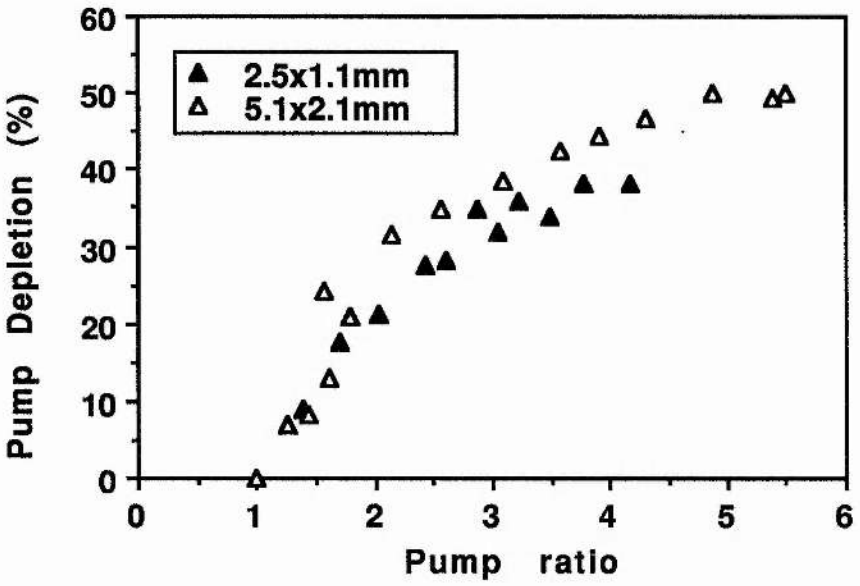

Fig. 6.12 (b) Pump depletion in a Type 1 BBO OPO as a function of pumping ratio for λ_S = 385nm, λ_i = 1.5μm. Conditions as in figure 6.11.

As discussed in 5.4.2(d), it is thought that as with the increase in oscillation threshold at higher beam compressions the reduction in conversion efficiency can be attributed to the restrictions on beam overlap imposed by the small beam dimension. Collinear phase-matching is limited by birefringent walkoff of the pump beam from the signal and idler, while noncollinear phase-matching is restricted by the walkoff of the idler and pump from the resonant signal

(d) Comparison of BBO with NCPM LBO for UV generation

The effect of switching the resonant wave, i.e. resonating the high wavelength rather than the low wavelength in the singly resonant OPO was studied in both BBO and Lithium Borate (LBO). This was carried out for the wavelength pair 385nm and 1.5μm, and the same measurements were performed in the 20mm BBO crystal and a noncritically phase-matched LBO OPO, for the purposes of comparison of BBO and LBO as materials for the generation of tunable ultraviolet radiation. The LBO crystal was

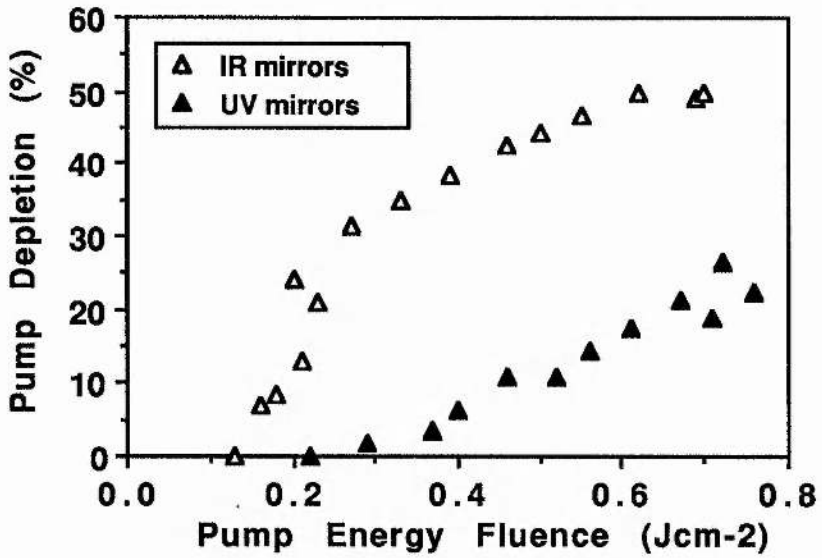

Fig. 6.13 Pump depletion in a Type 1 BBO OPO as a function of incident pump energy fluence for cavity reflectivities $R_1 = R_2 = 95\%$ at resonant wavelengths (a) 385nm and (b)1.5μm. l_c = 23mm, l = 20mm.

cut for propagation along the z axis and had dimensions x x y x z = 3 x3 x16mm [x, y, and z are the principal axes of the optical indicatrix with the convention $n_z > n_y > n_x$ and are related to the crystallographic axes (a,b,c) and the nonlinear (piezoelectric) axes through (x,y,z) = (a,c,b) = (X,Z,Y)] . In each case the cavities were formed by a pair of mirrors of 95% reflectivity at the resonant wavelength, placed as close as possible to the crystal faces. Cavity lengths were 18mm for LBO and 23mm for BBO. The pump beam was compressed by a factor of 7.5 to a dimension 2.5mm (in the BBO walkoff plane, and in the y-dimension in LBO) x1.1mm. In BBO it is clear from figure 6.13 that resonance of the ultraviolet wavelength is unfavourable to the total conversion efficiency. The threshold is around 50% greater than in the case of infra-red resonance. Furthermore, much stronger evidence of saturation is shown by the data for resonance of 385nm. A maximum pump depletion of 21% is observed at about 3 times threshold, compared to 39% for infra-red resonance. LBO shows a similar effect (fig. 6.14) in terms of saturation at a lower value of pump depletion for UV-resonance than IR-resonance. In LBO this can be interpreted as resulting from the tighter pump divergence requirement imposed by resonance of the ultraviolet wavelength- $\Delta\theta$ for half gain for a 1cm crystal is around 4mR as compared to 18mR for IR-resonance. However one cannot use this explanation in BBO since both the signal and idler are ordinary waves. The observation of increased threshold and reduced pump depletion in this case may possibly result from lower UV than IR transmission.

Figure 6.15 shows that at this level of beam compression, there is little to choose between BBO and LBO in terms of efficiency at a given pump intensity. Thresholds are similar and maximum depletion is around 40% in both cases. However, it has been shown (ref. 5) that the increase in threshold at small pump beam dimensions discussed in section 5.4.2(d). is a much greater restriction in BBO than in LBO. A minimum pulse energy of around 15mJ is required in BBO to allow the use of pump beams of sufficient dimension to reduce the threshold to a level sufficiently below the damage limit. LBO, by contrast, offers the possibility of efficient conversion to tunable UV wavelengths for small pulse energies.

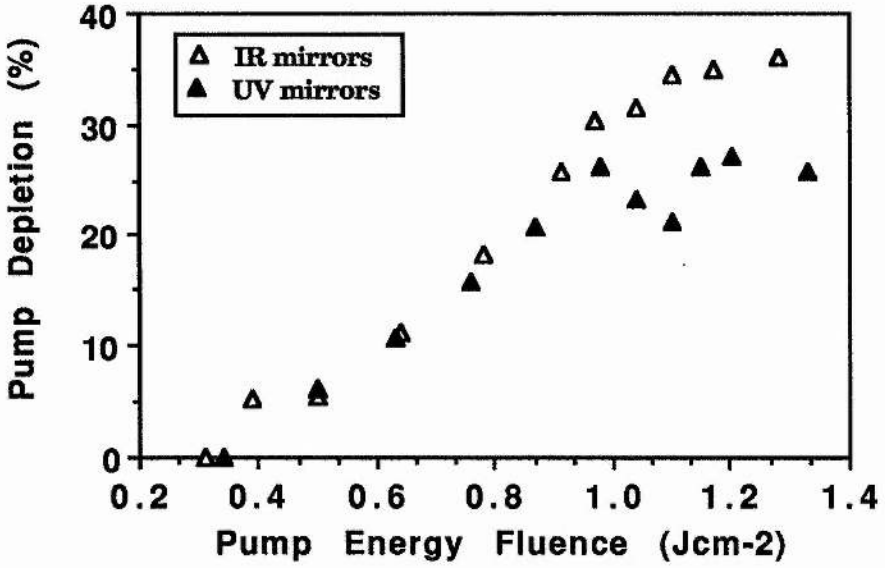

Fig. 6.14 Pump depletion in a Type 2 NCPM LBO OPO as a function of incident pump energy fluence for cavity reflectivities $R_1 = R_2 = 95\%$ at resonant wavelengths (a) 385nm and (b)1.5μm. l_c = 17mm, ℓ =15mm.

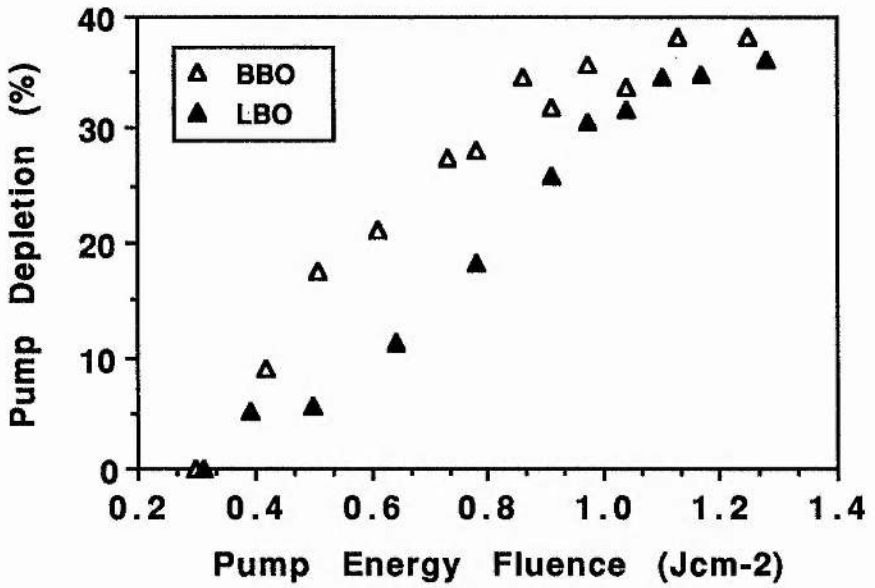

Fig. 6.15 Pump depletion in both a Type 2 NCPM LBO OPO and a Type 1 BBO OPO as a function of incident pump energy fluence for λ_s = 385nm, λ_i = 1.5μm and cavity reflectivities $R_1 = R_2 = 95\%$ @1.5μm.

6.6 Conclusion

In chapters 5 and 6 the most significant results have been observed in the comparative behaviour of the threshold and efficiency of the Urea and BBO OPOs. In both cases, a level of pump beam focussing was reached which was detrimental to operation of the OPO. Tightened pump focussing resulted in increased oscillation threshold, and decreased maximum attainable conversion efficiency. It was found that in terms of threshold, the NCPM Urea OPO was slightly more tolerant of pump beam compression than the BBO device. In both devices, the highest pump beam compressions used resulted in pump beam divergences which were in excess of the calculated angular acceptance angles, although by a much greater factor in BBO than in Urea. For BBO, even the lowest beam compression used resulted in a pump beam divergence well above the angular acceptance. The efficient operation of SROs under such circumstances must be explained by the occurrence of some degree of noncollinearly phase-matched operation, such that components of the pump beam which are not parallel to the cavity axis contribute to oscillation such that an off-axis idler wavevector fulfils the phase-matching condition. However, it has been observed that for high beam compressions, the excimer beam exhibits divergence well in excess of that predicted from the beam compression factor. In this case, it is believed that the beam dimension for high beam compressions restricts the overlap between noncollinear waves, and thus the highly divergent fraction of the pump beam can no longer contribute to parametric interaction.

In BBO, a second effect results in reduced three-wave interaction for small beam dimensions. The critically phase-matched Type 1 interaction takes place such that the extraordinary pump wave walks off from the ordinary signal and idler waves by 4^{o}. This results in a lateral walkoff of around 1.5mm over a 20mm interaction length. For beam dimensions below this value, significant reduction in beam overlap occurs, and hence, for beam compressions (7.5x) for which the NCPM Urea OPO threshold is unaffected, a considerable drop in saturated conversion efficiency is observed in comparison to BBO OPOs

operating with lower pump beam compression. In general it can be concluded that NCPM Urea is more tolerant of pump beam focussing than critically phase-matched BBO.

References

1 J. F. Bjorkholm, IEEE J. Quant. Elect. **QE-7**, p109 (1971).
2 Ewanizky, IEEE J. Quant. Elect. **QE-14**, p962 (1978).
3 J. E. Pearson, U. Ganiel and A. Yariv, IEEE J. Quant. Elect. **QE-8**, p433 (1972).
4 A. J. Henderson et al., J. Opt. Soc. Am. B **7**, p1402 (1990).
5 G. Robertson, A. Henderson, M.H. Dunn, Opt. Lett. **16**, p1584 (1991).
6 R. G. Smith, "Lasers", Vol. 4. Edited by A.K. Levine and A. J. De Maria. Marcel Dekker, New York (1976).

Chapter 7
OPO linewidth

7.0 Introduction

The Type 1 phase-matched OPO based on BBO has already established itself as a widely tunable and efficient source from the ultraviolet to the infra-red. However, as a tool for use in spectroscopy, it can rival the dye laser only if efficient narrow linewidth operation can be simply and reliably obtained over a substantial part of its tuning range. In this chapter we will report the progress of our efforts to fulfil this goal. A summary of the theory describing OPO linewidth is followed by a characterisation of the inherent linewidth behaviour of the excimer pumped-system. Our strategy for linewidth reduction of this system is then set out, and a comprehensive review of available line-narrowing techniques and previous OPO linewidth control work is given. Finally, the results of our own experiments are described.

7.1 OPO linewidth

The linewidth of the signal and idler output from a parametric oscillator is determined primarily by the parametric gain bandwidth. The gain bandwidth is defined by Byer[30] as the deviation of the signal or idler wavelength from perfect phase-matching ($\Delta k = 0$) which reduces the parametric gain to zero. This corresponds to the following condition:

$$\Gamma^2 \ell^2 = \pi^2 . \qquad (7.1)$$

Under conditions of low gain ($\Gamma_o^2 \ell^2 << \pi^2$) this is equivalent to the condition

$$\frac{\Delta k \ell}{2} = \pi . \qquad (7.2)$$

The phase mismatch Δk can be expanded to second order in terms of frequency as below:

$$\Delta k = \left(\frac{1}{u_i} - \frac{1}{u_s}\right)\delta\omega_s + \frac{1}{2}(g_s + g_i)(\delta\omega_s)^2$$

$$= \beta_{si}\,\delta\omega_s + \frac{1}{2}\,\gamma_{si}\,(\delta\omega_s)^2 \qquad (7.3)$$

where $u_j = \left(\frac{\delta k_j}{\delta\omega_j}\right)^{-1}$, $g_j = \left(\frac{\delta^2 k_j}{\delta\omega_j{}^2}\right)$, $\beta_{kl} = \left(\frac{1}{u_k} - \frac{1}{u_l}\right)$, and $\gamma_{kl} = (g_k + g_l)$.

We have chosen, in this text, to use an expression for the gain bandwidth defined as in Ref. 31 by the full width half power gain value, as given by expression (2.27). This is consistent with the expressions used for pump spectral and angular acceptance bandwidths in Chapter 2. Using expressions (2.27) and (7.3) we find the full width, half-maximum power gain bandwidth is

$$\Delta\omega_{s1} = \frac{2\pi}{\beta_{si}\ell} \qquad (7.4)$$

in frequency units. When β_{si} approaches zero (near wavelength degeneracy) the second order terms in expression (7.3) become dominant and the corresponding linewidth expression is

$$(\Delta\omega_{s1})^2 = \frac{4\pi}{\gamma_{si}\ell}\,. \qquad (7.5)$$

The ratio of the gain bandwidth under conditions of high gain to that for low gain[30], is

$$\frac{\text{Bandwidth(high gain)}}{\text{Bandwidth(low gain)}} = \sqrt{1 + \frac{\Gamma^2\ell^2}{\pi^2}}\,. \qquad (7.6)$$

These expressions give us the gain bandwidth for both signal and idler. In terms of wavelength, the idler (high wavelength) has a higher bandwidth than the corresponding signal. It is useful at this point to introduce an expression for the signal tuning rate as a function of tuning variable M as follows:

$$\frac{\partial \omega_s}{\partial M} = \frac{1}{\beta_{si}} \left[\frac{\partial k_p}{\partial M} - \frac{\partial k_s}{\partial M} - \frac{\partial k_i}{\partial M} \right]. \qquad (7.7)$$

It can be seen that the occurrence of β_{si} in both this expression and the bandwidth expression (7.4) implies a strong link between the tuning rate and the linewidth. In general a small tuning rate is accompanied by a small bandwidth. The gain bandwidth expression developed here assumes a monochromatic plane wave pump and collinear phase-matching. However in the parametric process, phase mismatch can result otherwise than from deviation of the signal wavelength from perfect phase-matching. Firstly, as discussed in section (2.2.4(a)) a certain finite pump linewidth can be tolerated such that the gain remains above half the maximum value. Secondly phase mismatch is introduced by the fraction of the pump beam whose momentum vector is not collinear with the signal wave axis, i.e. the pump beam divergence. Both of these effects result in additional broadening of the oscillator's operating linewidth. The linewidth broadening due to the above effects is found by equating the phase mismatch due to variation in signal frequency i.e.

$$\Delta k = \frac{\partial(\Delta k)}{\partial \omega_s} \Delta \omega_s \qquad (7.8)$$

to the contributions from pump beam divergence $\Delta\theta_p$

$$\Delta k = \frac{\partial k_p}{\partial \theta} \Delta \theta_p \qquad (7.9)$$

and the finite pump linewidth

$$\Delta k = \frac{\partial k_p}{\partial \omega_p} \Delta \omega_p \qquad (7.10)$$

The expressions derived from (7.8) - (7.10) for these signal linewidth components for the case of ordinary polarised signal and idler and extraordinary pump, are respectively

$$\Delta\omega_{s2} = \frac{\pi}{\lambda_p \beta_{si}} \frac{\delta n_p}{\delta\theta} \Delta\theta_p \qquad (7.11)$$

$$\Delta\omega_{s3} = \frac{\Delta\omega_p \beta_{pi}}{\beta_{si}} \qquad (7.12)$$

Expression (7.11) can equivalently be expressed as

$$\Delta\omega_{s2} = \frac{2\rho\Delta\theta_p}{\lambda_p \beta_{si}} \qquad (7.13)$$

where ρ is the walkoff angle. The total bandwidth is thus given by the sum of these three contributions

$$\Delta\omega_s = \Delta\omega_{s1} + \Delta\omega_{s2} + \Delta\omega_{s3} \qquad (7.14)$$

The idler wave bandwidth is given by an expression similar to (7.14) with the subscripts s and i exchanged. For a singly resonant oscillator, the actual operating bandwidth for the resonant wave is reduced by comparison to the gain bandwidth, by the effect of multiple passes in the nonlinear crystal. It can be shown[7] that for p passes the resonant wave linewidth $\Delta\omega_{res}$ reduces to

$$\Delta\omega_{res} = \frac{1}{\sqrt{p}} \Delta\omega \qquad (7.15)$$

The linewidth of the nonresonant wave in this case, is given by the convolution of the pump and resonant wave spectra, which generally results in a broader operating linewidth for the nonresonant wave than the resonant wave.

It has been shown[11] that in the steady state the singly resonant oscillator will operate on a single longitudinal mode for pump power levels below 4.61 times the steady state threshold value. In the context that 100% conversion efficiency can in theory be obtained at 2.46 times the threshold pump power, it is clear that high efficiency single mode operation of an SRO is possible. For pump power levels in excess of 4.61 times threshold, multimode behaviour is predicted. Under transient conditions, (i.e.

pulsed operation) however, a large number of modes under the gain profile are excited, and the linewidth is given by the expressions (7.13) and (7.14).

7.2 Inherent linewidth of a singly resonant BBO OPO pumped at 308nm

Studies of linewidth behaviour have been made in a Type 1 BBO OPO pumped by the Lambda Physik 308nm XeCl excimer laser. The device used in these studies was based on the 20mm interaction length sample of BBO described in section 3.4. Firstly, the linewidth of the OPO at both resonant and nonresonant wavelengths was measured across the tuning range. Multishot linewidth traces were recorded using a Monospek 1000 scanning monochromator of resolution better than 0.05nm, and a photomultiplier as a detector at the outlet slit. The OPO was set up in the configuration shown in fig 4.5(a) with mirrors 95% reflecting at the resonant wavelength separated by 23mm. The OPO was tuned from around 370nm to 610nm at a pump power level 2.4 times the oscillation threshold. The linewidths shown in figures 7.1(a) and (b) are full width half maximum values. The signal linewidths are displayed alongside curves representing calculated bandwidths $\Delta\omega_s$ and $\Delta\omega_{s1}$ (for a value of 1mR full angle pump beam divergence) according to expressions (7.14) and (7.4) respectively. It can be seen that the measured linewidth is, as expected, well in excess of $\Delta\omega_{s1}$ but below that predicted by the sum of the linewidth contributions $\Delta\omega_s$. This can be interpreted as resulting from multiple pass gain-narrowing as expressed in (7.15). The measured linewidth reflects the variation in tuning rate of the Type 1 tuning curve, with linewidths of around 0.2nm towards the UV where angle tuning is very slow, and linewidths of several nanometres towards degeneracy and the most rapid tuning point. For the OPO cavity the axial mode spacing in wavenumbers is given by

$$\Delta\nu\ (\mathrm{cm}^{-1}) = \frac{1}{2L(\mathrm{cm})} \qquad (7.16)$$

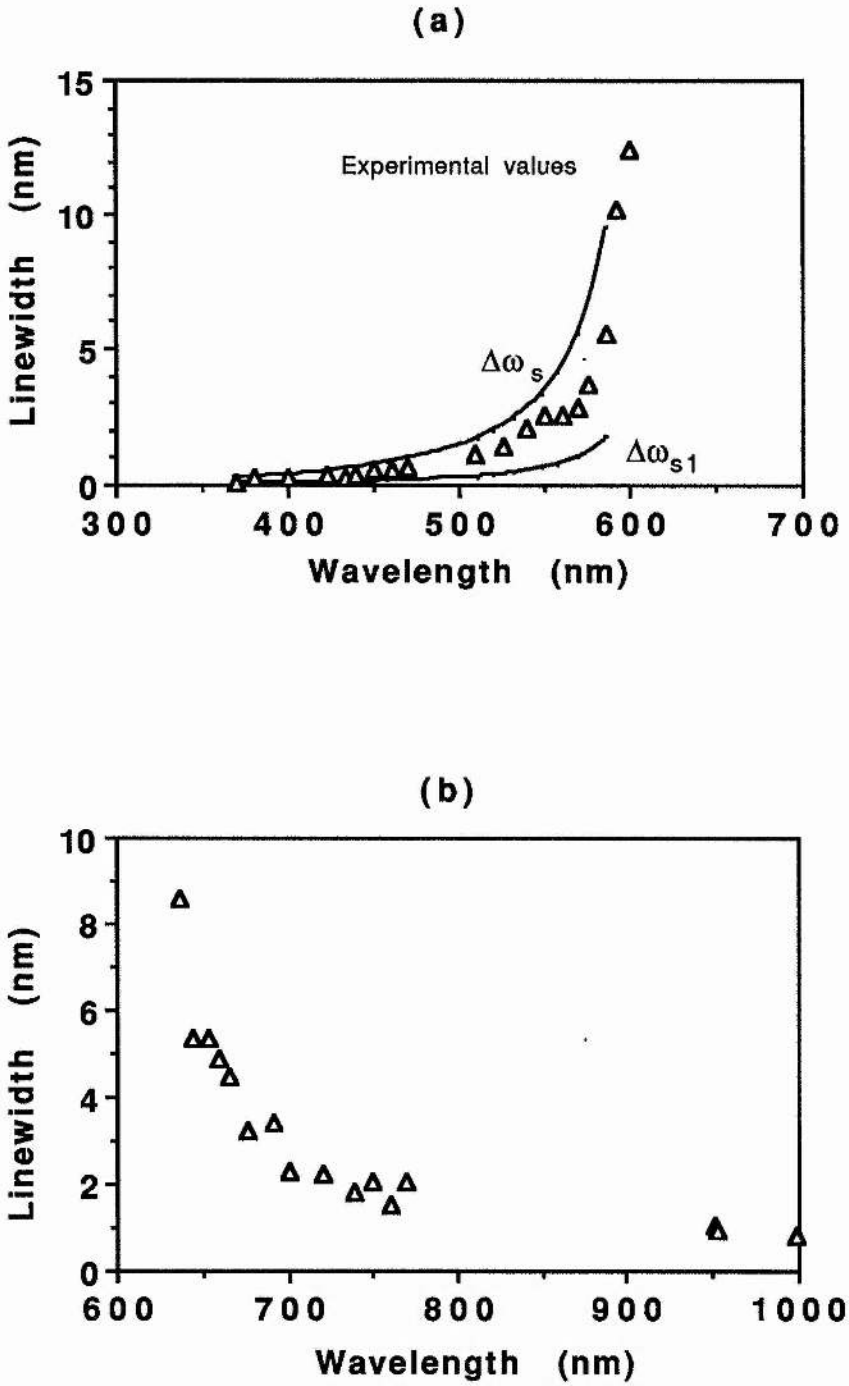

Fig. 7.1 Measured inherent linewidths in a BBO-OPO pumped at 2.4 times threshold for (a) signal, and (b) idler wavelengths. Calculated theoretical values of bandwidth expressions $\Delta\omega_S$ and $\Delta\omega_{S1}$ are also shown.

or in wavelength units

$$\Delta\lambda = \frac{\lambda^2}{2L} \qquad (7.17)$$

where L is the cavity optical length. In these experiments the cavity axial modes are separated by $0.14cm^{-1}$. For a signal wavelength of 370nm this means that the modes are spaced by 0.002nm. Thus the bandwidth covers around 100 cavity axial modes at this point. Near degeneracy at 600nm the linewidth encompasses nearer 2000 axial modes.

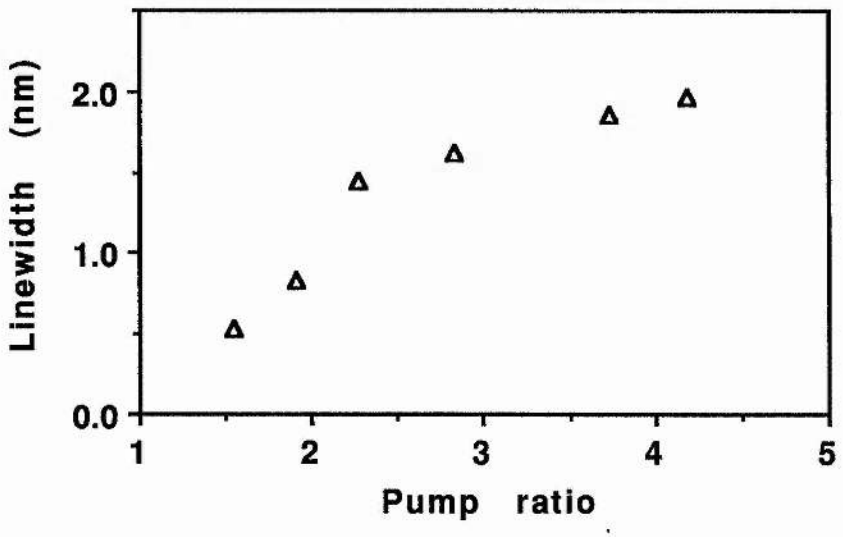

Fig. 7.2 Measured signal linewidth as a function of pumping ratio in a BBO-OPO operating at 515nm.

Figure 7.2 illustrates the typical pattern of variation shown by the OPO linewidth with increasing pump power. The graph shows the 515nm signal linewidth for an OPO based on the 20mm BBO crystal, in a 24mm cavity formed by two mirrors 95% reflecting at the signal wavelength. The linewidth shows an increase from 0.5nm just above threshold, to around 2nm at a pump energy four times the threshold value. The corresponding

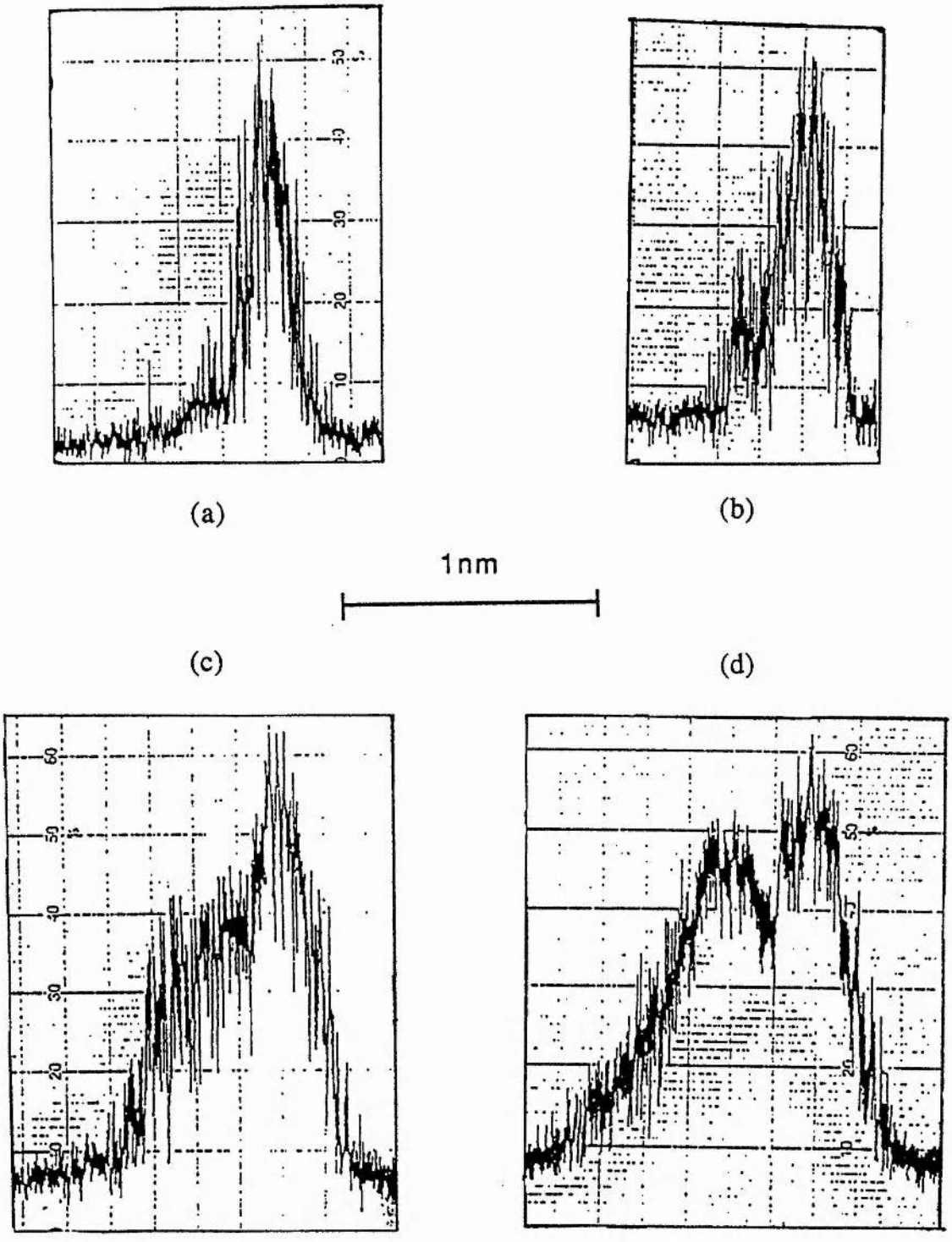

Fig. 7.3 Spectra of the signal wave of a BBO-OPO operating at 515nm, showing secondary maxima for pumping ratios of (a) 1.5, (b) 1.9, (c) 2.3 and (d) 3.7.

spectra in figure 7.3 show a noticeable secondary peak on one side of the maximum. This feature has also been observed in ourlaboratories in OPOs based on LBO and pumped by solid state lasers. It remains as yet unexplained.

The inherent linewidth of the 25mm NCPM Urea OPO was found to be 0.3nm at a pump intensity of four times threshold. Previous measurements in crystals of wider aperture and tunability showed the linewidth to be approximately independent of phase-matching angle. This relatively small bandwidth in Type 1 phase-matched Urea is associated with a relatively slow tuning rate by comparison with Type 1 phase-matched processes.

7.3 Linewidth control of pulsed singly resonant OPOs

Pulsed singly resonant OPOs oscillate with a broad linewidth covering many cavity longitudinal modes. In order to reduce this linewidth some discrimination must be provided between the amplification of the desired frequency band, and of those cavity modes which are to be suppressed. This can be achieved either through a supplementary frequency-selective loss in the resonator, or by giving the desired frequency a 'head start' through an external signal of magnitude greater than the parametric noise. The techniques of dispersive cavity line-narrowing and injection seeding, which find analogous application in laser linewidth control, have been used to produce single longitudinal mode operation of OPOs. The aim of our linewidth control work in BBO has been to develop a compact, efficient, narrow linewidth device tunable across the entire phase-matching range. Our initial approach to the problem has been to utilise dispersive cavity line-narrowing techniques. However, the inclusion of dispersive elements in the resonator brings associated losses due to reflection, absorption and scattering, and due to increased OPO risetime resulting from the increased cavity length. Thus it is inevitable that some increase in OPO oscillation threshold will result from this approach. Our strategy has been to split the task into two stages; firstly, to develop a relatively low power, continuously tunable, narrow linewidth OPO based on BBO,

in which the efficiency of conversion was not the prime factor; and secondly to utilise this device as a seed source for an efficient energy converter capable of reproducing the seed linewidth. This second stage device was envisaged as being a Type 1 phase-matched parametric amplifier or oscillator based on BBO, depending on the single pass gain achieved in crystals available. In contrast to previous work on injection-seeding of OPOs using lasers of fixed wavelength or of limited tunability, this would enable the complete ultraviolet to infrared tuning range to be accessed. Thus we have studied in parallel, both cavity line-narrowing and injection seeding of BBO-OPOs with a view to fusing our experience of the two options in one device. The following sections will discuss separately the theory of both the various dispersive cavity arrangements, and of OPO injection seeding, and in each case a review of relevant literature is given. These reviews are followed by details of our own experimental experience in BBO.

7.4 Dispersive cavity line-narrowing

In general, an optical resonator containing a gain medium has many modes which may experience gain, and the output of the device, whether it be a laser or a parametric oscillator, will consist of many discrete frequencies. Careful adjustment of the resonator dimensions can restrict oscillation to the fundamental transverse mode. The output will, however, still consist of a number of frequencies separated by c/2L (in Hz). Only if the cavity optical length is sufficiently short (i.e. if the mode separation c/2L is greater than the gain bandwidth, $\Delta\nu$) will the laser oscillate at a single frequency. However in both a laser and an OPO a certain volume (or length) of gain medium is necessary to allow sufficient gain to offset cavity loss. Thus, in general, one must find a method of suppressing the unwanted longitudinal resonances to obtain single frequency output. There are many ways of providing a frequency selective loss in an optical resonator such that net gain is experienced at only the desired

frequency. The more important of these are described in the following section.

7.4.1 Techniques and theory

In 1961 the first scheme was proposed by Kleinman and Kisliuk[12] for a complex resonator designed to produce single frequency laser operation. Their technique was soon experimentally demonstrated in a Helium-Neon laser by Kogelnik and Patel[13]. Over the following decade, the majority of currently-used line-narrowing techniques were first developed. Useful reviews of this subject have been compiled by P. W. Smith[26] and F. P. Schafer[27]. More recently used techniques for obtaining narrowband laser operation include the grazing incidence diffraction grating cavities developed simultaneously by Shoshan and Danon[14], and Littman[15], and the Fizeau wedge design used by Nenchev and Meyer[16]. The main characteristics of the most important wavelength selective feedback techniques will now be discussed.

Probably the simplest methods of frequency selection are those involving frequency dependent spatial separation. The Littrow mounted diffraction grating (fig. 7.4(a)) was first used as a line-narrowing device in a dye laser by Soffer and McFarland[17] . The grating is used to replace one of the resonator mirrors and provides feedback in its different diffraction orders. The basic grating equation is

$$m\lambda = d(\sin \alpha + \sin \beta) \qquad (7.18)$$

where m is the diffracted order, λ is the wavelength, d is the grating line spacing, α is the angle of incidence, and β is the angle of diffraction. For feedback, $\alpha = \beta$ and therefore the grating condition for cavity resonance is that

$$m\lambda = 2d \sin \alpha \qquad (7.19)$$

The grating angular dispersion is

$$\frac{d\alpha}{d\lambda} = \frac{m}{d\cos\alpha} \qquad (7.20)$$

Thus we can say that for a steady-state beam full-width half maximum divergence angle $\Delta\theta$ in the resonator, the passive spectral width is

$$\Delta\lambda_\alpha = \frac{d\cos\alpha}{m}\Delta\theta \qquad (7.21)$$

This gives an upper limit for the grating linewidth; in practice the resonator linewidth is likely to be considerably narrower on the basis of multiple cavity double passes. A sophisticated analysis of the multiple pass grating linewidth for a singly resonant OPO assuming diffraction-limited Gaussian beams is performed in ref. 7. This treatment develops expressions for contributions due to the grating-cavity steady state divergence angle, and to broadening due to the ability of wavelengths $\lambda + \Delta\lambda$ to resonate slightly off the cavity axis within the finite pump beam waist.

Inspection of expression (7.20) shows that an increase in the angle of incidence α towards grazing incidence on the diffraction grating will greatly increase the angular dispersion, and hence reduce the oscillator bandwidth. In practice the diffraction efficiency is very low and this technique is suitable only for high gain devices. Furthermore since the output coupling is via the reflected component from the grating its direction is altered with tuning. However, a non-Littrow arrangement as in Fig. 7.4(b) can be used such that a second mirror can provide feedback to a diffracted beam. The angular dispersion of such a configuration is given by

$$\frac{d\alpha}{d\lambda} = \frac{2\,m}{d\cos\alpha} \qquad (7.22)$$

which is twice that given by (7.20) for the same parameter values. Thus the single pass bandwidth of the cavity is

$$\Delta\lambda_\alpha = \frac{d\cos\alpha}{2\,m}\Delta\theta \qquad (7.23)$$

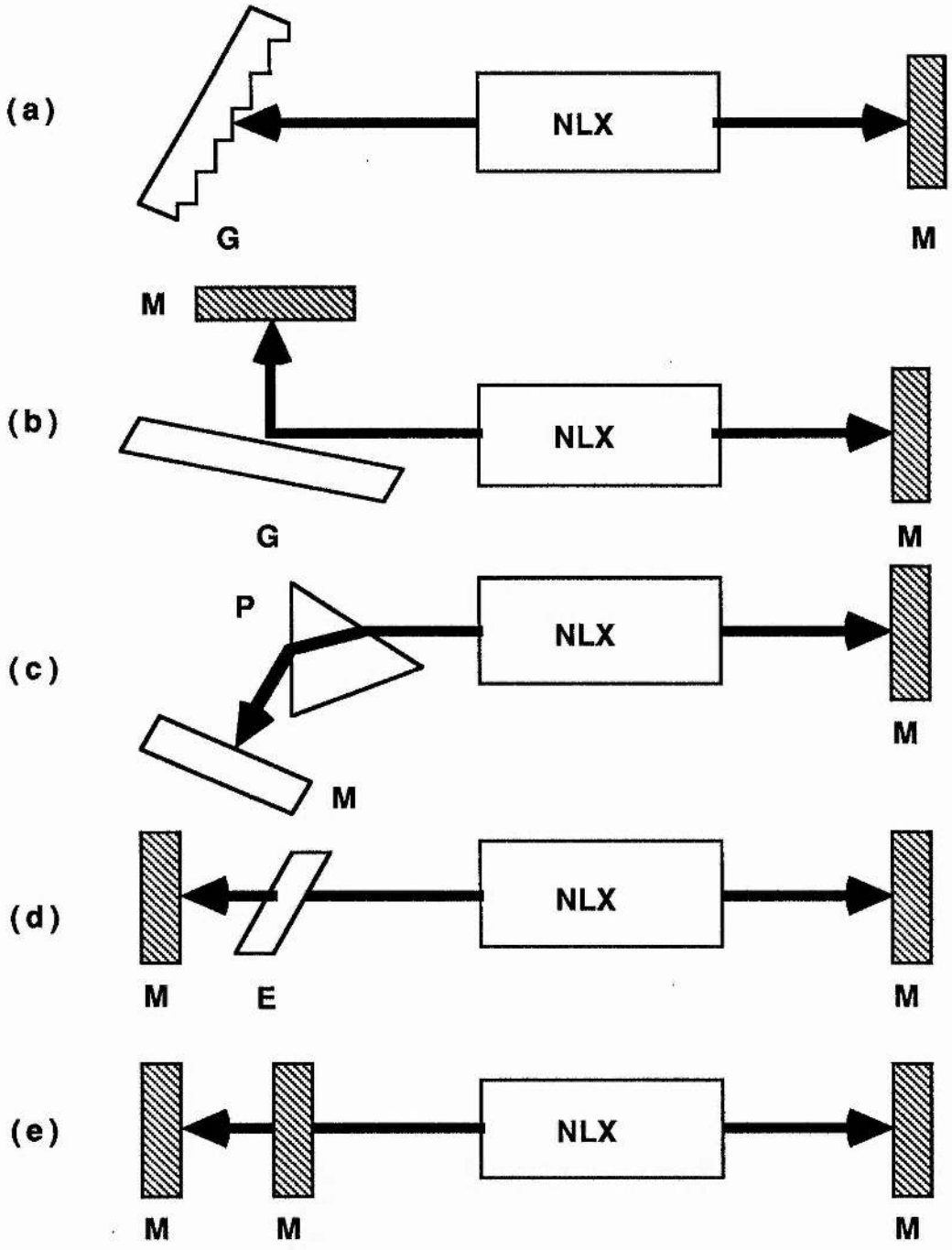

Fig. 7.4 Schematic diagrams showing various possible dispersive cavity designs. (a) Littrow-mounted diffraction grating. (b) Grazing incidence diffraction grating. (c) Prism. (d) Fabry-Perot etalons.(e) Resonant reflector. Here the letters M, G, P, E, and NLX represent cavity mirrors, diffraction gratings, prisms, etalons and nonlinear crystals respectively

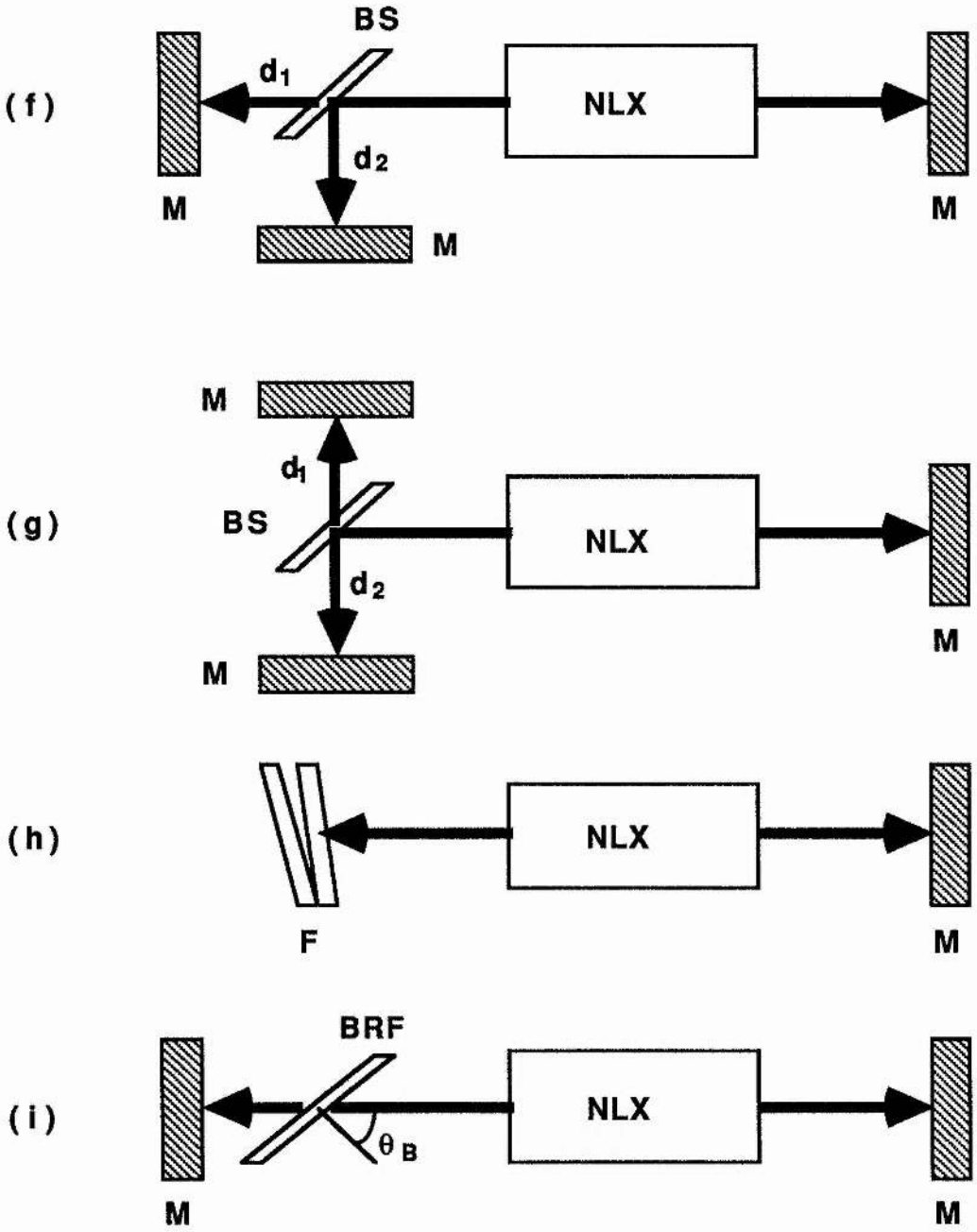

Fig. 7.4 (f) Fox-Smith interferometer. (g) Fox-Smith dual. (h) Fizeau wedge. (i) Birefringent filter. Here the letters BS, F and BRF represent beam splitter, Fizeau wedge and birefringent filter respectively.

for a pump beam divergence $\Delta\theta$. Again the output bandwidth would be expected to be somewhat narrower than this due to multiple passes in the cavity.

Spectral selection can also be achieved through spatial separation in intracavity prisms (fig. 7.4(c)). Assuming incidence at Brewster's angle α for maximum transmission, the angular dispersion of a prism is

$$\frac{d\alpha}{d\lambda} = 2\frac{dn}{d\lambda} \qquad (7.24)$$

where n is the prism refractive index. The corresponding passive spectral width is given by

$$\Delta\lambda_\alpha = \frac{\Delta\theta}{4}\left(\frac{dn}{d\lambda}\right)^{-1} \qquad (7.25)$$

In practice the selectivity of a single prism is rather limited, and as such it is more likely to be used as a coarse frequency selector for example between the multiple emission lines of gas lasers. However multiple prism designs (dispersion increases linearly with no. of prisms) are quite widely used for bandwidth narrowing in dye lasers, excimer lasers etc. The beam expansion which is introduced by prism selectors makes them useful in conjunction with diffraction gratings for which the dispersion increases with coverage of grating area. This scheme is used in commercial laser systems (e.g. Lambda Physik EMG 150 excimer).

A further range of line-narrowing techniques exists harnessing interference effects. Probably the most widely used of these is the insertion of one or more Fabry-Perot etalons (fig. 7.4(d)) into the resonator cavity. The wavelength λ of maximum transmission in kth order for an etalon of thickness t, refractive index n and with an angle α between its normal and the cavity axis, is given by

$$2nt\cos\alpha' = k\lambda\,, \qquad (7.26)$$

where α' is the refracted angle such that

$$n \sin \alpha' = \sin \alpha \, . \tag{7.27}$$

For small angles $\alpha' = \alpha/n$. The dispersion of the etalon is then given by

$$\frac{d\lambda}{d\alpha} = \frac{\lambda_o \alpha}{n^2} \tag{7.28}$$

where λ_o is the wavelength satisfying (7.26) for $\alpha = 0$. The free spectral range $\Delta\lambda_F$ between adjacent transmission orders is

$$\Delta\lambda_F = \frac{\lambda}{k} \tag{7.29}$$

or alternatively for small α,

$$\Delta\lambda_F = \frac{\lambda^2}{2nt} \tag{7.30}$$

The single pass spectral width of the etalon $\Delta\lambda_E$ is determined by the reflection coefficient R of the surfaces of the etalon such that

$$\Delta\lambda_E = \frac{\Delta\lambda_F}{F} \tag{7.31}$$

where

$$F = \pi \frac{\sqrt{R}}{1-R} \tag{7.32}$$

is the etalon finesse. Hence the etalon functions as an intracavity wavelength selector by transmitting a wavelength band of width $\Delta\lambda_E$ and reflecting frequencies outside this band at an angle 2α to the cavity axis so that they are ejected from the cavity. The actual multipass etalon bandwidth is given[7] for p passes by

$$\Delta\lambda_E(p) = \frac{\Delta\lambda_E(1)}{\sqrt{p}} \tag{7.33}$$

Tuning of the oscillation frequency may be achieved by adjustment of the etalon tilt angle. This is, however, limited by losses which accompany increasing tilt. The insertion loss γ results from the failure of the beams reflected from the first and second surfaces of the etalon to overlap completely-thereby preventing the complete elimination of the reflected light by destructive interference. This has been treated by Leeb[28] for CW laser cavities and found to be

$$\gamma = \frac{2F^2}{\pi^2}\left\{\frac{2t\theta}{nw_o}\right\}^2 \qquad (7.34)$$

where w_o is the beam diameter. In pulsed systems an additional loss mechanism arises from the effective increase in optical path length introduced by inclusion of the etalon. An extra propagation distance of 2Ft results on each pass through the etalon and this delay can become quite significant on the basis of a multiple pass build-up. Finally, imperfect parallelism of the etalon surfaces also results in a transmission loss which is proportional to the square of the finesse[19]. It can be seen that the losses are expected to increase in each of these cases with increasing etalon finesse.

The resonant reflector (fig. 7.4(e)) bears some resemblance in its behaviour to a Fabry-Perot etalon acting in reflection on the resonator cavity axis. Many designs have been proposed, the first being that by Kleinman and Kisliuk[12] in 1961. Double plate reflectors such as theirs provide a reflectivity profile similar to that of an etalon of optical path length equal to the reflector plate spacing, but further modulated by an envelope of period dictated by the optical length of the individual plates. The reflection properties of these and more complex designs have been studied numerically by Watts[20]. The resonant reflector has two major disadvantages by comparison with the transmission mode of a Fabry-Perot. Firstly it is not possible to reduce continuously the width of the reflection peaks by choosing plates of suitable reflectivity, and secondly the maximum reflectivity is always less than unity. However resonant reflectors have been successfully used in several high gain devices[21].

The Fox-Smith interferometer[22,23] as depicted in Fig. 7.4(f) makes use of a combination of a 45° beamsplitter and two mirrors to provide a reflectivity profile as a function of frequency which has essentially the same characteristics as a Fabry-Perot etalon in transmission. An alternative arrangement is shown in Fig. 7.4(g) which has identical properties to the Fox-smith device if the reflectivity and transmission of the beamsplitter in each are interchanged. The latter device has reflectivity peaks spaced in frequency by (i.e. has a free spectral range given by)

$$\Delta\nu_F = \frac{c}{2(d_1 + d_2)} \tag{7.35}$$

where d_1 and d_2 are as shown in Fig. 7.4(g). At frequencies on resonance it exhibits a peak reflectivity

$$R_{max} = \frac{R_m R^2}{(1-TR_m)^2} \tag{7.36}$$

where R_m is the reflectivity of the interferometer mirrors and R is the reflectivity and T is the transmission of the beamsplitter. Off resonance the reflectivity falls to a minimum value of

$$R_{min} = \frac{R_{max}}{\{1 + (2F/\pi)^2\}} \tag{7.37}$$

where F is the finesse of the etalon and is given by

$$F = \pi \frac{\sqrt{R_m T}}{(1 - R_m T)} \tag{7.38}$$

The use of this type of mode selector eliminates the insertion losses associated with Fabry-Perot etalons and has been used in gas lasers in several experiments[24]. They are, however, restricted by their physical dimensions, to situations requiring a selector of narrow free spectral range.

Single mode operation of dye lasers has been achieved[16] using a Fizeau wedge (fig. 7.4(h)) as a cavity reflector. These devices are made up of two plates forming an air wedge in

between, and set at a small angle to the cavity axis. A spatially localised component of the incident beam interferes constructively with a multiply reflected ray which has traversed some distance across the wedge, and a resulting narrow linewidth component is reflected on the cavity axis. By contrast with the feedback from a resonant reflector, this component can be progressively narrowed by increasing the reflectivity of the plates. The intensity of the reflected component can in fact be greater than the mean intensity of the incident beam in this device. The reflection peaks are separated in frequency, as in a Fabry-Perot etalon, by

$$\Delta\nu_F = \frac{c}{2d} \tag{7.39}$$

where d is the plate separation. This design has the further advantage of compactness, although the spatial limitation of the beam may be a difficulty in some applications.

A line-narrowing technique based on a different principle is the birefringent filter[29] as depicted in fig. 7.4(i). It is formed of a length of birefringent material, tilted at Brewster's angle to the cavity axis. Wavelength selection occurs with the filter because of the existence of two different crystal indices of refraction. For a wavelength corresponding to an integral number of full wave retardations, the cavity behaves as if the filter were not present. At any other wavelength, the polarisation is modified by the filter and suffers losses at the Brewster surfaces. Transmission for lossy wavelengths can be reduced by using multiple filters, or multiple Brewster surfaces on either side of the filter. The kth order transmission maxima are given by

$$k\lambda/2 = \Delta\mu x_o \cos\alpha \tag{7.40}$$

where α is the tilt angle, x_o is the crystal thickness, and $\Delta\mu$ is the birefringence (both for normal incidence). The actual transmission is dependent on the filter design.

7.4.2 Review

The first demonstration of tunable single-mode operation of a pulsed optical parametric oscillator took place as long ago as 1969[1]. Kreuzer's device was a Lithium Niobate OPO operating well away from degeneracy. An intracavity etalon narrowed an inherent linewidth of $8cm^{-1}$ down to a single longitudinal mode. Further demonstrations of SLM operation of $LiNbO_3$ OPOs soon followed . Pinard and Young[2] used a Fox-Smith dual arrangement to produce a linewidth of $0.001cm^{-1}$. Stability was limited by a thermal drift of $0.001cm^{-1}$/min. Hordvik and Sackett[3] narrowed an inherent linewidth of $0.3cm^{-1}$ to $0.001cm^{-1}$ (SLM) and found that long term stability (30mins.) was better than $0.001cm^{-1}$. The relatively narrow inherent linewidth enabled them to use only a single etalon to achieve the bandwidth narrowing. In 1976, a Littrow grating cavity was utilised[4] to produce sub-wavenumber radiation at 3.5μm and 16μm from a Cadmium Selenide OPO pumped at 2.9μm. This work was later extended[5] to achieve further bandwidth narrowing through the simultaneous use of a Littrow grating and etalon. The grating-etalon combination was used in several other experiments[6-9], including two separate extensive studies by Byer[6,7] and co-workers which this arrangement was compared with a number of alternative selection methods. Ref. 6. reported the achievement of linewidths less than $0.1cm^{-1}$ in $LiNbO_3$ OPOs using three different cavity arrangements. A Fabry-Perot etalon was used as the fine selection element in combination with a Littrow grating, a birefringent filter, and a second etalon. Each of these were reported to provide satisfactory primary selection. The 1979 studies[7] extended this work to reach single-mode operation. The Littrow grating cavity used accommodated beam expansion prisms to increase dispersion, and finer selection was provided by an intracavity etalon and resonant reflector. It was found that the single mode output was around 80% of the full multi-mode power under similar pumping conditions. A theoretical study of the line-narrowing by gratings, prisms and etalons was also presented.

All of the experiments so far mentioned were operated in the near to mid-infrared, and all but one was based on $LiNbO_3$. Since the introduction of the new UV-visible transmitting nonlinear materials urea, BBO and LBO, only one study of cavity line-narrowing has been published[10]. Several configurations of grating cavities were used to narrow the linewidth of a 355nm-pumped Type 1 BBO-OPO across its tuning range. First and second order Littrow cavities produced linewidths between 0.1 and 0.3nm with threshold increases of 50% and 100% respectively. A grazing incidence grating cavity gave a linewidth of 0.03nm but was accompanied by a threefold threshold increase.

7.4.3 Line-narrowing of an excimer-pumped Type 1 BBO-OPO

The aim of the first stage of our line-narrowing work was to develop a master oscillator OPO cavity which would reliably produce stable narrow bandwidth output. Although it was not essential that this device operate highly efficiently, it was necessary to operate at a pump intensity at least a few times in excess of the oscillation threshold, in order to avoid the large fluctuations in output power which result from pump power fluctuation near threshold level. Even though restriction of the oscillation bandwidth using cavity dispersive elements does not necessarily result in threshold increase, the accompanying increase in cavity length certainly does have a detrimental effect. In our case, with a 20mm BBO crystal, it can be seen from fig. 5.7(b) that an increase in cavity length to 20cm causes a fourfold increase in threshold. This is considerably more restrictive than for example, a similar cavity length for a 5cm $LiNbO_3$ crystal, as in ref. 7. If we take a value of $1Jcm^{-2}$ as a working pump fluence damage limit for optical components, we can see that such an increase in cavity length would make the feasibility of the device quite marginal. Thus, in comparing the various line-selection methods just described in terms of suitability to our task, a prime consideration was the compactness of the cavity dispersive elements. A second important factor was the enormous variation in inherent linewidth of the device, from a few tenths of a

nanometre to ten nanometres at degeneracy. A majority of the methods described in 7.4.1 are characterised by a finite free spectral range (FSR), i.e. a periodic spacing between frequencies which are selected by the element. Hence, if only one frequency band within the OPO gain bandwidth is to be selected, then a device with an appropriate FSR must be used, and thus the varying OPO bandwidth means that the line-narrowing problem is a somewhat complex one. In general, it can be said that it is difficult to achieve sufficient selectivity using a single element to reduce bandwidths as high as 10nm. The primary selection elements most prevalent in OPOs to date have been Littrow and Littman gratings, and birefringent filters. Birefringent filters have been shown to be a convenient, low loss, relatively compact option, although it has been noted[7] that they suffer the disadvantage of nonlinear tuning. Littman gratings have been used, but have incurred considerable threshold increase. Littrow gratings have been used successfully in several experiments, either with or without beam expansion prisms. Our initial experiments on Littrow grating selection will now be described.

(a) Primary line selection : Littrow grating

A diffraction grating blazed for 500nm (500 lines/mm) was used in the first order Littrow configuration as a primary line selection element for the 20mm BBO-OPO. The cavity was set up with one Brewster-angled beam steering plate introducing the pump beam into the cavity as in figure 7.5 This was separated from a rear 95% reflector for 500-600nm by 35mm distance. The beam compression was 3.75 and the linewidth measurements were made for a pump intensity 2.4 times in excess of the threshold value. Figures 7.6 (a) and (b) show that the linewidth was reduced over the range 500-600nm and over the complementary idler range, to less than 2nm. The inherent linewidths are shown for the same pump ratio. These grating cavity linewidths are equivalent to between $35cm^{-1}$ and $50cm^{-1}$. This is considerably in excess of the $7cm^{-1}$ linewidths observed by Tang[10] using an 1800l/mm grating in a 355nm-pumped Type 1 BBO-OPO. It is still further in excess of the values predicted for

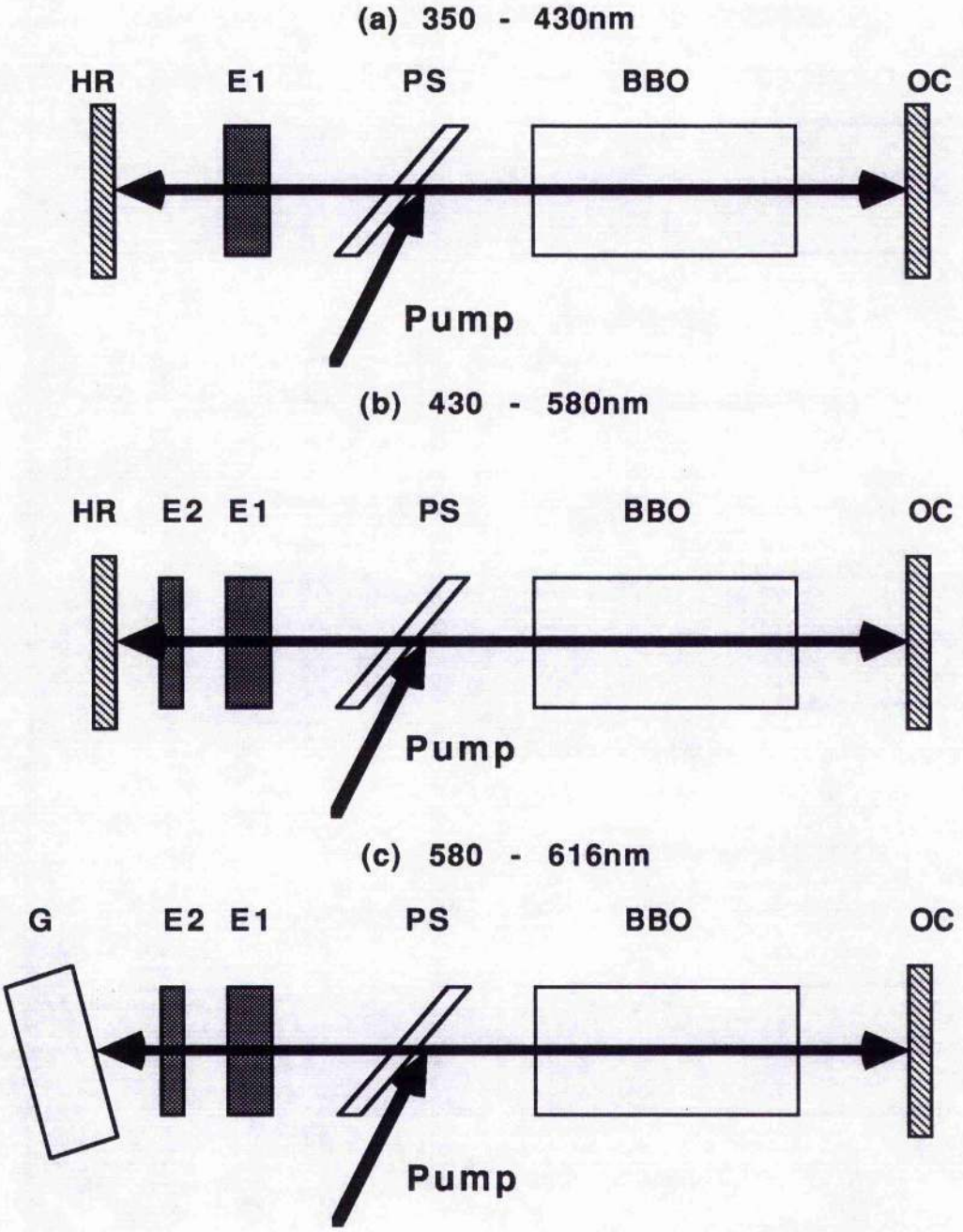

Fig. 7.5 Dispersive cavity designs employed to achieve single mode operation in a BBO-OPO. HR and OC are high reflectors and output couplers respectively. E1, E2 are solid etalons. PS is a pump steering plate and G is a Littrow-mounted diffraction grating.

Gaussian beams of similar dimension by expression (48) of ref. 7. However, it was found that the grating was a relatively efficient means of providing primary linewidth control. For example, for an OPO cavity of length 65mm, operating at 580nm with a 95% reflector at this wavelength as the rear mirror, it was found that the oscillation threshold was increased by only 33%. The pump beam in this case was compressed by a factor of 5.

The grating cavity provides a linewidth upper limit of 1.8nm over the tuning range and enables line selection elements of practically attainable free spectral range to be used for further line selection. A free spectral range of around 3nm is necessary to ensure a single frequency passband. In order to reach a level approaching single mode operation of the OPO with a single element of such a free spectral range, a very high 'finesse' would be required. Instead it was decided to opt for a combination of a thin and thick etalon each having moderate finesse, as a second level of frequency selection.

(b) Secondary line selection: Intracavity Fabry-Perot etalons

The selection of a two-etalon combination was guided firstly by the requirement for a 3nm ($80cm^{-1}$) free spectral range, and secondly by the aim of achieving efficient single-mode operation. A 30μm etalon of finesse 160 could be expected, according to expression (7.31), and on the basis of 25 cavity round trips, to restrict the oscillation to a single cavity mode in a cavity of length 50mm. However, the high circulating field in the etalon, would be very likely to damage the coatings. Hence, it was decided to split the line-narrowing task into two stages: firstly, to use a 30μm coarse selection etalon of finesse 10, and secondly a fine selection etalon of thickness 1mm and also finesse 10 (Etalons of thickness 0.5mm (F=10) and 0.2mm (F=3) were also available). Expression (7.33) predicts a resultant linewidth of $1.1cm^{-1}$ for such a 30μm etalon, after 25 round trips. This would similarly be reduced by the 1mm etalon (with f.s.r. $3.3cm^{-1}$) to $0.05cm^{-1}$. This is approximately half the cavity mode spacing for a 50mm OPO

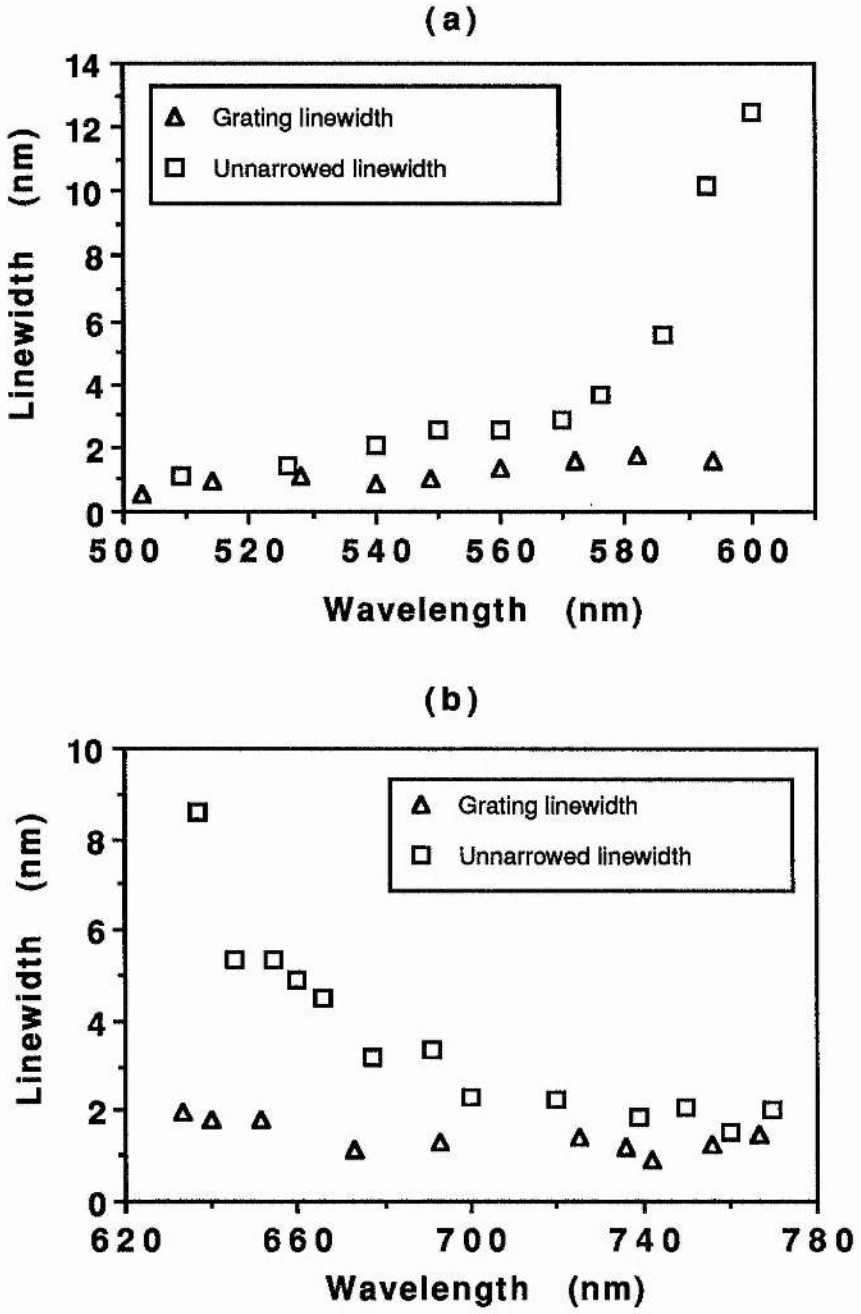

Fig. 7.6 Measured linewidths at (a) signal and (b) idler wavelengths in a Littrow grating narrowed BBO-OPO, pumped at 2.4 times threshold. Corresponding inherent linewidths are also shown.

cavity, and could thus be expected to select a single cavity mode. It was calculated that for a 4mm beam diameter, the insertion loss for rotation through 90mR (well in excess of the tilt required between adjacent transmission orders for either etalon) would be less than 2% for the 1mm etalon, and negligible for the 30μm etalon. In consideration of the high cavity losses already in existence, these figures would be predicted not to result in a significant increase in oscillation threshold. However the propagation delay of the thick etalon can be considered to be equivalent to an increase in cavity length of 20mm, which would cause a small threshold increase.

The results achieved using these etalons were broadly in agreement with the predicted behaviour, although the multipass bandwidth narrowing was somewhat less than expected. Initially, the performance of the OPO using the individual etalons was investigated. It was found that for resonant wavelengths above 580nm, where the inherent linewidth was greater than the 30μm etalon free spectral range ($80cm^{-1}$) more than one frequency band was selected, such that the bands were separated by approximately $80cm^{-1}$. Figure 7.7(b) shows three thin etalon modes in operation at a signal wavelength of 590nm. The spectral width of these etalon modes was monitored at a wavelength where only one etalon mode was in oscillation, by diverging the output through a 0.5mm, F=10 solid monitoring etalon. The resulting fringe pattern was recorded and analysed using a CCD camera and frame grabbing software on a microcomputer. A linescan of the fringe pattern (fig. 7.7(c)) for operation using the 30μm etalon indicated a linewidth of around $1.8cm^{-1}$, although this figure is limited in accuracy by the $0.7cm^{-1}$ resolution of the monitoring etalon. The thick etalons (i.e. those of thickness 0.2mm or more) as expected allowed many more etalon modes to oscillate, with much narrower frequency spacing. Figure 7.8(a) shows the unnarrowed signal spectrum at a wavelength of 491nm, while in figs. 7.8(b) to 7.9(c) are those for OPO operation with 30μm (F=10), 0.2mm (F=3), 0.5mm (F=10), and 1mm (F=10) intracavity etalons, respectively. It can be seen that the peak spacings correspond, as expected, to the etalon free spectral ranges, and that except in the case of the 30μm etalon, more than

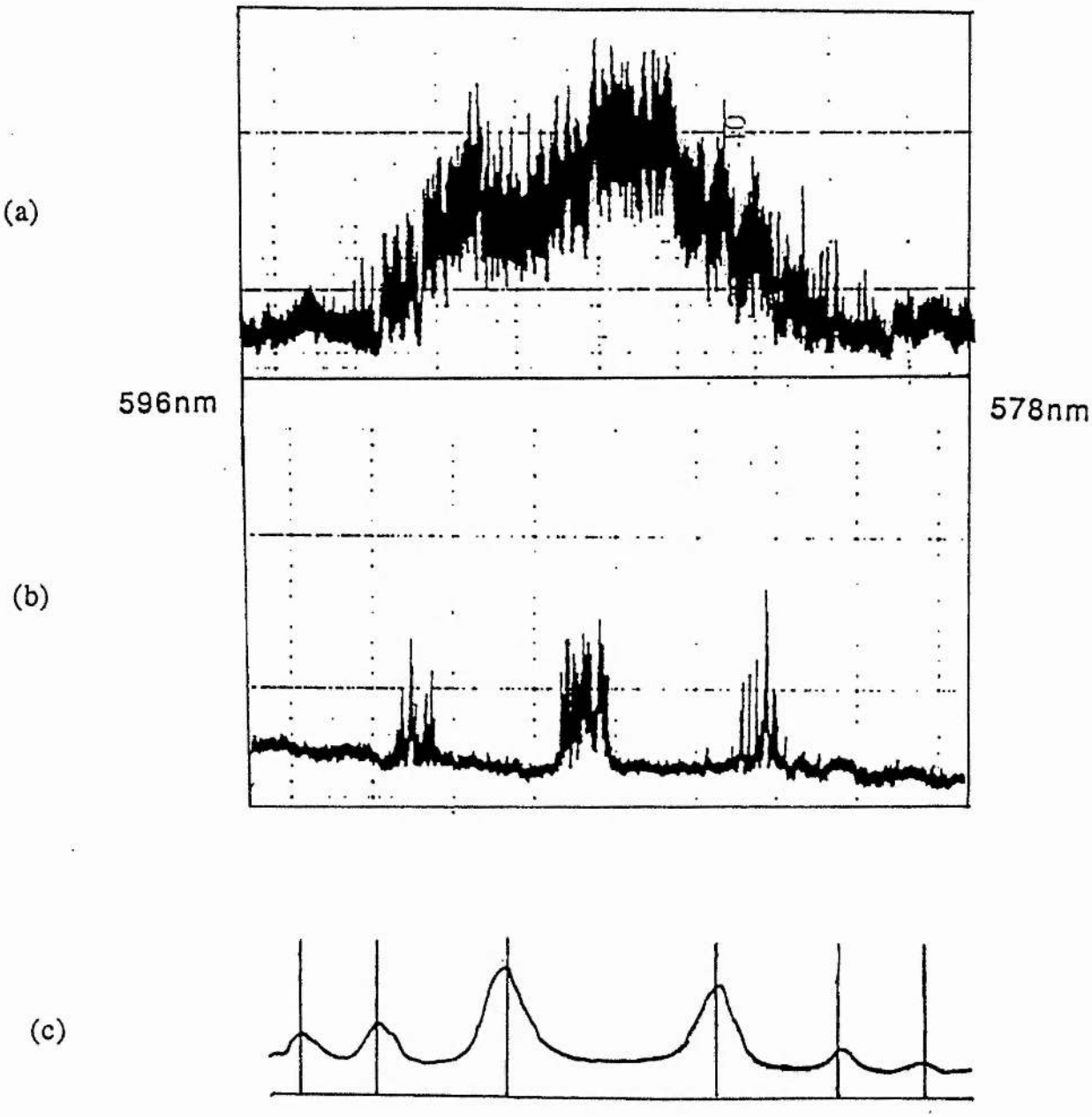

Fig. 7.7 Spectra of BBO-OPO operating at 590nm for (a) a simple two-mirror cavity, and (b) a 30μm intracavity etalon. A linescan of the fringe pattern, produced by diverging the OPO 520nm output through a 0.5mm solid monitoring etalon is shown in (c). At this wavelength only one thin etalon mode is in oscillation, and its width is estimated at $1.8cm^{-1}$.

one etalon mode is in operation. The 0.2mm (F=3) etalon peaks were monitored by diverging the beam through an air-spaced F = 25 etalon, and analysis of the fringe pattern showed that they had a spectral width of around 1.5cm^{-1}. As such, this etalon could be used as an alternative selection element to the 30mm etalon at wavelengths where the bandwidth was less than 25cm^{-1} (λ_s < 510nm). The low finesse of this etalon also meant that it incurred negligible threshold increase. At signal wavelengths below 580nm, the 30μm etalon could be used to select a single etalon mode of the 0.5mm and 1mm thick etalons. The reflectivity band of the etalon coatings extended between 420nm and 620nm, and the inherent linewidth over this range was always larger than the free spectral range of the 0.5mm etalon, so two etalons were always required over this range to restrict oscillation to a single frequency band.

The linewidth of the output for two-etalon OPO operation was monitored using air-spaced etalons of large mirror separation and corresponding high resolution. The ultimate lower limit in linewidth produced by the 0.5mm (F=10) fine selection etalon was determined at a signal wavelength of 480nm when using the 0.2mm (F=3) etalon to select a single thick etalon mode. The linewidth was monitored using an airspaced (F = 25) etalon. Fringes could be observed at an etalon spacing of 19mm, which corresponds to a free spectral range of 0.26cm^{-1}. On a shot-to-shot basis, simultaneous fringe patterns such as those shown in fig. 7.10 were seen, indicating that oscillation was occurring on between two or three cavity modes. This was entirely consistent with the cavity mode spacing of 0.08cm^{-1} at an OPO cavity length of 60mm. On the basis of this observation it was expected that subject to single thick etalon mode selection, single cavity mode behaviour could be produced by replacing the 0.5mm with the 1mm etalon. This was in fact confirmed. Single longitudinal mode operation of the OPO, as shown by the single fringe pattern observed with a 22mm airspaced monitor etalon (fig. 7.11), was demonstrated at a wavelength of 480nm. Mechanical instability of the cavity was reflected in the spatial instability of the fringe pattern, and also in occasional two mode behaviour when positions of the etalon transmission peaks were not well matched.

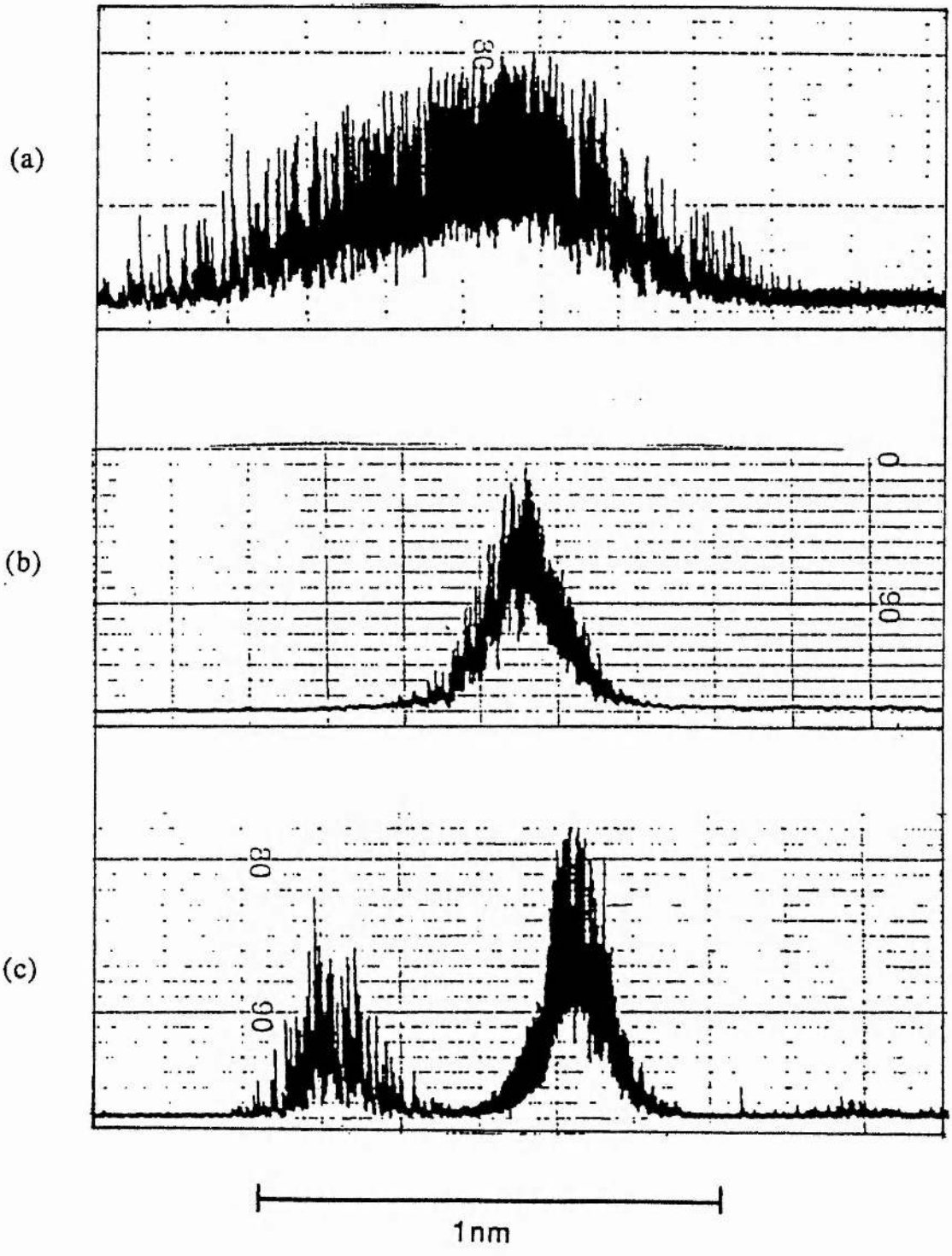

Fig. 7.8 Signal wave spectra for a BBO OPO operating at 491nm showing (a) unnarrowed output, (b) using a 30μm F=10 intracavity etalon, and (c) using a 0.2mm F=3 etalon.

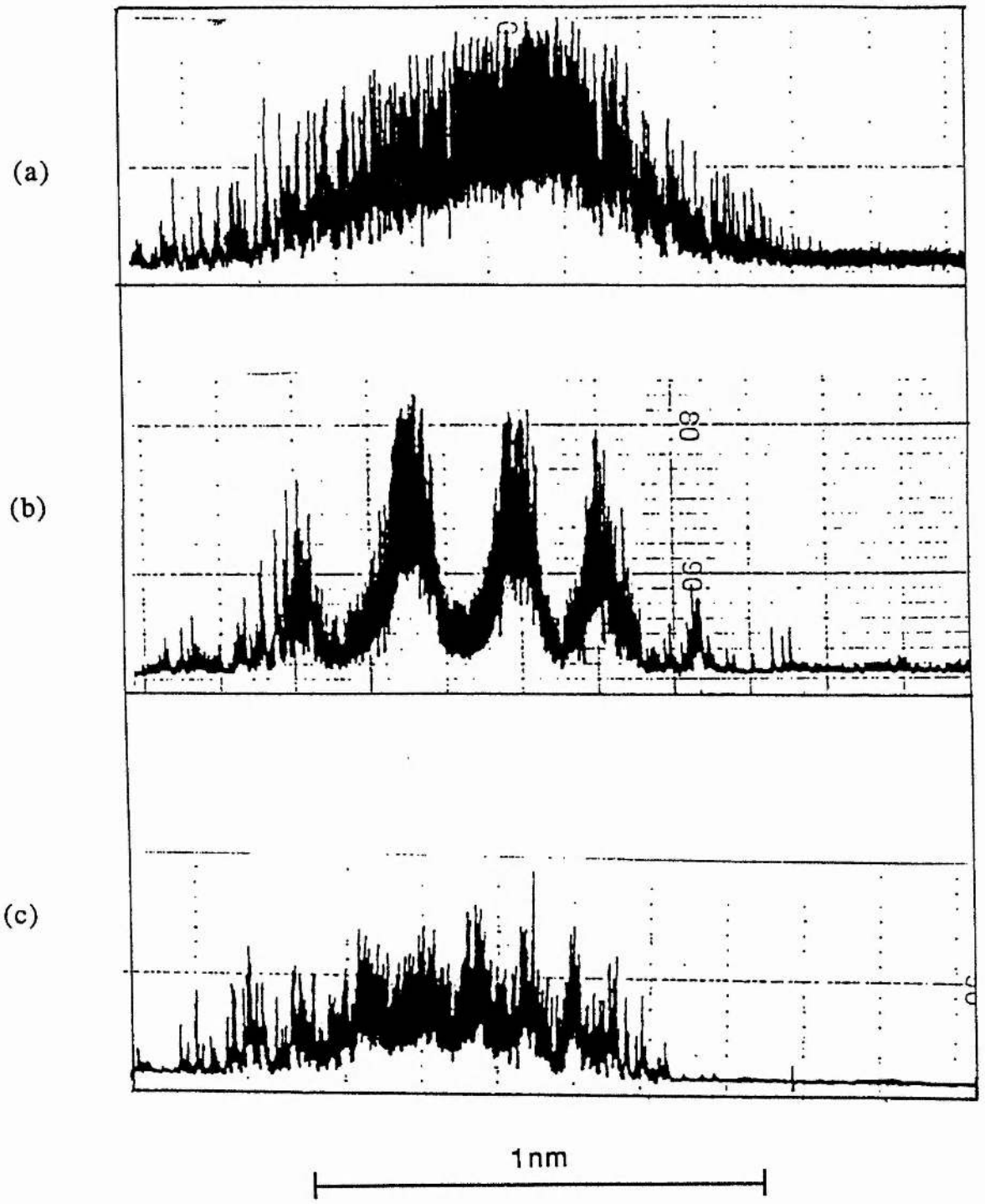

Fig. 7.9 Signal wave spectra for a BBO OPO operating at 491nm showing (a) unnarrowed output, (b) using a 0.5mm F = 10 intracavity etalon and (c) using a 1mm F = 10 etalon. The monochromator is barely able to resolve the etalon modes for the 1mm etalon.

As a result, it would be expected that the time-averaged linewidth would be considerably larger than the actual width of the cavity modes.

The performance of the device in terms of threshold increase was relatively encouraging. It was found that for small angles of tilt up to around 3mR, the thick (0.5mm and 1mm, F=10) etalons incurred less than 10% increase in threshold of the OPO under typical operating conditions. Much larger tilt angles exist between adjacent transmission orders for a thin etalon. However, it was found that despite operation at tilt angles of several degrees, the 30μm etalon typically produced a threshold increase of 30% in the 20mm BBO-OPO, and this may have been in part due to slight beam clipping by the limited aperture of the etalon mount. Simultaneous operation with thick and thin etalons increased the threshold by less than 50%. OPO performance was much more strongly affected when the thick etalons were tilted beyond 3mR. Table 7.1 shows typical figures for one particular cavity configuration (More detailed figures were not obtained due to etalon damage which made it difficult to obtain consistent results). The threshold increases for the high finesse etalons are not consistent with the expected insertion loss and with the effective increase in cavity length. We attribute this to insufficient etalon surface flatness; any nonuniformity in the etalon surfaces results in phase errors which reduce the transmission at the resonant wavelength. This problem of localised surface nonuniformity would be magnified by increasing etalon tilt, since the traversal of the etalon by internally reflected waves on each round trip increases with angle, introducing greater phase errors. The thick etalons of finesse 10 were found to have a peak transmission of only 90% for a He-Ne laser at 633nm. This is consistent with the hypothesis of insufficient surface flatness. Table 7.2 shows pump depletions for a fixed pump energy and corresponding relative threshold for single and double etalon operation. The relative efficiency values are close to those expected according to the corresponding threshold increases.

The tuning of the etalon-narrowed OPO has not been studied in great detail, but it has been observed that for two etalon operation, continuous tuning over around $3cm^{-1}$, i.e. within the

Table 7.1: OPO Threshold vs etalon tilt
Conditions: cavity length 65mm, 2x95% relectors
Beam compression x5, Signal 515nm

Etalon	Tilt	% threshold increase
1mm F=10	16mR	130%
0.5mm F=10	5.8mR	42%
0.5mm F=10	31mR	93%
1mm F=3	26mR	33%
0.5mm F=3	25mR	22%
30μm F = 10	72mR	30%

Table 7.2: Pump depletion and threshold for two-etalon OPO
Conditions: Cavity length 75mm, 2x95% reflectors
Signal 520nm, beam compression x5. 1mm etalon tilt < 3mR

Cavity elements	Pump depletion	Rel. threshold
No etalon	27%	1
1mm F=10 etalon	22%	1.10
1mm, 30μm F=10 etalons	11%	1.42

peak width of the 30μm etalon mode, can be achieved by tilting the thick etalon through theappropriate angle. This was observed by scanning through two fringes of a $1.7cm^{-1}$ f.s.r. solid monitoring etalon. However, this level of tuning involves

Fig. 7.10 Fabry-Perot ring pattern observed using a 19mm, F=25 airspaced etalon to monitor the output of the BBO-OPO operating at 480nm with 0.2mm, F = 3 and 0.5mm, F = 10 intracavity etalons. Operation on three longitudinal modes is shown.

Fig. 7.11 Fabry-Perot ring pattern observed using a 22mm, F=25 airspaced etalon to monitor the output of the BBO-OPO operating at 480nm with 0.2mm, F = 3 and 1mm, F = 10 intracavity etalons. This illustrates single longitudinal mode behaviour.

considerable threshold increase. For 1mm etalon tilt angles around 3mR such that the OPO threshold is not significantly increased, tuning of only $0.02cm^{-1}$ is possible. As a result it is anticipated that a more practical tuning scheme would be to use an airspaced pressure or piezo-electrically scanned etalon. It is hoped that this will be implemented in the near future (ref. 25).

7.5 Injection seeding

This section will take the form of a brief discussion of the ideas behind OPO injection seeding, followed by a review of previous work in this area, and a description of some preliminary experiments which have been conducted in our own laboratories. It is intended that this will provide some indication of the way in which a two-stage widely-tunable single-mode OPO will develop in the future.

7.5.1 Amplification of a nonzero input signal

As was mentioned in chapter 5, laser light incident on a nonlinear crystal gives rise to the process of spontaneous parametric emission, by which there is a finite probability that a driving pump photon will split into a signal photon and an idler photon. It has been shown[42] that electromagnetic zero-point power fluctuations produce an effective noise power per mode at the input surface of the crystal, equal to $\frac{1}{2} h\nu_s\Delta\nu_s$ at the signal frequency ν_s and $\frac{1}{2} h\nu_i\Delta\nu_i$ at the idler frequency ν_i, where h is Planck's constant and the $\Delta\nu$'s are the bandwidths of the parametric gains at ν_s and ν_i as limited by phase-matching tolerances. Typical bandwidth values mean that the equivalent noise input can be of the order of $1\mu W$ per mode. In the context that many lasers exist supplying several mW or more in a narrow bandwidth it can be seen that there exists the possibility of providing a seed signal several orders of magnitude in excess of the noise input. In the presence of a pump field, parametric amplification of such a seed signal reaches detectable levels well

in advance of those modes amplified from noise. Subject to sufficient parametric gain, sufficient preferential amplification of an injected seed signal may take place on a single-pass basis in a nonlinear crystal, or through multiple passes in an injection-seeded parametric oscillator. It can be shown from expression (2.17) that the parametric gain for zero phase mismatch in a crystal of length ℓ is given by

$$\text{Gain} = \cosh^2 \Gamma \ell \quad . \qquad (7.41)$$

As an example, in a Barium Borate crystal of length 20mm, a gain of 75 is to be anticipated at wavelength degeneracy for a typical 308nm pump intensity of 30MWcm^{-2}, assuming a value of 1.9pm/V for d_{eff}. This level of gain corresponds to a 17ns FWHM pump pulse of 100mJ in a 7 x 3mm beam. This level of gain would be sufficient on a single pass basis to provide a high level of depletion of the 100mJ pulse, given a milliJoule input seed pulse (quite a feasible level of output from a low power line-narrowed master oscillator). However, the greater level of amplification needed for a CW seed source would require that an optical resonator be employed. Injection-seeded OPOs allow a low-power narrow-band seed signal to be preferentially amplified subject to coincidence of the seed frequency with the OPO gain bandwidth. The modes amplified from the input seed signal begin to deplete the pump pulse and reduce the gain over the remainder of the gain bandwidth. However, even under conditions of reduced gain, those modes amplified from noise, whose frequencies lie closer to the centre of the gain bandwidth, may eventually "catch up and overtake" the seeded modes, and locking to the seed frequency may no longer be maintained. Hence there exists a limit in pulse length over which seeding at frequencies not exactly centred in the OPO gain bandwidth, can be effective.

The selection of a CW or pulsed seed source may be made on the basis of available gain, or on frequency characteristics, i.e. bandwidth, stability and tunability. As the injected power of a pulsed seed source is in general well in excess of that from a CW source, pump depletion in a pulse-seeded OPO takes place considerably earlier in the pulse, and as a result smaller loss

results from the OPO build-up time. However, for pulsed seeding the seed source is not always "on", and as a result the synchronisation of the seed and pump pulses must be carefully considered. A delay line may be utilised to provide maximum seed power at the optimum point during the pump pulse. In fact, both CW and pulsed injection-seeding have beneficial effects in terms of lowered threshold and increased conversion efficiency. These effects have been considered in detail in ref. 34. Other theoretical treatments of aspects of OPO injection seeding have been given in refs. 35 and 43 to 45.

7.5.2 Review

The first demonstration of OPO injection seeding was in 1969 by Bjorkholm and Danielmeyer[32]. This experiment amply demonstrated the potential of this approach to linewidth control. Stable single mode operation was achieved for CW injected powers at the resonant wave as low as 1μW when the cavity length was adjusted to maintain resonance at the seed signal wavelength. The details of this experiment and other subsequent work on injection-seeding are shown in Table 7.3 In general, during the 1970s, interest in linewidth control of OPOs switched to the use of cavity dispersive techniques, although the possibility of single-pass amplification of a narrowband seed signal was described in a paper by Massey and Johnson[46]. Amplification of around a factor of 10^5 was demonstrated for milliWatt inputs.

Since 1980, a substantial amount of work has been devoted to the study of external signal injection. Pulsed injection was used in the work described in refs. 33-35, Both Itskhoki[33] and Abdullin[35] showed that saturation in the achievable conversion efficiency was observed for pulsed inputs on the order of 1μJ at the resonant wave. The device demonstrated by Marunkov[34] required a minimum of only 10pJ in the OPO oscillation at the nonresonant wave to show seeding. The work of Abdullin was notable for the use of the long wavelength output of a $Ba_2NaN_5bO_{15}$ OPO as the seed source for a higher power $LiNbO_3$ OPO. Although the seed source here was not at the single mode level, it illustrated the feasibility of the master/slave oscillator

Table 7.3 : Injection seeding experiments

Reference	Seeded wave	Seeding laser	Seeding power	OPO	Seeded OPO linewidth
32 (1969)	resonant	CW Nd:YAG 1.064μ Single mode	Minimum of 1μW rising to 5mW, away from OPO peak gain	LiNbO pumped at 694.3nm	Single mode OPO output
33 (1980)	resonant	Pulsed Nd:YAG 1.064μ $\Delta\lambda = 1cm^{-1}$	Saturation in conversion efficiency for 1.5 μJ	LiNbO pumped at 632.8nm	OPO output 1cm-1
34 (1981)	nonresonant	Pulsed Dye laser 690nm $\Delta\lambda = 20nm$	10pJ to 1nJ in OPO bandwidth	LiNbO pumped at 532nm $\Delta\lambda = 2cm^{-1}$	:OPO linewidth unchanged
35 (1984)	resonant	Pulsed 532nm pumped BaNaNbO OPO 1-2 μ $\Delta\lambda = 0.5cm^{-1}$	50 to 500nJ Saturation in conversion efficiency for 0.5 μJ	LiNbO pumped at 1.064 μ $\Delta\lambda = 50cm^{-1}$	LiNbO OPO, linewidth 0.5cm-1
36 (1987)	nonresonant	CW HeNe laser 3394nm	Minimum 0.5mW	LiNbO pumped at 1.064 μ $\Delta\lambda = 2cm^{-1}$	OPO nonresonant linewidth equal to that of pump

Table 7.3 (contd.) : Injection seeding experiments

Reference	Seeded wave	Seeding laser	Seeding power	OPO	Seeded OPO linewidth
37 (1988)	resonant and nonresonant	Pulsed Single mode Nd:YAG 1.064μ and 532nm	Minimum 2.5μJ at nonresonant wave	BBO pumped at 355nm	OPO output linewidth 3GHz
38 (1991)	resonant	Pulsed single mode dye laser 562nm	less than 0.1mJ	BBO pumped at 355nm	OPO output linewidth 4GHz
39 (1991)	resonant	CW Single mode color centre laser 1.5μm	1.5μW	LiNbO pumped at 1064nm	Single mode OPO output
40 (1992)	resonant and nonresonant	CW Single mode Diode and dye lasers 650-980nm	less than 1mW	BBO pumped at 355nm	Single mode OPO output
41 (1992)	resonant	CW Single mode Diode laser 788nm	less than 0.5mW	KTP pumped at 532nm	Single mode OPO output

arrangement which our current work is aimed at. Demonstrations of pulsed seeding at the single mode level have also been reported; the work of Fan et al.[37] used the fundamental and frequency doubled outputs of a Nd:YAG laser to seed separately at the signal and idler in a BBO-OPO pumped by the third harmonic of the Nd:YAG. Single mode output was also obtained from a 355nm-pumped BBO-OPO by Haub et al.[38], who used a single frequency dye laser to seed at the resonant signal wavelength.

More recently, several further single mode OPOs[39-41] have used CW dye, colour centre and diode lasers as the seed source. In each case, seed powers of less than one mW were required. The main significance of these devices with respect to the early CW-seeded single-mode OPO demonstrated by Bjorkholm[32], was the tunability of the seed source. However, it must be noted that none of the devices mentioned have had the capability of producing narrowband seeded output across the complete OPO tuning range. This is a primary objective of our own work on broadly tunable Type 1 BBO-OPO.

7.5.3 Preliminary seeding experiments in BBO

In order to ascertain required seeding power levels, seeding of the 308nm-pumped OPO was first attempted using the 632.8nm output of a CW Helium-Neon laser. This laser was a Spectra-Physics model 124b with a linewidth of $0.5cm^{-1}$ and a maximum power output of 17mW in a 3.0mm $1/e^2$ diameter TEM_{00} beam. The OPO cavity was arranged as in Fig. 7.12, with one Brewster-angled steering plate coupling in the pump beam. The seed beam was injected through the rear mirror which had a low value of reflectivity at 633nm. The cavity was formed by the 20mm BBO crystal surrounded by two 95% reflectors over the range 500-600nm, separated by 40mm. The polarisation of the seed beam was parallel to that of the o-waves in the OPO, and the device was tuned to an idler output of 633nm (corresponding to the seeding wavelength). Evidence of seeding was observed by monitoring the OPO signal output around 600nm.

In general it could be said that evidence of amplification of the seed signal was observed through the appearance of a peak in

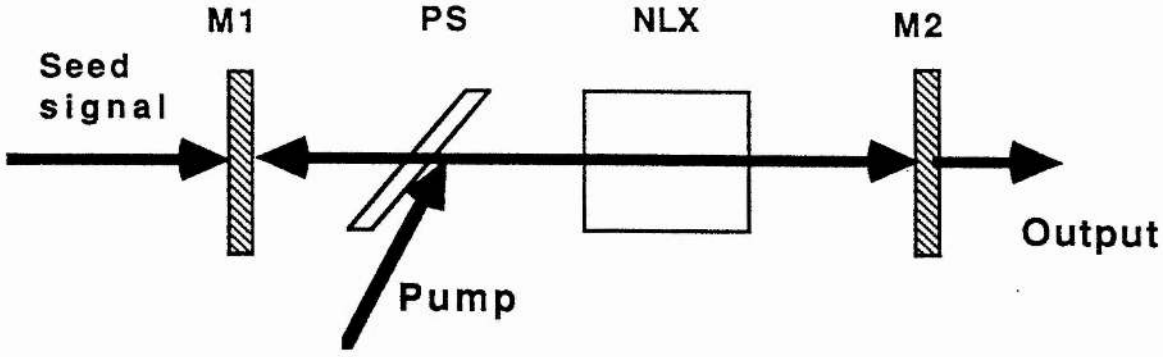

Fig. 7.12 Schematic diagram of the experimental arrangement for seeding of a BBO-OPO by a Helium Neon laser. M1 and M2 are 95% reflectors for 500-600nm, PS is a pump steering dichroic plate, NLX is a 20mm BBO crystal. The cavity length was 40mm.

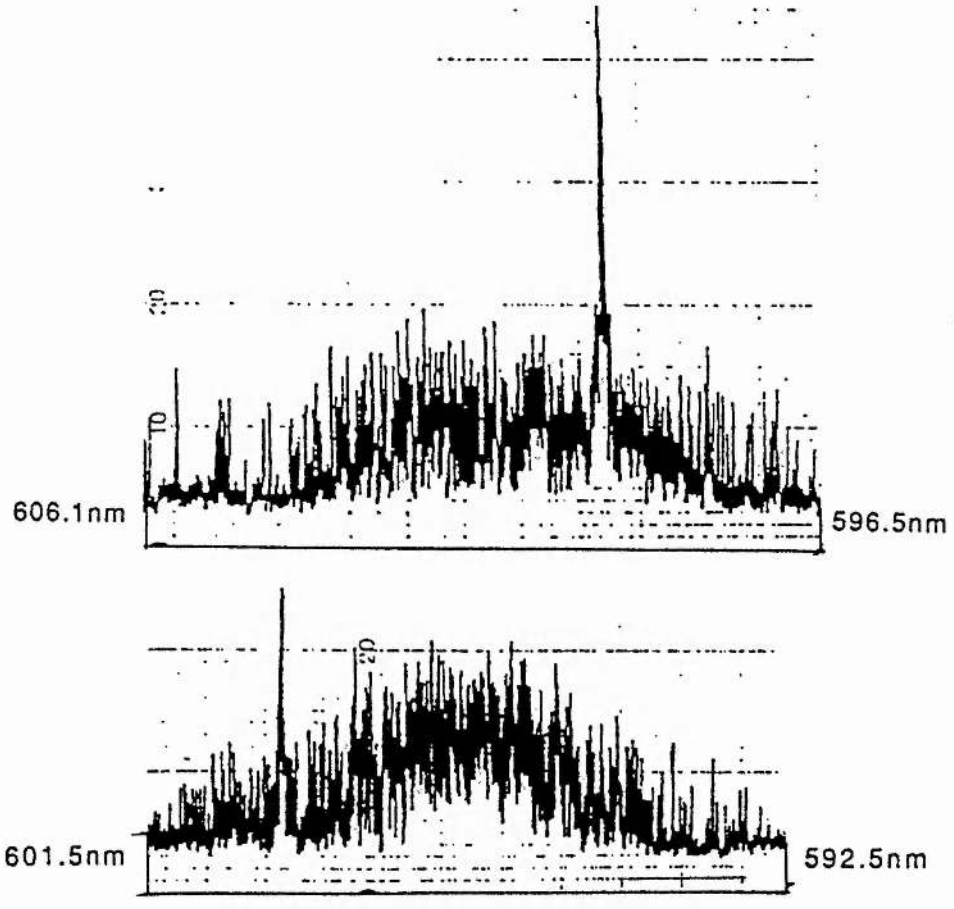

Fig. 7.13 (a) and (b) show signal wave spectra of BBO-OPO seeded by a Helium-Neon laser, for two different OPO operating wavelengths.

the signal spectra at 599.6nm, the complementary signal wavelength corresponding to 632.8nm. However, at no point did significant depletion of the original spectrum occur as a result. It was observed that the pump excess over threshold had little effect on seeding. The amplitude of the 599.6nm peak was seen to increase with its proximity to the peak of the OPO gain curve, as in figs. 7.13(a) and (b). This observation is consistent with a relatively strict tolerance of seeding under these conditions, to frequency detuning. It has been shown in ref. 45 that successful injection cannot be maintained for values of $\eta < 0.6$, where η is the ratio of the coupling constants of the injected mode and the mode having highest gain., i.e.

$$\eta = \frac{\sin(\Delta k\ell/2)/(\Delta k\ell/2)_{\text{injected mode}}}{\sin(\Delta k\ell/2)/(\Delta k\ell/2)_{\text{max. gain mode}}}$$

In the region near degeneracy, where the OPO tuning rate is extremely rapid, it was in practice very difficult to tune the OPO accurately to coincide with the HeNe output, and as a result "successful" injection seeding was not observed.

In the light of the limited success of CW injection seeding of the OPO it was decided to attempt seeding with a pulsed source. The pulsed seeding source used was the 670nm idler output from a noncritically phase-matched urea OPO pumped by a fraction of the power from the 308nm excimer. The 90mJ excimer output was split in the ratio 90:10%, such that the 10% was used to pump the urea device, as shown in fig. 7.14. The two excimer beams were compressed in separate beam compressors by factors of 7.5 and 5, to pump the urea and BBO devices, respectively. The pump beam for the BBO-OPO was delayed by the equivalent of 4ns with respect to that for the urea OPO, using a Z-fold delay line (Successful seeding was observed for delay times around this value, with pump pulse lengths similar to our own, in refs. 34 and 35). The urea OPO was pumped at a level around 6 times the oscillation threshold, and pulses of around 0.4mJ at 670nm were injected through an RG610 filter (to remove the 570nm component) into the simple linear cavity BBO-OPO. (This method was an alternative to an arrangement whereby the unconverted

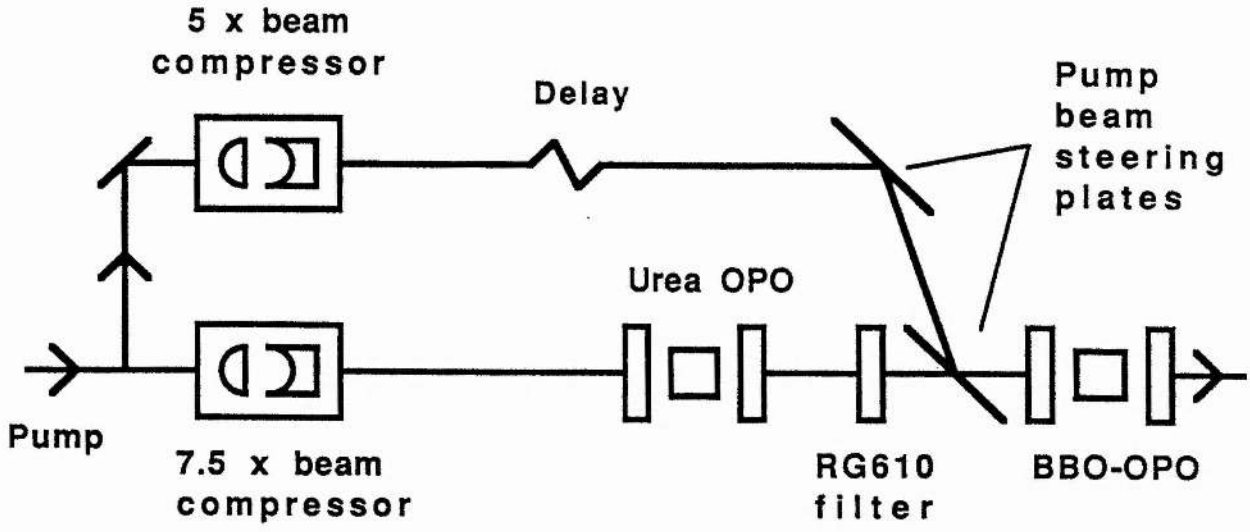

Fig. 7.14 Schematic diagram of the experimental arrangement for seeding of a BBO-OPO by the idler wave output from a 25mm NCPM urea OPO. Cavity lengths for the urea and BBO OPOs were 30mm and 25mm respectively.

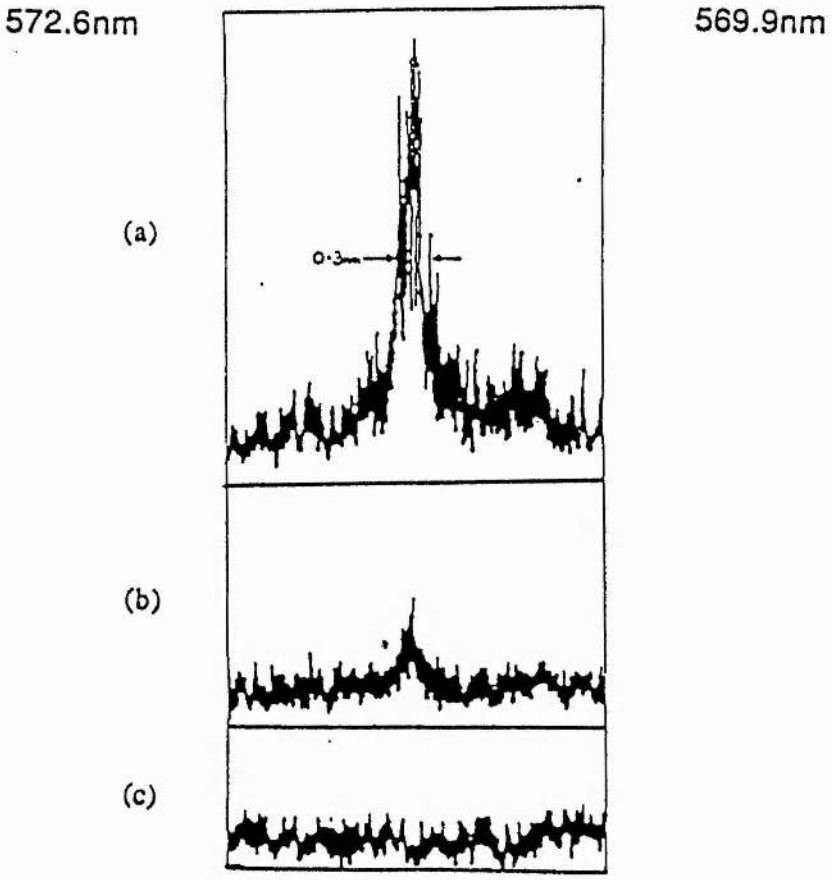

Fig. 7.15 Signal wave spectra for (a) BBO-OPO seeded by a urea OPO, (b) Urea OPO and (c) Unseeded BBO-OPO, showing that the pump intensity was below the unseeded oscillation threshold.

remainder of the pump beam from the primary OPO was used to pump the secondary OPO. This seemed potentially attractive since the pump light was used as efficiently as possible. However, this method was flawed by the need to propagate the compressed excimer beam to provide sufficient delay, since, as has been mentioned before, the beam had a tendency to break up on propagation).

It was found that pulsed seeding produced much more convincing results than CW injection. It was seen that that output was observed at 570nm from the BBO-OPO, when pumped at a level of $0.1Jcm^{-2}$, which was below the unseeded oscillation threshold. As shown in figs. 7.15 the spectrum of the 570nm output from the BBO-OPO had the same 0.3nm bandwidth as that from the urea OPO, and even under conditions of higher pump input to the BBO-OPO, no background "pedestal" was observed in the output spectrum. Although accurate tuning of the OPO was considerably easier than at 600nm, no particular steps were taken to ensure exact matching of the centre of the gain curve to the seed signal. Furthermore, no attempt was made to optimise the delay time between the pump pulses. Results achieved on this experiment were limited by the premature demise of the urea crystal through multishot damage. However, it was considered that the ease with which seeding was achieved was an indication that the use of a two-stage seeded OPO tunable throughout the range of the BBO-OPO was highly feasible.

1 L.B. Kreuzer, Appl. Phys. Lett. **15**, p263 (1969).
2 J. Pinard and J.F. Young, Opt. Comm. **4**, p425 (1972).
3 A. Hordvik and P.B. Sackett, Appl. Opt. **13**, p1060 (1974).
4 G.P. Arnold and R.G. Wenzel, Appl. Opt. **16**, p.809 (1977).
5 G.P. Arnold and R.G. Wenzel, Infrared lasers: Topical meeting on infrared lasers, Los Angeles, CA, USA, 3-5 Dec 1980 (Opt. Soc. Am. 1980) p. w-6/1-4.
6 R.L. Byer, R.N. Fleming and R.L. Herbst, "A broadly tunable IR source" in Proc. Second Int. Conf. on Laser Spectroscopy, Megeve, France, 1975, p. 206. Publ. Springer, Berlin (1975).
7 S.J. Brosnan and R.L. Byer, IEEE J. Quant. Elect. **QE-15**, p.415 (1979).
8 D. Andreou, Opt. Comm. **27**, p171 (1978).
9 D.W. Michael, K. Kolenbrander, J.S. Lisy, Rev. Sci. Inst. **57**, p1210 (1986).
10 W.R. Bosenberg, W.S. Pelouch and C.L. Tang, Appl. Phys. Lett. **55**, p1952 (1989).
11 L.B. Kreuzer, Proc. of the Joint Conf. on Lasers and Optoelectronics (Univ. of Southampton, I.E.R.E., London), p53 (1969).
12 D.A. Kleinman and P.P. Kisliuk, Bell System Tech. Journal **41**, p453 (1962).
13 H. Kogelnik and C.K.N. Patel, Proc. I.R.E. (Corresp.) **50**, p2365 (1966).
14 I. Shoshan, N.N. Danon and U.P. Oppenheim, J. Appl. Phys. **48**, p4495 (1977).
15 M.G. Littman and H.J. Metcalf, Appl. Opt. **17**, p2224 (1978).
16 Y.H. Meyer and M.N. Nenchev, Opt. Lett. **6**, p119 (1981).
17 B.H. Soffer and B.B. MacFarland, Appl. Phys. Lett. **10**, p266 (1967).
18 M. Hercher, Appl. Opt. **8**, p1103 (1969).
19 H.G. Danielmeyer, I.E.E.E. J. Quant. Elect. **QE-6**, p101 (1970).
20 J.K. Watts, Appl. Opt. **7**, p1621 (1968).
21 D.C. Hanna et al., Opto-electronics **3**, p163 (1971).
22 A.G. Fox, U.S. Patent no 3504 299.
23 P.W. Smith, I.E.E.E. J. Quant . Elect. **QE-1**, p343 (1965).
24 e.g. V.P. Belyaev et al., I.E.E.E. J. Quant. Elect. QE-5, p589 (1969).
25 G. Robertson, Ph. D. Thesis, University of St. Andrews (1993).
26 P. W. Smith, Proc. IEEE **60** no. 4 (1972).

27 P. Schafer 'Dye Lasers' , Springer-Verlag Berlin (1990).
28 W. Leeb, Appl. Phys. **6**, p267 (1975).
29 J.M. Yarborough and J. Hobart, Conf. Las. Eng. Appl. Wash. D.C. postd. paper (1973).
30 R.L. Byer, Chapter 9, "Optical Parametric Oscillators", in "Quantum Electronics: a treatise". Edited by H. Rabin and C. L. Tang (Academic, New York) Vol. 1, Pt B, pp 587-702 (1973).
31 R. G. Smith, "Lasers", Vol. 4. Edited by A.K. Levine and A. J. De Maria. Marcel Dekker, New York (1976).
32 J.E. Bjorkholm and H.G. Danielmeyer, App. Phys. Lett. **15**, p171 (1969).
33 I.Y. Itskhoki and S.L. Seregin, Sov. J. Quant. Elect. **10**, p515 (1980).
34 A.G. Marunkov, V.I. Pryalkin, and A.I. Kholodnykh, Sov. J. Quant. Elect. **11**, p869 (1981).
35 U.A. Abdullin et al., Sov. J. Quant. Elect. **14**, p538 (1984).
36 V.L. Boichenko, M.M. Novikov and A.I. Kholodnykh, Sov. J. Quant. Elect. **17**, p392 (1987).
37 Y.X. Fan, R.C. Eckardt, R.L. Byer, J. Nolting and R. Wallenstein, Appl. Phys. Lett. **53**, p2014 (1988).
38 J.G. Haub, M.J. Johnson, B.J. Orr and R. Wallenstein, Appl. Phys. Lett. **58**, p1718 (1991).
39 D.C. Hovde, J.H. Timmermans, G. Scoles and K.K. Lehmann, Opt. Comm. **86**, p294 (1991).
40 A. Fix, T. Schroder, K.-J. Boller and R. Wallenstein, in Technical digest, Conference on Lasers and Electro-optics (Opt. Soc. Am., Washington D. C. 1992) Paper CTuR3.
41 C.E. Hamilton and W.R. Bosenberg, in Tech. dig., Conf. on Lasers and Electro-optics (Opt. Soc. Am., Washington D.C. 1992) Paper CWQ3.
42 D.A. Kleinmann, Phys. Rev. **174**, p1027 (1968).
43 N.K. Dutta, J. Appl. Phys., **51**, p5629 (1980).
44 G.P. Dzhotyan and A.V. Mesropyan, Sov. J. Quant. Elect. **20**, p1450 (1991).
45 E.S. Cassedy and M. Jain, I.E.E.E. J. Quant. Elect. **QE-15**, p1290 (1979).
46 G.A. Massey, J.C. Johnson and R.A. Elliot, I.E.E.E. J. Quant. Elect. **QE-12**, p1243 (1976).

Chapter 8
Noncollinear Phase-matching

8.0 Introduction

As shown in chapters 5 and 6, efficient operation of a parametric oscillator based on BBO is strongly dependent on the use of pump beams of a dimension and pulse energy great enough to reduce the detrimental effects of birefringent walk-off of the pump from the signal and idler beams. The XeCl excimer laser used in this work was capable of providing pulse energies sufficient to maintain an energy density well above OPO threshold in beams of up to 7mm dimension. At this level, the incomplete beam overlap caused by lateral beam walkoff on the order of 2mm over the nonlinear crystal length has relatively little effect on OPO efficiency.

Increased beam overlap using pump beams of large cross section also facilitates efficient operation of the OPO in a noncollinearly phase-matched configuration. Optimal beam interaction in an OPO is generally achieved through collinear phase-matching of the pump, signal and idler wavevectors as in figure 8.1(a). However parametric interaction can occur for any trio of wavevector directions such that the energy conservation and phase-matching conditions (2.20) and (2.21) are satisfied. Noncollinear phase-matching has been utilised in various nonlinear optical processes in order to match the Poynting vector directions of interacting beams[1], and in OPOs, studies have pointed out advantages in terms of the avoidance of undesirable idler resonance[2], and the possibility of tuning by altering the orientation of the optical cavity or the pump beam rather than the crystal angle[3]. In our own work, the use of large beam waists and high pulse energies produces the necessary beam overlap to allow noncollinear operation of the angle-tuned OPO in two distinct configurations. These two regimes of operation, which will be discussed separately in the following two sections, occur when the pump beam propagates at internal angles θ to the crystal optic axis, either below or above the value θ_{deg}, at which the degenerate

wavelength is generated. They are referred to here as off-axis ($\theta < \theta_{deg}$), and on-axis pumping ($\theta > \theta_{deg}$), respectively, for reasons which will become apparent.

8.1 Off-axis pumping ($\theta < \theta_{deg}$)

Noncollinear phase-matching may be achieved in BBO at internal angles between the pump beam and optic axis, at which collinear phase-matching is the conventional mode of interaction. Fig. 8.2 shows a photograph of the typical output observed. The configuration of the OPO for these observations is shown in figure 8.3. In this case, as shown in figure 8.1(b), the pump beam direction is rotated around a vertical axis, orthogonal to the crystal angle-tuning rotation axis. Phase-matching is maintained by a signal wave resonant on the OPO cavity axis, and an off-axis single-pass idler wave, whose wavelengths and directions adjust to allow both (2.20) and (2.21) to be satisfied. Considerable frequency tuning was achieved through rotation of the pump beam by a small angle in this plane. Simple application of the cosine rule to the vector triangle in figure 8.1(b) produces the following expression for the internal angle δ between the signal and pump wavevectors:

$$\cos \delta = (k_p^2 + k_s^2 - k_i^2)/ 2k_pk_s \qquad (8.1)$$

The further constraints which determine an operating wavelength, are the energy conservation condition (2.20) and the defined signal wave direction for resonance parallel to the cavity axis.

This mode of operation was studied under the following conditions. The pump laser used was the Lambda Physik EMG 150 excimer laser. The beam was compressed by a factor of 5 to produce a 1.5 x 3.9mm collimated pump beam. Throughout this experiment, the OPO was pumped at a constant level of $0.73 Jcm^{-2}$. The OPO was based around the 12mm interaction length crystal of BBO. This was surrounded by one high reflector for 400-700nm

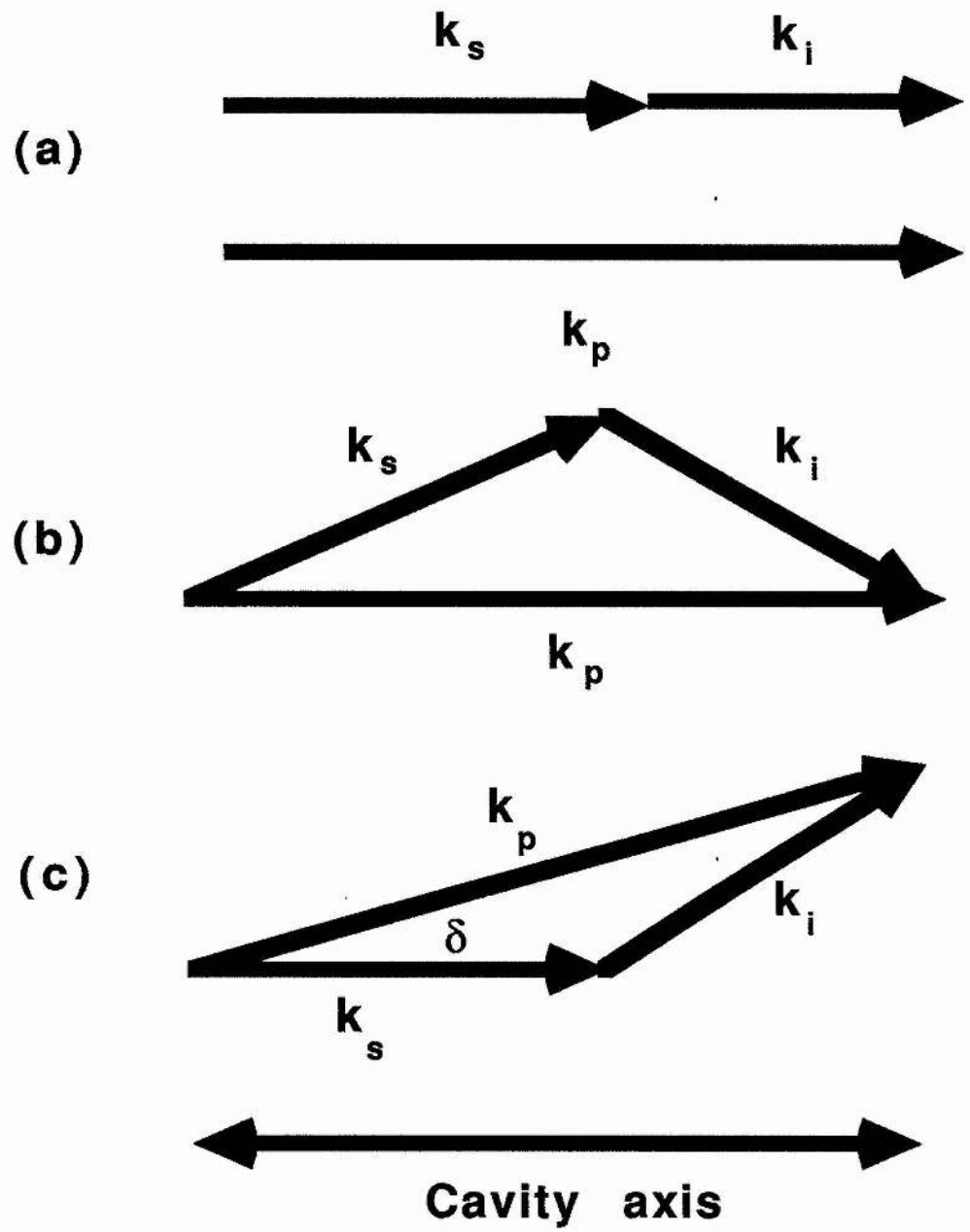

Fig. 8.1 : Arrangement of wavevectors in a singly resonant OPO cavity for (a) collinear phase-matching, (b) on-axis pumped noncollinear phase-matching and (c) off-axis pumped noncollinear phase-matching.

and one 95% reflector for 500-600nm, separated by a distance of 62mm to form a singly resonant cavity at the signal wave. The pump beam was injected into the cavity as in fig. 8.3 via a rotatable Brewster-angled dichroic plate adjacent to the nonlinear crystal, which reflected the pump wave and transmitted the orthogonally polarised signal wave. Here, as before, the pump

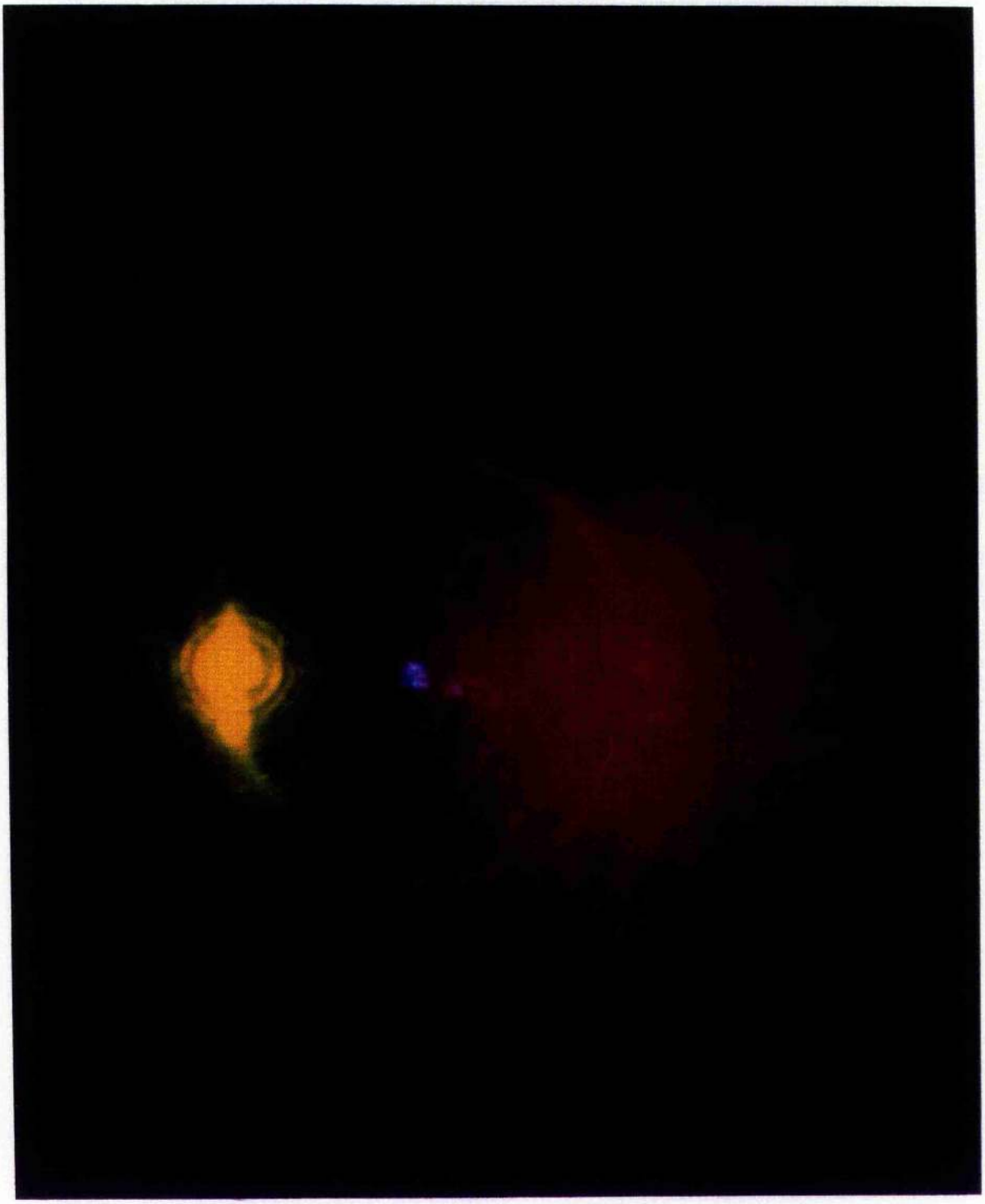

Fig. 8.2 Photograph of the output observed from an off-axis pumped noncollinearly phase-matched BBO-OPO.

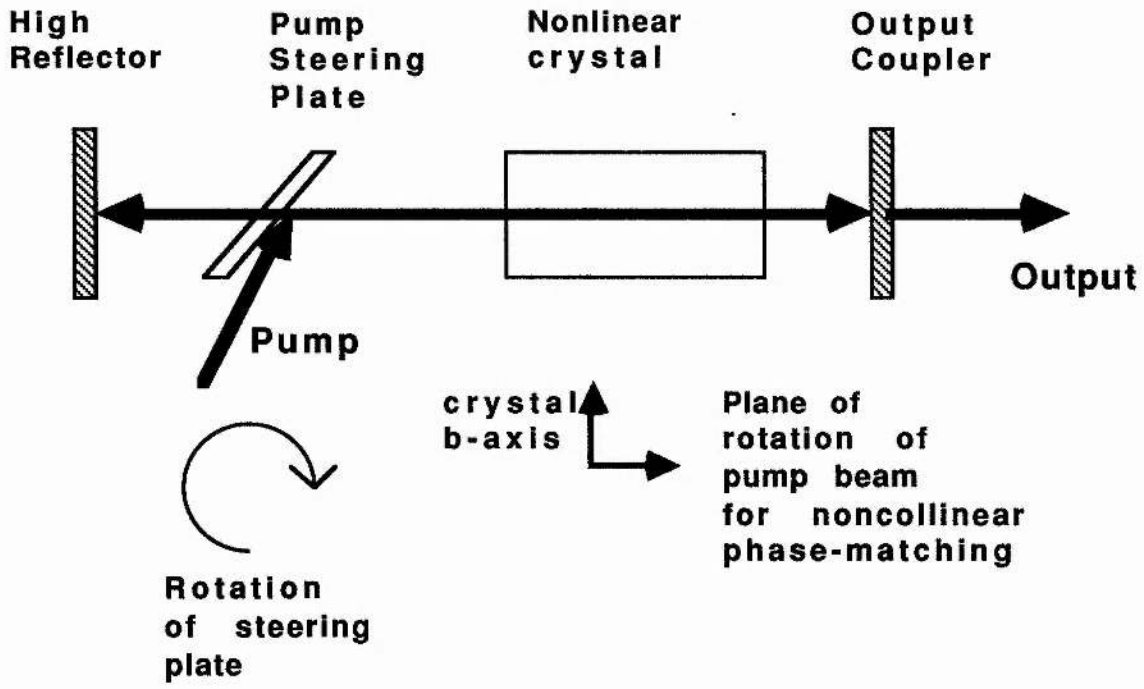

Fig. 8.3 : Configuration of BBO-OPO used during observations of off-axis pumped noncollinear phase-matching.

wave was polarised in the plane of the surface normal and the optic axis. Figure 8.4 shows the measured external angles of the idler and pump beams with respect to the cavity axis as a function of the measured resonant signal wave. These results were obtained by altering the pump beam direction from that corresponding to a collinearly phase-matched signal wavelength of 587nm. The idler angle was measured from the distance between the signal and idler spots on a screen a distance of 1m from the OPO, while the pump angle was measured from the Brewster plate rotation stage. Theoretical calculations also shown in the figure show excellent agreement with experiment. Figure 8.5 shows that the rate of tuning, as with tuning of the crystal in the conventional plane, occurs most rapidly when altering the pump beam angle from a collinear phase-matching wavelength near degeneracy. It can be seen that at this pump intensity, oscillation is observed only to a pump beam angle of 4.5°, at which point the pump beam can be calculated to have walked a lateral distance of1mm out of the signal beam, as compared with a pump beam waist in this dimension of 1.5mm. This decreased beam

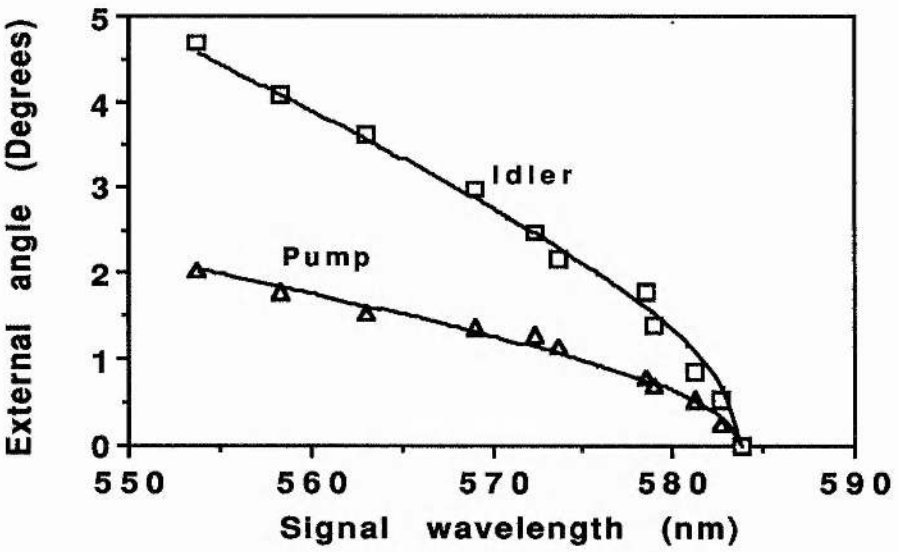

Fig. 8.4 : External angle between the cavity axis and the pump and idler beams as a function of the resulting resonant signal wavelength, for off-axis pumped noncollinear phase-matching at an initial collinear phase-match signal wavelength of 587nm. The solid curves represent theoretical calculations.

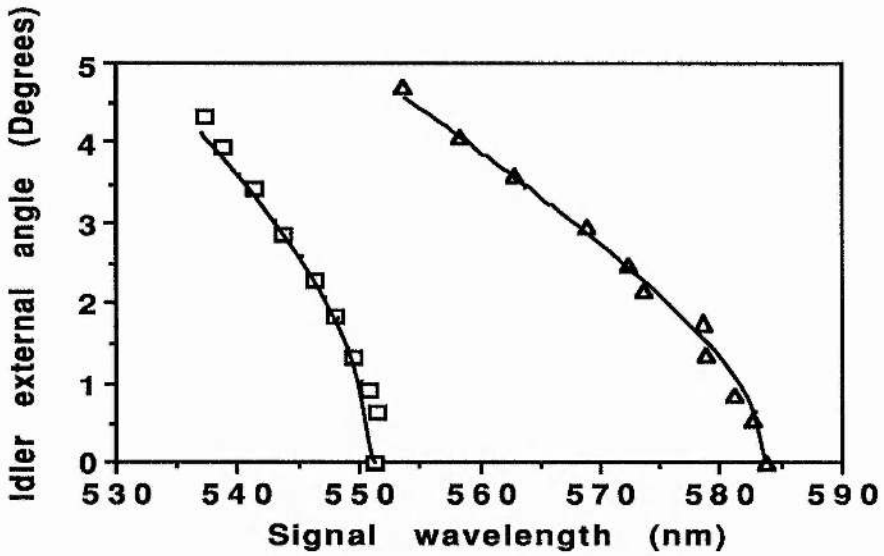

Fig. 8.5 : External angle between the nonresonant idler and the cavity axis as a function of the resonant signal wavelength, for two different initial collinear phase-match points.The solid curves represent theoretical calculations.

overlap is reflected in the fact that the lateral dimension of the generated signal and idler beams is seen to decrease progressively as the pump beam-cavity axis angle is increased. Figure 8.6 shows the corresponding increase in threshold with increasing off-axis angle of the pump beam, for an on-axis signal wavelength of 587nm. It can be seen that signal tuning of around 30nm can be achieved at a cost of around a factor of two threshold increase.

8.2 On-axis pumping ($\theta > \theta_{deg}$)

The second mode of noncollinear interaction observed in the OPO occurs on rotation of the nonlinear crystal in the angle-tuning plane beyond the degenerate point, with the pump beam propagating parallel to the cavity axis. For angles beyond that corresponding to the degenerate wavelength, collinear phase-matching is no longer possible. In this configuration, two distinct pairs of wavelengths were observed simultaneously, such that the output was in the form of complete rings (see figure 8.8) concentric to the pump beam, with intensity maxima at the vertical extremes. Their radii were seen to increase as the crystal is tuned further past degeneracy until a point was reached when oscillation threshold was no longer attained. Figure 8.1(c) illustrates the distinction between the arrangement of momentum vectors with respect to the cavity axis for the present case, and that of off-axis pumping. Here it is the wave-vector of the pump rather than the resonant signal which remains parallel to the cavity axis. For a Type 1 (e -o + o) process, the symmetry of the refractive indices around the pump wave-vector direction allows phase-matching to occur in the form of a cone around the pump beam, as depicted in fig. 8.9. We can use the same expression (8.1) for the internal angle between pump and signal wave δ for any particular signal-idler pair, as that for off axis pumping. The corresponding pump-signal external angle δ_{ext} is then found from the expression:

$$\delta_{ext} = \sin^{-1}\left(n_s \sin\left(\theta + /- \delta - 35.5^{o}\right)\right) - \sin^{-1}\left(n_p \sin\left(\theta - 35.5^{o}\right)\right) \qquad (8.2)$$

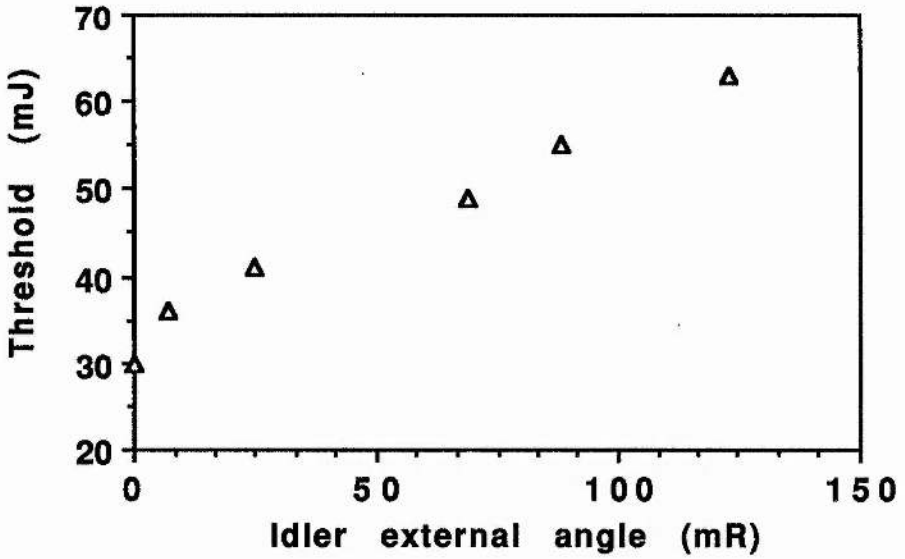

Fig. 8.6 : Oscillation threshold as a function of external angle between the nonresonant idler and the cavity axis for off-axis pumped noncollinear phase-matching at an initial collinear phase-match signal wavelength of 587nm.

where n_s and n_p are the signal and pump refractive indices, and the constant (35.5°) is the internal angle between the pump and the crystal optic axis for normal incidence.

This phenomenon was observed in an OPO based on the 20mm interaction length BBO crystal. The cavity arrangement was as in fig. 4.5(a), with the crystal surrounded by two plane 95% reflectors for the range 500-600nm, separated by 23mm. The OPO output was studied separately for beam compression ratios of 3.75 and 5, to produce collimated beams of dimension 2.1 x 5.1mm and 1.5 x 3.9mm, with the major dimension in the walkoff plane. The BBO crystal was cut with its normal incidence propagation direction at 35.5° to the optic axis. The OPO threshold at a signal wavelength of 600nm was found to be 0.15Jcm^{-2}, and the following results were obtained at a pump fluence 4 times this value. Below the degeneracy angle (θ = 39.14°) the OPO operates as a collinearly phase-matched singly resonant oscillator.

However, if the crystal orientation is altered such that the pump beam propagates at angles $\theta > \theta_{deg}$, the refractive indices no longer allow conditions (2.20) and (2.21) to be satisfied for collinear wavevectors, i.e.

$$n_e(\theta,\omega_p) > n_o(\omega_s) \geq n_o(\omega_i) \qquad (8.3)$$

for all pairs (ω_s, ω_i) satisfying (8.1), where n_e and n_o are the refractive indices experienced by the extraordinary and ordinary

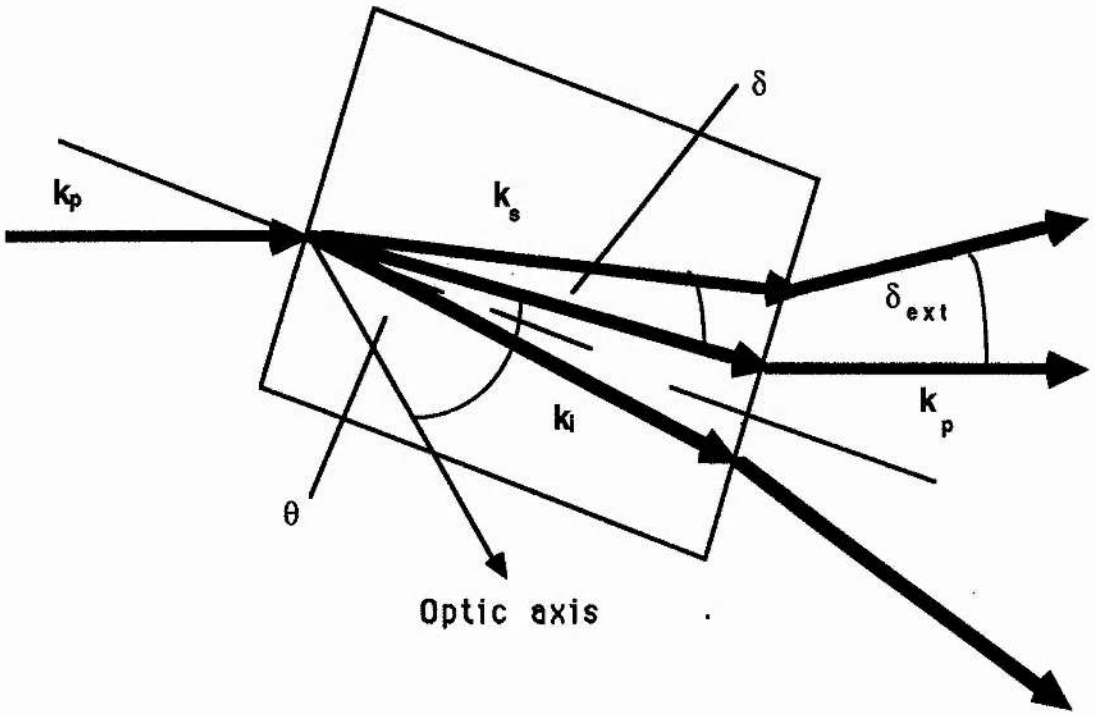

Fig.8.7 Pump, signal and idler wavevector directions in the nonlinear crystal in an on-axis pumped noncollinear phase-matching configuration.

polarisations respectively. In this regime it has been observed that oscillation occurs through noncollinear phase-matching, such that the resonant wave direction is not coincident with that of the cavity axis, as shown in fig. 8.1(b). The wavevector directions in the crystal, under these conditions, are illustrated in fig. 8.7. The wavelengths of the resultant ring patterns were measured for each of the two beam dimensions, and it can be seen in fig. 8.10 that each spot size produces noncollinearly phase-matched output

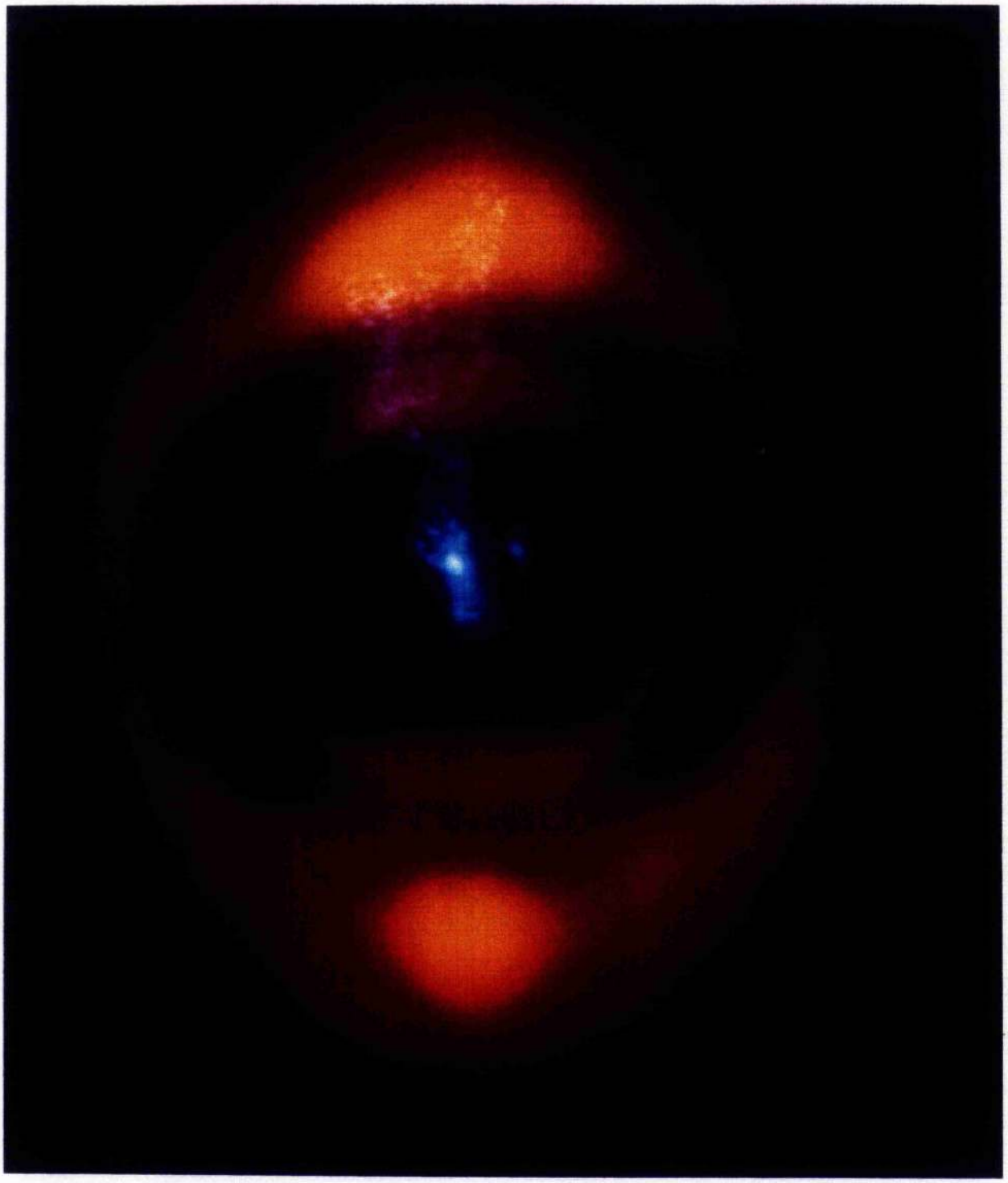

Fig. 8.8 : Photograph of the ring pattern observed at a distance of 1m from the OPO. Centre spot is remaining unconverted pump, while inner ring is of degenerate 616nm wavelength, and outer ring consists of components around 580nm and 650nm.

of approximately constant wavelength (the bandwidth of the output is in each case around 10nm). However, while for both dimensions the inner ring is of the degenerate wavelength at 616nm, the mean pairs of wavelengths for the outer ring are 575.0nm and 655.7nm for the 5mm beam, and 580.8nm and 650.8nm for the 4mm beam. In each case, the nondegenerate signal and idler output was observed with approximately equal ring diameter. This is as predicted from the phase-matching condition (8.1) for these wavelength pairs.

The measured external angles between the pump beam and the signal and idler beams are shown in fig. 8.11, along with theoretical calculations for signal wavelengths of 575nm, 581nm and 616nm which correspond approximately to the experimental values. A good level of agreement with theory is seen.

In the light of the continuous range of wavelengths phase-matchable in this noncollinear configuration, where we have no cavity resonance constraint, it is necessary to explain the wavelength selection mechanism of the OPO. Examination of the reflectivity profile of the mirrors indicates that

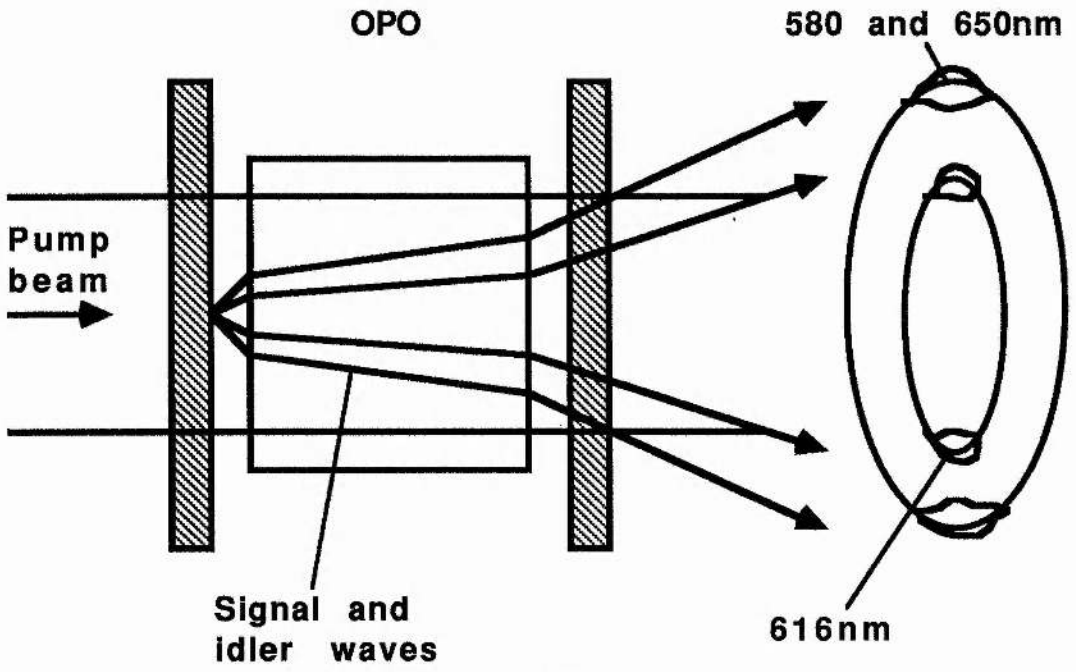

Fig. 8.9 Arrangement of signal, idler and pump rays with respect to the ring pattern output from an on-axis pumped noncollinearly phase-matched BBO-OPO.

the 580nm component is the resonant wavelength in the outer ring, while the inner ring is able, even at the low value of reflectivity for 616nm (18%), to operate as a doubly resonant oscillator. We believe that the OPO selects a resonant wavelength around 580nm through the occurrence of a local minimum in the oscillation threshold for these particular resonator mirrors. The cavity resonance condition is unimportant since the OPO bandwidth is such that at any angle to the cavity axis many off-axis cavity resonances are covered. Fig. 8.12 shows theoretical calculations of collinearly phase-matched OPO threshold over the mirror reflectivity range, made using expression (5.6), based on the Brosnan and Byer model (Ref. 4). We believe the threshold for noncollinear operation is influenced both by the cavity reflectivity, and by the number of cavity double passes during which the signal can experience parametric gain while still within the waist of the pump beam, as in fig. 8.13. For example, for the OPO cavity used in these experiments, a signal ray propagating at an external angle of 40mR to the pump takes around 5 double passes to walk from the centre to the edge of the 5mm pump waist in the vertical dimension, as opposed to 2, horizontally. Hence the occurrence of intensity maxima at the vertical extremes of the rings is due to the greater pump beam vertical dimension. Figure 8.12 also shows the value of δ for which the signal wavelength is phase-matched, at an internal angle $\theta = 39.15^{o}$ (just beyond degeneracy). It has been observed that the balance of the colour composition of the upper and lower extremes of the outer ring is strongly influenced by cavity alignment relative to the pump beam direction. Equal intensities of the 580nm and 650nm components are seen in both extremes when the cavity is aligned perpendicular to the pump beam, while rotation of the cavity around a horizontal axis normal to the propagation direction of the pump means that phase-matching is favoured where the direction of the resonant 580nm component is closer to the cavity axis, and thus one extreme becomes largely yellow and the other largely red. It is presumed that the thresholds for the doubly and singly resonant processes are equivalent, allowing simultaneous occurrence of both processes. Meanwhile, the observation of differing noncollinear wavelengths at different spot-sizes can be

explained by the need for compromise between the number of cavity double-passes and the cavity reflectivity at a particular phase-matched wavelength. The angular limit on phase-matching in this case as for predegenerate noncollinear phase-matching, is clearly determined by the reducing beam interaction with increasing cone angle.

7.3 Summary

In summary, we have observed simultaneous doubly and singly resonant noncollinearly phase-matched parametric oscillation in BBO, beyond the degeneracy point of the Type 1 tuning curve. We believe this to be the first recorded observation of this phenomenon. We have also quantified the frequency

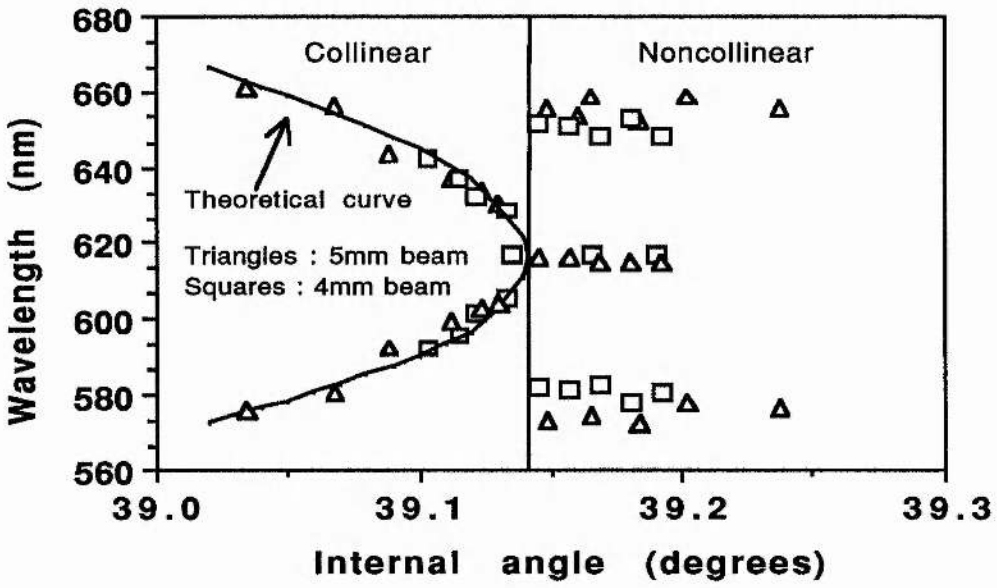

Fig. 8.10 : OPO output wavelengths versus internal angle between pump beam direction and optic axis, around degeneracy. The solid curve represents the theoretical tuning curve calculated from Sellmeier equations given in Appendix B. The two sets of data shown beyond the degenerate point represent output wavelengths for pump beam waists of 4mm and 5mm.

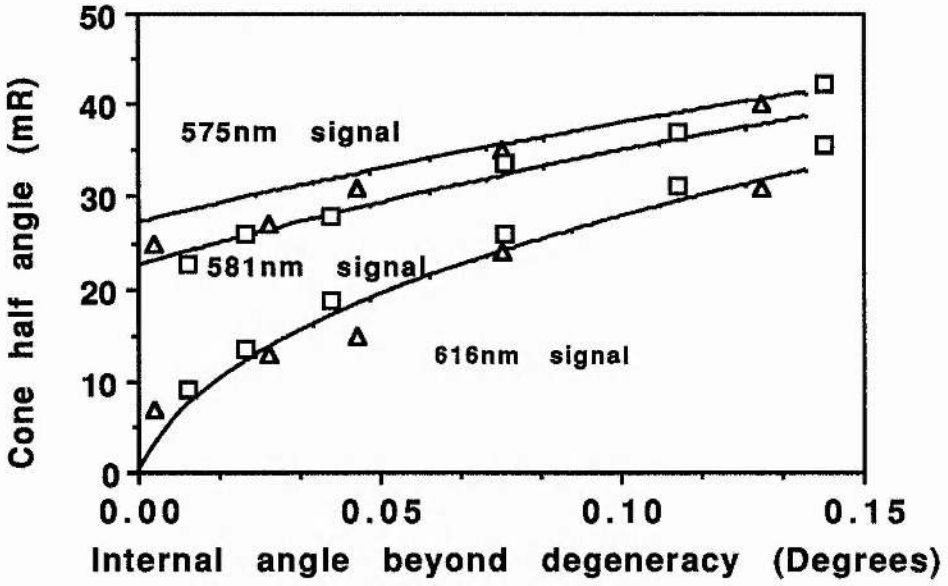

Fig. 8.11 : External angles δ_{ext} between signal/idler wavevectors, and pump wavevector, as a function of the internal angle beyond the degenerate point (θ = 39.14^o). Solid curves represent calculated theoretical values for approximate mean signal wavelength values of 575nm, 581nm and 616nm. The data is for beam sizes as in fig. 8.10.

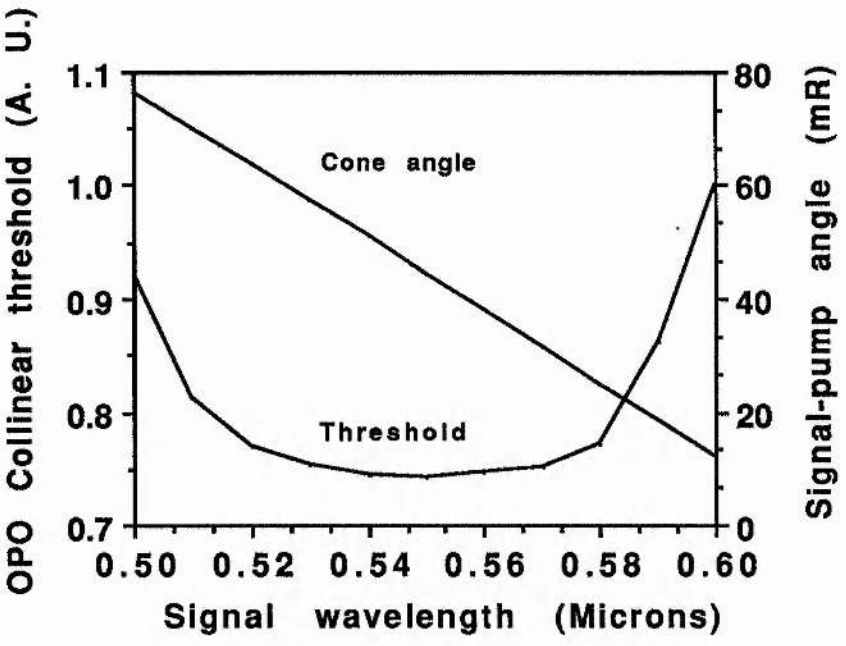

Fig. 8.12 : Theoretical values of collinearly phase-matched OPO threshold calculated using reflectivities of the cavity mirrors used. Superimposed on this are values of internal angle between pump beam direction and optic axis δ required to produce noncollinearly phase-matched parametric interaction, versus signal wavelength for θ = 39.15^o.

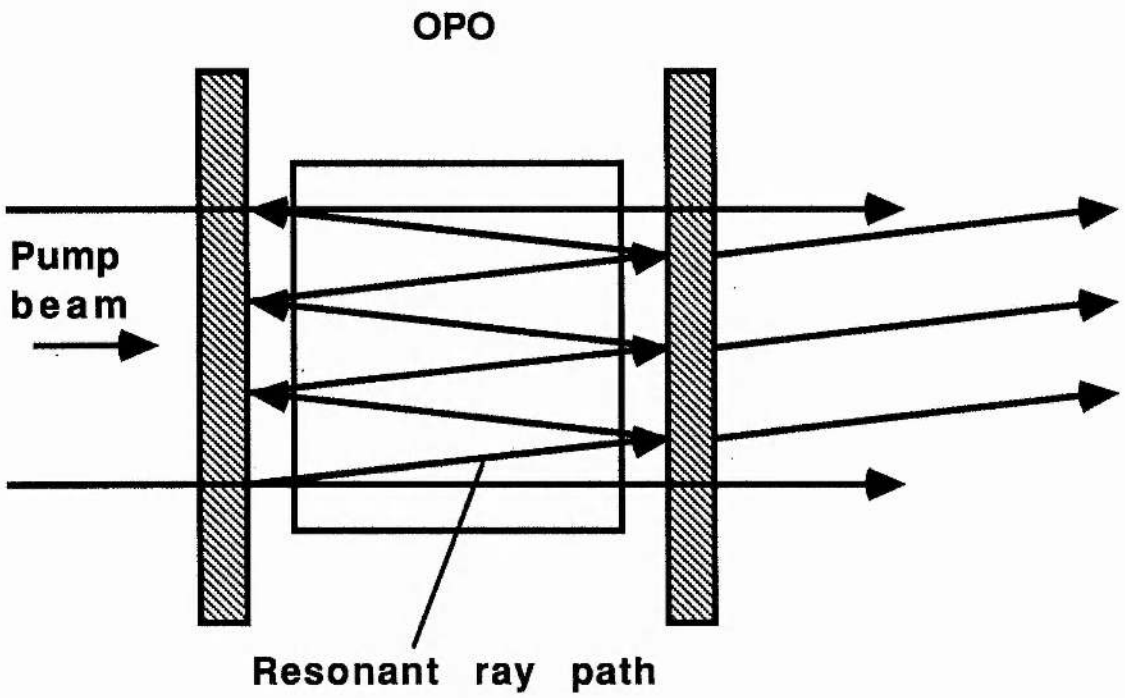

Fig. 8.13 Resonant ray path in an on-axis pumped noncollinearly phase-matched BBO-OPO.

tuning and associated threshold increase of predegenerate noncollinear phase-matching. These processes are enhanced through the use of large pump beam waists and energies, which are properties important in overcoming the problems of angular acceptance and walk-off in highly birefringent materials such as BBO. The need for production of crystals of larger aperture than currently available, in order to increase the efficiency of parametric processes, is emphasised.

References

1 H. Gerlach, Opt. Comm. **12**, p405 (1974).

2 D.C. Hanna, B. Luther-Davies and R.C. Smith, App. Phys. Lett. **22**, p440 (1973).

3 J. Falk and J. E. Murray, App. Phys. Lett. **14**, p245 (1969).

4 S. J. Brosnan and R. L. Byer, IEEE J. Quant. Elect. **QE-15**, p415 (1979).

Chapter 9
General conclusions and future work

This work describes characterisation of optical parametric oscillators for the generation of tunable radiation ranging from the ultraviolet to the near infrared, based on the materials Urea and β–Barium Borate and these devices were pumped by the 308nm output from an injection-seeded Xenon Chloride excimer laser, providing pulses of up to 150mJ in energy. Further studies of noncollinear phase-matching and linewidth control in the Barium Borate OPO are also reported.

Calculations shown in chapter 3, of figure of merit, pump bandwidth and angular acceptance limits for 308nm pumping, have been used to illustrate the potential advantages of Urea and BBO over established UV-transmitting nonlinear materials. These figures also highlight the comparative utility of the new material, Lithium Borate, for efficient ultraviolet generation. The angular acceptance calculations predict much greater tolerance to pump beam divergence in Type 2 phase-matched Urea OPOs than in Type 1 critically phase matched BBO OPOs. The predicted pump bandwidth requirements for the UV-transmitting materials considered show that the linewidth attainable from an injection-seeded excimer laser renders it suitable for use as a pump source for OPOs based on any of these materials.

Studies were made of the variation of the oscillation threshold pump energy fluence in Type 2 phase-matched Urea and Type 1 phase-matched BBO devices. The experimental values were compared with predictions made using the Brosnan and Byer expression, adapted to take into account the non-Gaussian nature of the pump beam. Variation of threshold with parameters such as cavity length, reflectivity etc., was satisfactorily predicted by the Brosnan and Byer model, assuming rather larger values of nonlinear coefficient than those currently accepted. It was found that the Barium Borate device could be an efficient energy converter only if relatively energetic pump pulses were available. A minimum energy of 5mJ was required for the device to reach threshold, and considerable increase in threshold energy fluence

was observed for pump beam waists below 2mm in the walkoff plane. The noncritically phase-matched Urea OPO, by contrast, was able to operate with pump energies of as little as 0.6mJ. However, threshold energy fluences were also seen to increase in this device for high beam compressions. It was considered that this was a result of difficulty in maintaining beam quality for tight focussing of the excimer beam.

Extremely high conversion efficiencies were obtained from both these OPOs. Maximum pump depletions of 64% and 72% were observed in BBO and urea respectively. High efficiencies were maintained throughout the tuning range of the BBO-OPO, while, with the lower pump pulse energies available from the original pump laser, the urea efficiency declined as it was tuned away from the noncritical condition. The degraded performance in terms of threshold increase resulting from the use of tightly focussed pump beams was also reflected in lower saturated conversion efficiencies under these conditions. It was also found that the external conversion efficiencies were restricted by the considerable Fresnel, absorption and scattering losses in the cavity.

Observations of noncollinearly phase-matched oscillation of the BBO-OPO have revealed unexpected modes of operation, and alternative tuning methods for the device. Tuning of tens of nanometres was observed by altering the pump beam direction independent of the OPO cavity, and relatively small associated threshold increase was observed. The first reported observation of operation of a Type 1 OPO at angles beyond the degenerate wavelength point was made. Output was in the form of two concentric ring patterns, reflecting simultaneous singly and doubly resonant operation.

Line-narrowing of the BBO-OPO was achieved through the use of intracavity Fabry-Perot etalons and a Littrow-mounted diffraction grating. Single longitudinal mode oscillation could be achieved over the majority of the tuning range, using a combination of two etalons, and an increase in threshold of less than 50% was observed for small etalon tilt angles. However, it was found that tuning using this method was very restricted due to higher-than-predicted thick etalon reflection losses at sizeable

tilt angles. It was thought that this was due to insufficient etalon flatness. We believe that future developments of the line-narrowed BBO-OPO may utilise air-spaced etalons operated close to on-axis and tuned piezo-electrically or by pressure variation, or better quality solid etalons. A considerable body of work remains to be done on this system in terms of investigation of its frequency stability and the practicality of tuning. The need for a third dispersive element towards wavelength degeneracy adds undesirable complexity, and it would be desirable to find an alternative means of operation at wavelengths with high inherent linewidth. Furthermore, this line-narrowed OPO was developed as a low-power first-stage for an oscillator/amplifier system with the aim of producing high average power single mode output. The development of the second stage of this system either as an injection seeded OPO or as an optical parametric amplifier is currently being undertaken.

A few general points can be made regarding the use of urea and BBO in conjunction with an excimer pump source. Firstly, urea possesses a major drawback in its susceptibility to multishot UV damage, while the transmission quality of BBO is in our own experience rather poor. These problems could perhaps be alleviated through advances in growth technique. Secondly, this thesis has demonstrated that the excimer laser can provide equivalent performance to alternative UV OPO pump sources and has advantages in terms of high average power and selection of wavelengths. Clearly, though, the desirability of high beam quality all-solid-state sources, and the increasing power capabilities of diode-pumped solid-state lasers, indicates that in future all-solid-state OPOs involving materials such as urea and BBO will be highly prominent. However current work seems likely to show that Lithium Borate will supersede these materials for some applications-in particular those involving low energy pump sources.

Appendix A : Crystal axis systems

Three axis systems are generally used to describe the properties of nonlinear optical crystals. These are the crystallographic axes (abc), the principal optical axes (xyz), and the tensor reporting frame axes (XYZ), otherwise known as the piezoelectric axes. The principal optical axes (xyz) are defined such that the associated principal refractive indices (n_x , n_y , n_z) are related by $n_z > n_y > n_x$. The current definition of these three axis systems (I.E.E.E./A.N.S.I. std. 176-1987) has these as right-handed frames of reference, and for a given crystal class there is a particular relationship between the different axes.

For a negative uniaxial crystal such as BBO this relationship is sufficiently defined by

$$x \equiv c \equiv Z.$$

For a positive uniaxial material such as Urea

$$z \equiv c \equiv Z.$$

A further frame of reference, known as the nonlinear optical (NLO) reporting frame (123) may be used (see ref. 1) to define the angles θ, ϕ in uniaxial crystals. For negative uniaxial crystals, (123) $\equiv$ (yzx), and for positive uniaxials, (123) $\equiv$ (xyz). In each case θ is measured from axis 3 towards the 1-2 plane, while ϕ is measured from 1 towards 2.

In an orthorhombic crystal of class mm2, such as LBO, the axes are related by

$$y \equiv c \equiv Z.$$

The definition of the relationship between the axes in orthorhombic crystals is currently the subject of review (ref. 1).

Ref. 1 D.A. Roberts, "Simplified characterisation of uniaxial and biaxial nonlinear optical crystals: a plea for standardisation of nomenclature and conventions", submitted to I.E.E.E. J. Quant .Elect (1992).

Appendix B : Sellmeier relations for nonlinear materials

The following Sellmeier relations were used in phase-matching calculations shown in figures 3.2 to 3.5:

Urea[1]

$$n_o^2 = 2.1823 + \frac{0.0125}{(\lambda^2 - 0.0300)}$$

$$n_e^2 = 2.51527 + \frac{0.0240}{(\lambda^2 - 0.0300)} + 0.0202\,\frac{(\lambda - 1.52)}{((\lambda - 1.52)^2 + 0.08771)}$$

Equations have also been developed[2] for urea doped with 0.1% Br.

BBO[3]

$$n_o^2 = 2.7405 + \frac{0.0184}{(\lambda^2 - 0.0179)} - 0.0155\lambda^2$$

$$n_e^2 = 2.3730 + \frac{0.0128}{(\lambda^2 - 0.0156)} - 0.0044\lambda^2$$

Alternative BBO Sellmeier relations are also given in refs. 4 and 5.

KDP[6]

$$n_o^2 = 2.259 + \frac{0.01009}{(\lambda^2 - 0.0129)} + \frac{0.0325}{0.0025 - 1/\lambda^2}$$

$$n_e^2 = 2.133 + \frac{0.00864}{(\lambda^2 - 0.0123)} + \frac{0.00807}{0.0025 - 1/\lambda^2}$$

LBO[7]

$$n_x^2 = 2.45316 + \frac{0.01150}{(\lambda^2 - 0.01058)} - 0.01123\lambda^2$$

$$n_y^2 = 2.53969 + \frac{0.01249}{(\lambda^2 - 0.01339)} - 0.02029\lambda^2$$

$$n_z^2 = 2.45316 + \frac{0.01412}{(\lambda^2 - 0.00467)} - 0.01850\lambda^2$$

Further Sellmeier coefficients have been published in refs. 8 to 13.

Appendix B

References

1 M.J. Rosker, K. Cheng and C.L. Tang, I.E.E.E. J. Quant. Elect. **QE-21**, p1600 (1985).

2 W.R. Donaldson and C.L. Tang, Appl. Phys. Lett. **44**, p25 (1984).

3 D. Eimerl et al., J. Appl. Phys. **62**, p1968 (1987).

4 C. Chen et al., Digest of Technical Papers of the Xiiith International Quantum Electronics Conference, 1984, paper MCC5 (unpublished).

5 K. Kato, I.E.E.E. J. Quant. Elect. **QE-22**, p1013 (1986).

6 F. Zernike Jr., J. Opt. Soc. Am. **54**, p1215 (1964).

7 S. Lin, B. Wu, F. Xie and C. Chen, Appl. Phys. Lett. **59**, p1541 (1991).

8 F. Hanson and D. Dick, Opt. Lett. **16**, p205 (1991).

9 C. Chen et al., J. Opt. Soc. Am. B **6**, p616 (1964).

10 S. Lin et al., Appl. Phys. Lett. **59**, p2805 (1991).

11 K.Kato, I.E.E.E. J. Quant. Elect. **QE-26**, p1173 (1990).

12 S. Velsko, M. Webb, L. Davis and C. Huang, I.E.E.E. J. Quant. Elect. **QE-27**, p2182 (1991).

13 T. Ukachi, R.J. Lane, W.R. Bosenberg and C.L. Tang, J. Opt. Soc. Am. B **9**, p1128 (1992).